Modelling Different Mechanical Damage Mechanisms of Ultra-high Molecular Weight Polyethylene Liners in Total Hip Replacements

Nicholas Benedict Cooper

Submitted in accordance with the requirements for the degree of
Doctor of Philosophy

The University of Leeds
School of Mechanical Engineering

November 2023

The candidate confirms that the work submitted is his own and that appropriate credit has been given where reference has been made to the work of others.

Acknowledgements

First and foremost, I would like to thank DePuy Synthes Joint reconstruction for financially supporting this project and for providing the components used in this Thesis for experimental testing and characterisation.

I would also like to give my warmest thanks all of the members of my supervision team:

To Ruth Wilcox and Sophie Williams, for your compassionate supervision and leadership that supported me and the whole office throughout the COVID-19 pandemic. Also, for providing me with so many opportunities to develop as a researcher and a person.

To Lee Etchels, for coming to so many supervision meetings where I didn't have anything for you but always being supremely helpful whenever I did.

To Sami Tarsuslugil and Oscar O'dwyer Lancaster-Jones, for providing such valuable inputs to help direct the research towards worthwhile goals.

In addition, I would like to give deepest thanks to many others who have supported this project including all of the technical staff who have worked in iMBE during this period. I would like to extend a special thanks:

To Nagitha Wijayathunga, for your kindness and for performing the micro-CT scans for this Thesis.

To Daniel Baker, for your generosity and for helping with Raman spectroscopy measurements.

To Camille Hammersley, for making a windowless metrology lab the best place to be and for your assistance with developing CMM programs.

To Andrew Stockdale, for being yourself and helping in countless different ways throughout the research.

To Keith Dyer, for having the magic touch with the hip simulator.

To Raelene Cowie and Amisha Desai, for your endless simulator wisdom and knowledge without which I would have stood no chance of completing this work.

And lastly to, Mackenzie Smeeton and Taiyibah Afzal – for being the most amazing people to have by my side through all of the ups and downs. I'm so proud of you both.

Finally, I would like to give my heartfelt thanks to my family and friends. A special thanks goes to my parents, Jane and Martyn, for raising me as you did; to Edward, Lucy, Kendall, Andrew, Guy, Mark, Pete and Harvey for your friendships during this PhD, and most importantly, to Eliza who has been through every step of the way with me. I'll never meet a kinder person in my life.

Abstract

Over 1 million total hip replacements (THRs) are performed around the world every year. Advances in the polyethylene liner materials have improved the wear resistance and longevity of well-functioning THRs. However, THRs with malpositioned components and unbalanced tissue forces can generate loading to the edge of liners that may limit their durability. Maintaining very low clinical rates of liner fatigue or fracture related revisions is important for maximising THR longevity. The aim of this research was to investigate the types of damage that occur to polyethylene THR liners when subjected to edge loading conditions to better understand possible damage mechanisms and risk factors.

The research combined experimental hip simulator studies with finite element (FE) modelling to simulate edge loading in THR components. New geometric and microstructural characterisation methods using a co-ordinate measurement machine (CMM) and Raman Spectroscopy were developed to analyse the development of damage at the liner edge which was also visualised by MicroCT scans.

Investigations of a clinically available liner (5 mm thickness) did not produce signs of liner damage or potential failure after 4 million cycles (Mc) of edge loading in the hip simulator. Changes to the liner edge geometry were linked to plastic strain accumulation in the FE model but stabilised early during this testing with no evidence for any progressive damage accumulation.

Specially thinned liners (3 mm thickness) were subsequently tested in the hip simulator to accelerate the progression of damage. The study was dominated by two separate adverse events related to the disruption of liner fixation and resulted in large deformations to liners (> 1 mm). After the 3 Mc test, microCT scans revealed damage initiated in some liners at the liner backside due to gaps related to the component locking mechanism. FE modelling of thinned liners showed that stresses and plastic strains could be transmitted through the liner thickness and particularly in the case of unsupported polyethylene.

The results suggest that when polyethylene liners were subjected to edge loading the interaction between the liner and shell locking mechanisms had the most potential for damage initiation. Ensuring that liners remain sufficiently thick and well supported helped them to be more resilient to the effects of edge loading.

Table of Contents

List of Tables

List of Figures

Abbreviations

A HXLPE	Annealed HXLPE
AO-HXLPE	Antioxidant HXLPE
CMM	Co-ordinate measurement machine
CT	Computer tomography
CPE	Conventional polyethylene
DSC	Differential scanning calorimetry
FE	Finite element
FHRs	Femoral head rotations
FWHM	Full width half maximum
GLS	Gaussian-Lorentzian sum (function)
HXLPE	Highly crosslinked polyethylene
Mc	Million cycles
NJR	National joint registry for England, Wales, Northern Ireland and the Isle of Man
NMR	Nuclear magnetic resonance
OA	Osteoarthritis
PSE	Plastic strain energy
RM HXLPE	Re-melted HXLPE
SA HXLPE	Sequentially irradiated and annealed HXLPE
SAXS	Small angle X-ray spectroscopy
SEM	Scanning electron microscopy
TEM	Transmission electron microscopy
THR	Total hip replacement
UHMWPE	Ultra-high molecular weight polyethylene
VE	Vitamin E
WAXS	Wide angle X-ray spectroscopy

Chapter 1 – Thesis introduction, aims and objectives

1.1 Introduction – the clinical need

Over 1 million total hip replacements (THRs) are performed around the world every year (Ferguson *et al.*, 2018). It is a very successful intervention for late stage osteoarthritis (OA) and one of the most successful surgical interventions in healthcare (Colic and Sedmak, 2016). The number of THRs is set to continue rising due to an aging population, increasing obesity levels and an increase of surgeries performed in patients under 60 years old (Pivec *et al.*, 2012). Obese patients are surgically more challenging and place more stress on replacement components during use. Younger patients need their components to last longer while also holding higher expectations of their activity levels. These factors alongside the backdrop of tighter healthcare budgets and means there is a clinical need to continue improving THRs.

A polyethylene liner made from ultra-high molecular weight polyethylene (UHMWPE) is the primary material of choice for the acetabulum bearing surface of THRs, accompanied by a metal or ceramic femoral head (NJR, 2023). UHMWPE is an ideally suited material because of exceptional wear resistance, biochemical inertness and low friction (Kurtz, 2016). However, the wear resistance of unmodified conventional UHMWPEs (CPEs) was previously a limiting factor in the clinical longevity of THRs largely due to wear particle induced osteolysis and aseptic loosening (Harris, 2001; Abu-Amer, Darwech and Clohisy, 2007; Kandahari *et al.*, 2016).

The current generation of UHMWPE materials used in THRs are irradiated to produce chemically crosslinked polyethylenes (HXLPEs) and antioxidants (AO) such as vitamin E (VE) may be added to produce AO-HXLPEs (Bracco *et al.*, 2017). These materials are used in over 97% of THRs today have been used clinically since 1998 and 2007 respectively (AJRR, 2022; Australian Orthopaedic Association, 2023). Chemical crosslinking greatly improves the wear resistance of UHMWPE and these modern polyethylenes exhibit wear rates – of beneath 0.1 mm per year – at which the occurrence of osteolysis is considered rare (Dumbleton, Manley and Edidin, 2002; Wilkinson *et al.*, 2005; Affatato *et al.*, 2012; Lindalen *et al.*, 2019; Moon *et al.*, 2020).

As polyethylene liners have become more wear resistant a greater focus has been possible on improving the stability of THRs. Dislocation was the second highest indication for revision (behind aseptic loosening) and primarily occurs in the first year after surgery (NJR, 2023). As with other causes of early failure, dislocation has a debilitating effect on the prognosis of THR surgery (Ong *et al.*, 2010). The risks of re-revision(s) or recurrent dislocations are increased with detrimental effects on the patient's outcomes, satisfaction and the economic cost of treatment (Kotwal *et al.*, 2009; Bozic *et al.*, 2015). Methods to improve stability include using larger bearing diameters, good head-neck ratios and design features such as extended rims (Sultan *et al.*, 2002; Takahashi, Tateiwa, Shishido, *et al.*, 2016b; Tsikandylakis *et al.*, 2018; Perticarini, Rossi and Benazzo, 2020). Combinations of larger heads with relatively small shells can produce thin regions of polyethylene and extended rims provide extra head coverage above the acetabular shell to improve stability.

Clinical case studies of liner failure or fracture provide evidence that without appropriate care design features such as these have the potential to initiate damage when liners are subjected to adverse loading to the liner edge (Halley, Glassman and Crowninshield, 2004; Tower *et al.*, 2007; Moore *et al.*, 2008; Duffy *et al.*, 2009; Furmanski *et al.*, 2009; Blumenfeld *et al.*, 2011; Waewsawangwong and Goodman, 2012; Ansari *et al.*, 2013; Beecher *et al.*, 2014; Bates and Mauerhan, 2015). Around 1% revisions were reported to be from acetabular liner related failures or fractures (Australian Orthopaedic Association, 2023). Ensuring that THR constructs retain very low rates of fatigue or fracture related revisions remains an important part of maximising their longevity.

There is a distinct clinical need to better understand the types of damage that occur to polyethylene THR liners when subjected to edge loading conditions. The majority of the experimental and computational research into polyethylene liner performance to date has focused on polyethylene wear and well-aligned components. Changes to the liner edge were generally not evaluated effectively or not predicted at all. Therefore, new research methods that are designed specifically to provide insights into the changes at the liner edge as a result of adverse loading are necessary. A better understanding of the possible damage mechanisms and risk factors involved in edge loading will be beneficial to ensuring that THR designs and surgical guidance are effective at preventing and being resilient to edge loading and its effects.

1.2 Project aim

The overall aim was to investigate the types of damage that occur to polyethylene THR liners when subjected to edge loading conditions and improve the understanding of potential damage mechanisms and how they may progress to liner failure or fracture.

1.3 Project objectives

The project was split into the following research objectives:

1. To develop novel geometric characterisation tools to analyse the progression of wear and deformation at the liner edge when liners are subjected to edge loading conditions (Chapter 3).

2. To develop Raman Spectroscopy and MicroCT characterisation methodologies to evaluate surface microstructural changes and the presence of surface or sub-surface cracking when liners are subjected to edge loading conditions (Chapter 4).

3. To conduct an experimental hip simulator study to subject polyethylene THR liners to edge loading and to examine progression of the damage using the characterisation methods developed in objectives one and two (Chapter 5).

4. To develop finite element (FE) models of a THR under edge loading to evaluate the internal stress-strain environment of the liner, with the aim of relating the field outputs of the FE model to the experimental characterisation of deformation and damage (Chapter 6).

5. To develop an experimental hip simulator approach to accelerate the initiation of damage using thinner liners, and combine these results with corresponding FE model predictions to provide insights into potential damage mechanisms and how they may progress to liner failure or fracture (Chapter 7).

Chapter 2 – Literature review

2.1 Preface

This Chapter is split into three parts. Firstly, the topic of total hip replacements was reviewed with a focus on the causes of revision surgeries. Secondly, UHMWPE as a material was reviewed which examines its microstructure and mechanical behaviours. Finally, the current experimental and FE modelling research relating to edge loading in THRs was reviewed.

2.2 Total hip replacements (THRs)

2.2.1 The natural hip and osteoarthritis (OA)

The hip joint is a synovial ball and socket joint which connects the lower limbs of the body to the torso. The head of the femur articulates against the acetabulum of the pelvis and it plays a key role in the movement and weight bearing of the body. Articular cartilage at the articulating surfaces provides a low friction contact and helps transmit loads to the underlying bone (Fox, Bedi and Rodeo, 2009).

Osteoarthritis (OA) is a degenerative joint disorder which involves biological and mechanical elements. OA is the fastest growing cause of disability worldwide (Conaghan *et al.*, 2015) and around 10% of adults over the age of 45 are reported to display symptomatic OA of the hip (Jordan *et al.*, 2009). Physiologically, it causes structural changes to the joint including cartilage loss, abnormal bone remodelling and the inflammation to joint tissues. This presents as painful and stiff joints in patients which can severely impede daily functions and can dramatically reduce quality of life.

2.2.2 Treatment of osteoarthritis by THR

A total hip replacement (THR) is the most common treatment for late stage OA in the hip. Over one million THRs have been recorded by the National Joint Registry for England, Wales, Northern Ireland and the Isle of Man (NJR) since 2003 and OA was documented as the reason in over 90% of cases (NJR, 2023). THRs are considered to be one of the most successful surgical interventions available and a cost effective treatment of hip disorders (Colic and Sedmak, 2016).

The number of primary procedures per year doubled between 2006 and 2018 and at the time of writing there were more than 90 000 procedures

performed each year (NJR, 2023). The increase was driven by an aging population, increasing levels of obesity and an increasing trend of implanting THRs in younger patients (under 60 years of age). The increase in surgical volume is accompanied by increasing patient expectations on the performance of their prosthesis as well.

In addition to primary procedures, revision surgeries are required to replace defective components when they are failing to function. Around 3-5% of THRs required revision surgery in their first ten years (Paxton *et al.*, 2019; NJR, 2023). This rate was reported to increase to 25% and 42% by 20 and 25 years of prosthetic use respectively (Evans *et al.*, 2019). This indicates that a large proportion of patients will require at least one revision surgery during their life. Revision surgeries have a higher rate of complications and economic cost than primary surgery (Ong *et al.*, 2010). To combat the growing economic burden and patient demands of THRs there is a clinical need to improve THRs outcomes and minimise the frequency of revision surgeries.

2.2.3 An overview of THR components

Sir John Charnley is considered to be the father of the modern hip replacement. THR designs today are still based on his pioneering design from the 1960s. The aim is to replace damaged tissue with an artificial anatomical reconstruction that optimally loads the replacement joint and surrounding tissues to provide pain relief, increased mobility and long-term survivorship of the implant.

The role of orthopaedic device manufacturers, in collaboration with surgeons, is to provide a catalogue of products which accommodate the wide diversity of anatomies and biomechanics observed in patients. The orthopaedic surgeons must then correctly select and implant the most appropriate device for each patient.

Like the natural hip, typical THR designs consist of femoral and acetabular components (Figure 2.1A). The femoral components consist of a femoral head, neck and stem (or body); femoral designs can be monolithic or modular. The femoral head (the articulating surface) is a ball made of cobalt chrome (CoCr) or ceramic material which attaches to the neck made from either a CoCr or Titanium alloy. The articulating surface of the acetabulum component is typically a polyethylene or ceramic liner fitted into a metal shell which is fixed to the residual bone. Figure 2.1B and C define more specific regions of polyethylene liners which are pertinent to edge loading.

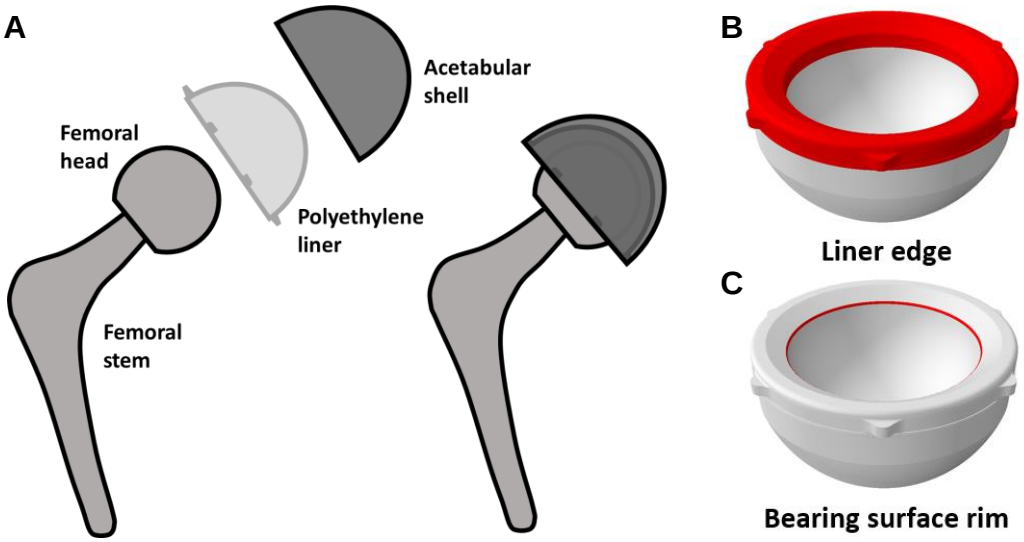

Figure 2.1 (A) A schematic of THR components. (B) For this research, the 'liner edge' defined the upper portion of the liner made up of the chamfer, top surface as well as the some of the bearing surface and liner backside (shown in red). (C) The 'bearing surface rim' more specifically defined the location where the bearing surface transitions onto the chamfer of the liner edge (shown in red).

2.2.4 Classification of THRs

Registries around the world collect long term data on the outcomes of THR surgeries. They provide feedback to surgeons, patients and the orthopaedic community on the current best practices in the field. The NJR uses three factors to primarily differentiate between THRs: fixation method, bearing type and head size (NJR, 2023).

2.2.4.1 Fixation method

There are two methods of fixation which can be used in different combinations for the acetabular and femoral components. Cemented fixations use bone cement to fix the femoral stem or acetabulum cup. For cementless fixations the components are pressed into place and fixed by osseous integration. Hybrid (cemented stem with cementless cup) and reverse hybrid (cementless stem with cemented cup) systems use a combination of these fixation methods (Table 2.1).

Table 2.1. How THRs are differentiated by fixation method.

Fixation method	***Cemented cup***	***Cementless cup***
Cemented stem	Cemented THR	Hybrid THR
Cementless stem	Reverse hybrid THR	Cementless THR

The use of fixation methods varies around the world. A universal trend was the growing use of cementless fixation, particularly for the acetabular component, which shows better results in patients under the age of 65 (Wyatt *et al.*, 2014). This method offers more surgical flexibility at both primary and revision procedures (Board, 2020). In the UK, a hybrid fixation was the most commonly used fixation method in 2022 (40.3%) (NJR, 2023). The use of hybrid fixation has continued to grow in favour over solely cementless (36.2%) and cemented (19.1%) fixation since 2012. Reverse hybrid was used in 2.3% of cases.

These statistics indicate an overall preference in the UK for cemented stems and cementless acetabular components. However, there is a role for both types of fixation to meet the patient's specific needs. For example, cemented fixation offered better results in patients over the age of 75 where periprosthetic fracture or poor bone quality is more of a prominent concern (Troelsen *et al.*, 2013). However, it is a more challenging surgical procedure with increased complexity at revision too (Board, 2020).

2.2.4.2 Bearing materials

The bearing materials are the surfaces in contact in the THR which articulate as the joint moves. They can be distinguished as either hard-on-soft (HoS) and hard-on-hard (HoH) bearings. The femoral head replacement is a 'hard' metal (CoCr) or ceramic (alumina or zirconia) material while the acetabular component may be a 'soft' polymer (polyethylene) or 'hard' ceramic. HoS bearings, were overwhelmingly the most common type of bearing and comprise of either metal-on-polyethylene (MoP) and ceramic-on-polyethylene (CoP). In 2022, these bearings were used in around 42% and 49% of THR procedures respectively (NJR, 2023).

Concerns over wear induced failure (osteolysis and aseptic loosening) with earlier polyethylene materials led to the development and use of hard-on-hard bearing materials (Kurtz and Ong, 2016). The philosophy behind hard-

on-hard bearings was to provide superior wear rates. However, ceramic-on-ceramic (CoC) bearings are the only HoH bearing used in any significant numbers (around 4% of THRs in 2022). Their use continues to decline in favour of CoP due to improvements to polyethylene materials and excellent survivorship of MoP and CoP constructs which are also cheaper (NJR, 2023).

Metal-on-metal (MoM) THRs were presented as an alternative to MoP constructs in the early 2000s. Large numbers of MoM THRs were implanted during the 2000s. As a much harder material, metal bearing surfaces resulted in much lower wear rates as expected. However, the resultant metal wear particles produced more severe adverse tissue reactions in the hip and increased revision rates. The failure of metal-on-metal THRs has been well documented (Silverman, Ashley and Sheth, 2016) and now only an extremely small number of them are implanted a year (<0.1% in 2022).

2.2.4.3 Bearing diameter

The bearing diameter or head size of a THR was historically considered a trade-off between stability (risk of dislocation) and long term THR survivorship due to polyethylene wear. Larger heads have a longer sliding distances and greater sliding speeds which increase wear (Girard, 2015). However, current polyethylenes with greater wear resistance have enabled larger heads to be adopted without as much concern over polyethylene wear. This was demonstrated by the fact that in 2022 a 32 mm (most common) or a 36 mm (second most common) were considered to be the optimal bearing sizes available (NJR, 2023). These diameters have replaced the more historically favoured 22-28mm heads that were more forgiving to polyethylene wear. Head sizes larger than 36 mm were reported to provide no functional benefits to THRs (Girard, 2015; Tsikandylakis *et al.*, 2018).

Using larger bearing diameters reduces the risk of dislocation by widening the impingement free motion and increasing the jumping distance (the distance required for dislocation to occur) of the THR (Girard, 2015; Zijlstra *et al.*, 2017). The range of motion increases because the head-neck ratio of the THR increases when larger bearing diameters are used (Tsikandylakis *et al.*, 2018). However, when large bearing diameters are combined with relatively small shell sizes it is possible to result in thin regions of polyethylene in the liners.

2.3 THR revision

The surgical aim of THRs is to restore the joints natural biomechanics and achieve a stable and long term fixation of the components to increase the patient's mobility and relieve pain. THRs not performing this function require a revision surgery to replace the defective components. Revision indications can be split into short-term or long-term causes depending on whether they predominantly increase or decrease in incidence over time. Figure 2.2 displays the indications of revision in order of their incidence rate (NJR, 2023). All the graphs in Section 2.3 use data from the 2023 NJR report which collates data from 2003 to 2022. Therefore, a variety of bearing materials – including MoM bearings and multiple generations of UHMWPE liner materials – contribute to the overall incidence rates.

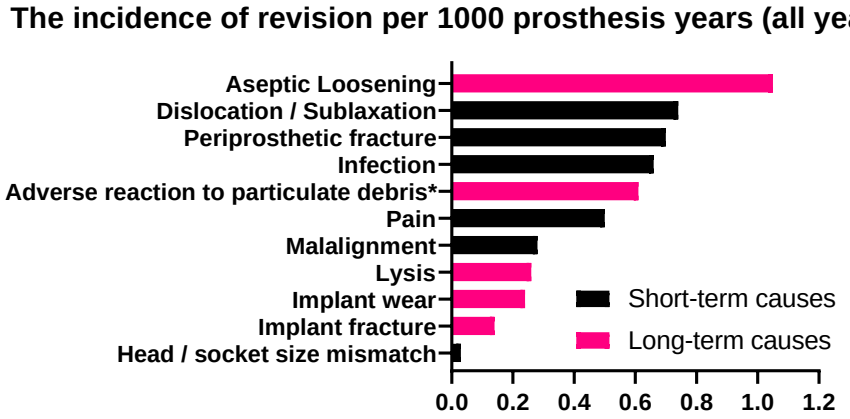

Figure 2.2 Indications of revision per 1000 prosthesis years where short- and long-term causes are indicated. *Data only from 2008 onwards when adverse reaction to particulate debris became an explicit option on the form recording data about revision (NJR, 2023).

2.3.1 Long-term causes of revision

Long term causes of revision increase in incidence over time (Figure 2.3). Aseptic loosening – or the loss of prosthesis fixation without infection – was the most commonly cited reason of all revision. The loss of mechanical fixation progresses symbiotically with the biological fixation loss induced by the accumulation of wear particles (Anil, Singh and Schwarzkopf, 2022). The wear particles induce osteolysis resulting in bone reabsorption around the prosthesis and over time contributes to fixation failure (or late loosening). Incidences of early loosing also occur but they were predominantly related to mechanical factors and the quality of the initial fixation.

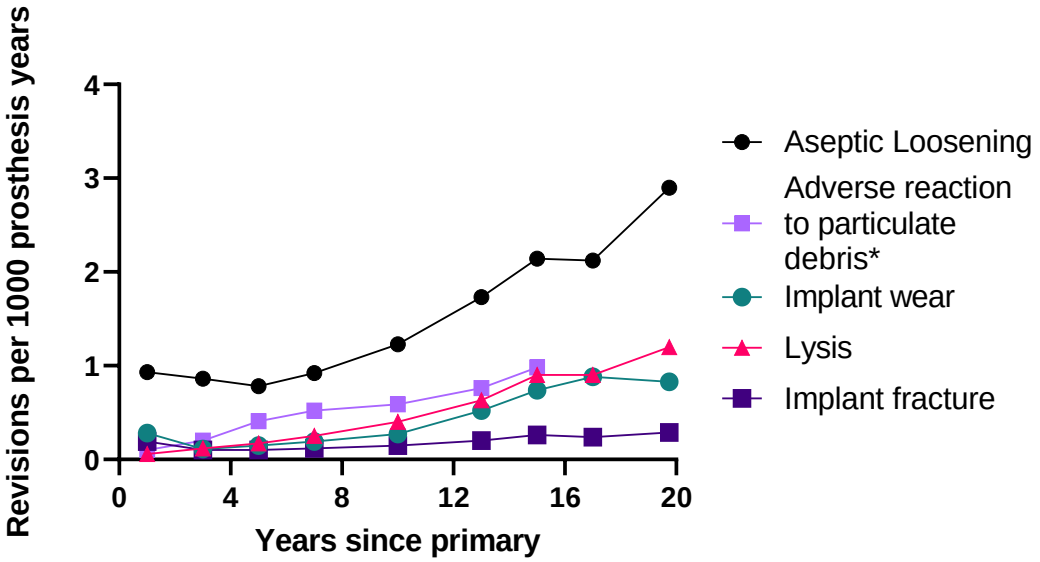

Figure 2.3 The long-term indicators for revision by years since primary surgery. *Data only from 2008 onwards when adverse reaction to particulate debris became an explicit option on the form recording data about revision. Hence the longest revision time data is missing (NJR, 2023).

Lysis and adverse reaction to particulate debris are also wear particle-based reactions although predominantly to metal debris. Therefore, their incidence rates were skewed upwards by MoM bearing surfaces that are no longer routinely used (NJR, 2023). However, the incidence of these indications for MoP and CoP prostheses still reached non-trivial levels as implant time increases due to debris from impingement between THR components (NJR, 2023).

Indications for implant wear and implant fracture relatively broadly cover the wearing out of components or mechanical based failures; the overall indication rates for these were much lower than other indications. The Australian Orthopaedic Association joint registry provides a more granular breakdown of these types of revision indications. With modern THR constructs it was reported that around 1% of revisions were attributed specifically to the breakage of acetabular components (Australian Orthopaedic Association, 2023). These are mostly linked to adverse loading conditions within the hip and mechanical fatigue-based failure of the acetabular liner.

Collectively, the long-term accumulation of polyethylene wear particles or metal debris from implant impingement continues to be a vital consideration for THR outcomes. However, their incidence has declined since the adoption of improved polyethylene liners materials which are more wear resistant (Australian Orthopaedic Association, 2023). By reducing wear-based revision instances, short-term indications have become an increasingly more significant limitations to THR survivorship (AJRR, 2022; Australian Orthopaedic Association, 2023). Ensuring future THR constructs retain low rates of polyethylene wear and very low rates of fatigue or fracture related revisions remains an important part of maximising their longevity.

2.3.2 Short-term causes of revision

Short term indications for revision are all at their highest risk in the first year after surgery (Figure 2.4). Dislocations and subluxations both relate to instability within the hip and result in the complete or partial displacement of the component bearing surfaces. These were the second most common indication for revision behind aseptic loosening (NJR, 2023). Component positioning, impingement occurrence and joint laxity were considered important factors in dislocation risk (Dargel *et al.*, 2014). Non-optimal component positioning increased the chances of impingement which contributed to dislocation by causing the femoral head to be levered out of the acetabular liner. In one retrieval study 94% of the liners removed for dislocation were also observed to have impingement damage (Won *et al.*, 2005). The surgeon can help reduce dislocation by using larger head sizes and an anterior surgical approach (Australian Orthopaedic Association, 2023).

Infection occurs when pathogens form a biofilm on the implant surface. This and the subsequent immunological and inflammatory response damage the surrounding tissue causing pain, loss of function and even the possibility of systemic illness or death. Infection was reported to occur in around 1% of THR cases (Lindgren *et al.*, 2014). It was most common in obese patients or patients with worse general health condition (ASA scores) which is associated with impairment of the body’s immune responses (Dobner and Kaser, 2018; Peters *et al.*, 2020).

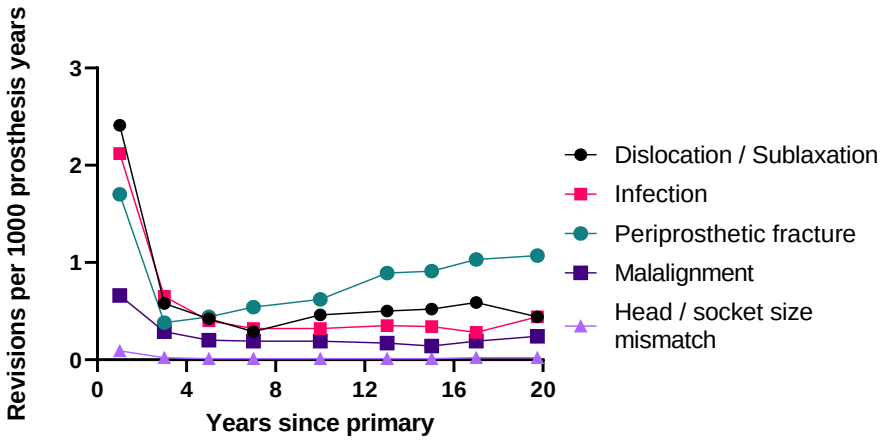

Figure 2.4. Short term causes for revision by years since primary surgery. (NJR, 2023)

Periprosthetic fracture is a fracture of the bone surrounding the prosthetic components. It can occur intraoperatively or post-operatively. Studies found higher rates of periprosthetic fracture in uncemented stems (Lindahl, 2007; Søren Solgaard and Anne Grete Kjersgaard, 2014). Elderly patients, female patients and those with higher ASA scores all had higher rates of periprosthetic fracture often linked to osteoporosis and reduced bone quality (Meek *et al.*, 2011; Berend *et al.*, 2016; Peters *et al.*, 2020). Dislocations, periprosthetic fractures and infections were all a higher risk for elderly patients (Ferguson *et al.*, 2018).

2.3.3 Revision surgery and the risk of re-revision

Revision surgeries have a higher rate of complications and a higher economic cost than primary surgeries. Patients undergoing a revision surgery were reported to be five times more likely to require a subsequent re-revision compared to a primary surgery (Ong *et al.*, 2010). In addition, patients with prosthesis that are revised within their first 12 months were around twice as likely to need re-revision surgery (for any timepoint) in the future compared to patients with primaries that lasted at least 5 years (NJR, 2023). This was most prominently due to an increased risk of dislocation and infection associated with revision surgery compared to primary THR surgery (NJR, 2023). These statistics demonstrate that the consequences of early revisions were more significant than long-term revisions because of the subsequent effect they had on THR prognosis resulting in worse patient outcomes and increased treatment costs. This underlines the desirability behind design features which increase THR stability and reduce dislocation – the most prevalent of early revision causes.

2.4 Factors influencing THR longevity

THR longevity is determined by a complex interplay of device, patient and surgical related factors. The breadth and interconnectivity of factors leads to a high degree of possible variability between patient outcomes.

2.4.1 Patient factors

The majority of THR surgeries were performed on patients between age 60 and 75 (NJR, 2023). Around 20% of THRs are implanted into patients under the age of 60 (Kumar, Bloch and Esler, 2017). The proportion of younger patients receiving THRs was expected to grow in proportion in years to come (Pivec *et al.*, 2012). Younger patients were consistently found to have higher rates of revision for both early and total revision (Santaguida *et al.*, 2008; Bayliss *et al.*, 2017). Patients who require THR surgery at an earlier age were more likely to have underlying factors which accelerate the osteoarthritis pathway to THR surgery and subsequently to THR revision surgery as well (Bayliss *et al.*, 2017). Furthermore, younger patients may hold higher expectations about their prosthesis and on average tend to be more active. This places their implants through both higher and more repeated loading which increases revision risk (Shia *et al.*, 2009; Pivec *et al.*, 2012).

A patient's anatomy and biomechanics influences how loads and strains are applied to the natural hip; this remains true for replacement joint prosthesis (Ardestani, Amenábar Edwards and Wimmer, 2017). The pathway from OA onset, progression to a THR (and revision surgery) was predisposed in patients with abnormal hip geometries and then accelerated by obesity (Lespasio *et al.*, 2018).

Musculoskeletal pathologies were also found to play an important role in co-morbidities through their impact on both mental and physical health. In one example of this, patients with higher ASA scores (indicating worse health) were found to have an increased risk of early revision (Peters *et al.*, 2020). Finally, the patient compliance to pre-surgical conditioning and post-surgery rehabilitation was shown to improve the functional outcomes of THR surgery (Monaghan *et al.*, 2017; Peters *et al.*, 2020).

2.4.2 Surgical factors

Orthopaedic surgeons must correctly select and implant the most appropriate prosthesis for each patient. The learning curve associated with THR surgery is relatively long; surgeons were found to need at least 50 surgeries before their revision rate began to level off (de Steiger, Lorimer and Solomon, 2015). Similarly, the centre and surgeon volume of procedures per year also impacted THR revision rates (Baker *et al.*, 2013).

There are several surgical approaches available to the surgeon. The literature suggested there was not necessarily a universally best approach (Higgins *et al.*, 2015). Each approach had different implications with regards to the recovery time and the relative risk of different revision causes (Zijlstra *et al.*, 2017). Therefore, patient specific factors could influence whether one particular approach is more favourable. For example, anterior approaches were found to reduce the risk of dislocation but it is disputed whether it is to the detriment of other revision causes compared to the posterolateral approach (Sheth *et al.*, 2015; Zijlstra *et al.*, 2017).

2.4.3 Stem design considerations

Secure fixation of the stem is achieved by minimising stem movement and enabling it to effectively transmit loads without high peak stresses (Scheerlinck and Casteleyn, 2006). Cementless stem designs, for example, can be coated to improve fixation, include different tapers and be collared or collarless. The surgeon will decide for each patient the best solution to achieve fixation while also minimising the risk of periprosthetic fracture.

The stem geometry (of any design) can be defined by its stem length, femoral offset (Figure 2.6B), neck shaft angle and version. The surgeon will select dimensions that achieve the correct leg length and femoral offset for each patient (Kim and Yoo, 2016). This is a key element in helping restore the joint’s natural biomechanics, reduce the risk of prosthetic or bony impingement and prevent soft tissue laxity (DePuy Synthes, 2018).

2.4.4 Polyethylene liner design considerations

Polyethylene liners are available in a variety of bearing sizes (Section 2.2.4.3) and configurations (Figure 2.5). The polyethylene liner thickness will largely be dependent on the relative bearing diameters of the polyethylene liner and the acetabular shell. Liner thickness may also be influenced by adopting non-neutral liner configurations. A neutral configuration provides around 180-degree coverage of the femoral head. The top of these liners sit almost flush within the acetabular shell backing.

Various liner configurations may provide additional stability to THR constructs. Liners with elevated rims purposefully protrude out of the shell to increase the femoral head coverage in the direction most at risk of instability. The material positioned above the acetabular shell backing can be viewed as being unsupported by the shell. While helping to reduce the risk of dislocation the elevated rim also reduces the available range of motion and increases the risk of impingement (Sultan *et al.*, 2002; Insull *et al.*, 2014).

Lateralised liners improve stability by increasing abductor tension while face changing liners (which are also lateralised) alter the liner inclination without a change to the acetabular shell orientation (Sheth *et al.*, 2016). These design configurations also introduce more unsupported polyethylene material than neutral liners or may alter liner thickness. Various locking mechanisms, including tabs, grooves and tapers provide liners with both pull-out and rotation resistance (Jaeger *et al.*, 2020). These ensure the liner remains firmly fixed in place within the metal shell. Gaps in the interface between the shell and the liner at the liner locking mechanisms may also introduce smaller regions of unsupported polyethylene.

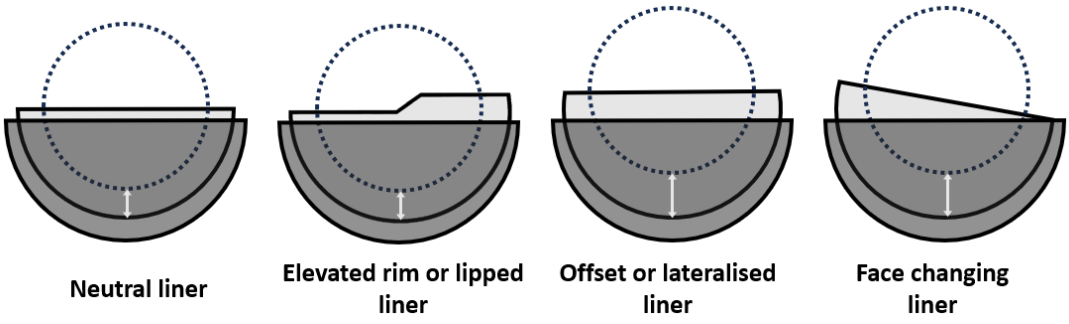

Figure 2.5. Various polyethylene liners configurations can provide additional liner stability but also potentially introduce thin or unsupported regions of polyethylene (by protruding out of the acetabular shell).

2.4.5 Component positioning and alignment

Correct component selection and placement of THR components optimises the articulation of the joint and provides the best chance of a secure fixation (Goyal, 2015). The surgical guidance which accompanies THR components describes the recommended position believed to minimise the risk of subluxation, edge loading or impingement for a THR system. For example, the reported optimal cup positioning for the DePuy Pinnacle system consisted of around 40 to 45 degrees of inclination and 15 to 20 degrees of anteversion (Figure 2.6A) (DePuy Synthes, 2018).

Several other ‘safe zones’ were reported in the literature with most suggesting a much wider range of acceptable angles (Goyal, 2015). One example, the Lewinnek safe zone, was commonly used to predict acceptable component position while investigating the occurrence of impingement or dislocation. However, the validity of this particular measure was highly questioned given that incidences of impingement and dislocation were still observed within the safe zone (Lewinnek *et al.*, 1978; Won *et al.*, 2005; Seagrave *et al.*, 2017). This highlights that establishing universal safe zones for a diverse patient group may be problematic. The scenario may be further complicated by the fact that acetabular version has been shown to be dynamic – to varying degrees – throughout a gait cycle (Vasiljeva *et al.*, 2020).

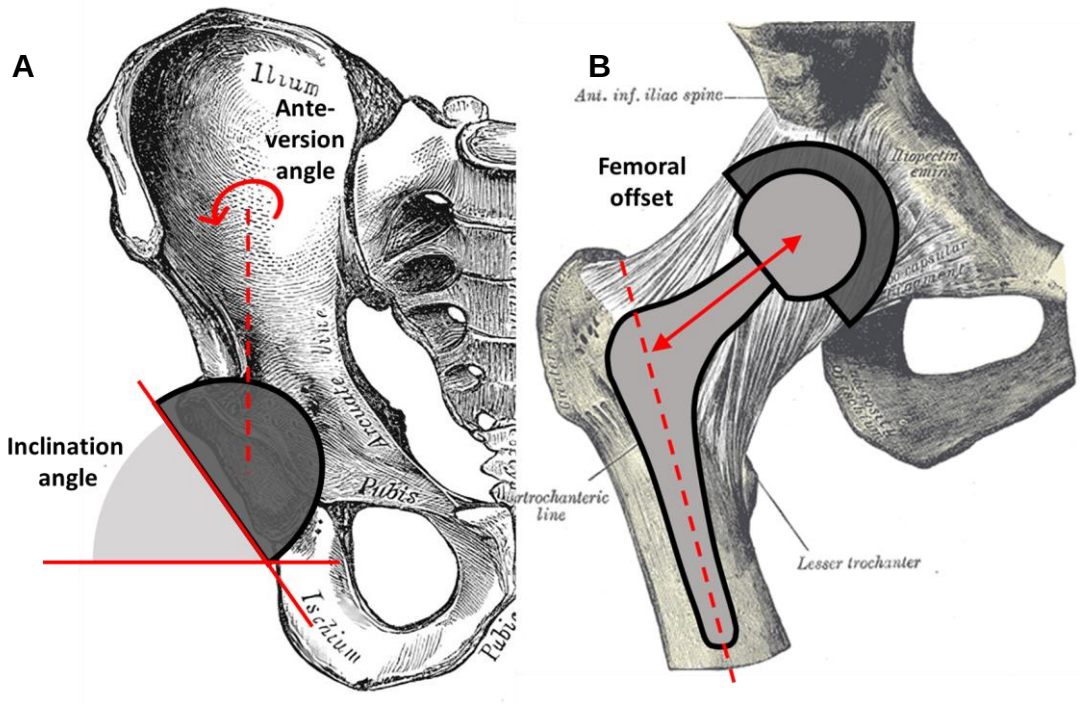

Figure 2.6. Adapted diagrams showing THR component positioning (Gray, 1918). (A) Acetabular inclination angle is the tilt away from the transverse plane in the coronal plane. The anteversion angle is the axial tilt away from the sagittal plane. (B) Femoral offset is the distance between the head centre of rotation and the central axis of the stem.

2.4.6 Adverse loading conditions

Adverse loading conditions, also referred to as edge loading, can be defined by the application of elevated loads or torques to the liner edge or liner locking mechanisms. Non-optimal positioning or mal-seated components

increase the occurrence and severity of edge loading (Moore *et al.*, 2008; Ast *et al.*, 2014). Across the literature edge loading was used to refer to multiple different types adverse loading. For this research, edge loading continues to be used as a general or umbrella term for loading to the liner edge (as illustrated in Figure 2.1B). The following definitions enable more specific types of edge loading to be referred to with precision.

Impingement loading is defined here by the unintended contact between two non-bearing surfaces. Figure 2.7A illustrates an example of prosthetic impingement where the femoral stem impinges on the edge of the polyethylene liner. Secondary to the primary impingement site there may also be edge loading at the egress site on the opposite side of the liner as the head is being levered out. Prosthetic impingements were linked to low inclination angles as well as a high combined anteversion angle between the femoral and acetabular components (Brown and Callaghan, 2008; Pryce, 2019). Bony impingements can also occur and result in instability or dislocation (Kessler *et al.*, 2008; Weber *et al.*, 2022).

Another specific form of edge loading occurs without impingement due to a separation (or subluxation) of the THR components. During component separations the femoral head contact is transferred from the central bearing surface to the rim of the bearing surface on the liner edge (Figure 2.7B). This contact generates elevated loads to the liner edge, especially during weight bearing. Edge loading by component separation was linked to malpositioned components, unbalanced tissue forces or joint laxity and it was exacerbated by excessive inclination angles (Hua *et al.*, 2016; Partridge, Tipper, *et al.*, 2018).

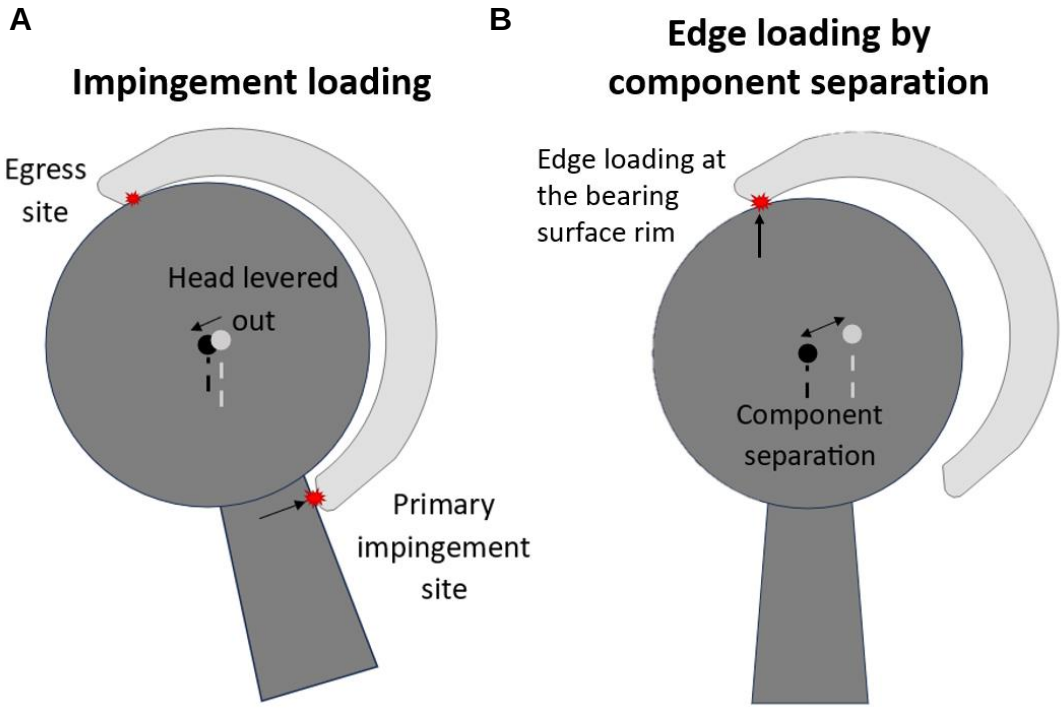

Figure 2.7. (A) impingement loading due to contact between the femoral neck and the liner edge. As the head is levered out there may also be edge loading at the egress site as the liner is levered out of the liner. (B) Edge loading by component separation occurs without impingement and causes the femoral head contact to transfer to the bearing surface rim.

2.4.7 Case studies of liner failure or fracture

Using joint registry data, Section 2.3 highlighted that revisions caused by liner failure or fracture have been an uncommon occurrence over the past 20 years. By understanding the confluence of factors necessary to produce liner failure or fracture to occur enables future THR constructs to remain resilient to these types of revision incidences. However, unlike long-term wear-based revision incidences, fatigue failures and fractures are unsuited to being studied longitudinally. Hence, the precise damage mechanisms which lead to fatigue failures or fracture are not as well understood as other revision causes. Clinical case studies are heavily relied upon to provide insights into the damage mechanisms from retrieved liners (Halley, Glassman and Crowninshield, 2004; Tower *et al.*, 2007; Moore *et al.*, 2008; Duffy *et al.*, 2009; Furmanski *et al.*, 2009; Blumenfeld *et al.*, 2011; Waewsawangwong and Goodman, 2012; Ansari *et al.*, 2013; Beecher *et al.*, 2014; Bates and Mauerhan, 2015).

2.4.7.1 Crack initiation and propagation

While multiple adverse loading scenarios were identified, the clinical case studies shared common patterns of crack initiation and propagation. Regions of thin polyethylene (usually between 2-4 mm) were a prominent factor across all of the case studies. These thin regions were particularly susceptible to crack initiation when located at the liner locking mechanism (Tower *et al.*, 2007; Moore *et al.*, 2008; Waewsawangwong and Goodman, 2012; Ansari *et al.*, 2013; Bates and Mauerhan, 2015) or in unsupported regions of polyethylene such as those in elevated rims (Halley, Glassman and Crowninshield, 2004; Duffy *et al.*, 2009; Furmanski *et al.*, 2009; Blumenfeld *et al.*, 2011; Beecher *et al.*, 2014).

In these studies, cracking was commonly initiated at these design features in the superior hemisphere of the liner on the backside as a result of stress concentrations when the liner experienced edge loading conditions. Cracking propagated radially inwards from the backside of the liner towards the bearing surface and in most cases extended laterally around the liner edge (between anti-rotation features) as well. The result was either the complete or partial fracture of a segment of the liner edge. Each of these processes is illustrated in Figure 2.8.

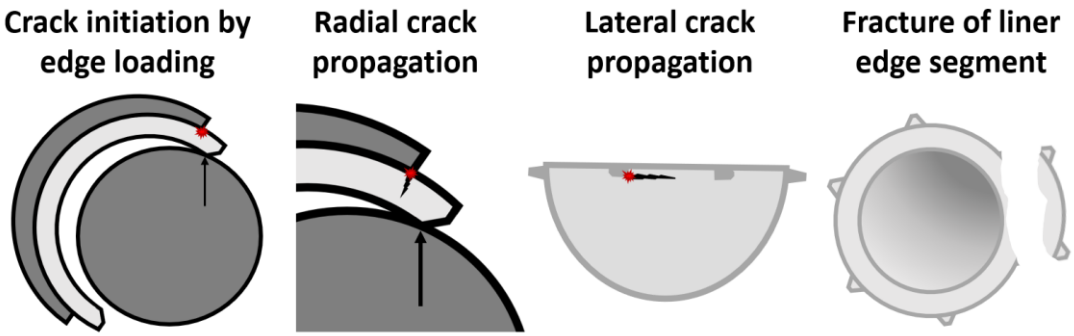

Figure 2.8. Schematic diagrams of processes of crack initiation, propagation and liner fracture described in the clinical case studies in Section 2.4.7.

2.4.7.2 Adverse loading scenarios: subluxation and high inclination

Tower *et al*. and Waewaswangwong *et* al. reported on a total of five liner failures across three patients (Tower *et al.*, 2007; Waewsawangwong and Goodman, 2012). A combination of thin polyethylene (less than 4 mm) at the liner edge and high inclination angles were prominent factors attributed to liner failure and subluxations during weight bearing were reported for all

three patients. The inclination of the liner and the subluxation both contributed to abnormally high stresses being placed on the liner edge and cracking was initiated superior quadrant of the groove of the locking mechanism. All five failures occurred between 7 and 27 months after implantation. Neither paper indicated the occurrence of any prosthetic impingement.

Halley *et al*. reported a similar case where a high inclination angle led to recurrent subluxation or dislocations events during extension (Halley, Glassman and Crowninshield, 2004). This generated adverse loading in the antero-superior region that was sufficient for crack initiation. The crack began in the elevated rim which was 6 mm thick but fracture only occurred once the crack propagated down into the equatorial region of the liner edge – which was only 3 mm thick – and then around the liner laterally. Revision of this HXLPE liner occurred after 10 months.

Blumenfeld *et al.* also attributed failure to repetitive subluxation and relocation of the femoral head. However, unusually in this case the failure occurred in the anterior quadrant (Blumenfeld *et al.*, 2011). Despite the difference in loading direction the crack initiation and failure mechanism were synonymous with those described above.

2.4.7.3 Adverse loading scenarios: unsupported polyethylene

Duffy *et al*. reported on the fracture of a lipped liner (Duffy *et al.*, 2009). The improper use of the elevated rim with a 4 mm liner lateralisation in this case led to repeated prosthetic impingement and after 24 months the fracture of the elevated rim region and failure of liner locking mechanisms.

Barrett *et al*. reported on fracture of a similar liner occurring secondary to the fatigue failure of the locking mechanism and anti-rotation features (Barrett, Van Citters and Hamilton, 2011). These initial failures allowed the liner to rotate and subsequently abnormal loading was generated at the junction between the shell and the elevated rim region.

Thin polyethylene at the superior locking rim (3.3 mm) was reported as a key factor in liner failure by Moore *et al*. (Moore *et al.*, 2008). Without excessive inclination or impingement loading it was the improper seating of the acetabular liner during primary surgery that led to the mechanical conditions for failure within 36 months. Cracking emanated from the locking ring which was protruding from the shell due to malpositioning and propagated around the liner edge.

2.4.7.4 Adverse loading scenarios: impingement loading

Furmanski *et al*. examined four cases with elevated rims and hypothesized that impingement loading due to malpositioned components was the fracture mechanism (Furmanski *et al.*, 2009). Cracking was initiated at stress concentrations in the unsupported regions of the liners. They propagated inwards towards the bearing surface and then around liner laterally in the plane of the upper edge of the metal shell until terminating at the adjacent anti-rotation feature.

Beecher *et al*. identified excessive anteversion (59 degrees) as the cause of the prosthetic impingement which ultimate led to liner fracture of an AO-HXLPE liner (Beecher *et al.*, 2014). Despite using a more fracture resistant material, the 5 mm lateralised design meant edge loading was applied to a thin (3.6 mm) and unsupported region of polyethylene. Fracture occurred in the antero-superior region of the liner after 16 months.

2.4.7.5 UHMWPE material factors

The case studies described in Section 2.4.7 also identified the reduction of fatigue and fracture resistance in HXLPEs (compared with CPEs) as a contributor to liner failure. The depletion of mechanical properties resulted from irradiation crosslinking and re-melting heat treatment processes used in the manufacture of HXLPEs (Section 2.5 extensively covers the types and processing of UHMWPEs used in THR liners).

Oxidation damage can further reduce the mechanical properties of UHMWPEs and was linked to liner fracture after seven years (Hara *et al.*, 2013). However, almost all of the case studies reported on fractures that occurred within three years of implantation and indicated that oxidation levels remained low (Tower *et al.*, 2007; Duffy *et al.*, 2009; Furmanski *et al.*, 2009; Beecher *et al.*, 2014; Bates and Mauerhan, 2015). Therefore, oxidation damage was certainly not a requirement for liner fracture to occur.

Cases of liner failure were not unique to HXLPE; examples of CPEs and AO-HXLPEs were also present in the literature (Berry *et al.*, 1994; Beecher *et al.*, 2014; Bates and Mauerhan, 2015). Overall, given the low rates of liner fracture across all polyethylene liner materials this suggests that the implant design and correct implantation (to avoid adverse loading) are likely to be the foremost considerations for reducing the risk of liner failure or fracture. Different UHMWPE materials will simply have some different degrees of tolerance to adverse loading conditions. A better understanding of these

limits will be beneficial to informing design practices and surgical guidance for future THR devices.

2.5 Ultra-high molecular weight polyethylene (UHMWPE) in THRs

2.5.1 Introduction

Ultra-high molecular weight polyethylene (UHMWPE) is a member of the polyethylene family. It is formed by polymerisation of ethylene gas (C_2H_4) into exceptionally long linear chains (Figure 2.9). The chains can fold, twist and rotate into crystalline lamellae structures which is surrounded by a matrix of amorphous chains resulting in a semi-crystalline microstructure. UHMWPE is the primary material of choice for the acetabulum bearing surface of THRs. It is ideally suited because of exceptional wear resistance, biochemical inertness and low friction properties and has a clinical history spanning over six decades (Charnley, 1961; Kurtz, 2016).

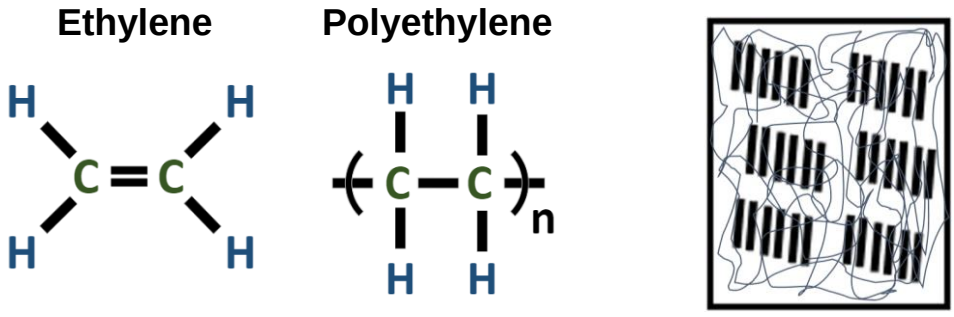

Figure 2.9. The chemical structure of Ethylene and Polyethylene and the microstructure of UHMWPE. Crystalline lamellae are surrounded by an amorphous matrix

2.5.2 UHMWPE classifications and liner manufacture

The manufacture of a conventional UHMWPE THR liner requires four major steps (Figure 2.10). The additional processing steps required to produce HXLPE and AO-HXLPEs are presented in Table 2.2. This table describes the effect different UHMWPE processing has on the material properties. Table 2.3 augments Table 2.2 by collating a selection of studies which illustrate numerically the differences observed between UHMWPEs.

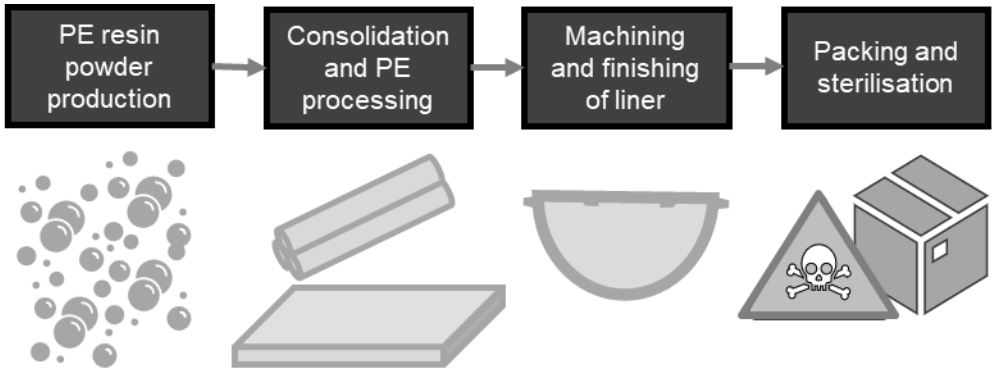

Step 1: Resin powder production by polymerisation of ethylene gas.

Step 2: Consolidation of resin powder by compression moulding (into sheets), ram extrusion (into rods) or direct-compression moulding (into near-net shaped implants).

Step 3: Machining and finishing into final form by milling and turning operations.

Step 4: Sterilisation and packaging is the final stage. Gamma or chemical sterilisation are the most common methods.

Figure 2.10. An overview of conventional polyethylene liner manufacture.

Table 2.2. A summary of clinical UHMWPEs and the impact of processing on their microstructure and mechanical properties.

Class	Clinical examples (year introduced)	Additional processing steps	Effect on microstructure and mechanical properties (also see Table 2.3)
CPEs	Clinical use of conventional UHMWPEs (**CPEs**) began in the 1960s. Today, they are rarely used.	Non-crosslinked or moderately crosslinked polyethylene (< 40 kGy dose) for sterilisation as per Figure 2.10.	Preferential chain alignment limits wear resistance to multidirectional sliding. Crystalline phases exist in a relatively mobile amorphous matrix providing toughness from ductile slip mechanisms.
HXLPEs	**RM HXLPEs** (re-melted): DePuy – Marathon (1998), AltrX (2007) Smith and Nephew – XLPE (2001) Zimmer – Durasul (1998), Longevity (1999) **A HXLPEs** (annealed): Stryker – Crossfire (1998), X3 (2005)	Chemical crosslinking by irradiation of the polyethylene (40-100 kGy dose) while in stock form followed by a stabilising heat treatment(s). **RM HXLPEs** are stabilised above the melt transition temperature (>137 degrees). **A HXLPEs** (e.g. Crossfire) are stabilised below the melt transition temperature (< 137 degrees). Sequentially annealed **(SA) HXLPEs** (e.g. X3) use a sequence of lower dosage irradiation and annealing steps.	Chemical crosslinking resists multidirectional wear but decreases toughness and ultimate properties. Re-melting prevents oxidation by recombining residual free radicals but diminishes crystalline properties reducing stiffness, strength and fatigue resistance. Annealing also recombines free radicals but maintains crystallinity. However, more free radicals may remain compared to re-melting.

AO-HXLPEs	**Blended** AO-HXLPEs: DePuy – AOX (2012) Zimmer – Vivacit-E (2012) Corin – ECIMA (2011) **Diffused** AO-HXLPEs: Biomet – E1 (2007)	AO is **blended** with the polyethylene powder before consolidation and irradiation. Or AO is **diffused** into the consolidated part after being irradiated. **Blending** impedes crosslink formation. **Diffusion** AO-HXLPEs require an additional post irradiation homogenisation step.	Chemical crosslinking resists multidirectional wear but decreases toughness and ultimate properties. Oxidation resistance exceeds even CPEs due to AO free radical scavenging without the need for a re-melting heat treatment. AO presence in the microstructure promotes chain mobility increasing creep and strain recovery.
Non-conventional UHMWPEs are the final class of UHMWPE (FDA, 2019). They include any UHMWPE material that does not fit into the other three types. These materials are not currently in any widespread use in THRs.			

Table 2.3. A selection of studies comparing the wear, mechanical and oxidative properties of the UHMWPEs (illustrative only).

Material property	CPE	A HXLPE	RM HXLPE	AO-HXLPE	Additional details	Source
Clinical wear rate (mm/year)	0.137	0.042		~	Weighted average of 2D linear penetration rates (meta-analysis). HXLPEs were analysed collectively.	(Kurtz and Patel, 2016)
	0.086	~	0.028	~	Linear wear rate of CPE (n=22) and HXLPE liners (n=112) with 15-18 years follow up.	(Moon *et al.*, 2020)
	~	~	~	0.02	Linear wear rate of VE-HXLPE liners (n=40) with 6 years follow up.	(Lindalen *et al.*, 2019)
Hip simulator wear (mg/Mc)	15	~	< 0	~	CPE 22 mm bearing diameter liners versus HXLPE 46 mm bearing diameter liners.	(Muratoglu and Bragdon, 2016)
	10	~	~	1	CPE 28 mm bearing diameter liners versus AO-HXLPE 36 mm bearing diameter liners.	(Oral et al., 2006)
Young's Modulus (MPa)	932	994	779	~	Compressive test at 20°C. CPE: 30 kGy, RM HXLPE: 100 kGy (150°C), A HXLPE: 100 kGy (110°C)	(Pruitt, 2005)
	748	~	636	803	Compressive test at 20°C. CPE: 0 kGy, RM HXLPE: 75 kGy (> 137 °C), VE HXLPE: 100 kGy (VE blend).	(Lu *et al.*, 2018)

Yield stress (MPa)	27.4	27.9	24.5	~	True tensile yield stress at 20°C. CPE: 30 kGy, RM HXLPE: 100 kGy (150°C), A HXLPE: 100 kGy (110°C)	(Pruitt, 2005)
	24 / 28	~	~	25 / 25	Non-aged / Aged tensile engineering yield stress. CPE: 25 kGy, AO-HXLPE: 85 kGy (VE diffused + 120°C homogenising anneal)	(Oral et al., 2006)
	10.8	~	8.8	13.1	Compressive true offset yield stress at 20°C. CPE: 0 kGy, RM HXLPE: 75 kGy (> 137 °C), VE HXLPE: 100 kGy (VE blend)	(Lu *et al.*, 2018)
Yield strain (%)	0.126	0.12	0.136	~	Tensile true yield strain at 20°C. CPE: 30 kGy, RM HXLPE: 100 kGy (150°C), A HXLPE: 100 kGy (110°C)	(Pruitt, 2005)
	2.2	~	3	2.6	Compressive true offset yield strain at 20°C. CPE: 0 kGy, RM HXLPE: 75 kGy (> 137 °C), VE HXLPE: 100 kGy (VE blend)	(Lu *et al.*, 2018)
Ultimate stress (MPa)	223	162	123	~	Tensile true ultimate stress at 20°C. CPE: 30 kGy, RM HXLPE: 100 kGy (150°C), A HXLPE: 100 kGy (110°C)	(Pruitt, 2005)
	52 / 33	~	~	46 / 45	Non-aged / Aged tensile engineering ultimate stress. CPE: 25 kGy, AO-HXLPE: 85 kGy (VE diffused + 120°C homogenising anneal)	(Oral et al., 2006)

Ultimate strain (%)	373	248	232	~	Engineering tensile strain at 20°C. CPE: 30 kGy RM HXLPE: 100 kGy (150°C). A HXLPE: 100 kGy (110°C)	(Pruitt, 2005)
	347 / 434	~	~	230 / 234	Non-aged / Aged tensile engineering strain. CPE: 25 kGy, AO-HXLPE: 85 kGy (VE diffused + 120°C homogenising anneal)	(Oral et al., 2006)
ΔK_{incep} ($MPa.m^{0.5}$)	1.19	~	0.56	0.77	Fatigue resistance. CPE: 25 kGy, AO-HXLPE: 85 kGy (VE diffused + 120°C homogenising anneal)	(Oral et al., 2006)
K_C ($MPa.m^{0.5}$)	4.5	2.8	3	~	Fracture resistance. CPE: 30 kGy, RM HXLPE: 100 kGy (150°C), A HXLPE: 100 kGy (110°C)	(Pruitt, 2005)
Oxidation index	0.84	3.39	0.03	~	After 128 weeks real time aging. CPE: gamma sterilised (25-40 kGy), A HXLPE: 75 kGy (130°C) + gamma sterilised, RM HXLPE: 95 kGy (150°C) + EtO sterilised.	(Wannomae *et al.*, 2006)
	1.9	~	~	0.1	After 4 weeks of accelerated aging. CPE: 32 kGy. AO-HXLPE 100 kGy, VE diffused and 122 homogenising anneal.	(Haider *et al.*, 2012)

2.5.3 Thermodynamic formation of UHMWPE microstructure

UHMWPE microstructure is dynamically determined by the material's thermal history and the mobility of its chains during that time. This is governed by the minimisation of Gibbs free energy (Equation 2.1) and reptation model of chain reconfiguration.

Equation 2.1

$$\boldsymbol{Gibbs\ free\ energy = Enthalpy - Entropy\,.Temperature}$$

At high temperatures, above the melt transition temperature (Tm), entropy dominates (Equation 2.1). A disordered, amorphous polymer melt state is energetically most favourable. On cooling through Tm – around 137°C (Kurtz, 2016) – enthalpy begins to dominate and crystalline structures will start to form. This is because of the reduction in internal energy associated with ordered crystalline phases and as secondary forces are introduced when chains become more densely packed. At room temperature roughly 50% of the chains in polyethylene are in a crystalline state but this varies with UHMWPE processing conditions (Turell and Bellare, 2004; Lombardo *et al.*, 2016). Further crystallisation is restricted by the high entanglement density in the polymer melt which limits chain mobility (Bracco *et al.*, 2017).

Reptation model indicates that chain reconfiguration is a diffusion driven process. The chains require sufficient time as well as thermal energy to reconfigure. Therefore, the crystalline characteristics will depend on both the processing conditions and cooling rates. For example, processing at temperatures nearer to Tm with slow cooling rates enables a higher crystalline percentages and thicker lamellae to form because the nucleation density will be lower and crystals have time to mature. Higher processing temperatures and slower cooling rates will increase the cost and decrease the production rate of polyethylene processing though.

Ultimately, the resultant mechanical and wear performance of different UHMWPEs can be interpreted through the prism of their microstructure and chain mobility. The microstructure will primarily be a result of processing conditions because of the elevated temperatures and forces applied during them. Whereas chain mobility is a critical component determining the yielding and wear behaviours of UHMWPE.

2.5.4 UHMWPE mechanical and wear behaviours

Several review papers examined the literature investigating structure-property relationships of UHMWPEs including their deformation and wear mechanisms (Pruitt, 2005; Ries and Pruitt, 2005; Rimnac and Pruitt, 2008; Sobieraj and Rimnac, 2009; Ansari *et al.*, 2016; Bracco *et al.*, 2017). They establish that UHMWPE exhibits strain hardening behaviour. Prior to any deformation, lamellar crystals are distributed randomly throughout the bulk material and provide isotropic mechanical response. Under loading the material will initially respond elastically. This is followed by a progression of ductile slip mechanisms involving chain and crystal alignment first followed by eventual fragmentation and destruction of the lamellae until ultimate fracture.

Wear of UHMWPE was widely attributed to take place through plastic deformation as well. Preferential sliding directions lead to molecular alignment and the drawing out of fibrils. The material becomes strengthened in these primary directions while simultaneously being weakened to transverse sliding. Hence, when subjected to multidirectional sliding in THRs wear particles are generated from the fibrils due to the cross shearing.

2.5.5 Crosslinking and oxidation of UHMWPE

The use of highly crosslinked polyethylenes (HXLPE) and antioxidant HXLPEs (AO-HXLPE) have replaced the historically used conventional UHMWPE in THRs (Table 2.2). Collectively, HXLPEs and AO-HXLPEs were used in >99% and >97% of procedures in 2022 in the USA and Australia respectively with the proportion of AO-HXLPE increasing each year (AJRR, 2022; Australian Orthopaedic Association, 2023). Table 2.3 compares various wear, mechanical and oxidation properties for CPEs, HXLPEs and AO-HXLPEs to illustrate potential differences. The precise material properties measured will be strongly influenced by the broad variety of UHMWPE processing that exists within and between classes as well as the experimental methodologies used. Therefore, the results from different studies were not necessarily directly comparable.

Chemical crosslinking, as a result of ionising irradiation, bonds adjacent chains to form a network structure. The reduction of chain mobility severely impedes orientation hardening mechanisms and produces a polymer which retains exceptional wear resistance even under multidirectional loading. As a consequence the reduction in chain mobility also reduces the toughness and strain at failure of HXLPEs.

The ionising radiation also introduces free radicals to the material. These highly reactive species can initiate auto-sustaining oxidation reactions which over time causes a decline in mechanical performance and toughness. Consequently, heat treatments or antioxidants (a free radical scavenger) are required to quench free radicals and prevent oxidation damage. Overall, AO-HXLPEs currently provide the best balance of wear resistance, oxidation resistance and mechanical performance required in THR liners. They demonstrate at least equitable *in vivo* wear performance to HXLPE (Lindalen *et al.*, 2019; Moon *et al.*, 2020) while their oxidation resistance was superior to even non-irradiated UHMWPEs (Bracco *et al.*, 2007). A re-melting heat treatment which reduces the crystalline properties (discussed in Section 2.5.7) is also not required. Therefore, the mechanical properties of AO-HXLPEs are not diminished this way either. The antioxidant presence in the microstructure also appears to increase chain mobility which increases creep deformation and strain recovery processes (Takahashi, Tateiwa, Shishido, *et al.*, 2016a).

2.5.6 Relationships between microstructural properties and mechanical performance

Research has established several relationships between the microstructure of UHMWPEs and its mechanical performance (Ries and Pruitt, 2005; Bracco *et al.*, 2017; Malito *et al.*, 2018). Higher crystallinity resulted in higher yield strengths and elastic moduli. The lamellar thickness produced a trade-off between more fatigue resistant (large crystals) and wear resistant (small crystals) UHMWPEs – although chemical crosslinking has a far greater effect on wear resistance. Toughness, ductility and ultimate strength all relied on chain mobility within the amorphous phase. This mobility allowed strain hardening slip mechanisms to occur while UHMWPE is being deformed. Chain mobility was also a key in creep behaviour.

The reduction of ductility and fatigue-fracture resistance associated with chemical crosslinking was also well established (Ries and Pruitt, 2005; Oral, Malhi and Muratoglu, 2006; Malito *et al.*, 2018). Chemical crosslinking greatly improved wear resistance by network formation which reducing chain mobility. This also reduced toughness by the prevention of ductile strain hardening slip mechanisms. These ductile mechanisms are also important in fatigue resistance by blunting the crack tip and slowing crack propagation.

In addition, chemical crosslinking reduced lamellar growth during the initial crystallisation process. Thereby limiting the crystallinity and lamellae thicknesses obtained which would be more effective at deflecting crack tips.

The re-melting of HXLPE further reduced fatigue and fracture performance by decreasing crystallinity (Medel and Furmanski, 2016).

2.5.7 Microstructural characterisation of UHMWPE

2.5.7.1 Differential scanning calorimetry (DSC)

Differential scanning calorimetry (DSC) was identified as the most widely used technique to determine the crystalline phase percentage (and Tm) of UHMWPE. It is a thermo-analytical method which is standardised by ASTM F2625. The heat flow of a sample (5-10mg) is measured in relation to an empty reference chamber as both chambers undergo a heating-cooling cycle up to 200°C at a rate of 10°C per minute. Melting and crystallisation events alter heat flow and present as peaks on the DSC trace. The melting endotherm is integrated between 50°C to 160°C and normalised against the heat of fusion from a 100% crystalline sample (289.3 J/g) to provide the measurement of crystallinity. The peak shape can give some indication to lamellar size distributions but quantitative analysis of lamellae structures is limited (Medel *et al.*, 2013). UHMWPE's crystalline percentage determined by DSC is typically around 50% but varied between 40-70% depending on processing conditions (Baker, Bellare and Pruitt, 2003; Turell and Bellare, 2004; Simis *et al.*, 2006; Medel *et al.*, 2007, 2013; Barron and Birkinshaw, 2008; Oral *et al.*, 2009; Lombardo *et al.*, 2016; Malito *et al.*, 2018).

2.5.7.2 Small angle x-ray spectroscopy (SAXS) and wide angle x-ray spectroscopy (WAXS)

X-ray spectroscopy techniques are also thermo-analytical. They measure how x-ray diffraction events, caused by specific crystallographic planes, change with temperature. The strength of the signal at specific angles and temperatures provides insight into various microstructural detail. WAXS and SAXS differ only in the angle of diffraction that is being collected. WAXS is capable of measuring crystalline percentage. However, it was believed to be a less accurate method than DSC (Barron *et al.*, 2008).

SAXS was often used to compliment DSC measurements and to measure lamellar properties such as lamellar thickness and lamellar spacing (Baker, Bellare and Pruitt, 2003; Turell and Bellare, 2004; Simis *et al.*, 2006; Barron and Birkinshaw, 2008; Lombardo *et al.*, 2016; Malito *et al.*, 2018). These nanoscale details otherwise need transmission electron microscopy (TEM) to visualise and (semi-) quantitatively measure (Kurtz *et al.*, 1999; Medel *et al.*, 2007, 2013). In one study, SAXS results showed that crosslinking restricts the growth of lamellae by reducing chain mobility and therefore

impeding the ability of crystalline lamellae to recruit more polymer segments (Ries and Pruitt, 2005)**.**

The thickness of crystalline lamellar was typically measured as between 10 nm and 30 nm while the amorphous thickness was measured as around 20 nm (Turell and Bellare, 2004; Lombardo *et al.*, 2016; Malito *et al.*, 2018). The exception to these values occurred in highly crystalline polymers processed under high pressures where lamellar thicknesses over 100 nm were reported (Simis *et al.*, 2006).

In other research, SAXS identified that different crystal populations contributed to the overall crystalline percentage. Researchers measured the emergence of a secondary crystal population cause by irradiation or aging (Stephens *et al.*, 2005; Barron *et al.*, 2008). These chain scissioning events allowed enough chain mobility to be regained for a secondary smaller crystalline population to emerge around the existing microstructure. While these secondary crystals would contribute to overall measured crystalline percentage they would not contribute in the same manner to the materials mechanical performance. Both irradiation and aging are well-established to reduce mechanical properties. This illustrated how UHMWPE microstructures are dynamic and complex. A singular viewpoint of crystallinity in these cases would be insufficient to predict the mechanical response of the material.

2.5.7.3 Raman spectroscopy

The use of Raman spectroscopy for UHMWPE microstructural measurements was first proposed by Strobl and Hagedorn (Strobl and Hagedorn, 1978). Spectra are produced by measuring the shifts in wavelength as a laser (monochromatic light) interacts with UHMWPE. Peak positions are related to specific molecular interactions. The relative positions and intensities of these peaks can be used to indicate microstructural details such as phase percentages and molecular orientations. A major advantage of this measurement technique is that it is a non-contact and non-destructive. However, even after five decades of use the precise methods used by researchers were still varied. Compared to DSC, Raman spectroscopy had been less widely adopted and undergone considerably less standardisation (Spiegelberg, Kozak and Braithwaite, 2016).

Raman spectroscopy, with support from nuclear magnetic resonance (NMR) research, provides evidence for the existence of a third polyethylene phase that was not recorded by DSC or x-ray diffraction techniques (Bergmann and

Nawotki, 1967; Strobl and Hagedorn, 1978; Mutter, Stille and Strobl, 1993; Barron and Birkinshaw, 2008; Yao, Jiang and Rastogi, 2014; Tapash, Deslauriers and White, 2015; Hansen and Hassani, 2022). The third phase, also termed the ‘intermediate’ or ‘transitional’ phase, occurs at the interface between crystalline and amorphous phases. The chains here possess more order and rigidity than the amorphous phase but lack the denser regular packing of the crystalline phase. The phase was believed to possess an influential role in the ductile slip mechanisms that provide UHMWPE its toughness. While some papers have raised questions about the ability of Raman spectroscopy to accurately determine third phase fractions they were both explicit that they did not question the presence of the third phase itself (Naylor *et al.*, 1995; Lin *et al.*, 2007).

Raman spectroscopy research demonstrated how the microstructure and chain orientations of UHMWPE were a result of its history of processing, loading and *in vivo* exposure. Confocal Raman spectroscopy studies identified distinct near-surface and bulk regions in UHMWPEs with significant gradients in microstructural details in the near-surface region (< 100 μm) (Pezzotti *et al.*, 2007; Takahashi, Masaoka, Pezzotti, *et al.*, 2014; Takahashi, Sugano, *et al.*, 2014). Crystallinity tended to be highest in the bulk polymer and declined by up to ten percent approaching the surface.

After uniaxial compressive loading, CPEs and HXLPEs both displayed marked increases in surface crystallinity (Takahashi *et al.*, 2015; Takahashi, Yamamoto and Pezzotti, 2015; Puppulin *et al.*, 2016; Takahashi, Tateiwa, Pezzotti, *et al.*, 2016). Increased surface crystallinity after wear was also found by some research groups using hip simulators (Bertoluzza *et al.*, 2000; Trommer *et al.*, 2015). However, other hip simulator studies found no significant changes to microstructural phases or chain alignment at the surface after wear (Affatato *et al.*, 2002; Taddei *et al.*, 2002; Taddei, Di Foggia and Affatato, 2011).

As observed by SAXS, crosslinking UHMWPE was found to generally increase its crystallinity (Barron and Birkinshaw, 2008; Taddei, Di Foggia and Affatato, 2011; Takahashi, Yamamoto, *et al.*, 2014). It also reduced the ability for chain orientation and phase transitions by reducing chain mobility (Takahashi, Sugano, *et al.*, 2014; Takahashi, Pezzotti and Yamamoto, 2016).

The inclusion of AO in the microstructure increased chain mobility and promoted randomness in the chain orientations (Takahashi, Masaoka, Yamamoto, *et al.*, 2014; Takahashi, Yamamoto, *et al.*, 2014; Takahashi,

Yamamoto and Pezzotti, 2015; Takahashi, Pezzotti and Yamamoto, 2016). In contrast to non-AO UHMWPEs, loading induced transitions to the amorphous or third phases in AO HXLPEs (Takahashi, Yamamoto and Pezzotti, 2015; Takahashi, Tateiwa, Pezzotti, *et al.*, 2016). This was beneficial to the reducing strain softening, improving creep resistance and improving fatigue resistance (Takahashi, Masaoka, Yamamoto, *et al.*, 2014; Takahashi, Yamamoto, *et al.*, 2014; Takahashi, Tateiwa, Pezzotti, *et al.*, 2016).

Analysis of retrieved CPE and HXLPE components found that crystallinity broadly increased with *in vivo* exposure time regardless of wear (Pezzotti *et al.*, 2007; Takahashi *et al.*, 2010). HXLPEs with longer *in vivo* time also possessed more residual strain (Kumakura *et al.*, 2009). These microstructural changes correlated strongly to measurements of *in vivo* oxidation. They demonstrate the importance of the physical and chemical environment on UHMWPE microstructure that may be underappreciated when equating *in vitro* research with *in vivo* performance (Pezzotti, 2017). Equivalent research on retrieved AO HXLPEs was not currently present in literature. One could speculate that AO presence would limit the crystalline transition in two ways by minimising oxidative reactions and by its role in promoting chain randomness.

2.5.8 UHMWPE fatigue and fracture behaviours

2.5.8.1 Fatigue resistance testing

The progression of fatigue damage in UHMWPE is still not well understood. Fatigue damage is defined as a localised damage occurring under cyclic loading (Medel and Furmanski, 2016). There are five stages in the progression of fatigue damage: permanent damage via microstructural changes, microcrack initiation, growth and coalescence of microcracks, stable propagation of macrocrack and finally fracture.

Two predominant approaches were used to analyse the fatigue performance of UHMWPE (Medel and Furmanski, 2016). Total life fatigue testing studies considered all of the five stages of fatigue damage by measuring the number of cycles for a theoretically unflawed sample to fracture. This approach is more challenging in polymers than metals because the nucleation of defects is less well understood (Medel and Furmanski, 2016). Williams and DeVries provide evidence that chemical bonds in polymers break every loading cycle and the microscopic damage accumulates over time (Williams and DeVries, 1970). However, a key limitation of total life-fatigue testing research in

UHMWPEs was that – despite the accumulation of microscopic damage – it rarely resulted in rupture below the material's ultimate tensile strength (Medel and Furmanski, 2016). The implication being that UHMWPEs were able to withstand large numbers of cycles and large strains without fracturing due to the extensive ductile slip mechanisms described in Section 2.5.4.

To overcome this limitation a 12% strain was often used as an alternative failure criterion to represent the formation of microscopic damage (Baker, Bellare and Pruitt, 2003; Urriés *et al.*, 2004; Puértolas *et al.*, 2006; Medel *et al.*, 2007). However, the criterion provides little indication about the progression of microscopic damage to macroscopic cracks or ultimately the failure of specimens. Therefore, the use of the 12% strain criterion (in isolation) as a predictor for material failure is wholly insufficient.

Clinical and experimental evidence highlighted the importance of stress concentrating features for the propagation of fatigue cracks to fracture (Furmanski *et al.*, 2009; Sobieraj *et al.*, 2013; Medel and Furmanski, 2016). Hence, fatigue crack propagation (FCP) research – an alternative to total life cycle analysis – proved a more prevalent approach in UHMWPEs. FCP studies disregarded the initiation of macroscale damage by analysing the material response to cyclic loading after purposefully introducing notches or a sharpened crack into test samples.

FCP research was able to show that static mode crack growth was the dominant mechanism of crack growth in UHMWPEs (Furmanski and Pruitt, 2007, 2018; Sirimamilla, Furmanski and Rimnac, 2013). For most ductile materials the rate of stable crack growth is correlated to the applied stress intensity range (ΔK) as governed by the Paris equation. However, UHMWPE and other fatigue-brittle materials show poor agreement with the Paris equation. Instead, the rate of stable crack growth correlates better with the maximum stress intensity factor (K_{max}). This indicates that crack growth was dependant on the peak magnitudes and durations of the stress experienced as opposed to requiring a significant loading and unloading cycle.

An outstanding challenge for this area of research is to reliably predict crack initiation and propagation under fatiguing conditions. It was established by various methods that FCP resistance was reduced by increased radiation doses and re-melting heat treatments (Table 2.3) (Medel and Furmanski, 2016). In addition, decreases to notch radius or increases to cycle frequency and loading rate all appeared to decrease the time needed for crack initiation (Sirimamilla, Rimnac and Furmanski, 2018; Sirimamilla and Rimnac, 2019).

However, the research practices to evaluate specific notch geometries and loading scenarios and predict crack behaviour were not yet established.

Static mode viscoplastic FCP predictions appear to be the approach with most promise (Sirimamilla, Rimnac and Furmanski, 2018). At the time of writing, the evidence behind this approach was limited to just two UHMWPE formulations and a static loading scenario though. Therefore, it was quite removed from applications in specific liner geometries under physiologically relevant loading conditions.

2.5.8.2 Fracture resistance testing

Fracture resistance testing of UHMWPEs faces similar challenges to FCP research. Uniaxial tensile testing and impact testing methods were able to provide useful comparative estimations of the fracture resistance of UHMWPEs (ASTM, 2022). However, quantitative measurement of fracture toughness requires the evaluation of stable crack extension conditions (Medel and Furmanski, 2016). Generally, fracture toughness is measured using critical stress intensity factors (calculated using linear elastic fracture mechanics, LEFM) or by relationships describing the energy consumed during crack growth (J-integral approach).

It was demonstrated that LEFM was a poor method for UHMWPE because of non-linear, plastic and time-dependant effects with UHMWPEs that invalidate the assumptions underpinning LEFM. J-integral approaches were more effective at overcoming the limitations of LEFM by considering the energy dissipated due to crack growth (Medel and Furmanski, 2016). Several variants of the j-integral approach have been proposed but at the time of writing there was no standardised experimental technique available for UHMWPE (Medel and Furmanski, 2016). Methods based on crack tip opening displacement and specimen hysteresis are promising alternative approaches to overcome the shortcomings of fracture resistance research (Lewis and Nyman, 1999; Varadarajan and Rimnac, 2008; Malito *et al.*, 2019).

Despite these challenges the effect of different processing methods on the fracture resistance was well established (Table 2.3). Multiple researchers found that irradiation reduced the fracture toughness of UHMWPE by around 50% (Pascaud *et al.*, 1997; Lewis and Nyman, 1999). In addition, fracture toughness was further diminished by re-melting heat treatments while annealing would allow the material to either retain or slightly improve on the fracture toughness of as-irradiated UHMWPE (Medel *et al.*, 2007).

2.5.8.3 Stress concentrating features and mechanical response

Soberiaj *et al.* examined the effect of introducing notches or other stress concentrators into tensile testing of UHMWPE (Sobieraj, Kurtz and Rimnac, 2005; Sobieraj *et al.*, 2008). The notches generate a multi-axial stress state in the UHMWPE. This impeded orientation hardening mechanisms because the principle axis of stress was less dominant. This increased the yield strength (referred to as notch strengthening) but decreased the ultimate properties versus unnotched samples. These studies demonstrate how the mechanical response of UHMWPE material near to stress concentrating features in THR liners may be different to bulk areas of the liner. It was considered most likely that stress concentrating features could be introduced into the liner design as part of the liner locking mechanisms.

Under cyclic loading, notched samples made from HXLPE displayed a better average fatigue performance than samples made from CPE (Sobieraj *et al.*, 2013). In HXLPE samples orientation hardening was impeded and therefore the material remained stronger to the multi-axis stress field present in notched samples. However, there was considerably more variance in the HXLPE results which exhibited both the highest and lowest cycles to failure. This suggested while HXLPE performed better as an average it was also more susceptible to inherent and random flaws than CPE samples. Therefore, when using HXLPEs more careful consideration needs to be given to the incorporation of stress concentrating features in liner designs compared to CPEs.

The same research also noted differences in the observed fracture mechanisms which were either described as ductile or brittle in nature. All HXLPE notched samples exhibited a brittle fracture mechanism. While higher strain rates increased the likelihood of brittle fracture even in CPE notched samples. Despite CPEs possessing more chain mobility it was possible for the increased strain rate to prevent chain alignment processes from having sufficient time to occur. In the cases of a brittle mechanism fast fracture was exhibited without a period of stable crack growth during which gradual microcrack formation and coalescence would normally be occurring.

2.6 Adverse loading of polyethylene THR liners – *in vitro* research

Experimental hip simulators and other *in vitro* research methods are used to apply physiologically relevant loading conditions to THR components in a

controlled and repeatable manner. This Section focuses on the research which introduced adverse factors into THR testing. Most prominently this related to edge loading, thin polyethylene and unsupported polyethylene because they were the factors most strongly identified in the case studies discussed in Section 2.4.7. Currently, ISO 14242-4 (2018) for a walking gait with edge loading by component separation and ASTM F2582 (2020) for dynamic impingement provide standardised methods for assessing edge loading conditions.

Other methods of introducing adverse factors into testing included adding third body particles, increased surface roughness, aging components and alternative kinematic motions. However, studies which primarily focused on polyethylene wear under a concentric gait cycle were considered more distant from the scope of this research and may have been excluded.

2.6.1 Edge loading by high inclination and component separation

ISO 14242-4 (2018) defines the hip simulator methodology to subject THR components to edge loading by component separation (as defined in Section 2.4.6). The standard is synonymous with ISO 14242-1 for a standard walking gait cycle but introduces a component mismatch in the medial-lateral axis in the form of a spring which induces component separation and edge loading during the swing phase. Using ISO 14242-4, the magnitude of dynamic separation was strongly linked to the magnitude of component mismatch and the inclination angle of the acetabular components (Ali *et al.*, 2023).

Edge loading, as a term, was also used by studies which incorporated high inclination angles without a component separation – particularly prior to the release of ISO 14242-4 in 2018. Multiple researchers found that edge loading by high inclination alone did not increase polyethylene wear by a clinically significant magnitude and in some cases wear decreased (Patil *et al.*, 2003; Kelly *et al.*, 2010; Halma *et al.*, 2014; Korduba *et al.*, 2014; Loving *et al.*, 2015; Saikko, 2019).

The results from studies with edge loading by component separation were mixed. Williams *et al.* and Partridge *et al.* both found dynamic separation significantly decreased polyethylene wear in pneumatic hip simulators (Williams *et al.*, 2003; Partridge, Tipper, *et al.*, 2018). Jahani *et al.* speculated this may be due to a reduction in contact area and possible changes to the lubrication regime (Jahani *et al.*, 2021). Both studies retained an inclination angle of 45 degrees and component separations were below 1

mm. These can be described as moderate conditions compared to those possible under ISO 14242-4.

Despite a decrease in wear rate, Partridge *et al.* noted a marked increase in damage observed at the bearing surface rim of aged CPE liners subjected to edge loading by component separation. The damage was located predominantly at the thinnest areas of the liner close to locking mechanism features. Damage was not observed in non-aged HXLPE liners. This suggested that when damage mechanisms were accelerated by artificial aging the liner locking mechanism and thin regions of polyethylene would be most susceptible to damage.

The wear results of Williams *et al.* and Partridge *et al.* were not replicated in an electromechanical hip simulator even under equivalent loading conditions (Ali *et al.*, 2023). In addition, Ali *et al.* found increasing both inclination angle (up to 65 degrees) and translational mismatch (up to 4 mm) increased wear. The combination of the higher inclination angle and the highest mismatch resulted in the maximum separation distances (> 2 mm) of the conditions tested. Their results suggested that translational mismatch had a more significant effect than cup inclination angle. The same author had also previously noted differences between outcomes using pneumatic and electromechanical simulators in a comparative study using standard walking which provides some indication on the possible difference in wear results (Ali *et al.*, 2016).

Bowsher *et al.* compared the wear of CPE (33 kGy) and HXLPE (50 kGy) under dynamic separation conditions (1-1.5 mm separation) (Bowsher *et al.*, 2008). With smooth heads the HXLPE wear resistance was around two times greater than the CPE. However, when roughened heads were used the wear rate of HXLPE increased by around nine times and performed similarly to the CPE. In this study, the increased crosslinking of the HXLPE offered limited benefit to wear resistance under the combined effect of edge loading by component separation with roughened femoral heads.

Puppulin *et al.* subjected HXLPE liners of two thicknesses to edge loading using high cup inclination angles (65 degrees) (Puppulin *et al.*, 2016). Only the thinner (5.9 mm) HXLPE liner displayed a statistically significant increase in wear rate although it remained clinically low. Surface analysis by Raman spectroscopy showed this liner had increased in crystallinity at the wear surface and the highest oxidation levels compared with thicker liners. This suggested that high contact stresses in thinner liners may be able induce microstructural changes and potentially accelerate oxidation damage.

This was the only paper found to have combined edge loading testing with characterisation methods which specifically aim to examine the initiation or progression of damage mechanisms. However, both the thickness of liner and the loading conditions tested can be considered as relatively moderate. Further research would be insightful to evaluate whether the use of edge loading by component separation or the use of even thinner liners would produce more substantial microstructural changes in polyethylene liners.

2.6.2 Impingement loading

The fatigue or fracture of polyethylene liners was more commonly assessed using impingement loading conditions. Takahashi used an axial-torsional materials testing machine to compare the response of HXLPE and AO HXLPE liners to impingement loading (Takahashi, Tateiwa, Pezzotti, *et al.*, 2016). The presence of vitamin E appeared to improve protection against surface cracking whereas crosslinking without vitamin E diminished the fatigue resistance of the polyethylene. Undoubtedly, the liner thickness of 7.5 mm helped to prevent any cracking from progressing to fracture before the test's 100 000 cycles elapsed.

Holley compared CPE (28 kGy) and HXLPE (100 kGy) liners in a hip simulator study which included impingement loading within each cycle (Holley *et al.*, 2005). The HXLPE liners displayed improved wear properties over a CPE group. Both groups showed a similar appearance with macroscopic cracks and edge damage due to impingement. Like Takahashi *et al*. above the use of 10.5 mm thick liners prevented any fracture even after six million cycles.

Oral tested CPE and AO-HXLPE under impingement conditions for two million cycles (Oral *et al.*, 2006). At 3.7 mm, the minimum liner thickness used in this study was comparable to the thickness of liners in the clinical case studies reviewed in Section 2.4.7. All liner groups showed a slight depression at the impingement site but there was no evidence of cracking or other surface damage in any liners. Comparison of these results to a HXLPE without vitamin E would have enhanced this study as both of the materials used are considered to have better fatigue resistance than HXLPEs.

Kamada *et* al. utilised a similar set up as Takahshi *et al.* to test very thin liners (2.45 mm) to failure under impingement loads (Kamada *et al.*, 2019). They observed that impingement at unmated scallops progressed to failure significantly faster than mated ones due to the presence of gaps between the liner and the shell. Unmated scallops aim to minimise the number of

shell design variations required but evidently also acted as stress risers in this study.

The study also noted a lower amount of liner offset (Figure 2.5), which resulted in a lower volume of unsupported polyethylene, failed more quickly than larger liner offsets (while rim thickness remained constant). This was attributed to higher impact stresses in the smaller liner offsets. It appears the larger volumes had a greater capacity to deform and withstand stresses before reaching the critical points of crack initiation and propagation. Offset liners are used to help retain liner thickness but this research demonstrated that there may be consequences from using designs with unsupported polyethylene.

2.6.3 Thin and unsupported polyethylene liners

Several researchers have demonstrated that the use of thin HXLPEs did not increase the wear rate (Muratoglu *et al.*, 2001; Herrera *et al.*, 2007; Kelly *et al.*, 2010; Shen, Lu and McKellop, 2011; Saikko, 2019). These studies included the use of high inclination angles. None of the authors reported evidence of fatigue damage to any liners. This supported clinical evidence that vulnerable design features may only become problematic under adverse loading conditions.

Essner used hip simulators to test very thin (2.5 mm) and purposefully unsupported (by 4 mm) liners under standard walking (Essner *et al.*, 2005). The occurrence of fracture was the only output measure which occurred at the thinnest portion of the liner edge. RM HXLPEs failed considerably more (64% and 100% for 50 kGy and 100 kGy conditions respectively) than both SA HXLPE (11%) and unirradiated controls (20%). This study was one of the few to investigate liner fatigue or fracture under physiologically relevant conditions. The results clearly demonstrated that thin and unsupported UHMWPE, especially with reduced mechanical properties, were strong factors for the potential of liner failure. The use of fracture percentage as the only outcome measure was a limitation of the research. More sophisticated characterisation methods were warranted to better understand the damage mechanisms that lead to liner fracture.

2.6.4 Other adverse loading conditions

Bowsher and Shelton simulated walking and walking with added stumbling and jogging sequences (Bowsher and Shelton, 2001). They were tested with both smooth and roughened heads. The only instance to result in a significant increase in wear was when the increased head roughness was

combined with the additional movements. Hadley *et al.* tested more adverse loading by introducing different stop-dwell-start protocols (Hadley *et al.*, 2018). Only the most adverse case (with the longest dwell periods) produced a pronounced increase in wear rate. This was attributed to the disruption of the lubrication regime.

Grupp *et al.* examined the combined effect of third body particles and artificial aging on the wear of HXLPEs (Grupp *et al.*, 2014). They showed that third body particles had little effect on HXLPEs but when combined with artificial aging the wear rates of HXLPEs dramatically increased. Comparatively, wear rates of AO HXLPE liners which were resistant to the aging process remained low. Collectively, these studies highlight how different adverse factors can interact to influence the performance of THR components. The effect of individual adverse factors may be underestimated if they are only examined in isolation or under simplified loading conditions.

2.6.5 Summary of *in vitro* research into adverse loading

In summary, many different methods of generating adverse loading were present in the literature. However, the majority of the papers possessed a wear dominated perspective to their research. The assessment of polyethylene wear was not part of the primary aims of this research which focused on the damage mechanisms associated with edge loading and how they may progress to liner failure or fracture. There were relatively few papers which have examined the fatigue and fracture performance of liners. These studies tended to rely on qualitative analysis of damage or relatively crude measures such as absolute failure. There was a distinct lack of characterisation tools equipped to assess the progression of damage mechanisms up to the point of failure. Development of these methods have the potential be utilised with existing and established methods of generating adverse loading such as those described in ISO 14242-4 (2018) and ASTM F2582 (2020).

2.7 Finite element (FE) modelling of polyethylene liners

2.7.1 Introduction

Finite element (FE) modelling is a numerical technique capable of resolving mechanical problems and has been utilised to examine a wide array of orthopaedic challenges since the 1970s (Taylor and Prendergast, 2015). FE has helped to address the short comings of experimental and clinical

research which can be expensive and time-consuming to carry out. Through parametric studies, FE modelling is well equipped to research the effects of isolated design or loading variables in a manner that would often be unfeasible or impossible for experimental or clinical testing. Despite these advantages, FE models cannot replace the need for experimental or clinical studies as they are often dependant on them for input variables and measures to validate solutions against.

Polyethylene wear modelling has received considerable investigation since the 1990s when it was linked to osteolysis and aseptic loosening. An extensive review of FE modelling of polyethylene wear has already been published (Wang *et al.*, 2019). Fewer studies have examined the risk of liner failure or the performance of liners under adverse loading. Figure 2.11 illustrates a workflow for either of these THR FE models. Despite possessing different aims, both types of model share many common decisions in their model set up. Hence examination of the choices made by researchers in both model types was beneficial in preparation for the development of FE models which investigated edge loading in THRs.

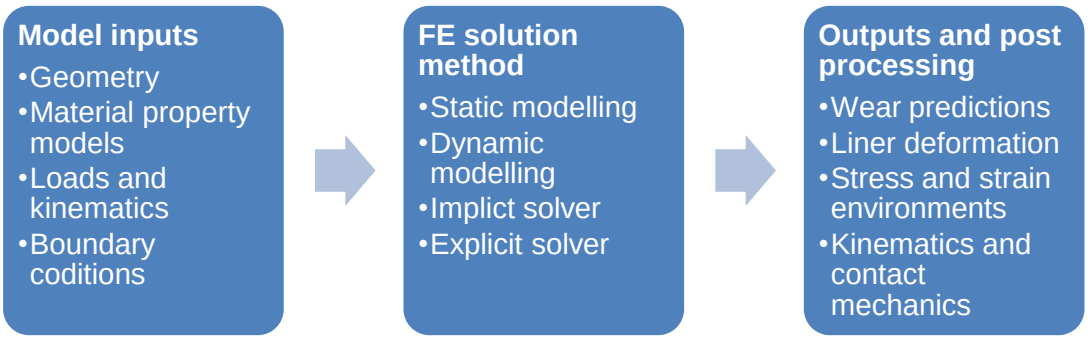

Figure 2.11. A workflow of THR FE models.

2.7.1.1 Model inputs

FE modelling of hard-on-soft THR bearings widely articulated the deformable polyethylene liner against a rigid ball used to represent the femoral head. This was justified because the stiffness of the metal is over 100 times greater than the polymer liner and so femoral head deformation would be negligible (Wang *et al.*, 2019). The metal shell (and the surrounding bony anatomy) was sometime included although often it was omitted and accounted for by the boundary conditions on the liner's (or shell's) outer

surface. The loads, kinematics and boundary conditions used depended on the scenario that the FE model was designed to represent.

2.7.1.2 Material property models

The material property model defines the mechanical response of the UHMWPE liner in the FE model. Bowden and Bergström reviewed the various material property models possible for polyethylene in their chapter in the UHMWPE handbook (Bowden and Bergström, 2016). However, in the past two decades an elastic-plastic material property model by far the most widely implemented typically using data derived experimentally from uniaxial loading tests. Pre-yielding behaviour was governed by a Young's modulus (Table 2.3) and a Poisson's ratio value of 0.46 (Bowden and Bergström, 2016). Non-linear stress-strain data defined the post yielding behaviour. Peak stresses observed within the FE model are limited by the peak stress defined in the material model (Figure 2.12). Beyond this point the FE model behaves in a perfectly plastic manner and stress is redistributed to adjacent nodes. The main limitation of all of these models was that the properties were generally derived from only one loading case. Whereas the stress-strain behaviour of UHMWPE exhibits both strain rate and temperature dependence. The material's mechanical response also includes time-dependant viscoelastic and viscoplastic components.

More complex constitutive material property models were capable of better predicting the mechanical response of UHMWPE even under multiple loading scenarios. Bowden and Bergström described a 'hybrid model' which was defined by 13 material parameters (although it reduced to four parameters because nine of them were insensitive to UHMWPE processing) (Bowden and Bergström, 2016) and other similar approaches were also reported in literature (Alotta *et al.*, 2018; Garcia-Gonzalez, Garzon-Hernandez and Arias, 2018; Wiersma and Sain, 2023).

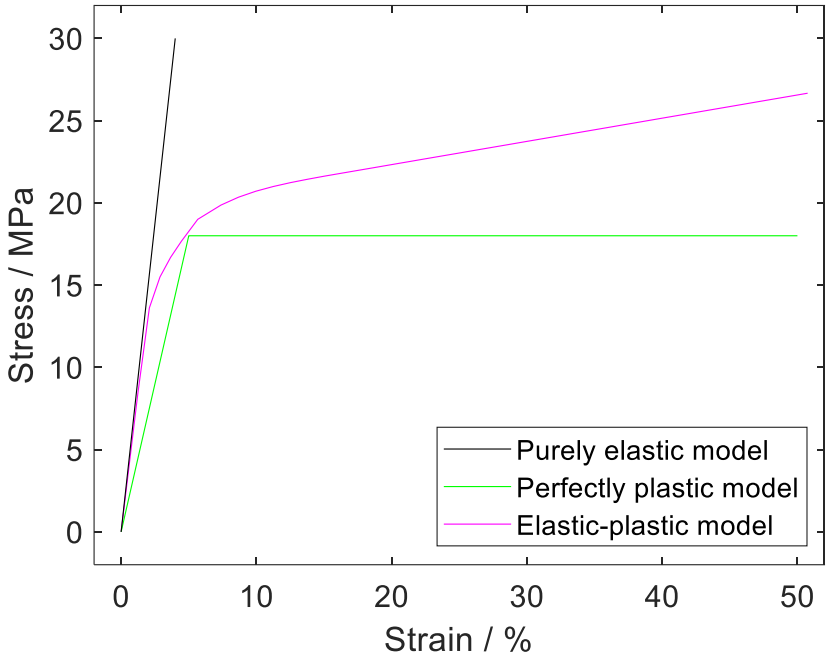

Figure 2.12. A stress-strain plot for perfectly plastic and elastic-plastic material property models.

To the authors knowledge such material models had not been combined with THR geometries and loading. Therefore, the effect of introducing these more sophisticated material models on the material response and computation time was not known. By introducing time-dependant components into the predicted material response they could potentially enhance predictions of strain accumulation (and other outputs) particularly over multiple cycles of loading. Existing FE models predicted that plastic strain accumulation mostly occurs in the first loading cycle and completely stabilises after just a few cycles (Jamari *et al.*, 2014; Etchels *et al.*, 2023).

2.7.1.3 FE Solution method

A high majority of FE modelling of THRs have involved (quasi-) static modelling and utilised an implicit solution method (Taylor and Prendergast, 2015; Wang *et al.*, 2019). The implicit solver was recommended in (quasi-) static modelling scenarios for which it is computationally more efficient (Dassault Systèmes, 2016). Explicit modelling utilises a more incremental approach which has enabled it be used to resolve non-linear problems such as dynamic analyses and force controlled simulations of THRs more effectively than an implicit solver (Higa *et al.*, 2014; Gao, Zhang and Jin, 2015; Huff, Myers and Rullkoetter, 2020; Jahani *et al.*, 2021). Understanding the aim and requirements of the particular FE model determined whether an implicit or explicit solution method was more appropriate.

2.7.2 Polyethylene wear modelling

Figure 2.13 illustrates an algorithm for predicting wear in an FE model. For each iteration of the algorithm the wear depth at each node on the bearing surface is predicted. This value is scaled to enable millions of cycles of wear to be predicted while only a few kinematic cycles are solved within the FE model. The geometry of the liner is subsequently updated accordingly. This was typically governed by variations on Archard's wear law which states volumetric wear is proportional to the contact pressure (load, L) and sliding distance (d). The proportionality is determined the wear factor, k (Equation 2.2).

Equation 2.2 $$\boldsymbol{V = k\,.\,L\,.\,d}$$

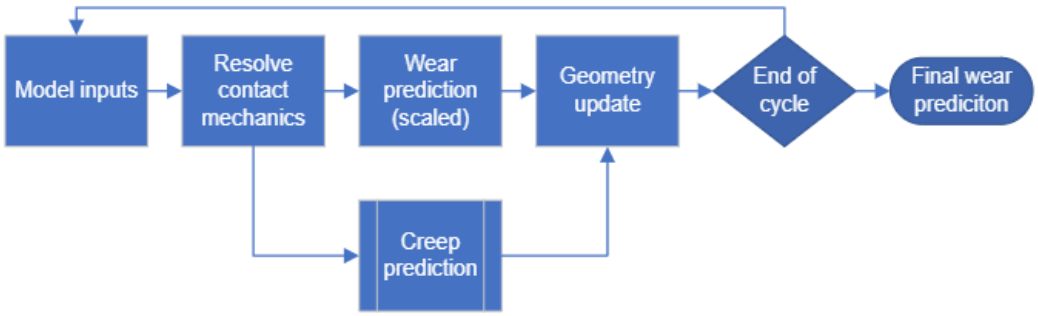

Figure 2.13. A typical algorithm for predicting wear adapted from (Wang et al., 2019).

The effects of bearing diameter, liner thickness and inclination angle on the predicted polyethylene wear are presented in Table 2.4. Linear wear was defined as the penetration into the surface as a result of wear which was measured as the linear distance between the unworn and worn surfaces. In contrast, volumetric wear was defined as the total volume of material removed.

Table 2.4. The effects of liner geometry and positioning factors on predicted wear and FE model outputs.

Factor	Effect	References
Increased bearing diameter	Increasing bearing diameter by 4 mm increased volumetric wear by approximately 16-20%.	(Maxian *et al.*, 1996a; Bevill *et al.*, 2005; Kang *et al.*, 2006; Penmetsa *et al.*, 2006; Liu *et al.*, 2011).
	Increasing bearing diameter by 4 mm decreased linear wear by approximately 5% (for liners between 28 mm and 36 mm).	(Maxian *et al.*, 1996b; Bevill *et al.*, 2005; Kang *et al.*, 2006).
Decreased liner thickness	The linear and volumetric wear rates were very weakly affected by liner thickness. Differences of 2.5% or less were observed for cases below 8 mm thick.	(Maxian *et al.*, 1996a, 1996c; Bevill *et al.*, 2005)
	For each millimetre the liner thickness decreased the contact stresses increased by between 8% to 16%.	(Kurtz, Edidin and Bartel, 1997; Plank *et al.*, 2007; Shen, Lu and McKellop, 2011)
High inclination angle	Decreased the contact area and increased the contact stress.	(D'lima, Chen and Colwell, 2001; Korhonen *et al.*, 2005; Hua, Li, *et al.*, 2014; Lin, Wu and Chen, 2016)
	High inclination angle had mixed effects on linear and volumetric wear. In Wang *et* al.'s review, studies most commonly found high inclination angles increased linear wear rate but reduced volumetric wear rate.	(Wang *et al.*, 2019)

2.7.2.1 Motion inputs and wear modelling

Liu *et al*. determined comparable wear rates for three-dimensional gait derived and ISO 14242 motion patterns (14.0 mm^3/Mc versus 13.4 mm^3/Mc); both were slightly higher than simplified two dimensional motion inputs from a hip simulator (12.2 mm^3/Mc) (Liu, Fisher and Jin, 2013). This FE modelling would suggest that the ISO 14242 loading and motion inputs provide a good representation of a clinical scenario. However, in a different wear model Fialho *et al.* found a substantial difference of 7.6 mm^3/Mc between the volumetric wear rate using gait patterns measured from two different patients (18 mm^3/Mc versus 25.6 mm^3/Mc) (Fialho *et al.*, 2007). Therefore, it can be simultaneously acknowledged that ISO 14242 loading and motion inputs provide a singular case which is likely to sit within a highly diverse patient population. The differences between wear volumes in these two studies were likely due to differences in the wear calculation formula. Where, for example, only Liu *et al*. incorporated cross shear effects into their calculation.

Some studies have looked at the effect of more rigorous activities than walking, such as stair climbing (Onişoru, Capitanu and Iarovici, 2006; Lundberg *et al.*, 2007; Matsoukas and Kim, 2009) and jogging (Fialho *et al.*, 2007). These more dynamic motions put the hip through greater forces and range of motion and were found to increase wear rates. Similarly, Lundberg found changes to the loading cycle or intermittent loading has been found to increase wear; variable motion was particularly important when surface roughness was increased (Lundberg *et al.*, 2007).

2.7.3 FE modelling of edge loading by component separation

The research in this Section extended beyond just placing the liner at high inclination angles which has already been covered in Table 2.4. Three FE models were identified in literature which investigated edge loading by component separation as defined in Section 2.4.6. In optimally positioned components, the liner's centre of rotation is aligned to the femoral head's centre of rotation. These models purposefully offset the component centres of rotation to generate separation of the bearing surfaces and edge loading during a gait cycle. The component offset was a model input relating to the initial distance between the component centres of rotation prior to loading. The resultant magnitude of component separation was a model output influenced by the magnitude of component offset applied and liner inclination (Jahani *et al.*, 2021).

Table 2.5 summarises the input conditions and stress outputs of the three FE models. In all cases of edge loading produced stresses which exceeded the yield stress of UHMWPE (example properties are located in Table 2.3). Crowninshield *et al.* observed that a 4 mm subluxation more than doubled the maximum predicted tensile stresses in the liner (Crowninshield *et al.*, 2004). The tensile stress increased from around 14 MPa to 33 MPa and above the material yield strength. However, this particular study has limited clinical validity because the only case where component separation was introduced was using an inclination angle of 90 degrees.

Table 2.5. A summary of THR FE models of edge loading by component separation.

FE model	**Crowninshield *et al.***	**Hua *et al.***	**Jahani and Etchels *et al.***
Max load	2669 N	2500 N	3000 N
Liner inclinations	90 degrees	35-65 degrees	45-65 degrees
Max component offset	4 mm	2 mm	4 mm
Separation kinematics	Static	Dynamic	Dynamic
Max stress (type)	34 MPa (tensile)	28 MPa (von Mises)	>30 MPa (von Mises)
Max contact pressure	-	53 MPa	65 MPa

Two of the FE models investigated polyethylene liners under conditions of edge loading with a dynamic separation of the bearing surfaces. The most recent was reported by Jahani and Etchels *et al.* (Jahani *et al.*, 2018, 2021; Etchels *et al.*, 2019, 2023). This modelling followed on from the research published by Hua *et al.* (Hua, Li, *et al.*, 2014; Hua, Wang, *et al.*, 2014; Hua *et al.*, 2016). While some of these papers predate the publication of the ISO 14242-4 (2018) the manner in which edge loading by component separation was performed by the researchers was synonymous with the loading conditions defined in this ISO standard.

Hua *et al.* introduced component mismatches of up to 2 mm to study edge loading (Hua, Li, *et al.*, 2014). In their static model it was observed that less component separation was required for edge loading to occur as the inclination angle increased. Increased contact pressures and plastic strain accumulation were observed as component mismatch increased. The model went on to be used to assess edge loading under different activities of daily living by altering the direction and orientation of forces applied to the head (Hua *et al.*, 2016). Walking and stair climbing motions resulted in edge loading under steep cup inclination conditions. However, no edge loading was predicted for standing, sitting or knee bending activities in this study.

Etchels *et al.* and Jahani *et al.* demonstrated that a static rigid model was largely sufficient for predicting separation behaviour during edge loading (Etchels *et al.*, 2019; Jahani *et al.*, 2021). However, they also concluded that dynamic modelling to introduce inertial effects and a highly refined mesh (as well as an elastic plastic material model) were critical in the prediction of plastic strain behaviour (Jahani *et al.*, 2021; Etchels *et al.*, 2023). This combination was computationally very demanding and the model required both explicit modelling and mass scaling to reach suitable solution times. Explicit modelling was found to converged more quickly than implicit modelling for this non-linear scenario. Mass scaling is a modelling technique which helped to increase the stable time increment required by artificially increasing material density. The model was one of only a few examples of dynamic and explicit FE modelling of polyethylene liners in total hip replacement.

The effect of dynamics on the edge loading model was further explored by Etchels *et al.* who examined the effect of swing phase load, fixture mass and spring dampening (Etchels *et al.*, 2023). All of these factors affected the inertia involved in the recentralising of components and hence they influenced the load that was applied to the rim during heel strike. The overall separation behaviour was not greatly affected – only the speed of it.

2.7.4 FE modelling of impingement

FE modelling of impingement has focused on the occurrence of stem-on-liner impingement and the associated risks of increased wear, edge damage and most prominently dislocation occurrence. It should be noted that dislocation can also occur from bony impingement or a hybrid of the two as well (Scifert *et al.*, 1998). Experimental data indicated that implant impingement was more prevalent with smaller head sizes and bony impingement occurs more for larger heads (Brown and Callaghan, 2008).

Table 2.6 summarises the input conditions used and stress outputs determined by FE modelling of impingement. A consistent observation from FE modelling of impingement was that it generated two locations of stress in the liner (Scifert *et al.*, 1997, 1998; Kluess *et al.*, 2007; Higa *et al.*, 2014; Ezquerra *et al.*, 2017). The primary impingement site was located where contact was made between the stem and the liner. As the head is being levered out of the socket stresses were also applied at the egress site which was located near the bearing surface rim (Figure 2.1C) opposite to the primary impingement site. In most cases the stresses at both locations exceeded the yield stress of UHMWPE (Scifert *et al.*, 1997, 1998; Scifert, Brown and Lipman, 1998; Kluess *et al.*, 2007; Ezquerra *et al.*, 2017).

Scifert *et al.* investigated different designs of the liner edge (Scifert *et al.*, 1997, 1998). It was found that using chamfered edges increased the range of motion, moment resisting dislocation and reduced the maximal von Mises stresses predicted in liners. However, these stresses still remained above the material yield strength and stresses at the egress site actually increased in chamfered designs due to a reduction in contact areas here.

Changes to either head size and neck design resulted in a trade-off between range of motion and the moment resisting dislocation where the use of larger heads or head-neck ratios increased range of motion (Scifert *et al.*, 1997, 1998). Larger heads also resulted in lower egress stresses (Kluess *et al.*, 2007; Ezquerra *et al.*, 2017). Huff *et al.* demonstrated that the correct use of lipped liners, positioned at the egress site, increased the impingement resisting moment (Huff, Myers and Rullkoetter, 2020). However, when the kinematics were reversed – switching between anterior or posterior dislocation movements – the protruding lip becomes a point of impingement earlier in that range of motion.

Pedersen *et al.* evaluated a wide range of cup positions and movements (Pedersen, Callaghan and Brown, 2005). They distinguished between two modes of dislocation. Firstly, where stem-on-liner impingement resulted in the head being levered out the cup. This was most prevalent posteriorly in a stooping movement or anteriorly during a standing pivot movement. Secondly, dislocation was possible without impingement. Primarily during leaning over, shoe tie or pick up movements where a posterior egress site was observed.

Table 2.6. A summary of FE modelling of impingement. (*) indicates where stress values reached the limit of the material model used. The stress outputs were von Mises stresses (VMS) unless specified otherwise.

FE model	Impingement loading method	Total load	Movements considered	Stress outputs (VMS)
Scifert *et al.*	Displacement controlled	620 N or 942 N (axial only)	Leg crossing	36-55 MPa*
(1) Callaghan *et al.* and (2) Pedersen *et al.*	Force controlled	Muscle force derived	Impingement, subluxation, and dislocation	(1) > yield strength (2) 58 MPa
Kluess *et al.*	Force controlled	506 N or 1288 N	Anterior and posterior dislocation	104 MPa
Furmanski *et al.* and Ansari *et al.*	Distributed pressure applied to liner	500 N	Impingement	43 MPa (tensile)
Higa *et al.*	Force controlled	Muscle force derived	Flexion	18 MPa
(1) Saputra *et al.* (2013, 2014), (2) Ismail *et al.* and Jamari *et al.*	Force controlled	506 N	(1) 'Western style', 'Japanese style', (2) salat	(1) 49 MPa (2) 24 MPa*
Saputra *et al.* (2016)	Displacement controlled	3000 N (axial)	Impingement	38 MPa
Ezquerra *et al.*	Displacement controlled	-	Impingement	26 MPa*

All cup positions saw at least some impingement although often without dislocation. The authors noted that instances of impingement and dislocation were poorly correlated which was a finding supported by Higa *et al.* (Higa *et al.*, 2014). While impingement caused UHMWPE damage it did not necessarily result in dislocation. Pedersen *et al.* concluded that muscle tensions and the dislocation resisting moment were more important considerations for evaluating dislocation resistance.

The papers discussed thus far predominantly viewed impingement from a dislocation perspective. When evaluating the effect of impingement on polyethylene wear Callaghan *et al.* concluded that impingement would contribute to wear at the liner edge (Callaghan *et al.*, 2003). Their research also highlighted that subluxation events had the potential to draw debris into the articulation space which could result in increased wear rates due to the subsequent presence of third body particles in the articulation (Callaghan *et al.*, 2003).

Research from Saputra *et al.* recognised that activities of daily living display substantial cultural variation. They investigated impingement occurrence and severity in relation to self-described ‘Western-style’ and ‘Japanese-style’ movements (Saputra *et al.*, 2013, 2014) as well as salat movements of Muslim prayer (Ismail *et al.*, 2014; Jamari *et al.*, 2014). Of the ‘Western-style’ and ‘Japanese-style’ movements only a ‘picking up’ movement resulted in impingement and yielding stresses. While the performance of salat was predicted to produce multiple instances of impingement. Most notably during sujud – a position of high hip flexion. When repeated impingement events were tested around 95% the plastic strain occurred during the first cycle and the plastic strain had stabilised after four cycles (Jamari *et al.*, 2014). The von Mises stress decreased slightly with each repetition because the contact areas increased due to deformation.

Furmanski *et al.* and Ansari *et al.* were the only FE modelling research found to specifically examine impingement in relation to liner failure mechanisms (Furmanski *et al.*, 2009; Ansari *et al.*, 2013). Furmanski *et al.* observed that the peak magnitudes of tensile stresses occurred near to the observed crack initiation sites that had been identified in the clinical case studies from the same paper. This FE modelling was also the only one to omit the femoral component from their model and simulated impingement as a constant distributed pressure directly onto the liner. Therefore, the stresses observed at the egress site were neglected.

The analysis performed in this research predicted that the tensile stresses required for crack inception at a stress concentrating edge design features was only 8.8 MPa – less than half the material yield strength. However, the subsequent growth of cracks was believed to be inhibited by the low stress state of the liner interior. A finding they supported with their clinical fractography assessments. The authors hypothesized that the presence of sub-critical cracks – initiated at stress concentrating design features – had the potential to remain dormant in the liner and reach a critical size under subsequent adverse loading events that may occur years after the initial crack inception.

2.7.5 Shell and liner thickness

Goebel *et al.* used FE modelling to evaluate the effect of shell and liner thickness during surgical implantation (Goebel *et al.*, 2013). They found that In the case of thin shells the clearance of components could be affected due to deformation from impaction being passed from the shell to the liner. Liner thickness did not have a strong effect on its deformation because of the magnitudes of difference between the material stiffnesses of the metal shell and polyethylene liner. During subsequent physiological loading (non-adverse) decreasing the bearing diameter or liner thickness resulted in higher von Mises stresses but all stresses remained at sub-yield levels. The transmission of stresses from the shell to the liner was a perspective that was neglected by some FE models of THRs which simulate the shell through boundary conditions applied to the backside of the liner.

2.7.6 Summary of FE modelling research

In summary, FE modelling was a valuable tool for evaluating the stress-strain environment within liners. Edge loading by component separation and impingement loading were both widely predicted to result in stresses that exceeded the yield strength of UHMWPE. Analysis of cohorts of retrieved components indicate that impingement, for example, was a common occurrence with some researchers reporting rates of above 50% (Marchetti *et al.*, 2011). Given the comparative rarity of clinical liner failure this suggests that that material yielding is not an effective predictor for the occurrence of liner failure. This illustrates a limitation of the current literature which examined the stress strain environments but was lacking in attempts to relate it to potential damage mechanisms or the risk of liner failures.

Furmanski ***et al.'s*** research was almost unique in this regard. They cautioned that crack inception could occur at stress concentrating design

features as a result of sub-yield stresses (Furmanski *et al.*, 2009). They hypothesized that cracks could propagate to a critical size by an adverse event years after they have been initiated. Equally given the clinical rarity of liner failures it can also be suggested that, regardless of crack inception, the conditions necessary for crack propagation are not prevailing ones. A more detailed understanding of how particular design features and stress-strain environments may increase the risk of liner failure be beneficial to ensuring THR constructs remain resilient to edge loading.

.

Chapter 3 – Development of geometric characterisation methods to analyse edge loading of THR liners

3.1 Introduction

There is a clinical need to better understand the types of damage that occur when polyethylene liners are subjected to edge loading conditions. ISO 14242-4 and ASTM F2582 provide standardised models for generating edge loading by component separation and impingement for *in vitro* and *in silico* research. However, polyethylene wear of the bearing surface was still the dominant perspective of most of the research investigating edge loading conditions. Consequently, the characterisation methods used to evaluate changes to the liner edge were lacking and the research was unsuited to provide insights into the types of damage that occur and whether they may progress to liner failure. By developing new characterisation methods and using existing standardised models of edge loading a deeper understanding can be gained about the effects of edge loading on polyethylene liners.

The primary aim of this Chapter was to develop a geometric characterisation method to evaluate changes to the liner edge during edge loading. This aim was split into the following objectives:

- Define the context and criteria for the creation of new characterisation methods.
- Develop a novel analysis method for geometric assessment of changes to the liner edge.
- Perform preliminary studies of gravimetric and geometric measurements to understand the sources and scales of measurement error.

3.2 Context and criteria for the development of new characterisation methods

This study preceded an experimental hip simulator study that aimed to characterise the changes to polyethylene liners when subjected to edge loading by component separation. The geometric characterisation methods developed in Chapter 3 would be used alongside gravimetric measurements of volumetric wear and microstructural characterisation methods by Raman spectroscopy developed in Chapter 4.

To understand the progression of wear and deformation measurements were planned at one million cycles intervals throughout the hip simulator study. The statistical power of the hip simulator study was pre-empted as a limitation because the maximum number of test stations was six and variation between stations was observed in previous experimental hip simulator studies (Ali *et al.*, 2023). Therefore, the development of non-destructive characterisation methods was viewed as a requirement to enable all test stations to complete the whole period of testing and retain as much statistical power as possible. It was thought the alternative – sacrificing liners at different timepoints – would not provide as robust conclusions. An additional advantage of developing non-destructive characterisation methods was that they remained appropriate for liners from other tests or retrievals where destructive testing may not be an option.

Multi-million cycle hip simulator studies are complex tests that take many months to be completed. Ensuring that all the measurements planned would take place on a suitable timescale was critical to prevent substantial delays (months) to the completion of the study. To fit with a suitable test schedule it was determined that all of the measurements (eight liners) needed to be completed within two days. Hence a time limit of one day of measurement was set for both geometric measurement and microstructural measurement methods (comparatively the gravimetric measurement time was insignificant).

In summary, the context of the experimental hip simulator study planned enabled the following criteria to be established for the development of new characterisation methods:

- Progressive measurement of the changes to polyethylene liners
- Non-destructive characterisation methods.
- Total measurement time to be less than two days for eight liners.

3.3 Materials and study design

3.3.1 Materials

The nine liners characterised in this study were acquired from previous experimental tests. All liners were neutral configurations of a commercially available design (Pinnacle, DePuy Synthes Joint Reconstruction, Leeds, UK). They were made from Marathon polyethylene – a HXLPE (50 kGy) with a re-melted heat treatment. Table 3.1 defines the bearing diameter, number

of cycles and quantity for each of the liner groups used in the measurement studies in Chapter 3.

Table 3.1. A summary of the liners measured for the gravimetric and geometric measurement studies.

Liner loading	Bearing diameter	Cycles	Quantity
Edge loaded by component separation	28 mm	3 Mc	3
Untested	32 mm	0 c	3
Impingement loaded	32 mm	40 000 c	3

The edge loaded liners (Figure 3.1) had been subjected to three million cycles of edge loading as defined by ISO14242-4 (*Unpublished report received by private communication with Dr M. Al-Hajjar*, no date). The ISO14242-4 testing methodology for edge loading by component separation is described in Chapter 5.

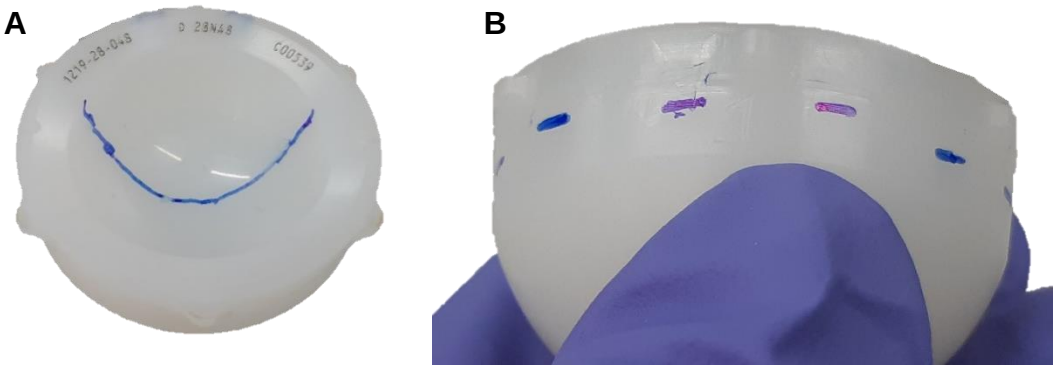

Figure 3.1. A polyethylene liner subjected to three million cycles of edge loading by component separation. (A) The locations of visible wear extended from the bearing surface onto the bearing surface rim. (B) Signs of plastic deformation were visible on the backside of the liners without any signs of surface fatigue damage (e.g. cracking or delamination). They were most prominent in the superior segment of the liner.

The untested liners and the impingement loaded liners (Figure 3.2) were the same liner design. A hip simulator was also used to subject liners to impingement. These liners were tested for 40 000 cycles using an input profile which moved components to 5 degrees past the point of impingement while a constant medial load of 200 N was applied. The maximum axial load during the impingement loading cycle was 800 N (Pryce, 2019).

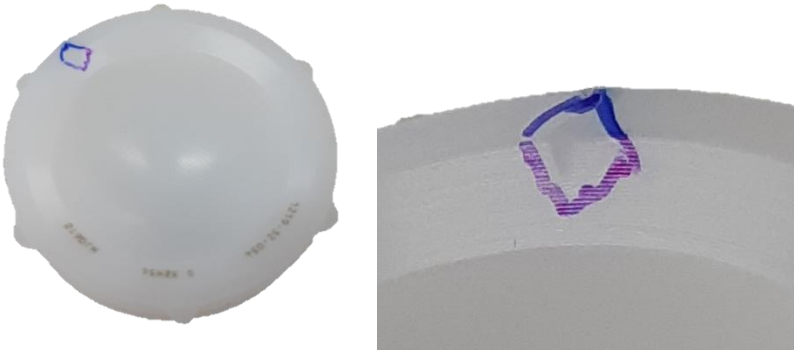

Figure 3.2. A polyethylene liner subjected to 40 000 cycles of impingement loading. (A) Impingement loading generated a diamond shaped deformity on the liner edge spanning a portion of the chamfer and top surfaces. There were no visible signs of fatigue damage (e.g. cracking or delamination).

3.3.2 Study design

Three repeat gravimetric and geometric measurements were made for the nine liners described in Section 3.3.1. The aim of the mass measurements was to assess the effect of fluid uptake on the mass of components during a soak period. The CMM measurements provided a bank of co-ordinate measurement data that was used to develop new analysis methods for evaluating the geometric changes to the liner edge. The repeat measurements were subsequently used to assess the repeatability of the CMM measurement and analysis procedures.

Before each measurement repeat the liners were placed in dH_2O for a two week soak period. The liners were cleaned, acclimatised and measured following the gravimetric measurement procedure (Section 3.4.1). Geometric measurements were taken after the gravimetric measurements and on completion the liners were placed back into dH_2O for the next soak period. This pattern of soak and measurements was chosen to replicate the two week periods in fluid that occur while running a hip simulator study.

3.4 Assessment of the effect of fluid uptake on gravimetric measurement

3.4.1 Gravimetric measurement method

The three repeat gravimetric mass measurements were taken with a balance with a precision of +/- 10 μg (XP205, Mettler Toledo, Columbus, Ohio, US). Prior to measurements the liners were cleaned using a protocol of detergent and isopropanol solution before being place into the balance room to acclimatise for 72 hours (+/- 6 hours). Prior to each measurement an anti-static ioniser was used to reduce the amount of static charge. The final mass measurement was determined as the mean of five measurements once five measurements had been acquired within 100 μg of each other.

A repeated measures ANOVA was performed in in SPSS 28 to determine whether there was a statistically significant differences between the repeat mass measurements for the two liner sizes (Laerd Statistics, 2015).

3.4.2 Gravimetric results and discussion

Figure 3.3 illustrates how the mass measurements mass of liners changed due to fluid absorption during the soak periods. The repeated measures ANOVA indicated that the mass increases of 0.7 mg and 1.1 mg for measurement repeat two and three respectively were statistically significant ($p < 0.01$). For this test analysis of the studentized residuals showed that there was normality in the data and no outliers were present as assessed by a Shapiro-Wilk test of normality and by having no studentized residuals greater than +/- 3 standard deviations, respectively. The assumption of sphericity was also met, as assessed by Mauchly's test of sphericity ($p > .05$).

The adjustment of gravimetric measurements for fluid absorption using soak control liners is an established practice in simulator wear testing using ISO 14242. A recent study reported that the wear rate of Marathon UHMWPE under a standard concentric walking gait was 12.9 mm^3/Mc which equated to a mass change of 12.0 mg/Mc (Ali *et al.*, 2023). The present study suggested that it was possible for fluid absorption to contribute at least 1.1 mg or equating to around 10% of the mass change during 1 Mc. Therefore, mass correction for fluid absorption using soak control components was concluded to be necessary for accurate gravimetric wear measurement.

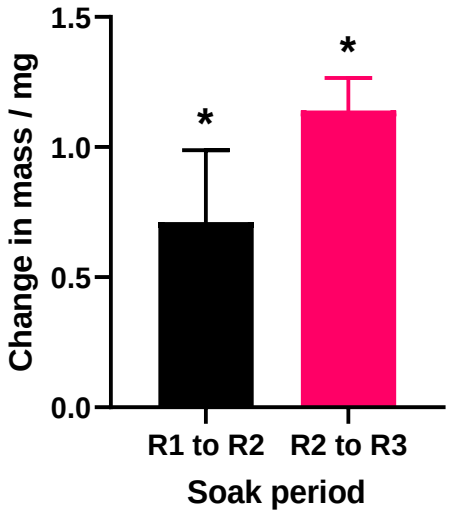

Figure 3.3. The mean change in mass between repeat measurements plotted with error bars displaying the 95% confidence interval. On both occasions a statistical significant difference (*) was found between the measurements taken before and after the soak.

3.5 Geometric measurement method

Geometric measurements of polyethylene liners used a Legex 322 CMM (Mitutoyo, Halifax, UK) with a 1 mm ruby ball stylus. A 1 mm diameter stylus was selected as the smallest available size because it has a lower measurement error than larger styli. The uncertainty of measurements was less than 0.9 µm where uncertainty in micrometres equals 0.8 µm + 2L/1000 and L is the trace length in millimetres (Mitutoyo, 2015). Liners were positioned in contact with the measurement table and supported on multiple sides with plasticine. The liners were allowed to rest for 30 minutes before the reference co-ordinate system was defined to allow the plasticine to settle and minimise movement during measurement.

3.5.1.1 Defining a reference co-ordinate system

A reference program was used to orientate the machine to the position and alignment of the liner (Figure 3.4A). A basal plane (XY plane) was aligned to four points on the flat top surface of the liner. The origin was defined by the centre of rotation of the bearing surface measured by seven points – one point at the pole and a circle of six points around the bearing surface. Finally, the rotational orientation around the Z axis was defined using either drilled holes on the top surface of the liner edge or by using the anti-rotation tabs.

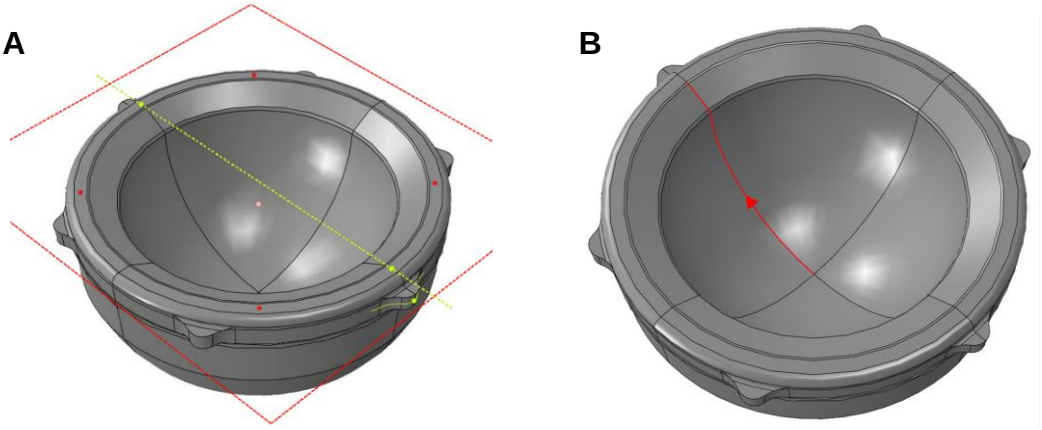

Figure 3.4. (A) The reference co-ordinate system generated for each liner prior to measurements was defined by a basal plane (red), an origin point (orange) and an alignment axis (green). (B) The measurement traces (red) began at the liner pole and proceeded up the bearing surface and liner edge.

3.5.1.2 CMM measurement traces

Co-ordinate data of the liner surface was measured by a series of 72 CNC controlled measurement traces at five degree intervals. Each trace began at the pole and proceeded up the bearing surface and out onto the chamfer (Figure 3.4B). The traces ended on either the chamfer or top portion of the liner edge.

Alternative measurement traces were explored during attempts to reduce measurement time. Consultation with the CMM manufacturer determined that the initial probing direction must approach the measurement surface in a normal direction or an error was caused by incorrect probe compensation. In addition, measurement traces were also more effective when pulling up a surface compared to pushing down one. Therefore, the liner pole was the ideal starting position for all traces and so this was not changed.

3.6 Developments to the CMM measurement method

3.6.1 Sequential measurement programs

Previous measurement programs were only capable of measuring one liner at a time and required the user to set up the next measurement each time. A method of looping the measurement program was developed which enabled all nine liners to be placed on the measurement table and measured in one sequence. All of the reference co-ordinate systems were stored at the

beginning and the ‘repeat counter’ variable was used to iterate the program to the next liner (using ‘loop counter’ caused measurements to slow down because the data hopper would keep expanding).

The sequential measurement program enabled the measurement scans to run uninterrupted overnight while the lab was closed to users. By utilising this previously inaccessible time the criteria for measuring liners within one day was comfortably achieved. An additional benefit was that the machine was more available to other users which became significant when multiple hip simulator studies were running simultaneously that all required CMM measurements.

Caution was required when using this method for liners which were at risk of ‘collision’ events during measurements which result in the program being paused. Therefore, the first set of measurements for any liners were supervised to ensure that the measurement program proceeded successfully. Subsequent liners measured which were highly deformed or damaged were also supervised.

3.6.2 Non-destructive reference co-ordinate system generation

Previous measurement methods involved drilling holes in the liner to provide a consistent orientation axis for CMM measurements. This was performed as far from the wear area as possible on the top surface of the liner edge (Figure 3.4A). An alternative method of aligning the orientation axis using the anti-rotation tabs was devised to mitigate any potential effect the drilled holes had on the mechanical performance of the liner. Furthermore, the method could be utilised or adapted for liners where destructive methods were not possible such as for retrievals. The new method measured the outermost point of two of the anti-rotation tabs to create the axis of alignment (Figure 3.4A). In the event that one or all of the tabs were damaged or missing, the program could be adapted so that any scribed mark or point of interest could be used in replacement.

3.6.3 Adaptive measurement programs and data logging

The measurement programs used information collected by the reference co-ordinate system to define the end point of measurement traces. This enabled looped programs to be used even when liners of different bearing sizes were being measured as was the case during the repeatability study.

Greater scrutiny of the measurement process was achieved by recording details of the reference co-ordinate system and measurement scans for each scan. This improved the transparency and reproducibility of

measurements particularly given that the measurements were less supervised when using sequential measurement programs.

3.7 Development of the CMM data analysis method

The developed method of analysing CMM data was a two stage process performed on each liner individually by custom MATLAB scripts. In stage one of the analysis, the liner's pretest data was analysed to acquire the average radius of the bearing surface and a single representative profile for the liners edge prior to any loading or wear.

The pretest edge profile of each liner was generated as an average profile of the liner edge across all 72 of the measurement traces. This profile was constructed from a bearing surface radius, a rim arc and a chamfer liner of best fit (with small transitions regions in between to stitch the geometries together). Section 3.7.1 describes how these geometric features were determined. Each liner was analysed individually due to the geometric variation between liners related to machining tolerances.

In stage two of the analysis, the liner's test data was compared to the pretest geometry profiles to evaluate the changes that had occurred at the bearing surface and liner edge. If no pretest data was measured then an adapted version of the scripts was used to make an estimate of the pretest profiles from the test data.

3.7.1 Stage one – Analysis of pretest data

The flow chart in Figure 3.5A outlines the steps taken during the analysis of pretest data. First the liner was divided into bearing surface, rim, chamfer and top regions by selections made by the user. An example of the construction liners generated by the user to separate these regions is illustrated in Figure 3.5B.

The pretest geometry profiles of the liner were then generated by fitting the data in each region to the appropriate geometry. The bearing surface was fitted to a sphere using the MATLAB program 'Ellipsoid fit' (Yury, 2015) to determine the bearing surface diameter and centre. The co-ordinate data of the liner was also centred around the origin of this sphere. The chamfer and top surfaces of the liner were fitted by straight lines using the in-built MATLAB function 'polyfit' to determine the surface's gradients and locations.

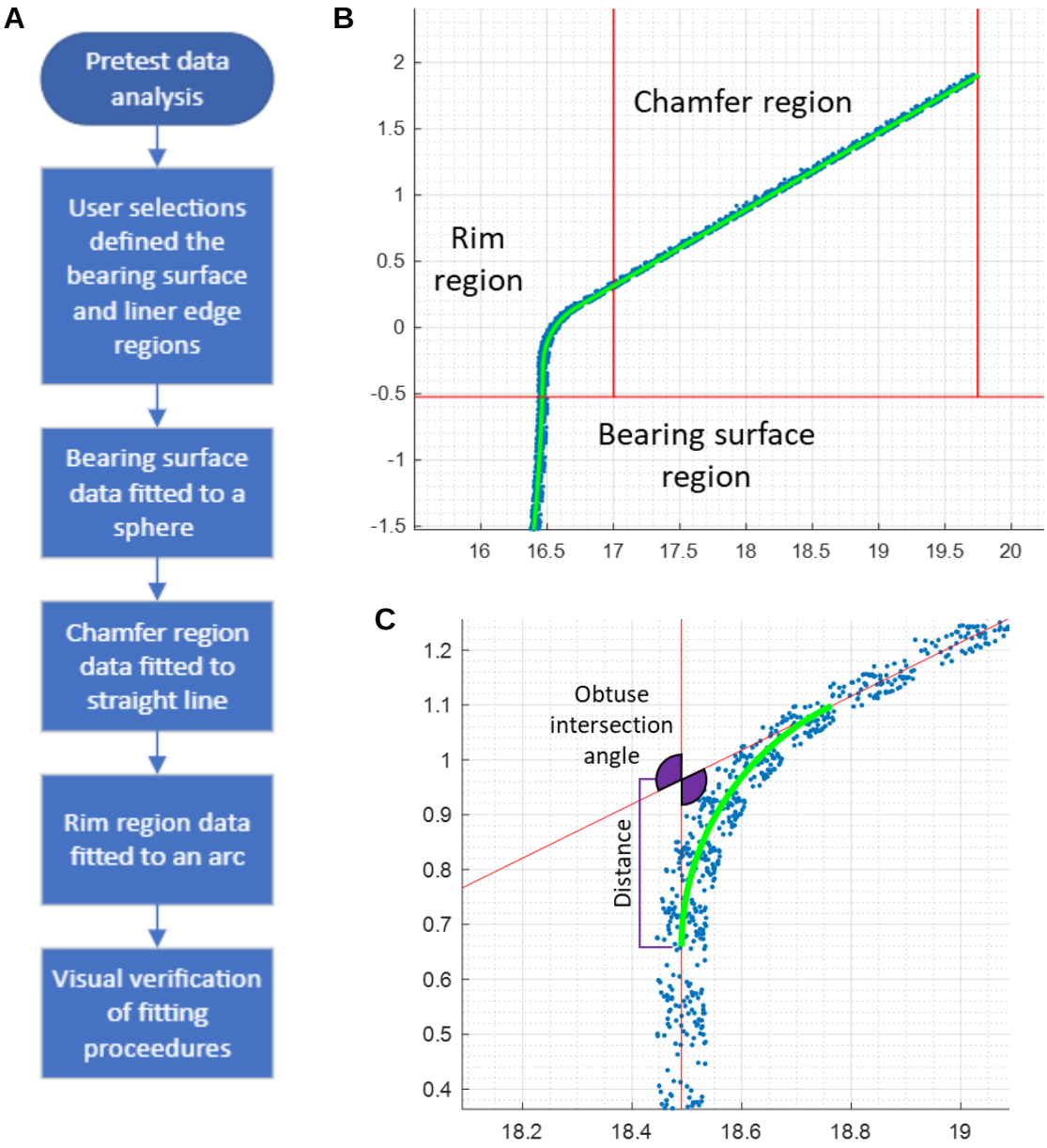

Figure 3.5. (A) A flow chart defining the steps taken to analyse the pretest data. (B) A plot of all the data points at the liner edge in a two-dimensional profile. The red lines illustrate the construction lines used to divide the bearing surface, chamfer and rim regions. The resultant fitted line at the liner edge is displayed in green. (C) The rim geometry was defined as an arc between two tangents. The distance and the obtuse intersection angle indicated in the diagram were used to calculate the rim radius using Equation 3.1.

The rim geometry represents the transition between the bearing surface and the chamfer. It was defined by an arc made between two tangents as illustrated in Figure 3.5C. The first tangent was an extension of the line of best fit from the chamfer region. The second tangent was a vertical line selected by the user which aimed to be bisect the data points located at the

top of the bearing surface. A user selection was used for this vertical line rather than the calculated bearing diameter. This manual approach was favoured over an automated one because the calculated bearing diameter was an average of the whole bearing surface; it did not necessarily reflect the precise position of the data at the near rim region. In addition, at this instance of the analysis an automated approach that was attempted failed to deal effectively with liners with different designs. For example, difference between a 28 mm Pinnacle design and a 32 mm Pinnacle design was enough to prevent the script from being used universally without adaptation of threshold values.

The rim geometry was generated by the user selecting the rim radius which most closely matched the arc to the data in the rim region. This was achieved by iterating the height at which the rim started from which the rim radius was calculated. Equation 3.1 displays the trigonometric relationship used to calculate the rim radius using the obtuse angle at the tangent intersection point and the distance between the tangent intersection point and the start of the rim. The distance and obtuse intersection angle used are illustrated in Figure 3.5C.

Equation 3.1

$$\textbf{Rim radius} = \textbf{distance} \times \tan\left(0.5 \times \textbf{obtuse intersection angle}\right)$$

Figure 3.6 illustrates the geometric variation of the bearing surface and liner edge for an untested liner. The outcome of stage one was the calculation of the average bearing surface radius and the generation of a 2-dimensional profile of the liner edge. The test data was then compared to these geometries in stage two to assess the scale and locations of geometric changes.

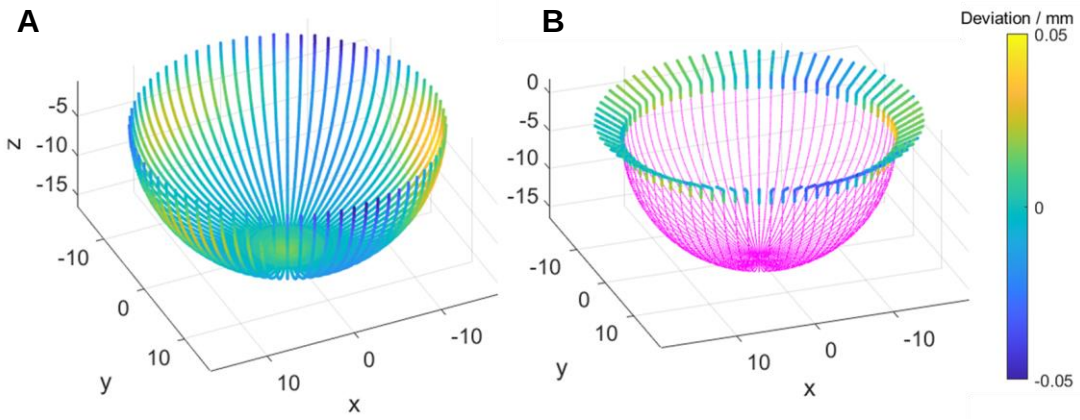

Figure 3.6. The geometric variation of (A) the bearing surface and (B) the liner edge of an untested liner which remained below the machining tolerance of the liner (0.05 mm). The pink data (B) is to provide a nominal liner shape to increase the clarity of the edge figures.

3.7.2 Stage two – Geometric deviation measurements

The flow chart in Figure 3.7A outlines the steps taken during the analysis of test data. The pretest profiles of the liner were retrieved from stage one of the analysis. The measured test data was centred around the centre of rotation of the liner and the geometric changes were evaluated as deviations from the pretest geometry profiles. Locations where the liner surface was translated outwards (also termed penetration in literature) were indicated by positive deviations. This was because at these locations the surface's radial position had increased. Conversely, locations where the liner had translated inwards (as a consequence of deformation) were indicated by negative deviations. This was because at these locations the surface's radial position had decreased.

The liner's bearing surface was approximated as a sphere. Therefore, the radial position of data on the bearing surface was simply compared to the calculated pretest radius. The process for the edge geometry was more complex. The pretest edge profile consisted of a series of very finely spaced points. For every measured data point on the liner edge the MATLAB script searched for the closest point on the pretest edge profile. The minimum distance determined was returned as the geometric deviation. In contrast to the bearing surface this distance could be in any direction.

3.7.2.1 Bearing surface visualisations

A three-dimensional surface deviation heatmap of the bearing surface was generated using the geometric deviations. Figure 3.7B illustrates a bearing surface after 3 Mc of edge loading by component separation. The yellow

regions of positive deviation are where edge loading has taken place and the liner surface has been worn and deformed outwards. The dark blue regions of negative deviation can be seen adjacent to the edge loaded area. Edge loading has deformed the liner which has resulted in these regions contracting inwards.

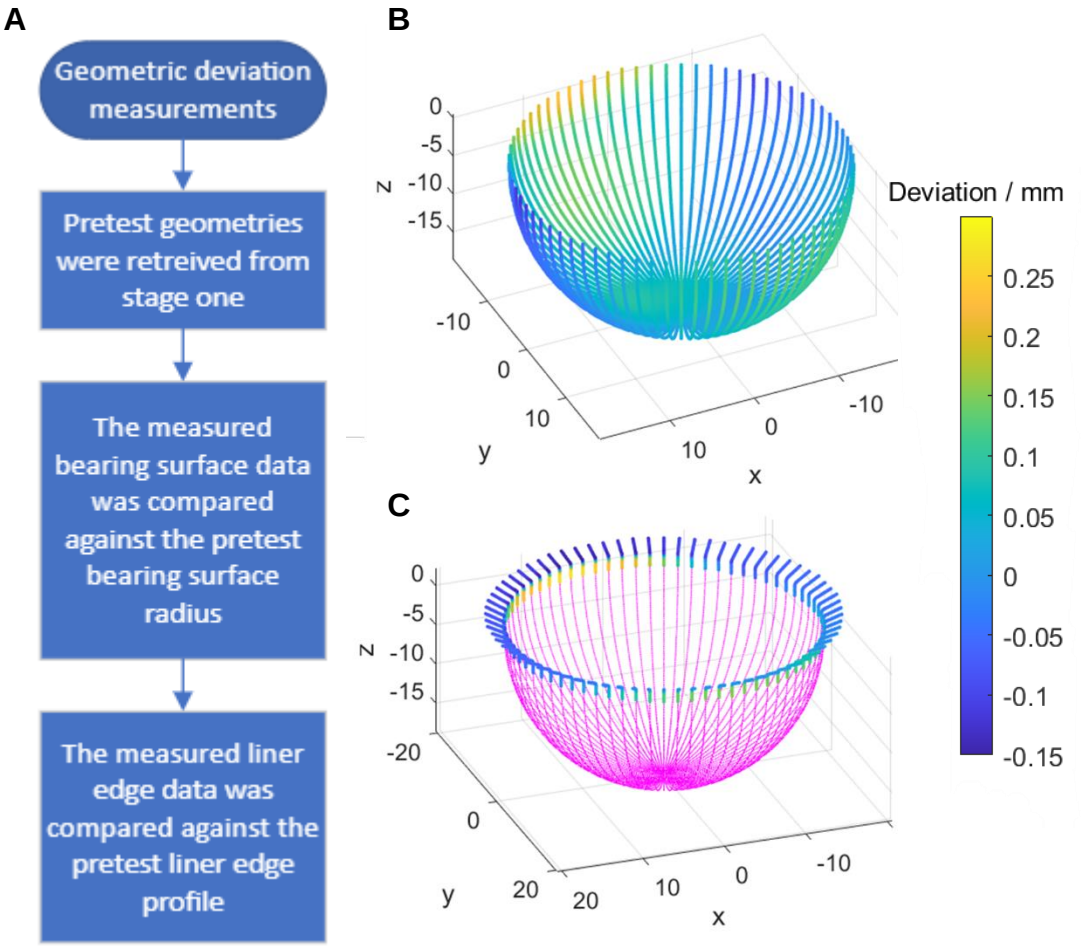

Figure 3.7. (A) Flow chart defining the steps taken to analyse a test liner which uses the pretest profile of the liner from part A. (B-C) The geometric deviation at the bearing surface and liner edge respectively after 3 Mc of edge loading. The colour scale indicates the deviation from the pretest geometry profiles. The pink data (C) is to provide a nominal liner shape to increase the clarity of the liner edge figures.

3.7.2.2 Liner edge visualisations

The same principle was applied to the liner edge geometry. Figure 3.7C illustrates the three-dimensional surface deviation heatmap of the liner edge that corresponds to the edge loaded bearing surface in Figure 3.7B. The

pink data in these figures provided a nominal liner shape which aimed to increase the clarity of the liner edge figures. These were well suited to identifying the locations and the general scale of geometric changes.

To provide further insight into the localised geometric changes of the liner edge an iterative two-dimensional in-profile plot was developed to enabled the data of individual traces to be visualised against the predicted pretest profile. The MATLAB script could cycle through adjacent traces to explore how the localised geometry of the liner edge was being altered. This enabled, for example, the changes to the liner rim morphology after edge loading to be visualised which were analysed in greater detail in Chapter 5 (Figure 3.8).

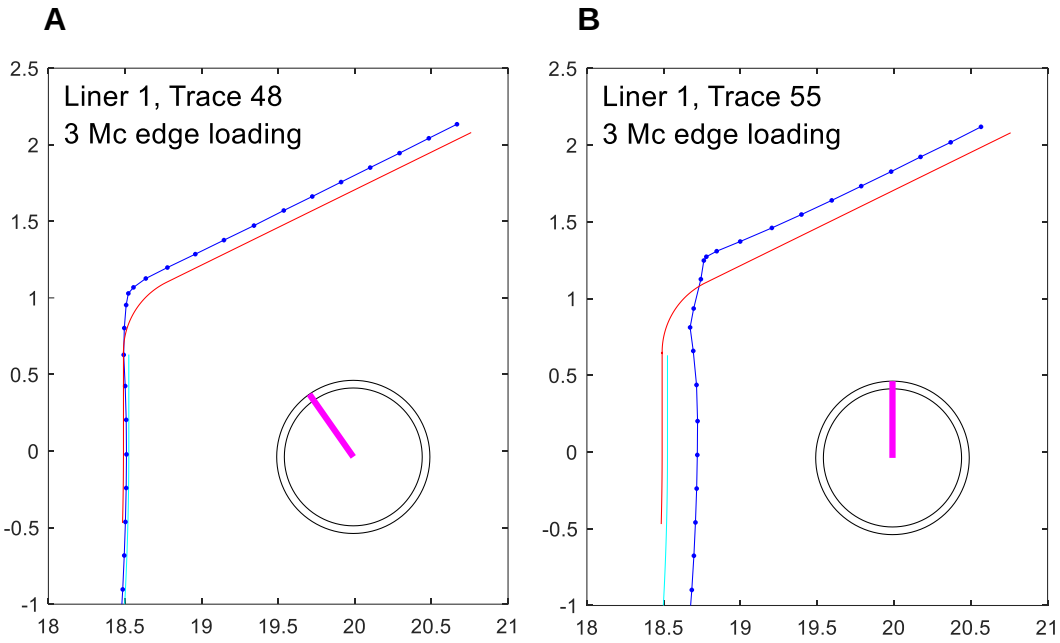

Figure 3.8. Example plots using the iterative two-dimensional in-profile plot. The cyan line is the pretest profile of bearing surface. The red line is the pretest profile of the liner edge. The dark blue line and points are the measured CMM data. The clockface schematic with the pink hand indicates where on the liner the trace is located relative to the XY plane of the heatmap plots (12 o'clock equates to the superior direction).

3.7.2.3 Estimating the contribution of wear and deformation to geometric change

For the liners subjected to edge loading by component separation an estimation was made for the separate contributions of wear and deformation to the geometric deviation. Visual inspection of the liners indicated that wear occurred in the superior hemisphere of liner only. Using the same analysis of the bearing surface but excluding traces with greater than +0.1 mm of deviation from the superior hemisphere a high majority of the remaining deviation was known to result from deformation only (Figure 3.9). This enabled the greatest positive deviation in the inferior hemisphere and the greatest overall negative deviation on the liner to be easily identified. These values related to changes to the bearing surface at non-loaded locations. The deformations here occurred in a more global sense as opposed to the more localised changes characterised by the analysis of the liner edge. By assuming these global deformations occurred relatively symmetrically around the liner the contribution of deformation in the superior hemisphere was estimated. The remainder of geometric deviation was attributed to wear. These estimates were considered as illustrative values and not as a direct measurement.

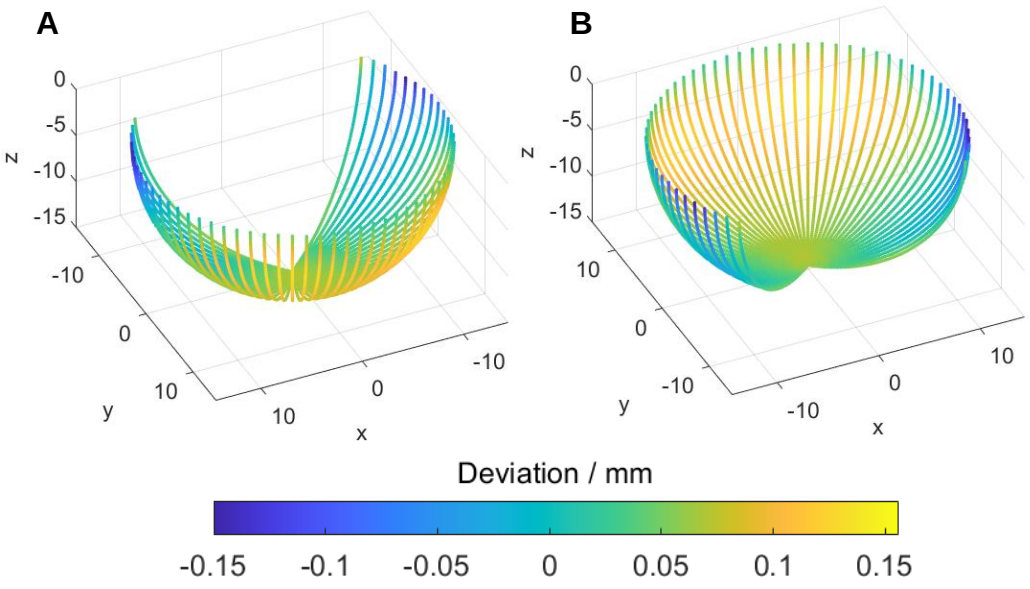

Figure 3.9. Estimations for the geometric changes as a result of deformation only were made by from the same bearing surface analysis but by removing traces on which wear was apparent. (A) and (B) show the exact same data from superiorly and inferiorly orientated views respectively.

3.8 Geometric analysis of edge loaded liners and repeatability study

3.8.1 Methods

Details of the nine liners characterised in this study and the overall study design were described in Section 3.3. For each liner three repeat geometric measurements of the liner surface were taken using a Legex 322 CMM (Mitutoyo, Halifax, UK) with a 1 mm ruby ball stylus as described in Section 3.5. The analysis method for the bearing surface and the liner edge was reported in Section 3.7. Pretest data for edge loading and impingement loaded specimens (measured at the time of the testing) was analysed to generate the pretest geometry profiles for these liners.

Repeated measures ANOVAs were performed in SPSS 28 to determine whether there was a statistically significant differences between the repeat measurements of geometric deviation at the bearing surface and liner edge respectively for the three loading conditions (Laerd Statistics, 2015). However, the tests did not meet the assumption of normality likely due to the fact that there were only three liners in each independent group. Therefore, the statistical significance results were not considered valid and were not presented.

3.8.2 Results and discussion

The geometric data at the bearing surface was analysed separately to the data at the liner edge. In both regions the largest positive (surface displacement outwards) and negative (surface displacement inwards) geometric deviations were measured. Figure 3.10 collates the results of each of these measures for the three loading conditions and measurement repeats. Untested liners showed geometric deviations equivalent to the machining tolerance of the liners (+/- 0.05 mm) in all measures. The impingement loaded liners were only substantially different from the untested liners in the positive direction on at the liner edge because of the localised nature of the deformation created in this testing. Edge loading by component separation caused clear increases in all of the geometric measures compared to untested liners as a result of wear and deformation. It was estimated that on average 50% of the geometric deviation was from material deformation and 50% from polyethylene wear.

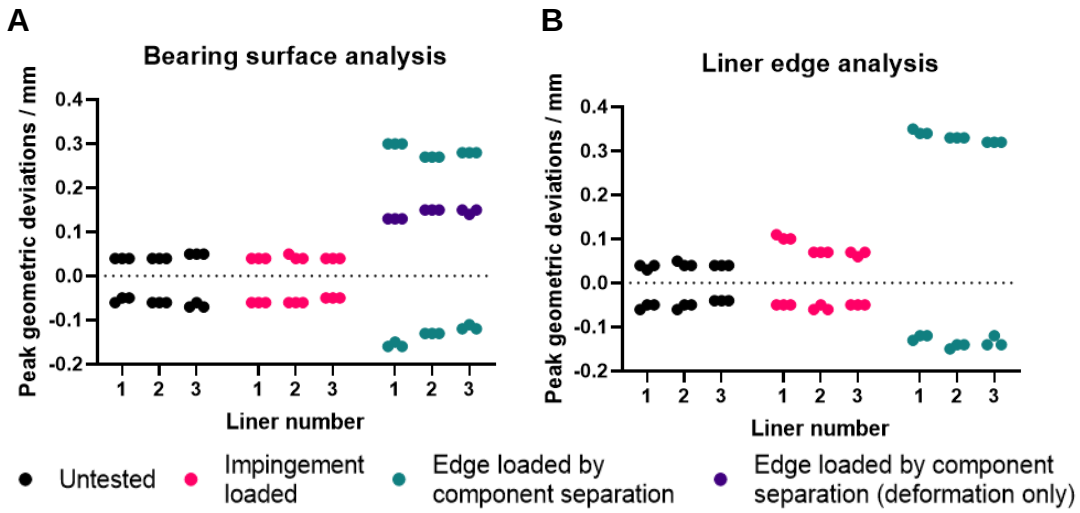

Figure 3.10. The greatest magnitudes of positive and negative geometric deviation measured for untested, impingement loaded and edge loaded liners at (A) the bearing surface and (B) the liner edge. The estimated maximum deformation at the bearing surface was also plotted for liners which were edge loaded by component separation. The individual repeat values each liner (N=3, R=3 for each loading condition) are displayed.

The repeatability of measurements was assessed by looking at the absolute differences between repeat measurements for each of the five geometric measurements made. Figure 3.10 illustrates that the variation of all geometric deviations measured across the three repeat measurements was very low. There was a difference of 0.01 mm or less in 97% of the measurements. Compared to the natural variation in the liner already from manufacture (+/- 0.05 mm) the level of variation likely to be introduced by the measurement and analysis methods would not have any substantial effect on the measurements and hence the repeatability of the methods was established with good confidence.

Figure 3.11 displays representative visualisations from a liner edge loaded by component separation. The greatest deviations occurred in the directly superior traces (Figure 3.11C) but edge loading sharpened the transition of the superior bearing surface rim for approximately 120 degrees (Figure 3.11D). The largest magnitudes of negative deviations were located laterally and medially – adjacent to the deformed rim region – and slightly into the superior hemisphere (Figure 3.11E). Positive deformations were located around the inferior quadrant of the liner (Figure 3.11F).

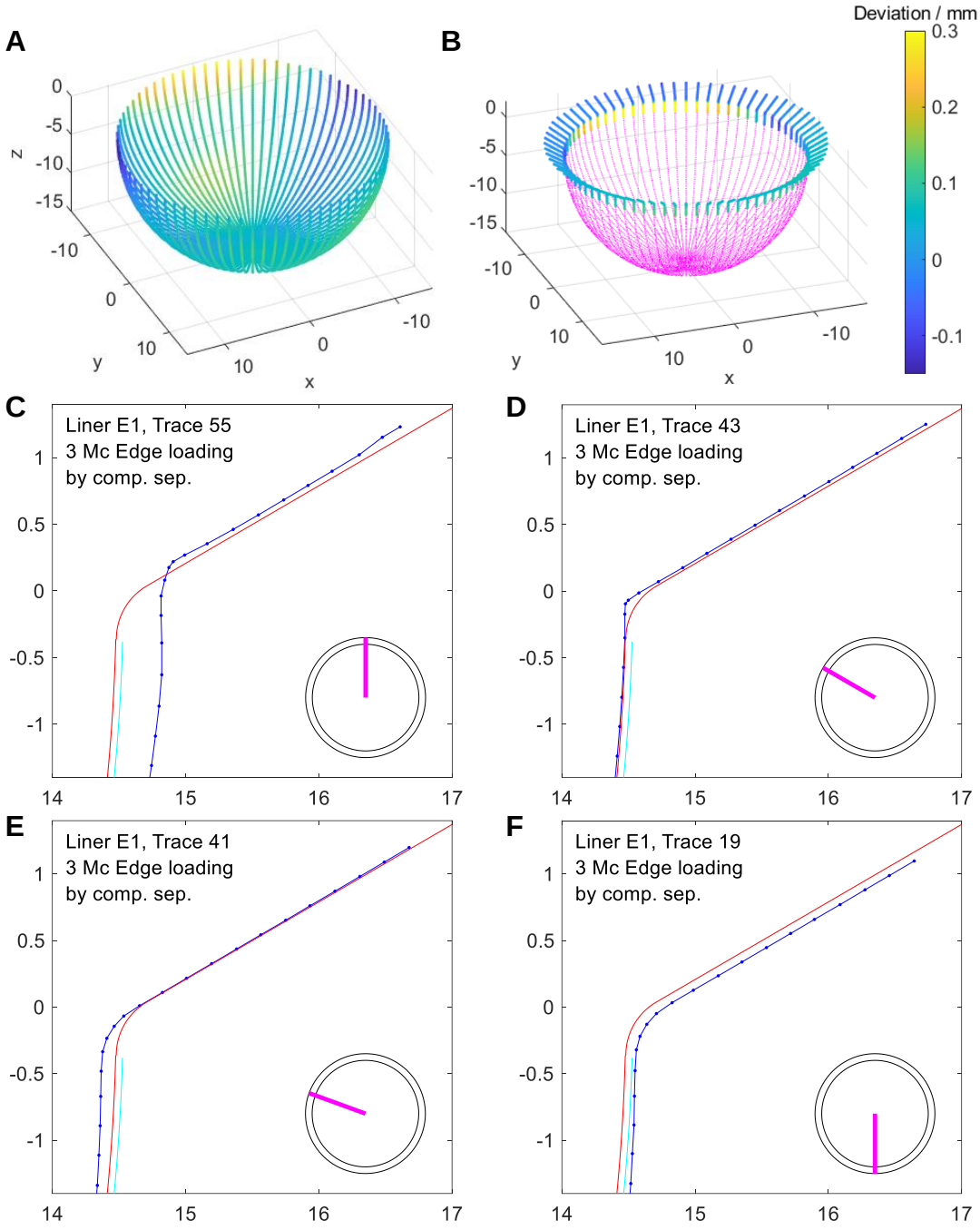

Figure 3.11. (A-B) Surface deviation heatmaps at the bearing surface and liner edge after edge loading by component separation. The pink data (B) is to provide a nominal liner shape to increase clarity. (C-F) The two-dimensional in profile view of changes to the liner edge (dark blue) compared to the pretest profiles of the liner edge (red) and bearing surface (cyan). The clockface schematic with the pink hand indicates where on the liner the trace is located relative to the XY plane of the heatmap plots (12 o'clock equates to the superior direction).

Figure 3.12 displays representative visualisations from an impingement loaded liner. Geometric deviation caused by impingement was highly localised and only a small region at the end of one measurement trace

displayed any geometric deviation. Figure 3.10 provided confidence that the analysis methods were being performed repeatably but the visualisations suggest that for this particular test the CMM measurement program used was unsuited to evaluate the geometric deviations. The traces stopped short of some of the impingement scar and the 5 degree inter-trace angle was too large to effectively characterise it. This study preceded a hip simulator study of edge loading by component separation so the limitations identified here would not be impactful but should be considered when designing measurement programs for liners with localised damage patterns.

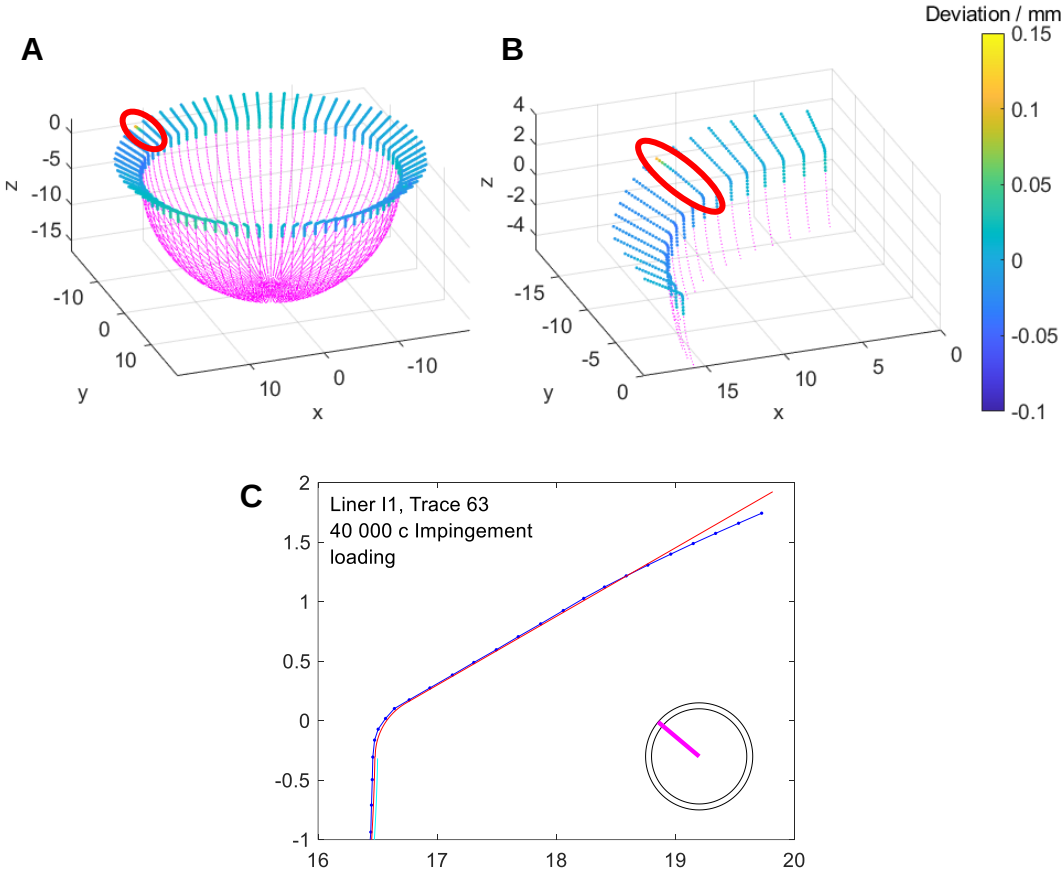

Figure 3.12. (A-B) Geometric deviation at the liner edge of an impingement loaded liner. Deviations exceeding +/- 0.05 mm were only located on one trace (circled in red). (C) The two-dimensional profile view of the deformed trace.

3.9 User-input sensitivity study

The geometric analysis required four user-selected inputs to generate the pretest edge profile. The sensitivity of the profile to the inputs used was examined to assess the objectivity of the analysis. The calculation of the bearing surface radius was influenced by the bearing-rim cutoff only (Input 1). Similarly, the chamfer line was influenced by the chamfer-rim cutoff only (Input 2). Figure 3.13 displays the sensitivity of the bearing surface radius and chamfer line to these inputs. A wide range of possible inputs values resulted in less than 0.01 mm of difference in the profile produced.

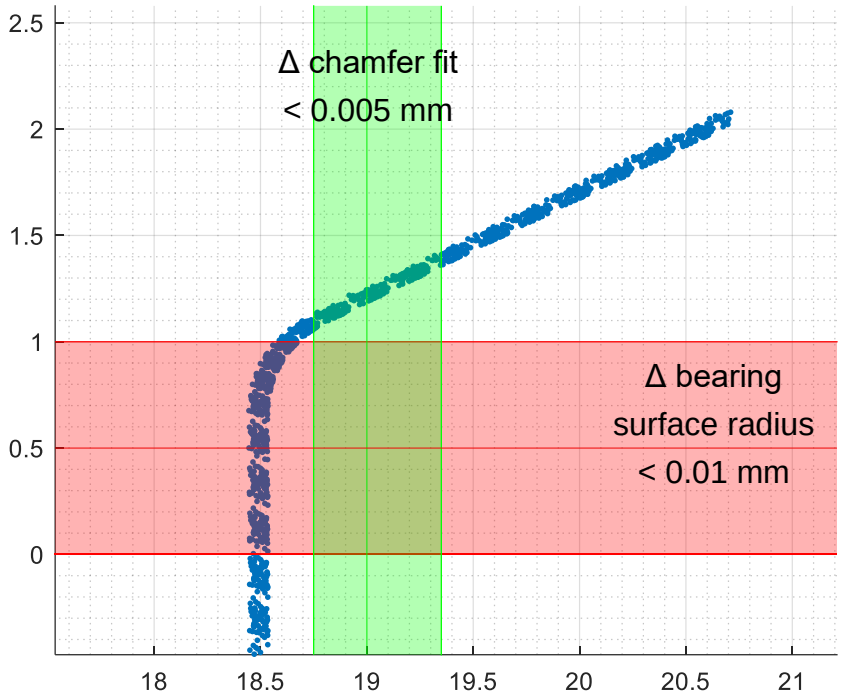

Figure 3.13. The sensitivity of bearing surface radius and chamfer to inputs for dividing the liner into separate regions. The red input region for the bearing surface-rim cut off (Input 1) altered the bearing surface radius by less than 0.01 mm. The green input region for the chamfer-rim cut off (Input 2) altered the chamfer liner of best fit by less than 0.005 mm.

The rim geometry was directly influenced by two user inputs: an X coordinate (Rim-X) and a Z coordinate (Rim-Z) indicating more precisely where the bearing surface ends and the rim begins. For both inputs, a spread values +/- 0.03 mm from the actual selection was tested. The suggested precision of both inputs (indicated in the MATLAB script) was 0.01 mm.

Figure 3.14A displays how Rim-X directly translated the profile produced on a 1:1 basis at the upper bearing surface region. By the end of the rim arc the effect of this input has diminished to zero. Figure 3.14B illustrates the spread of values tested at the point of input selection. The instruction accompanying this selection asked the user to bisect the data within the red rectangle with an input precision of 0.01 mm. The 0.06 mm spread input values tested almost covered the whole spread of the data so while aiming to bisect the data many of the inputs tested would clearly have been erroneous. It was thought unlikely that inter-user variability would exceed +/- 0.01 mm for the selection of Rim-X. Therefore, despite the profile having the most sensitivity to Rim-X the predicted subjectivity caused by this input did not exceed that of the other inputs.

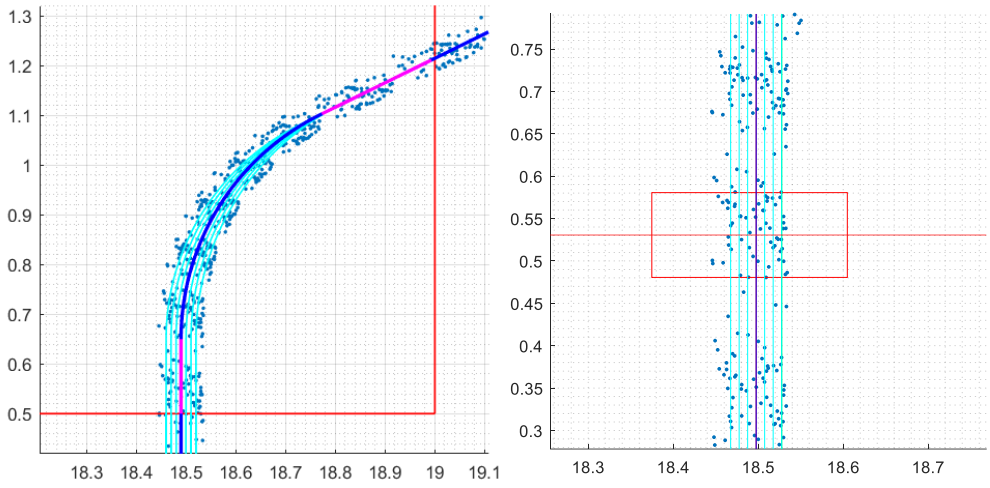

Figure 3.14. (A) A representative scatter plot of all traces from a pretest measurement of a liner. The dark blue lines indicate the optimal bearing surface, rim and chamfer lines determined. The pink sections are the transitions between these the geometric regions. Cyan lines indicate the effect of altering the Rim-X input (+/- 0.03 mm) while retaining a constant Rim-Z input. The suggested input precision for the user provided in the script was 0.01 mm. (B) Illustrates the spread of input values tested at the point of the user selection. The dark blue line represents the actual selection and the cyan lines are up to +/- 0.03 mm away from this line.

The Z co-ordinate was only a proxy used to calculate the radius of the rim. The same range of rim-Z inputs were tested. Figure 3.15 displays that as the rim-Z input was altered by +/- 0.03 mm the resultant change in the profile was less than 0.01 mm.

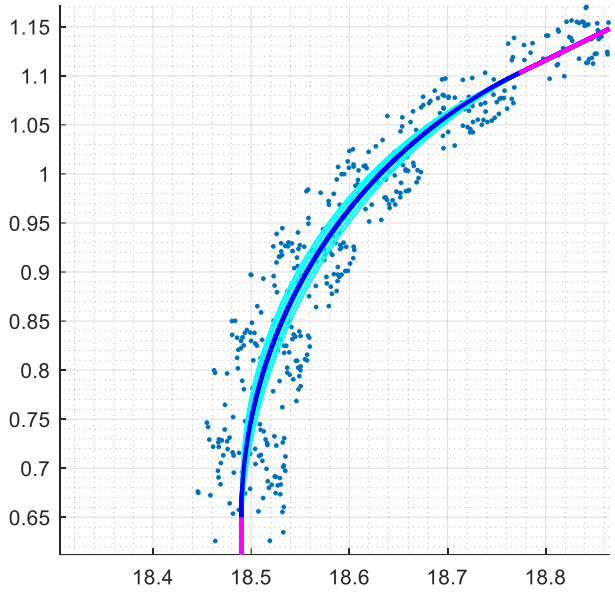

Figure 3.15. A representative scatter plot of all traces from a pretest measurement of a liner. The dark blue lines indicate the optimal rim line determined. The pink sections are the transitions between the rim and the bearing surface and chamfer regions. Cyan lines indicate the effect of altering the Rim-Z input (+/- 0.03 mm) while retaining a constant Rim-X input. The suggested input precision for the user provided in the script was 0.01 mm.

In conclusion, this sensitivity study has demonstrated that user-selected inputs were highly unlikely into introduce subjectivity into the analysis. The liner profile was very insensitive to three of the four user inputs. The final input (Rim-X) did have the capability to influence the liner edge profile. However, following the guidance provided at this selection more than 0.01 mm of subjectivity was not expected. This magnitude of uncertainty was insubstantial when compared to the geometric variability induced during machining (0.05 mm).

3.10 Discussion

There were few examples in literature which attempted to determined geometric changes at the liner edge. Partridge *et al.* analysed a limited subsection of the liner edge (5 traces at ten degree intervals) using a contacting profilometer (Talysurf) (Partridge, Buckley, *et al.*, 2018). The traces were analysed in profile to provide insights into geometric changes of retrieved liners. Pryce used a CMM to measure the whole circumference of the liner edge and produce heatmaps of geometric deviation. However, only the chamfer region of the edge was analysed (Pryce, 2019). Both of these

methods were less effective when evaluating retrieved liners because of difficulty producing an as-manufactured geometry to quantify geometric changes from.

Takahashi *et al.* also used a CMM to evaluate geometric changes after subjecting liners to *in vitro* impingement (Takahashi, Tateiwa, Pezzotti, *et al.*, 2016). Maximum deviation was their primary output measure which made comparisons between test groups simple but their analysis of impingement resistance – the aim of their study – weighed more heavily on other results from SEM and Raman spectroscopy characterisation.

Finally, Choudhury *et al*. measured the surface deviation of retrieved UHMWPE liners using micro-CT by comparing scans to those taken of a separate as-manufactured liner (Choudhury *et al.*, 2018). MicroCT was not considered for geometric characterisation because the measurement time required and resource availability of the microCT made it unfeasible for the planned hip simulator study. In addition, the measurement precision achieved by Choudhary *et al*. was 0.05 mm – five times greater than the CMM measurements in this research.

The acquisition of surface geometry data by CMM satisfied all of the criteria outlined in Section 3.2. However, the current methods of data analysis in literature were insufficient for the primary aims of this research which was to evaluate the damage mechanisms at the liner edge. Therefore, new analysis methods were developed to overcome the current limitations in the literature and provide better insights into the effects of edge loading on the liner.

A critical component of the analysis was the generation of a pretest profile of the liner edge. The key principle behind this was splitting the liner geometry into a series of simple geometric shapes. For the liners analysed in this research this was a bearing surface sphere, a rim arc and a chamfer line only. This particular analysis script would not work for all liner designs if they deviated from this form. However, the tools and philosophies that embodies the analysis provide a solid basis for similar analyses. Liner designs without rotational symmetry were anticipated to be the most challenging scenario. In this circumstance comparing measured data directly to the component's CAD design on a three-dimensional basis would be advised.

The user-input sensitivity study provided strong evidence that the generation of larger geometric regions (the bearing surface and chamfer here) were very insensitive to a wide range of user inputs. The user inputs for smaller regions (the liner rim) needed to have more influence over the profile

generated. Guidance written into the MATLAB analysis script suggested the appropriate level of precision needed for each user selection to attempt to minimise the potential inter-user variability. The risks of inter-user variability were further assuaged by the transparency of the user selections. It was possible to precisely replicate any analyses which enabled the decision making and subsequent analysis to be scrutinised.

Further automation to all but eliminate of inter-user variability was desirable but attempts to do this generated issues when analysing liners with even slightly varied designs. The more pragmatic approach that was developed coupled with high transparency user inputs provided a simple effective way to deal with small and complex geometric features. It was a philosophy that better equipped these methods to deal with more complex cases – such as retrievals – that previously had been problematic (data not presented in this Thesis).

In contrast to Choudhury *et al*., the method developed in this research generated pretest profiles on an individual liner basis rather than using a separate as-manufactured control or alternatively a collective average. While measuring liners prior to THR surgery would be highly impractical the effect this has on measurement uncertainty can still be examined. In this Chapter, the deviations (< 0.3 mm) were not insignificant compared to the machining variability of the liners (0.05 mm) which motivated the choice to analyse liners individually. However, the scale of geometric changes in the retrieved liners was much greater (> 1 mm) than those analysed in this Chapter. Despite increasing the measurement uncertainty, the effect of the variation from machining was fairly nominal for Choudhury *et al*. Ultimately, understanding the scale of variation in as-manufactured liners in comparison to observed changed should be factored into any geometric analyses to determine whether it will be influential.

On a similar theme, the analysis of the liner edge was separated from the analysis of the bearing surface in this research. This was because the bearing surface radius was determined as an average of the whole bearing surface and so did not necessarily best reflect the precise location of the data captured at upper regions of the bearing surface where the liner edge begins. Even in untested liners the upper bearing surface region tended to be contracted inwards compared to the rest of the bearing surface. This was attributed to material relaxation after manufacture and was at a magnitude sufficient to influence the edge measurements.

A second critical finding from the development process was the importance of combining quantitative and qualitative perspectives to provide the most comprehensive understanding of the geometric changes to the liners. The quantitative element provided perspective and sense of scale to the analysis. Changes to the bearing surface were well suited to being evaluated quantitatively where surface deviation heatmaps indicated the locations and scale of wear and deformation. This was because the surface geometry of the bearing surface does not substantially get altered. In previous research, these surface deviation heatmaps were often viewed as two-dimensional projections viewed from above the liner. However, this can distort the spatial distribution of the changes and data in the upper regions of the bearing surface can appear much closer together than reality. Hence three-dimensional plots were utilised in this research.

Quantitative assessment remained an important part of the analysis of the liner edge but in isolation would fail to appreciate localised changes to the surface morphology. Therefore, a suite of visualisation and evaluative tools were developed to allow the changes to the liner edge to the evaluated through a combination of quantitative and qualitative perspectives. Three-dimensional surface deviation heatmaps enable the locations and distribution of geometric deviation to be evaluated in a more global sense. The iterative two-dimensional in-profile plots were critical for providing insights into the localised geometric changes. The progression of these localised changes was thought to be vital to understanding the types of damage that occur when liners are subjected to edge loading.

3.11 Conclusion

In conclusion, this chapter described and demonstrated the successful development of a geometric characterisation method to evaluate changes to the liner edge during adverse loading. The methods met all of the development criteria set in Section 3.2 and the quantitative measures of geometric variation determined were shown to be highly repeatable. It was thought that to gain the fullest picture of the changes to the liner edge a combination of quantitative and qualitative assessment was required. The three-dimensional surface heatmap plots and the two-dimensional iterative in-profile plots developed were well suited to characterise the changes to liner geometry during an experimental hip simulator study of edge loading.

Chapter 4 – Development of microstructural and sub-surface characterisation methods to analyse edge loading of THR liners

4.1 Introduction

Polyethylene wear has been the dominant perspective of most of the research relating to edge loading in THRs. The characterisation methods used have been unsuited to provide insights into the types of damage that occur and whether they may progress to liner failure. Limitations to geometric analysis methods were identified and addressed in Chapter 3. This Chapter focused on the development of characterisation methods to assess microstructural changes and sub-surface damage in liners subjected to edge loading. The microstructural characterisation methods were developed under the same context that underpinned the development of geometric characterisation methods and hence the development criteria were the same (Section 3.2).

Section 2.5 established the importance of the UHMWPE microstructure its mechanical response. Raman spectroscopy was previously used to show that UHMWPE microstructural transitions could occur as a result of the loading applied in uniaxial compression tests and hip simulator studies (Bertoluzza *et al.*, 2000; Takahashi *et al.*, 2015; Takahashi, Yamamoto and Pezzotti, 2015; Trommer *et al.*, 2015; Puppulin *et al.*, 2016; Takahashi, Tateiwa, Pezzotti, *et al.*, 2016). However, other hip simulator studies found that no significant microstructural transitions were produced (Affatato *et al.*, 2002; Taddei *et al.*, 2002; Taddei, Di Foggia and Affatato, 2011).

It was hypothesized that microstructural changes might occur as a result of edge loading in an experimental hip simulator. Characterisation of microstructural changes may provide insights into the formation or progression of macroscopic damage in the liner. Raman spectroscopy was selected to test this hypothesis as the only characterisation method identified to non-destructively measure UHMWPE microstructure. Previous finite element modelling of edge loading by component separation predicted that plastic strain accumulation peaked just below the surface at the bearing surface rim (Etchels *et al.*, 2023). Therefore, the measurements would focused on this location.

A method of visualising sub-surface cracking using MicroCT was developed previously (Partridge, 2016). During hip simulator studies of edge loading by component separation sub-surface cracking was only observed in aged polyethylene liners. However, the testing used a pneumatic hip simulator and component translations of less than 1 mm was measured. Therefore, the edge loading conditions can be considered much milder than the conditions subjected to liners in this research (i.e. the edge loaded by component separation described in Section 3.3.1). Therefore, these liners were examined using MicroCT for signs of sub-surface cracking or damage.

The primary aim of this study was to develop a microstructural characterisation method using Raman spectroscopy to evaluate changes to the liner edge during edge loading. A secondary aim was to assess edge loaded liners for signs of sub-surface cracking using MicroCT.

These aims were split into the following objectives:

- Determine the methods of spectral acquisition and spectral analysis that had most potential to be used from the existing Raman spectroscopy literature.
- Establish the optimal methods for acquiring and analysing Raman spectra based on the robustness and repeatability of the analysis.
- Perform a repeatability study of Raman spectroscopy to understand the sources and scales of measurement error.
- To use micro-CT scans to assess whether any sub-surface damage was visible in liners that had been subjected to edge loading by component separation.

4.2 Materials

The liners used in this study were acquired from previous experimental tests and were also used in the development of geometric characterisation methods in Chapter 3. All liners were neutral configurations of a commercially available design (Pinnacle, DePuy Synthes Joint Reconstruction, Leeds, UK). They were made from Marathon UHMWPE – a HXLPE (50 kGy) with a re-melted heat treatment. Three liners - one untested liner (32 mm inner bearing diameter), one impingement loaded liner (32 mm inner bearing diameter) and one edge loaded liner (28 mm inner bearing diameter) - were used. Details of the loading conditions applied to each liner was reported in Section 3.3.1.

4.3 The development of Raman spectroscopy methods

4.3.1 Introduction

Strobl and Hagedorn first proposed the use of Raman spectroscopy to evaluate the microstructure of biomedical UHMWPE (Strobl and Hagedorn, 1978). Raman spectra are acquired using a microscope to focus a laser on the surface of the sample. Each spectra is acquired from a localised area or focal point. The signal was estimated to be recorded from the first 25 µm of the sample's surface where the peak of the signal was from a depth of 3 µm (Zerbi *et al.*, 1989; Fagnano *et al.*, 2001). Alternatively, confocal Raman spectroscopy was used to measure values at specific depths from the material's surface. Studies generally reported up to a depth of 100 µm but at least 1000 µm was possible (Pezzotti, 2017). Pezzotti also highlighted the need for a statistical element to quantitative microstructural measurements by Raman spectroscopy. In both confocal and non-confocal Raman spectroscopy, each microstructural measurement resulted either from multiple spectral acquisitions or accumulation periods of the Raman signal.

Analysis of the Raman spectra splits them into three distinct regions between 950 cm^{-1} and 1600 cm^{-1} based on the dominant mode of molecular vibration at different wavenumbers. The spectra consist of a series of sharper crystalline and broader amorphous peaks or bands. The relative positions and intensities of specific peaks are used to indicate microstructural details such as microstructural phase percentages and molecular orientations.

Figure 4.1 outlines the four steps required for Raman spectroscopy analysis. Typically, the methods of acquiring Raman spectra were reported thoroughly in literature. However, details of the spectral analysis methods performed were regularly reported with far less rigor despite being a critical component of the final measurements (Rull *et al.*, 1993; Naylor *et al.*, 1995). Finally, once the spectra have been decomposed into individual but overlapping peaks there were a multitude of methods used to evaluate various microstructural details.

A review of the existing methods in literature attempted to identify the most suitable methods. However, the variety and inconsistent reporting of methods meant that an investigation was still required at each step to establish the most appropriate approach. The different acquisition and analysis strategies assessed are also displayed in Figure 4.1. The most

suitable methods for steps A to C were established first before the effectiveness of different microstructural evaluation methods were evaluated.

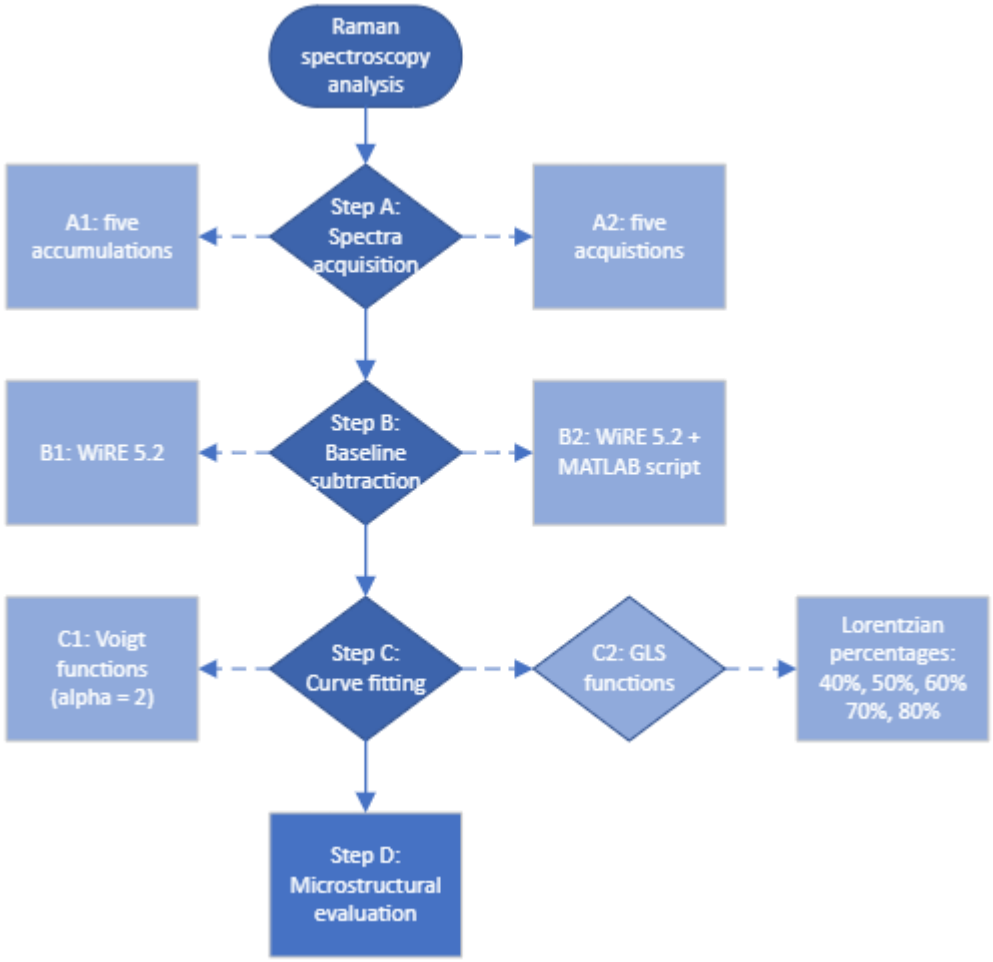

Figure 4.1. An overview of the four steps of Raman spectroscopy analysis and the different analysis strategies assessed.

4.3.2 Spectral acquisition method (Step A)

Raman spectra of the UHMWPE liners were acquired using a Renishaw inVia Raman Microscope and Renishaw WiRE 5.2 software (Renishaw, Wotton-under-Edge, UK) to measure surface crystalline, amorphous and third phase percentages. A 532 nm laser was used with a power of 10 mW. The laser was focused through a 20x objective lens and the signal from wavenumbers of 689 cm^{-1} to 1848 cm^{-1} was accumulated for 30 s. Table 4.1 defines several terms relating to the acquisition of Raman spectra to avoid ambiguity in the description of methods.

Table 4.1. Definitions of terms used to describe the acquisition of Raman spectra.

Term	Definition
Accumulation	The length of time the Raman signal was recorded for.
Acquisitions	The number of spectra recorded per focal point.
Measurement location	The macroscale location of measurement (e.g. edge loaded rim).
Focal point	The microscale location at which the laser was focused to acquire Raman spectra.
Microstructural measurement	Each microstructural measurement (e.g. crystalline percentage) was the mean value obtained from all spectra recorded at all of the focal points of a particular measurement location.

Raman spectra were acquired from one measurement location on each liner. This was at the edge loaded rim, the impingement site and the (unloaded) rim for the edge loaded, impingement loaded and untested liner respectively. Each of the microstructural measurements were an average from the spectra at three focal points. Three repeat measurements were made on separate days to assess the repeatability of measurements.

Two spectral acquisition conditions were assessed because of ambiguity in the use of the terms accumulation and acquisition in the literature (Table 4.2). Condition A1 acquired one spectra over five accumulation periods at each focal point. Condition A2 acquired five spectra at each focal point where each spectrum was the result from one accumulation period. Figure 4.2 provides a diagram of spectral acquisition method A2.

Table 4.2. The two spectral acquisition conditions used to assess the effect of the number of acquisitions and accumulations (per focal point) on microstructural measurements.

Condition	Accumulation time	Number of accumulations	Number of acquisitions	Measurement time
A1	30 s	5	1	150 s
A2	30 s	1	5	150 s

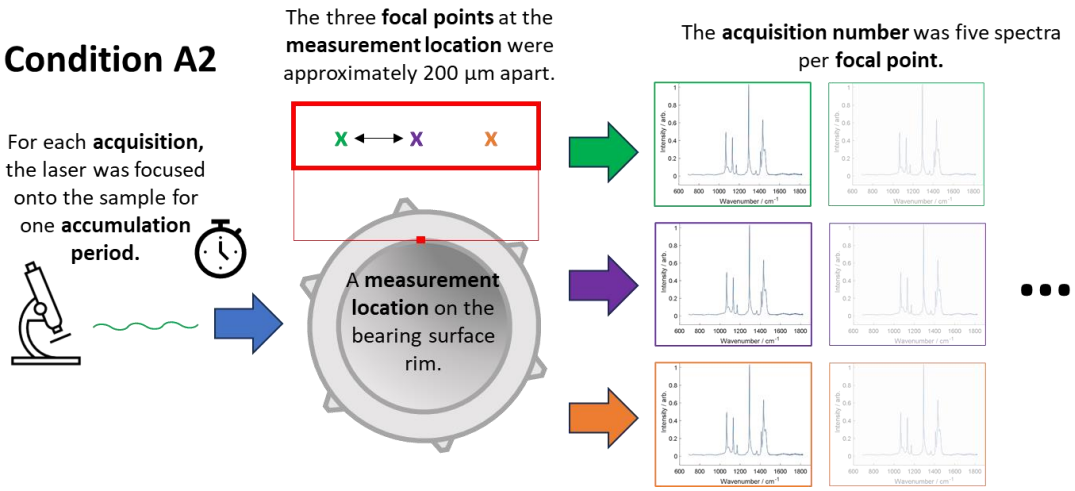

Figure 4.2. A diagram of the measurement processes for spectral acquisition method A2.

4.3.3 Baseline subtraction method (Step B)

Unprocessed Raman spectra contain the Raman signal as well as a general non-linear background signal caused by varying degrees of fluorescence (Rull *et al.*, 1993; Renishaw, 2023). A baseline subtraction procedure was required to remove the background signal. Two methods of baseline subtraction were assessed. In condition B1 this was performed by WiRE 5.2 software only (Figure 4.3).

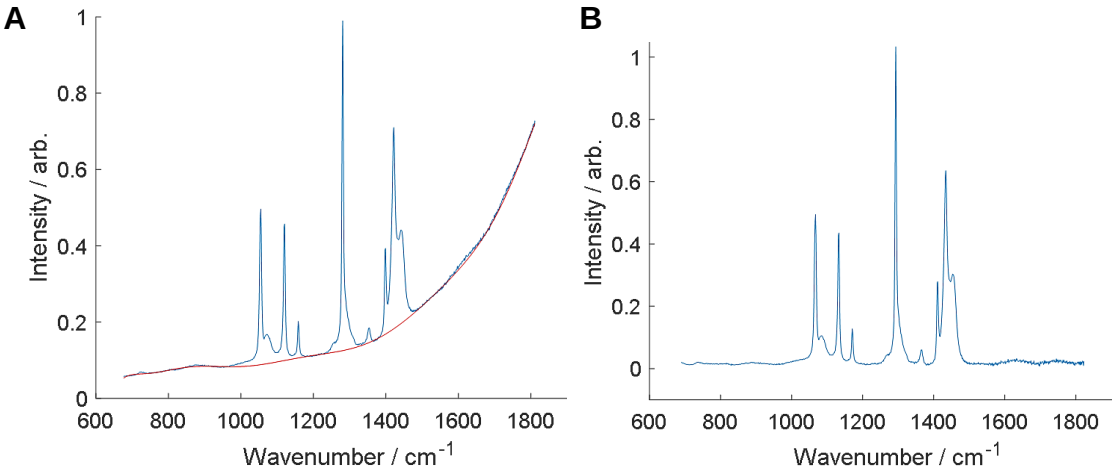

Figure 4.3. (A) An example of an unprocessed Raman spectrum. The red line indicates the baseline fitted by WiRE 5.2 software. (B) The Raman spectrum after baseline subtraction by WiRE 5.2 software (condition B1).

Raman spectra were split into three distinct regions to be analysed. While performing analyses using the baseline subtraction condition B1 it was observed that the signal did not return to zero at the edges of each region. Figure 4.4 illustrates example of a ‘raised’ signal from region I where the signal sits above the x-axis. These ‘raised’ signals tended to increase the broadness and area of the amorphous bands (1083 cm^{-1} and 1303 cm^{-1}) because the wings of these bands were able to contributed more area.

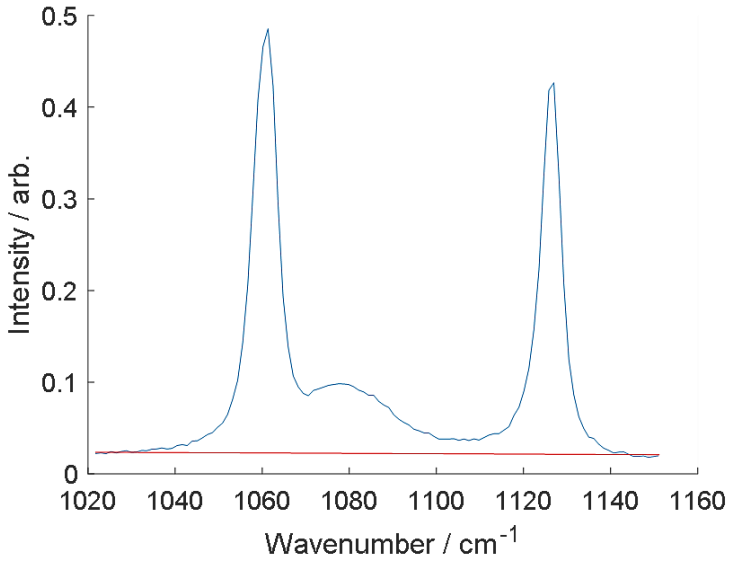

Figure 4.4. An example of the Raman spectrum in region I fitted with a linear baseline indicated in red (condition B2). Without the linear baseline the whole signal was raised above zero.

Raised signals were thought to potentially cause an issue because the amount that the signal was raised was not consistent. This introduced variability into the microstructural measurements which was believed to be as a result of the analysis method and not the signal in the spectra. Therefore, the reproducibility of the analysis method using baseline subtraction method B1 was questioned.

The development of baseline subtraction condition B2 was an attempt to improve the consistency of the curve fitting and ensure that microstructural measurements were (as much as possible) a result of the Raman signal and not the spectra analysis processes. Following the baseline subtract performed by WiRE 5.2 software, in the B2 condition a linear baseline subtraction was also performed using a published MATLAB script ‘peakfit.m’ (O’Haver, 2022). The red baseline displayed in Figure 4.4 is an example of a baseline generated for condition B2 (i.e. it would become the x axis).

4.3.4 Curve fitting method (Step C)

Analysis of the Raman spectra splits them up into three distinct regions between 950 cm^{-1} and 1600 cm^{-1} based on the dominant mode of molecular vibration at different wavenumbers (Table 4.3). To determine microstructural details from UHMWPE curve fitting procedures decomposed the spectra into a series of individual overlapping peaks. Table 4.3 identifies the locations of peaks which were fitted within each region of the Raman spectra and the microstructural phase which produced the signal. Other smaller peaks were present in the spectra but were not fitted as part of the analysis (for example at 1170 cm^{-1} and 1370 cm^{-1}).

Table 4.3. Peaks fitted during the decomposition of Raman spectra. The vibrational modes of polyethylene relate to vibration of either the carbon-carbon (C-C) or carbon-hydrogen (C-H_2) chemical bonds.

Region	Vibrational mode	Peak wavenumber	Phase
I	C-C stretching	1063 cm^{-1}	Crystalline (*trans*)
	C-C stretching	1083 cm^{-1}	Amorphous
	C-C stretching	1130 cm^{-1}	Crystalline (*trans*)
II	CH_2 twisting	1295 cm^{-1}	Crystalline
	CH_2 twisting	1310 cm^{-1}	Amorphous
III	CH_2 bending	1416 cm^{-1}	Crystalline (orthorhombic)
	CH_2 bending	1441 cm^{-1}	Amorphous
	CH_2 bending	1463 cm^{-1}	Amorphous

Several possible methods of curve fitting UHMWPE Raman spectra were identified in the literature. Literature suggested that theoretical band shapes produced by Raman spectra of UHMWPE would be Lorentzian in nature but due to instrumental related broadening the bands take on some Gaussian character (Rull *et al.*, 1993; Naylor *et al.*, 1995). This was reflected in the two curve fitting functions identified with the most promise – the Voigt function (Mutter, Stille and Strobl, 1993; Naylor *et al.*, 1995; Lagaron, 2002) and Gaussian-Lorentzian sum (GLS) functions (Keresztury and Foldes, 1990; Pigeon, Prud'homme and Pézolet, 1991; Rull et al., 1993; Lin et al., 2007;

Galetz and Glatzel, 2010; Taddei, Di Foggia and Affatato, 2011; Pezzotti, 2017).

GLS functions are a linear combination of Gaussian and Lorentzian functions. Lorentzian functions are broader than the Gaussian functions and so the higher the percentage of Lorentzian weighting the broader the GLS function becomes. Voigt functions are a convolution of Gaussian and Lorentzian functions and resulted in the broadest band. Figure 4.5. illustrates examples of Gaussian, Lorentzian, GLS and Voigt functions.

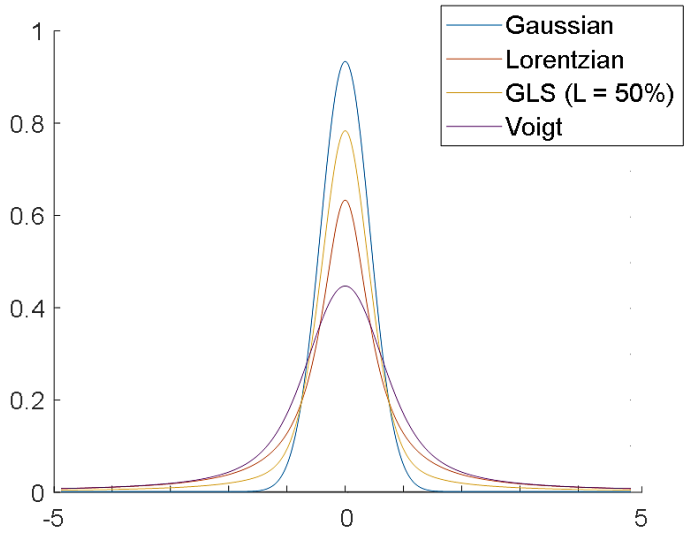

Figure 4.5. Plots of Gaussian, Lorentzian, GLS and Voigt functions where the values of the Gaussian and Lorentzian full-width-half-maximums (FWHM) equal 1. FWHM is the width of the peak at half its height. The peak 'area' relates to the integrated area under the curve. The areas of these plots were within 4% of each other. The 'broadness' of the peaks increases from the Gaussian (sharpest) to GLS to Lorentzian to Voigt (broadest) functions as peak maximum reduces and the (roughly equal) peak area is spread across a wider range of wavenumbers.

Curve fitting procedures were performed using a published MATLAB script 'peakfit.m' (O'Haver, 2022). The Voigt functions were fitted with an alpha value of 2 (ratio of the Lorentzian FWHM to the Gaussian FWHM). This alpha value was selected after performing best during some initial curve fitting trials. Five GLS functions with different Lorentzian percentages were assessed (40%, 50%, 60%, 70%, 80%). These values were selected because they spanned they range of values that were used by researchers in literature.

Examples of the curve fitting in region I, II and III are presented in Figure 4.6, Figure 4.7 and Figure 4.8 respectively. The spectral data (blue dots) was decomposed into the individual peaks (green curves) that were identified in Table 4.3. The red lines indicate the resultant fit of the spectra. The peaks used during the microstructural evaluation are also labelled.

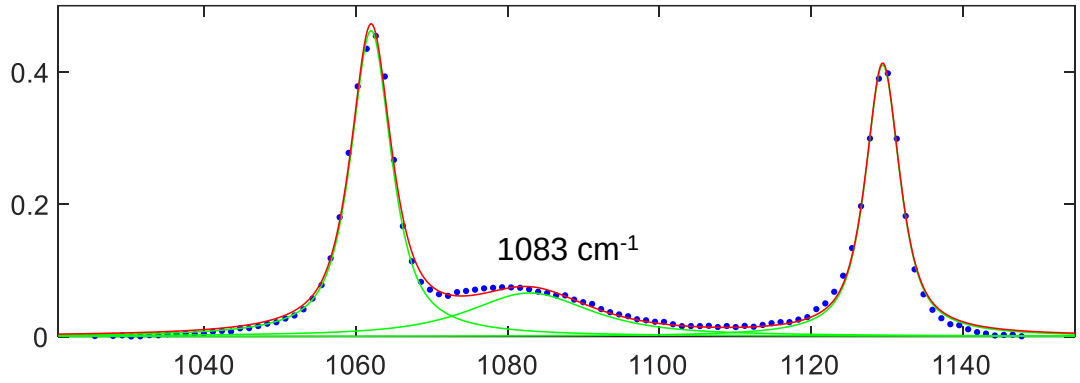

Figure 4.6. The peaks in Region I result from C-C stretching vibrations. Displayed is an example of Region I fitted with three GLS functions (80% Lorentzian). The band at 1083 cm^{-1} was used to determine amorphous phase percentage.

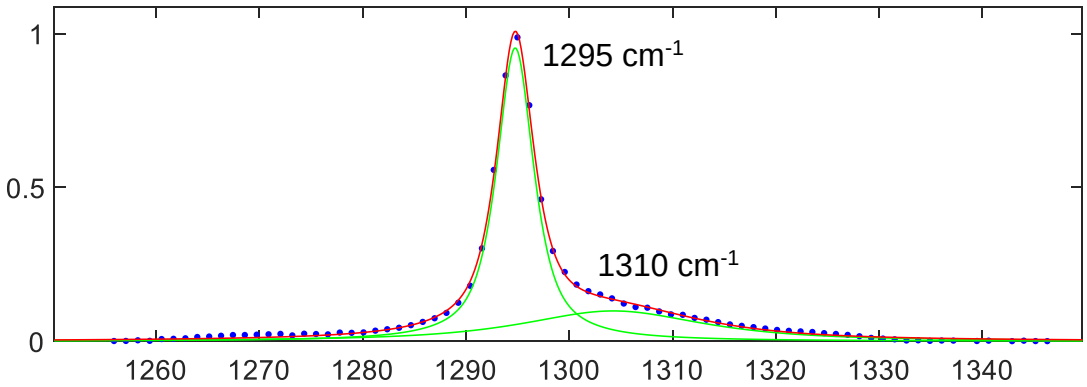

Figure 4.7. The peaks in Region II result from CH_2 twisting vibrations. Displayed is an example of Region II fitted with two GLS functions (80% Lorentzian). This region was used as the internal standard because the total integrated area was insensitive to chain conformations. The 1310 cm^{-1} band was used to determine amorphous phase percentage.

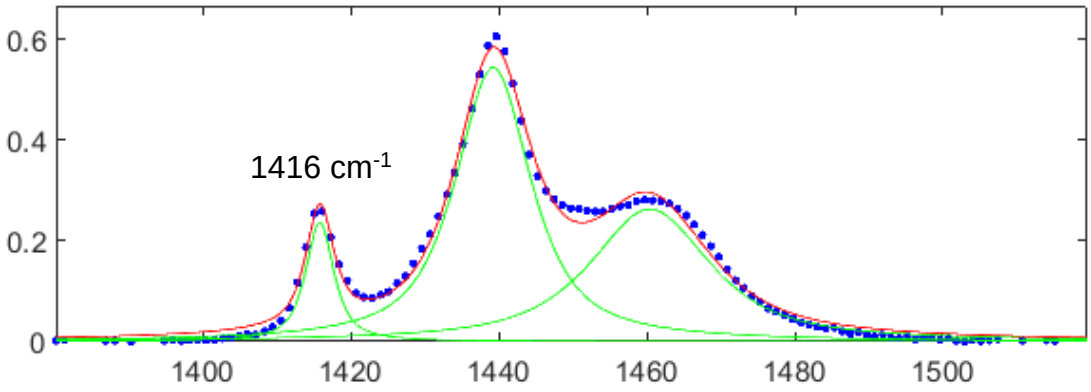

Figure 4.8. The peaks in Region III result from CH_2 bending vibrations. Displayed is an example of Region III fitted with three GLS functions (80% Lorentzian). The 1416 cm^{-1} band was used to determine the crystalline phase percentage belonging specifically to the orthorhombic phase.

4.3.5 Microstructural evaluation (Step D)

Once the spectra had been decomposed into their component peaks the relative integrated areas of the peaks (indicated by $I_{wavenumber}$) were used to evaluate microstructural phase percentages. Strobl and Hagedorn proposed both Equation 4.1 and Equation 4.2 as methods to determine the UHMWPE amorphous phase fraction (α_a) and Equation 4.3 to determine the crystalline phase fraction belonging specifically to the orthorhombic crystalline phase (α_o) (Strobl and Hagedorn, 1978).

Equation 4.1
$$\alpha_a = \frac{I_{1310}}{I_{1295+1310}}$$

Equation 4.2
$$\alpha_a = \frac{I_{1083}}{0.79 \times I_{1295+1310}}$$

Equation 4.3
$$\alpha_o = \frac{I_{1416}}{0.46 \times I_{1295+1310}}$$

All of these equations required an internal standard to normalise the measured peak intensities. Region II, dominated by CH_2 molecular twisting, was used for this because the summed integrated area ($I_{1295+1310}$) in this region was shown to be insensitive to chain conformation (Strobl and Hagedorn, 1978).

Strobl and Hagedorn noted that a summation of purely amorphous and purely crystalline spectra failed to produce the spectra obtained from semi-crystalline samples (specifically in region III). Furthermore, the crystalline and amorphous phase fractions determined by the equations above did not account for 100% of the material. The remainder was deduced to arise from a third intermediate phase (α_b) which was determined using Equation 4.4 (Strobl and Hagedorn, 1978).

Equation 4.4 $$\boldsymbol{\alpha_b = 1 - \alpha_a - \alpha_o}$$

4.3.6 Overview of spectral analysis methods

Two baseline subtraction methods were evaluated. Condition B1 used the in-built baseline subtraction procedure of the Renishaw WiRE 5.2 software only. Condition B2 used the Renishaw WiRE 5.2 software followed by a linear baseline subtraction within each region using the MATLAB script ‘peakfit.m’ published by O’Haver (O’Haver, 2022).

All curve fitting procedures were also performed using ‘peakfit.m’ (O’Haver, 2022). The spectra were fitted with Voigt functions (alpha = 2) and GLS functions (40%, 50%, 60%, 70% or 80% Lorentzian) to evaluate which of the six functions was most suitable.

A custom MATLAB script – within which ‘peakfit.m’ was used – was created to perform the analysis. The script ran ‘peakfit.m’ with multiple initial start positions and peak FWHMs for each region. The best resultant fit from the initial start parameters was selected. If the error of the fit was above a threshold value then the user was prompted to view the spectra. The option to accept the fit was provided or new start parameters could be attempted until satisfied.

4.4 The assessment of Raman spectroscopy methods

The overview of the four steps of Raman spectroscopy analysis presented in Figure 4.1 indicates that there were 24 possible permutations of the spectral acquisition and analysis methods (steps A to C) prior to the microstructural evaluation step. The most suitable baseline subtraction method was established first followed by the curve fitting function and then the spectral acquisition method. Only the most pertinent subsets of data are presented to communicate the findings and observations made as effectively and succinctly as possible. Finally, once the methods of acquiring and analysing the spectra were chosen the different equations used for evaluating the UHMWPE microstructure were assessed.

4.4.1 Baseline subtraction method (Step B)

Results

Figure 4.9 displays the crystalline and amorphous phase percentages determined for the three liners using two different baseline subtraction methods (Section 4.3.3). The data presented used spectral acquisition method A1 and the spectra were fit with GLS-L80% functions.

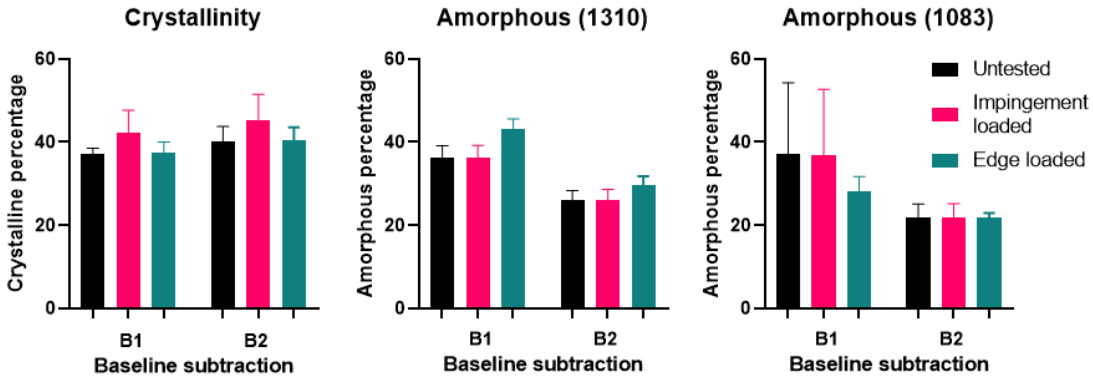

Figure 4.9. Crystalline and amorphous percentages for each liner comparing B1 and B2 baseline subtraction conditions. The mean values from the three repeat measurements with 95% confidence intervals are plotted for each liner.

The crystalline percentages measured were consistently 3% higher when the B2 condition was used compared to B1. The amorphous (1310 cm^{-1}) percentages were between 9% and 12% lower when the B2 condition was use compared to B1. Both of these measures showed similar levels of measurement variability with B1 and B2 conditions (indicated by the 95% confidence intervals).

The amorphous (1083 cm^{-1}) percentages showed the highest sensitivity to the baseline subtraction method demonstrated by the very high measurement variability using the B1 condition. When the B2 condition was used the amorphous values obtained decreased by several percent and the variability of the measurements reduced to similar levels that were observed in the determination of crystallinity and amorphous (1310 cm^{-1}) measurements.

Discussion

The baseline subtraction method had a substantial impact on the amorphous percentages determined while there was also a smaller effect on the crystallinity. For the crystallinity and amorphous (1310 cm^{-1}) plots despite the differences in the absolute values obtained the trends observed between liners were well preserved and not sensitive to the baseline subtraction method (Figure 4.9).

The marked improvement of the variability of the amorphous (1083 cm^{-1}) measurements suggested that the B2 condition was a more robust method of baseline subtraction. This finding was supported by observations that the curve fitting procedures were computed more smoothly and spectra were visibly more consistent the B2 condition was used. These findings and observations were the major contributors to the decision to use the B2 condition of baseline subtraction for subsequent analysis.

In addition, it was noted that the trends of the amorphous phase obtained using the 1310 cm^{-1} band were far less sensitive to the baseline subtraction method than those obtained by the 1083 cm^{-1} band. This suggested that the 1310 cm^{-1} band was potentially a more robust method of determining amorphous percentage.

4.4.2 Curve fitting function (Step C)

The data presented in Section 4.4.2 to evaluate different curve fitting methods used spectral acquisition method A1 and the baseline subtraction method B2. The most suitable GLS function was established first and then compared to the results from the Voigt function.

4.4.2.1 Comparison of GLS functions

Results

As the Lorentzian weighting was increased in the GLS functions the crystalline and amorphous phase percentages decreased in a very linear manner (Figure 4.10). The crystalline band was affected the least (4-5%)

and the 1310 cm^{-1} amorphous band was affected the most (12-13%). The range of values from the 1083 cm^{-1} amorphous band by different GLS functions was 7%. While the absolute values were sensitive to the Lorentzian percentage used, the trends observed between liners were well preserved and were not particularly sensitive to Lorentzian percentage.

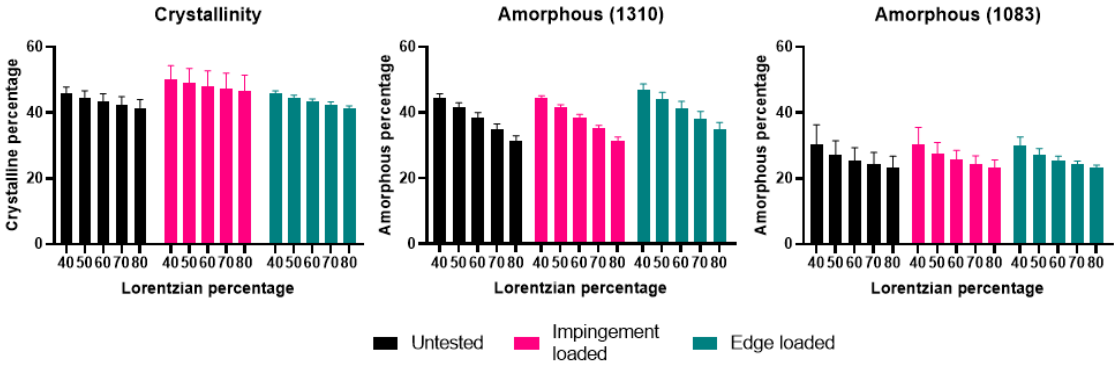

Figure 4.10. Crystalline and amorphous phase percentages for each liner determined by GLS functions with different Lorentzian percentages. The mean values and 95% confidence intervals were plotted.

Discussion

The Lorentzian weighting of GLS functions had a substantial effect on phase percentages determined. Increasing the Lorentzian percentages increased the broadness of the bands produced which also meant they got narrower around the maxima of their peaks (Figure 4.5). This resulted in lower phase percentages being determined for all bands and the effect was stronger when the broader amorphous bands (1083 cm^{-1} and 1310 cm^{-1}) were being evaluated.

The selection of the most suitable GLS function was primarily based on the ability of each curve function to accurately fit the critical parts of the spectra. The aim of this perspective was to ensure that the spectra were fit as robustly as possible and to minimise the potential for researcher bias in the selection based on the measurements obtained.

The fit of the 1440 cm^{-1} band in region III was the most sensitive band to the Lorentzian percentage. The 1440 cm^{-1} band overlaps with the 1416 cm^{-1} band used to determine crystallinity (Figure 4.8). Therefore, it was considered a priority to ensure the best possible fit of this band. As Lorentzian percentage increased the 1440 cm^{-1} band was fit more

successfully which suggested that the 80% Lorentzian GLS function was the most suitable.

However, as the Lorentzian percentage reached 70 or 80% the ability to fit bands in region I was slightly worsened. The amorphous phase percentage can either be determined by region I or region II of the spectra. In Section 4.4.1 it was suggested that the method of determining the amorphous content using the 1303 cm^{-1} band was more robust than the 1083 cm^{-1} band. By following on from this suggestion the worsened fit in region I by using a Lorentzian percentage of 80% would be inconsequential. The fit of region III could still be prioritised and the amorphous phase percentage determined using region II. As a result an 80% Lorentzian percentage was identified as the most suitable of the GLS functions.

4.4.2.2 Comparison of Voigt and GLS-L80% functions

Results

When the results from using Voigt and GLS-L80% functions were compared the differences observed were very consistent across all three liners (Figure 4.11). The values of crystallinity and from the 1083 cm^{-1} amorphous band were consistently 1% higher using the GLS-80% function compared to the Voigt function. The values from the 1310 cm^{-1} amorphous band were 5% higher using the GLS-L80% functions compared to the Voigt functions.

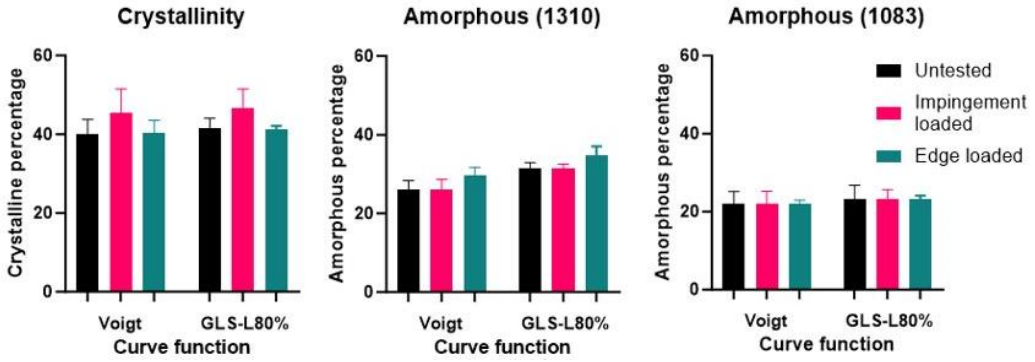

Figure 4.11. Crystalline and amorphous phase percentages for each liner determined by Voigt and GLS-L80% functions. The mean values and 95% confidence intervals were plotted.

Discussion

For the same reasons as described in Section 4.4.2.1 the selection of the most suitable curve function was primarily based on the ability of each function to fit each region of the spectra. During the curve fitting procedures

the Voigt function was considerably more sensitive to the initial start positions that were provided than the GLS-L80% function. As a result the curve fitting procedures using the Voigt function were more challenging, more varied and the fit errors obtained were higher. Therefore, the GLS-L80% function was identified as the most suitable function and was used in subsequent analyses.

4.4.3 Spectral acquisition method (step A)

Results

Figure 4.12 displays the crystalline and amorphous phase percentages determined for the three liners using two different spectral acquisition methods (Section 4.3.2). The data presented used baseline subtraction method B2 and the spectra were fit with GLS-L80% functions. The agreement between the phase percentages obtained by the two acquisition methods was high (around 1%) for all measurements and all liners.

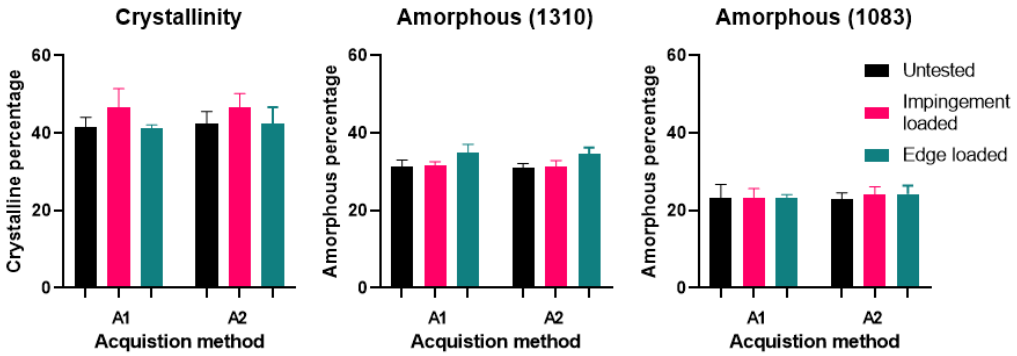

Figure 4.12. Crystalline and amorphous phase percentages for each liner comparing A1 and A2 spectral acquisition conditions. The mean values and 95% confidence intervals were plotted.

Discussion

The phase percentages obtained were insensitive to the acquisition method used and so either method was equally suitable. However, a slight preference was indicated for the use of 5 accumulation periods (method A1) because of some improvements to the analysis process. When using multiple accumulations the noise in the spectra was visibly reduced which resulted in less error during the curve fitting procedures. In addition, this method was slightly less computationally demanding during the analysis because five times fewer spectra needed to be analysed. However, these evidently did not influence the measurements themselves.

4.4.4 Microstructural evaluation (step D)

The aim of Section 4.4.4 is to assess the validity of the microstructural measurements themselves which were obtained using the equations reported in Section 4.3.5 (Equation 4.1 to Equation 4.4). In particular, this included evaluating which of the equations to determine the amorphous percentage was more suitable.

To achieve this the measurements were compared to those published in literature. Completely direct comparisons with the literature were not possible because there were no papers found which had performed Raman spectroscopy on Marathon UHMWPE. Three papers were identified which measured two other RM HXLPEs – Longevity (Takahashi, Sugano, *et al.*, 2014; Takahashi *et al.*, 2015) and XLPE (Takahashi, Masaoka, Pezzotti, *et al.*, 2014; Takahashi *et al.*, 2015). The most notable difference between these HXLPEs was the irradiation dose where Marathon (50 kGy) used a lower dose than Longevity and XLPE (both 100 kGy).

In addition, the three papers all used confocal Raman spectroscopy to measure values at specific depths from the material's surface which had not undergone any loading. In contrast, measurements from the present study were estimated to be recorded from the first 25 µm of the sample's surface where the peak of the signal was from a depth of 3 µm (Zerbi *et al.*, 1989; Fagnano *et al.*, 2001). Only the untested liner was measured at an unloaded location.

4.4.4.1 Crystalline percentage

Excellent agreement was observed when comparing the crystallinity measurement of the untested Marathon liner to the confocal measurements from literature and in particular with the near surface region < 25 µm (Figure 4.13). This provided good confidence that the measurement of crystalline percentage by the Raman spectroscopy methods developed was valid. Further confidence was provided by the fact that the crystallinity values obtained were relatively insensitive to the wide array of spectral analysis methods tested (< 5%).

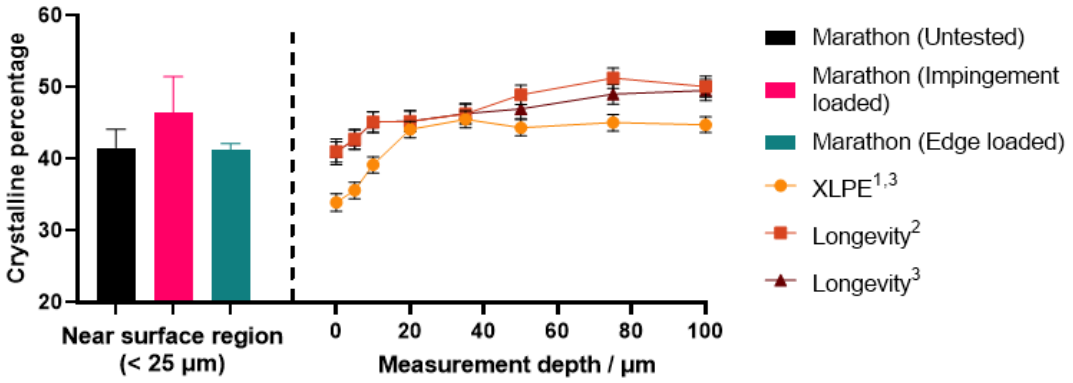

Figure 4.13. Crystallinity measurements for Marathon UHMWPE compared to values in literature for XLPE and Longevity measured by confocal Raman spectroscopy. [1](Takahashi, Masaoka, Pezzotti, *et al.*, 2014) [2](Takahashi, Sugano, *et al.*, 2014) [3](Takahashi *et al.*, 2015).

4.4.4.2 Amorphous and third phase percentage

Two methods of determining amorphous content were assessed and as such there were also two methods of determining the third phase percentages. Robustly fitting the broader amorphous bands was more challenging than the crystalline peak at 1416 cm^{-1}. This was perhaps reflected in that only one of the three papers reported amorphous and third phase percentages (Takahashi, Masaoka, Pezzotti, *et al.*, 2014).

It has already been noted that the 1310 cm^{-1} band was fit more robustly than the 1083 cm^{-1} band. This aligned with findings in the literature that region I was fit less effectively than region II (Keresztury and Földes, 1990; Rull *et al.*, 1993; Naylor *et al.*, 1995). Despite this both the 1083 cm^{-1} band (Taddei, Di Foggia and Affatato, 2011; Pezzotti, 2017) and the 1310 cm^{-1} band (Mutter, Stille and Strobl, 1993; Lin *et al.*, 2007; Galetz and Glatzel, 2010; Puppulin *et al.*, 2016) were commonly used throughout the literature.

Figure 4.14 and Figure 4.15 clearly illustrated that the amorphous phase percentages using the 1310 cm^{-1} band showed better agreement to the values in literature than those using the 1083 cm^{-1} band. The combination of these findings and the superior curve fitting in region II enabled the method using the 1310 cm^{-1} band to be concluded as the most suitable to use.

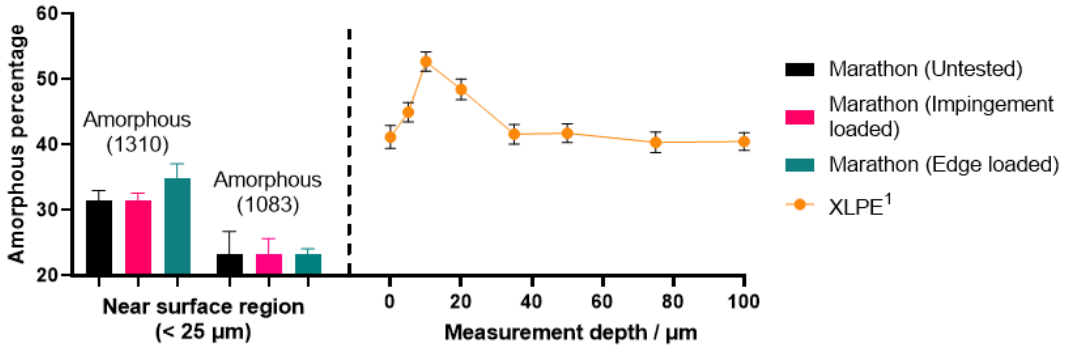

Figure 4.14. Amorphous measurements for Marathon UHMWPE compared to values in literature for XLPE measured by confocal Raman spectroscopy. [1](Takahashi, Masaoka, Pezzotti, *et al.*, 2014).

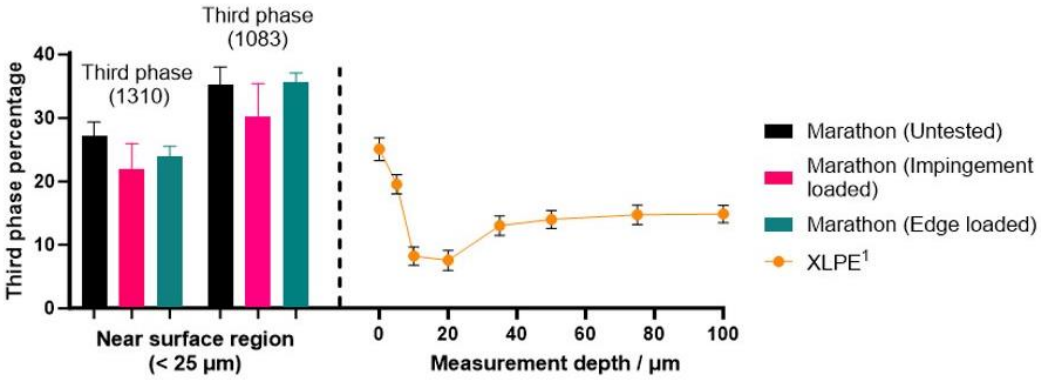

Figure 4.15. Third phase measurements for Marathon UHMWPE compared to values in literature for XLPE measured by confocal Raman spectroscopy. [1](Takahashi, Masaoka, Pezzotti, *et al.*, 2014).

However, the values obtained using the 1310 cm^{-1} band were still several percent lower than those that were reported in literature for the near surface region (< 25 µm) (Figure 4.14). By extension the third phase percentages were several percent above those reported (Figure 4.15). It was thought the amorphous phase percentages may have been suppressed by the use of baseline subtraction method B2 (Figure 4.9). A limitation of these comparisons with literature was that the measurements were only compared with one publication (Takahashi, Masaoka, Pezzotti, *et al.*, 2014). This was the only publication identified which reported amorphous and third phase values for a RM HXLPE. Further comparable results would have provided greater confidence in the comparisons and enhanced the ability to make decisions around Raman spectroscopy analysis methods. Examples were found for other classes of UHMWPE but due to the differences in processing methods the microstructures would not necessarily be particularly similar. Therefore, comparisons to these publications were not considered valid.

The amorphous percentage obtained using the 1310 cm^{-1} band were undoubtedly sensitive to the baseline subtraction method and curve fitting function used. Therefore, the ability of Raman spectroscopy to obtain objective measurements of amorphous phase percentage was questioned. However, the preservation of measurement trends across different analysis conditions provided good confidence that while objectivity may be challenged Raman spectroscopy could be used to make comparative assessments during the hip simulator study.

4.4.4.3 Assessment of repeatability

The repeatability of the measurements was assessed by examining the standard deviations of the measurements. Across the three liners the highest standard deviations observed in the crystalline percentage and amorphous phase percentages were 2.0 and 0.9 respectively. This suggested that in normally distributed data 95% of measurements would lie within a range of 4% for crystalline measurements and of 1.8% for amorphous percentages. Despite considerably more sensitivity to the analysis methods the determination of amorphous phase percentages were found to be more repeatable that crystalline percentages.

A limitation of this analysis was its very small sample size. The level of subjectivity and variability observed during this study highlighted the importance of providing statistical backing to measurements by Raman spectroscopy. Therefore, in the hip simulator study the number of focal points measured per measurement location was increased from three to five to go with an increased sample number compared to this study. Even with these statistical improvements microstructural phase transitions of several percent were still considered to be necessary to confidently assert that they arose being subjected to edge loading (or other measurement conditions).

4.5 Comparison study of crystalline phase measurement by Raman Spectroscopy and DSC

4.5.1 Introduction

In Section 4.4 a method of microstructural evaluation using Raman spectroscopy was established. The variety of possible spectral analysis methods introduced a degree of subjectivity into the Raman spectroscopy measurements. It was believed that DSC would provide a more objective measurement of UHMWPE crystallinity and hence could be used to verify

the measurements of crystallinity made by Raman Spectroscopy. DSC could not be adopted for the hip simulator study because as a destructive characterisation method it was incompatible with the development criteria established in Section 4.1. This small scale study directly compared measurements of crystallinity using Raman spectroscopy and DSC on samples produced from a Marathon bar.

4.5.2 Methods

Approximately 2 mm cube samples (N=10) were prepared from Marathon bar using a milling machine. Measurements of crystallinity were first made by Raman spectroscopy followed by DSC.

Each Raman spectroscopy measurement was an average of three focal points at which five spectra were acquired each with an accumulation time of 30s. Spectral analysis was performed by a custom MATLAB script in which curve fitting procedures were performed by a published MATLAB script 'peakfit.m' (O'Haver, 2022). After a baseline subtraction procedure (B2) the spectra were fitted with GLS-L80% functions. Crystallinity was determined using the crystalline band at 1416 cm^{-1} as reported in Equation 4.3.

DSC was performed by a Q 2000 instrument (TA Instruments, New Castle, USA). Around 5 mg of UHMWPE (equating to two samples) was sealed in each aluminium sample pan. The sample pan and an empty reference pan were placed into the DSC chamber and heated from 0°C to 200°C at a rate of 10°C per minute while heat flow was measured. The resultant melting endotherm was integrated from between 50°C to 160°C. The crystallinity percentage was calculated by comparing the heat of fusion of the sample to the heat of fusion for a 100% crystalline sample (289.3 J/g).

4.5.3 Results and discussion

The crystallinity determined by DSC had a mean of 51.2% compared to 43.8% for Raman spectroscopy (Figure 4.16). Raman spectroscopy measurement of crystallinity from Marathon bar showed good agreement with both those obtained from the liners made from Marathon and with the values reported in literature (presented in Figure 4.13). The measurements of crystallinity from DSC were also placed around the centre of values which had been previously been reported in literature for Marathon UHMWPE (Table 4.4). Despite the confidence provided by these comparisons to literature, the DSC measurements of crystallinity were 7.6% higher than Raman spectroscopy. This was attributed to fundamental differences in the measurement techniques.

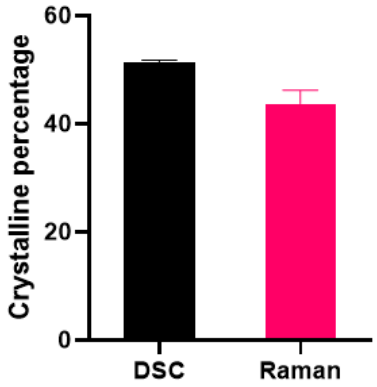

Figure 4.16. The mean crystallinity and 95% confidence intervals determined by Raman spectroscopy and DSC from samples produced from Marathon bar.

Firstly, the DSC measurements framed the UHMWPE microstructure differently to Raman spectroscopy by implying that UHMWPE possessed a two phase structure. Both the crystalline phase and the third phase were expected to contribute to the measurement of heat flow. In contrast, Raman spectroscopy – with support from NMR research – provides evidence for the existence of a third polyethylene phase (Bergmann and Nawotki, 1967; Strobl and Hagedorn, 1978; Mutter, Stille and Strobl, 1993; Barron and Birkinshaw, 2008; Yao, Jiang and Rastogi, 2014; Tapash, Deslauriers and White, 2015; Hansen and Hassani, 2022). Hence, the decomposition of Raman spectra separates the contributions of crystalline, amorphous and third phases.

Table 4.4. DSC crystallinity percentages for Marathon UHMWPE reported in literature.

DSC crystallinity	Liners	Polymer condition	Source
43 +/- 1.9	1	As received	(Collier *et al.*, 2003)
46 +/- 0.1	1	28 day aged	(Collier *et al.*, 2003)
56 +/- 1	3	As received	(Willie *et al.*, 2006)
53 +/- 4	3	2 year shelf aged	(Willie *et al.*, 2006)
55.5 +/- 0.3	1	Retrieved	(Duffy *et al.*, 2009)
53 +/- 1.4	12	Retrieved	(Rowell *et al.*, 2011)

Secondly, the measurements made by DSC and Raman spectroscopy provided information from the samples on completely different locations and length scales. The samples prepared were approximately 1 mm cubes. DSC measurements determined the crystallinity as an average from the whole sample volume. The crystallinity measurements by Raman spectroscopy were averages from just a few focal points on the sample's surface and the signal recorded was estimated to be acquired from the first 25 μm only (Zerbi *et al.*, 1989; Fagnano *et al.*, 2001). Confocal Raman spectroscopy showed that significant surface gradients can occur in UHMWPE and bulk values of crystallinity were several percent higher than at the surface (Figure 4.13). Hence explaining why bulk dominant DSC measurements would be higher than the surface dominated Raman spectroscopy measurements.

In conclusion, this study made it evident that there were fundamental differences between the two measurement techniques which meant the verifications of Raman spectroscopy by DSC were not possible regardless of whether DSC was more objective than Raman spectroscopy or not.

4.6 Discussion of Raman spectroscopy

The subjectivity involved in the Raman spectroscopy method has already been established as a limitation and discussed throughout Section 4.4. To mitigate the effects of bias as a result of measurement subjectivity the selection of the most suitable analysis methods was based primarily on the performance of each method during the curve fitting processes. The aim of this perspective was to ensure that the spectra themselves were fit as robustly as possible and enable the signal within the Raman spectra to be the major determinant of microstructural measurements.

However, objectively demonstrating analytical robustness that was the basis for the selection of analysis methods was a limitation of the development process as well. The decisions relied heavily on the experience gained from the process of developing and performing curve fitting analyses. These limitations underpin the key challenge of using spectroscopic analysis where (unlike DSC) standardisation of the methods has not been possible. This was largely as a result of a lack of generalisability across Raman spectrometers and UHMWPEs.

The current literature was severely weakened by the lack of or superficial reporting of spectral analysis methods. Heightening the level of transparency in the analysis methods used was identified as key step to ensuring that methods can be scrutinised and held accountable. This could be enhanced further by the open research practices involving sharing raw Raman spectra themselves. This would provide a route to demonstrating the reproducibility, replicability, robustness and generalisability of methods and measurements by Raman spectroscopy (The Turing Way Community, 2022).

4.7 Assessment of edge loaded liners by MicroCT

4.7.1 Introduction

MicroCT is a computerized x-ray imaging technique which has been used to assess wear and subsurface damage of UHMWPE liners (Macdonald, Bowden and Kurtz, 2016; Partridge, 2016). Previously, a method of generating 2D reconstructions of subsurface cracking with a very high resolution (10μm) was developed and identified subsurface cracking in retrieved liners as well as aged liners subjected to edge loading in a hip simulator study (Partridge, 2016). The aim of this study was to examine whether the polyethylene liners which had been subjected to edge loading showed any evidence of subsurface cracking.

4.7.2 Methods

Three UHMWPE liners which had been subjected to 3 Mc of edge loading (described in Section 3.3.1) were imaged using a MicroCT100 (Scanco Medical AG, Switzerland) at 6μm isotropic resolution with a pulse voltage of 55V, current of 200μA, 400ms integration time. This was a higher resolution than had previously been used (10μm) to successfully identify subsurface cracks in aged polyethylene liners under edge loading. The liners were placed inside a sample chamber bearing side down and a small dot of plasticine was used to identify the side of the liner subjected to edge loading. The resulting image dataset was exported as TIF files and viewed using ImageJ (Version 1.52, National Institute for Health, USA).

MicroCT scans were performed by Nagitha Wijayathunga, senior Research Fellow in the School of Mechanical Engineering at the University of Leeds.

4.7.3 Results

Two of the three liners imaged showed signs of potential subsurface damage. Figure 4.17 displays the subsurface damage in Liner 1. It was located on the side of the liner which was subjected to edge loading but it was located very close to the top surface of the edge. Figure 4.18 displays the possible subsurface damage in Liner 2. This was located further from the top surface than Liner 1 but opposite to the location of edge loading.

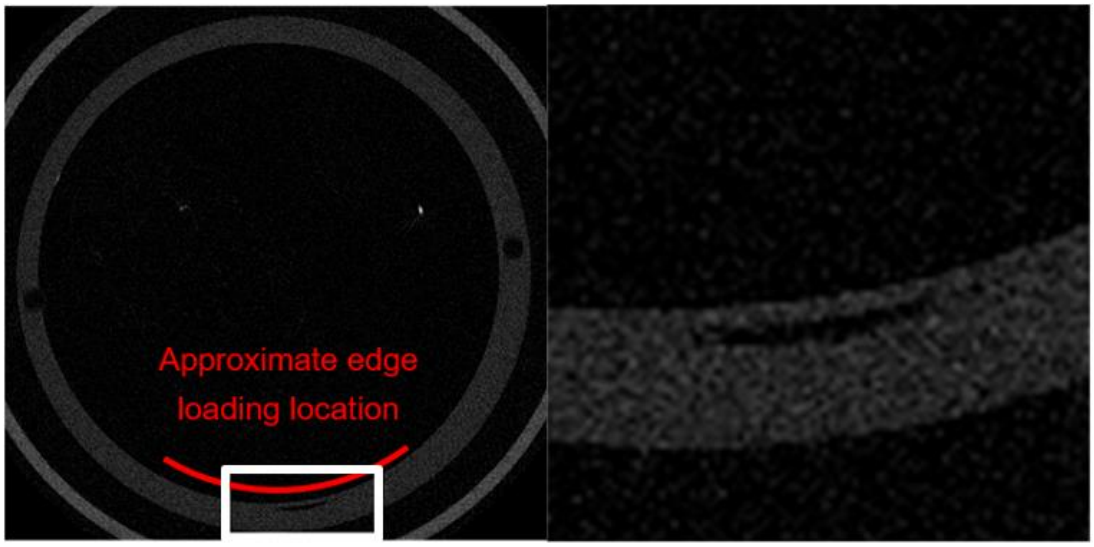

Figure 4.17. Possible subsurface damage in Liner 1 after being subjected to edge loading. The holes at the sides of the liners were intentionally drilled and used to align CMM measurements.

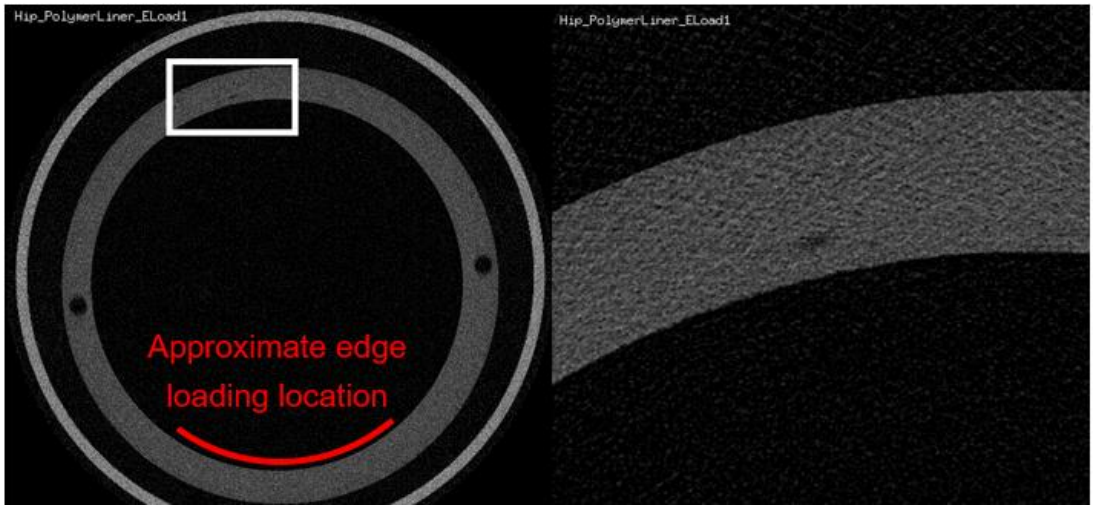

Figure 4.18. Possible subsurface damage in Liner 2 was located opposite to the location of the liner that was edge loaded.

4.7.4 Discussion of the MicroCT study

Despite using a higher resolution than previous scans of UHMWPE liners the scans were not yet optimised for best image quality. Nonetheless two of the three liners imaged showed signs of potential sub-surface damage. However, in both liners it was not clear to be as a result of the edge loading. Only liner one displayed subsurface damage close to where the liners had been subjected to edge loading but the cracking was located very close to the top surface. Therefore, it was speculated that the damage could be caused by surface damage or crevices that were not related to the loading. The subsurface damage in Liner 2 was even less clear and located away from the edge loaded region of the liner. Overall, the scans were inconclusive around the presence subsurface damage in UHMWPE liners as a result of edge loading.

4.8 Conclusions

In conclusion, this Chapter successfully developed a suitable method of characterising the microstructural phase percentages at the surface of polyethylene liners for a hip simulator study. The method was non-destructive and the measurement time required was below the criteria set of one day. Measurement objectivity was identified as a limitation of Raman spectroscopy because of the sensitivity of microstructural measurements to the spectral analysis methods used. Therefore, the power of the Raman spectroscopy method developed to make comparative measurements (between or within liners) was perceived as stronger than its ability to make absolute measurements to a high degree of certainty. The technique will be used to assess the microstructural changes that occur to liners as a result of edge loading and hence whether any changes can be linked to the progression of damage mechanisms or failure modes related to edge loading conditions. The use of microCT replicated previous findings where sub-surface cracking was not observed in liners subjected to edge loading by component separation without aging the polyethylene.

Chapter 5 – Experimental hip simulator study of edge loading in total hip replacements

5.1 Introduction

Clinical case studies linked edge loading to the failure of polyethylene liners where the presence of thin polyethylene at the liner's locking mechanism was identified as being a vulnerability (Tower *et al.*, 2007; Blumenfeld *et al.*, 2011; Waewsawangwong and Goodman, 2012). However, the damage mechanisms that lead to liner failure in polyethylene liners under edge loading are currently not well understood.

Experimental research of edge loading in THRs was more prevalent in relation to hard-on-hard bearings where edge loading was linked to increases of wear and ion release in MoM bearings (Williams *et al.*, 2004; Leslie *et al.*, 2009; Matthies *et al.*, 2011; Al-Hajjar, Fisher, Tipper, *et al.*, 2013; Hart *et al.*, 2013) or squeaking and stripe wear in CoC bearings (Al-Hajjar *et al.*, 2010; Traina *et al.*, 2012; Al-Hajjar, Fisher, Williams, *et al.*, 2013; Wu *et al.*, 2016; O'Dwyer Lancaster-Jones *et al.*, 2018). The dominant perspective of the current edge loading research involving polyethylene liners was polyethylene wear (Bowsher and Shelton, 2001; Williams *et al.*, 2003; Partridge, Tipper, *et al.*, 2018; Ali *et al.*, 2023). The characterisation methods used in these studies were poorly suited to provide insights into changes that occurred to the liner edge or related to liner failure.

A greater understanding of the damage mechanisms that occur to the polyethylene liners under edge loading would help inform design and surgical guidance to ensure that THRs are preventing and are resilient to edge loading and its effects. Therefore, new characterisation methods that were designed specifically to evaluate changes to the liner edge under adverse loading conditions were developed in Chapter 3 and Chapter 4.

A combined experimental and FE modelling investigation was planned to study the effects of edge loading on polyethylene liners. In this chapter, an experimental hip simulator study was performed, using the newly developed characterisation methods, to prospectively characterise the changes that occurred at the liner edge after edge loading. The study aimed to use the knowledge gained to provide insights into the possible damage mechanisms and failure modes related to edge loading conditions.

5.2 Materials

Clinically available components were used in the study. The acetabular components consisted of a neutral liner with a 36 mm inner diameter press fit into a titanium alloy (Ti-6Al-4V) modular shell with a 56 mm outer diameter (Pinnacle, DePuy Synthes Joint Reconstruction, Leeds UK). The liners were made from Marathon UHMWPE – a HXLPE (50 kGy) with a re-melted heat treatment. A taper lock mechanism anchors the liner within the shell and six anti-rotation tabs mated with scallops on the shell to provide rotational resistance. A locking barb which ran round the outer circumference of the liner was removed prior to testing to prevent excess material loss when the liner was removed from the shell for gravimetric measurements. The liner was articulated against 36 mm cobalt chromium heads (Articul/eze femoral heads, DePuy Synthes Joint Reconstruction, Leeds, UK).

5.3 Methods

5.3.1 Simulator testing

A six station electromechanical Prosim hip simulator (Simulator Solutions, Stockport, UK) was used to assess the wear and damage of the THR liners described in Section 5.2. Five liners were subjected to four million cycles (4 Mc) of standard walking (ISO 14242-1) in the hip simulator followed by 4 Mc of edge loading (ISO 14242-4). The hip replacement components were tested in a lubricating serum (25% (v/v) new born calf serum) with 0.03% (w/v) sodium azide to retard bacterial growth.

The lubricating serum was exchanged every 0.33 Mc. The study was stopped every 1 Mc to make gravimetric and geometric measurements to assess the wear and deformation of the liners. Measurements by Raman spectroscopy were made at the end of the test to assess the changes to the crystalline, amorphous and third phases at the liner surface as a result of the hip simulator loading cycles.

5.3.1.1 Standard walking conditions (ISO 14242-1)

During standard walking conditions the femoral heads were mounted on metal spigots with the liners and shells fixed anatomically above the heads. The inclination angle of the face of the liners was aligned to 35 degrees to the horizontal with 0 degrees of anteversion. This positioning resulted in an application of axial loads that was equivalent to 45 degrees *in vivo*.

A twin peak axial loading cycle with a maximum load of 3000N and swing phase load of 300N was applied by electric motor controlled cams to the acetabular fixtures (Figure 5.1A). As the axial force was applied, the rotational positioning of the femoral components was controlled by electric motors. The angles for flexion/extension spanned +25° to -18°, the internal/external rotation +2° to -10° and the adduction/abduction +7° to -4° during the loading cycle (Figure 5.1B).

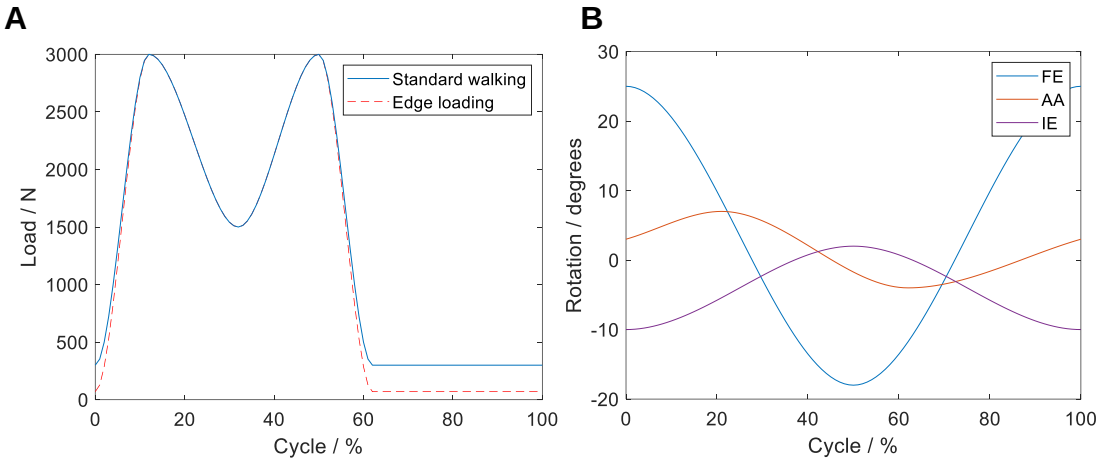

Figure 5.1. ISO 14242 loading (A) and kinematics (B) profiles for standard walking and edge loading.

5.3.1.2 Edge loading conditions (ISO 14242-4)

Edge loading conditions used the methods described in Section 5.3.1.1 with the following exceptions:

The inclination angle of the liners was increased to 55 degrees. This positioning resulted in an application of axial loads that was equivalent to 65 degrees *in vivo*. The axial load during the swing phase was reduced to 70 N (Figure 5.1). Dynamic separation of the articulating surfaces was generated during the swing phase by a spring (100 N/mm^2) placed in the medial-lateral axis which applied a force to the acetabular fixtures as a result of applying a component offset of 4 mm between the centres of rotation of the femoral head and the polyethylene liner (Figure 5.2).

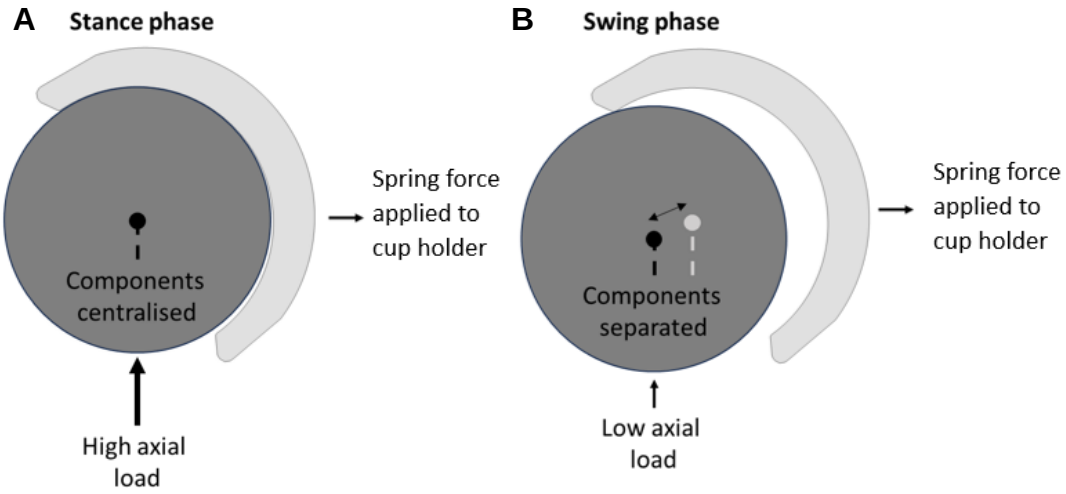

Figure 5.2. A schematic of dynamic separation. (A) During the stance phase the high axial load overcomes the spring force and the components were centralised. (B) In the swing phase – when there was a low axial load – the spring force resulted in component separation and edge loading. The peak loads at the liner edge were applied during heel strike.

5.3.2 Gravimetric measurements of liner wear

Gravimetric measurements of the liners were taken every 1 Mc using a balance with a precision of +/- 10 μg (XP205, Mettler Toledo, Columbus, Ohio, US) to determine volumetric wear rates.

Prior to each set of measurements the liners were cleaned following a protocol using detergent and isopropanol solution before being place into the balance room to acclimatise for 72 hours (+/- 6 hours). An anti-static ioniser was used prior to each measurement to reduce the amount of static charge. The mass measurement of each liner was determined as the mean from five measurement repeats once five measurements had been acquired within 100 μg of each other.

The change in mass measured over each measurement period was corrected to account for fluid absorption by subtracting the value obtained from a loaded soak control liner (N=1) from the values obtained for the test liners. The loaded soak control liner received the same axial loads and lubrication as test components but without any rotation of the femoral components. The mass change as a result of wear was converted to a volumetric change using the density of UHMWPE (ρ = 0.934 g/cm^3). The mean volumetric wear rates (mm^3/Mc) and 95% confidence intervals were calculated for the periods of standard walking and edge loading conditions.

5.3.3 Measurements of geometric change by CMM

Geometric measurements of liners were taken every 1 Mc using a Legex 322 CMM (Mitutoyo, Halifax, UK) to assess the geometric changes to the bearing surface and liner edge. Co-ordinate data of the liner surface was measured by a series of 72 CNC controlled measurement traces at five degree intervals. Each trace began at the pole, proceeded up the bearing surface and finished on the chamfer of the liner. The bearing surface and liner edge were analysed using custom MATLAB scripts to determine the geometric deviation of the liners from their pretest geometry measurements. An estimation was also made for the separate contributions of wear and deformation to the geometric deviation. A full description of the methods used was presented in Chapter 3 (Section 3.5 and 3.7).

5.3.4 Non-destructive microstructural measurements by Raman spectroscopy

Microstructural measurements of the liners were taken at the end of the test using a Renishaw inVia Raman Microscope and Renishaw WiRE 5.2 software (Renishaw, Wotton-under-Edge, UK) to assess the changes to the surface microstructure as a result of the hip simulator loading cycles.

A 532 nm laser with a power of 10 mW was used to acquire the Raman spectra. The laser was focused through a 20x objective lens and the signal from wavenumbers of 689 cm^{-1} to 1848 cm^{-1} was accumulated over a 30 s period. Measurements were taken at four locations on the liner: the unworn bearing surface (UB), the worn bearing surface (WB), the unworn rim (UR) and the worm rim (WR) (Figure 5.3). At each location the microstructural measurements were the average of five focal points. At each focal point five spectra were acquired with one accumulation period each.

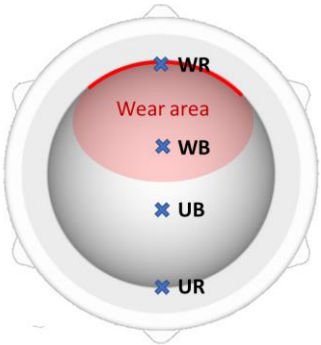

Figure 5.3. Microstructural measurements by Raman spectroscopy were taken at four measurement locations: the unworn bearing (UB), worn bearing (WB), unworn rim (UR), worn rim (WR).

Spectral analysis was performed by a custom MATLAB script in which curve fitting procedures were performed by a published MATLAB script ‘peakfit.m’ (O’Haver, 2022). After a baseline subtraction procedure (B2) the spectra were fit with GLS-L80% functions. Measurements of crystalline, amorphous and third phase percentages were determined using Equation 4.1, Equation 4.3 and Equation 4.4 (Section 4.3.5). A full description of the methods used was presented in Chapter 4.

A two-way repeated measures ANOVA was performed in SPSS 28 to assess the effects of measurement location and wear on the crystalline, amorphous and third phase percentages determined. However, the tests did not meet the assumption of normality likely due to the fact that there were only five liners in the test. Therefore, the statistical significance results were not considered valid and are not presented.

5.3.5 Microstructural measurements by Raman spectroscopy and DSC on sectioned components

At the end of the test two liners were sectioned for further microstructural evaluation. The liners were cut into sections using a band saw. Sections were machined down to a thickness of 1 mm using a milling machine. Final sample preparation of approximately 1 mm cubes was performed using a Stanley knife to punch through the sections. Surface and sub-surface samples (1-2 mm depth) were produced from the unworn rim and the worn rim locations (Figure 5.3). Raman spectroscopy measurements of crystallinity, amorphous and third phase percentages were made followed by DSC measurements of crystallinity.

The method for Raman microstructural measurements was described in section 5.3.4 except that measurements on each sample were an average of three focal points. On each cube sample the spectra were acquired from the side facing the bearing surface.

DSC was performed by a Q 2000 instrument (TA Instruments, New Castle, USA). Around 5 mg of UHMWPE was sealed in aluminium sample pans. The sample pan and a reference pan were placed into the DSC chamber and heated from 0°C to 200°C at a rate of 10°C per minute while heat flow was measured. The resulting melting endotherm was integrated from 50°C to 160°C. The crystallinity percentage was calculated by comparing the heat of fusion of the sample to the heat of fusion for a 100% crystalline sample (289.3 J/g).

Comparisons between sample groups were made between group means without statistical analysis because the number of liners evaluated was only two.

Figure 5.4. Three sections were cut superiorly through the liner. Cube specimens were prepared from the bearing surface (B) and the liner rim (R) at worn (W) and unworn (U) regions of each section. The sub-surface specimens (green) were taken approximately 1 mm below the surface specimen (red).

5.3.6 Test measurement discrepancies

The test began with six liners. Due to an error in component positioning one liner was rotated 180 degrees with respect to its shell after the standard walking test period. This liner was removed from all test results.

There were also issues encountered while running the hip simulator (which consisted of two separate banks of three stations) and two additional gravimetric measurement points were required between the planned measurement points. The disruption to the test schedule also led to the two simulator banks were run out of sync for part of the test. Therefore, some gravimetric measurements used an unloaded soak control liner (suspended in serum without any loading) to adjust for fluid absorption instead of the loaded soak control liner.

The effect of using the unloaded soak was assessed. Across 5 Mc of directly comparable mass measurements the use of the unloaded soak as a control would have increased the calculated wear rate of liners by a mean of 0.5 mm^3/Mc (range 0.2 mm^3/Mc to 0.8 mm^3/Mc) compared to using the loaded soak.

5.4 Results

5.4.1 Gravimetric measurements of polyethylene wear

The volumetric wear of liners subjected to 4 Mc of standard walking followed by 4 Mc of edge loading in an experimental hip simulator was gravimetrically assessed. Figure 5.5A indicates that after 4 Mc of standard walking the mean wear volume accumulated was 50.1 mm^3 at a rate of 12.5 mm^3/Mc. After 4 Mc of edge loading a further 90.7 mm^3 of wear had been accumulated at a rate of 22.7 mm^3/Mc. There were two overlapping wear areas as a result of the standard and edge loading test periods caused predominantly by the differences in inclination angle (Figure 5.5B).

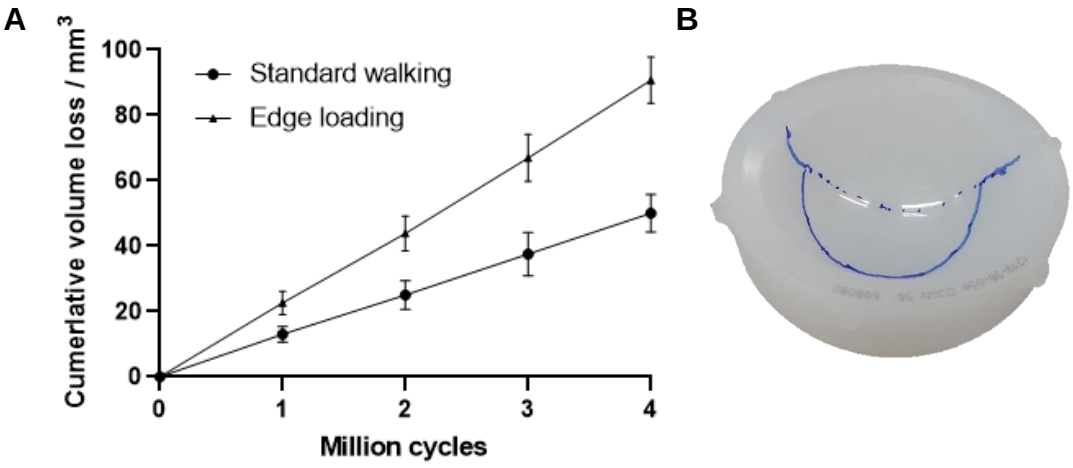

Figure 5.5. (A) The mean accumulated volumetric wear (N=5) of the liners was plotted with 95% confidence intervals for standard walking and edge loading conditions. (B) The wear area visually identified on liner 1 at the end of the test.

5.4.2 Measurements of the geometric change by CMM

The scale of geometric deviation at the bearing surface and the liner edge was calculated as a mean of the five liners at 1 Mc intervals throughout the test by comparing the measured data to its respective pretest geometry profiles. Figure 5.6 displays the progression of the geometric deviations measured at the bearing surface (the liner edge of the liner showed the same trends). Pretest measurements indicated that the geometric deviations of the liners before hip simulator loading was very similar to the machining tolerance of the liner manufacture (+/- 0.05 mm).

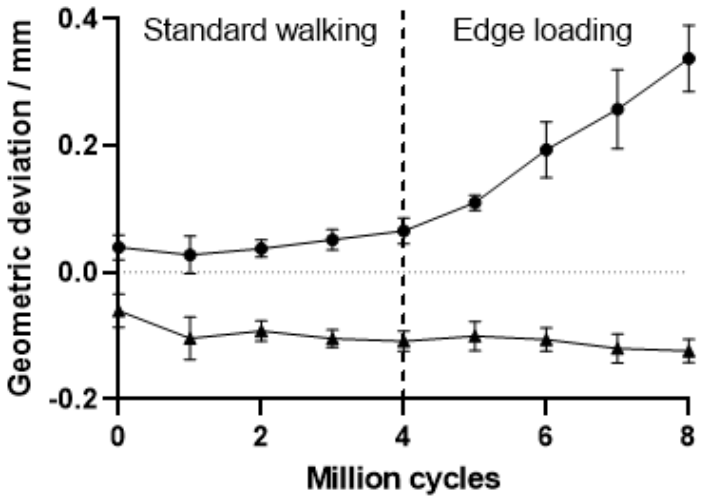

Figure 5.6. The scale of the geometric deviations for each liner at the bearing surface. Positive deviations indicate the amount surface was moving outwards from wear and deformation. Negative deviations indicate the amount the surface was contracting inwards from deformation only. The mean values (N=5) were plotted with 95% confidence intervals.

After 1 Mc of standard walking the negative deviation (the extent that the liner surface was deforming inwards) had increased to -0.10 mm. Figure 5.6 illustrates how this value remained largely unchanged for the remaining 7 Mc of the test at which point the measurement was -0.12 mm. The surface deviation heatmaps indicated that the negative deviations were located at the upper bearing surface adjacent to the loading direction (Figure 5.7).

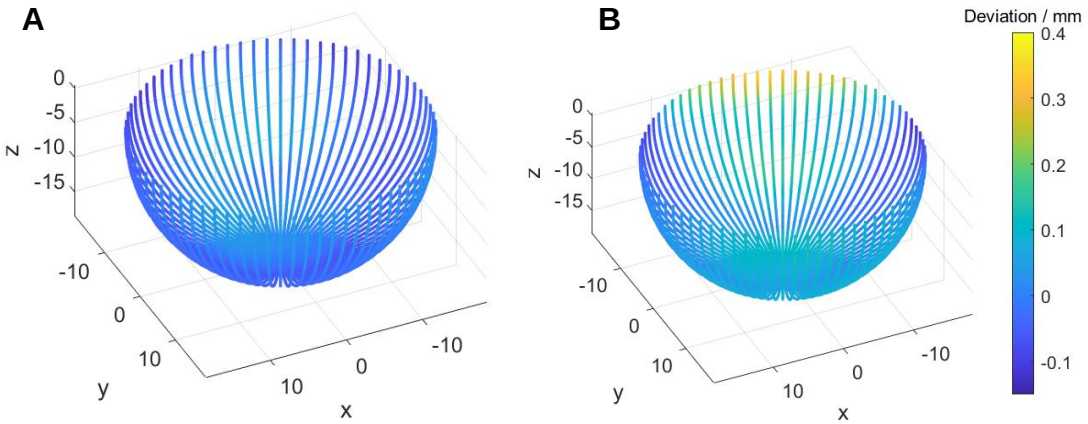

Figure 5.7. Representative surface deviation heatmaps of a liner after (A) 4 Mc (standard walking only) and (B) 8 Mc (standard walking and edge loading). The same scale was used for both plots.

After 4 Mc of standard walking conditions the positive deviations (the extent the liner surface was wearing and deforming outwards) had increased from 0.04 mm to 0.07 mm. These small positive deviations were located within the bearing surface without extending to the liner rim. After the liners were subjected to a further 4 Mc of edge loading the positive deviation was 0.34 mm. Edge loading conditions had increased the rate of the geometric change (Figure 5.6) and location of the geometric change shifted to the liner rim (Figure 5.7). The geometric changes progressed in a linear manner at a rate of 0.07 mm/Mc during edge loading compared to 0.01 mm/Mc for standard walking.

Figure 5.8 uses two-dimensional profile plots to illustrates the changes to the rim morphology throughout the test and enable qualitative assessments to be made. The same trace on the same liner is depicted at four timepoints in the test. Only edge loading was adjudged to have caused any changes to the rim morphology because it remained smooth and rounded throughout the standard walking test period. The rim morphology generated after 1 Mc of edge loading was interpreted as being extremely similar to the rim morphology after 4 Mc of edge loading. In both cases the rim had been flattened resulting in a sharper transition between the bearing surface and the chamfer region. As edge loading progressed the processes of liner wear and global deformation caused the surface to shift outwards but without altering the rim morphology.

The results in Section 5.4 so far displayed the combined contributions of wear and deformation to the geometric change of the liner. An estimation was also made for the separate contributions of wear and deformation to the geometric deviation by repeating the analysis of the bearing surface while excluding traces on which wear was apparent. This method quantified the positive deviation that was observed in the inferior portion of the liner (Figure 5.7) and made the assumption that deformation in this manner occurred equally on opposing sides of the liner. The negative deviations determined by this method were the same as those presented previously (Figure 5.6).

Figure 5.9 displays the progression of geometric deviations that were estimated to be as a result of deformation only. At the end of the test the deformation in the liners was 0.16 mm. By subtracting the deformation from the overall geometric deviation (0.34 mm) the contribution of wear was estimated to be 0.18 mm.

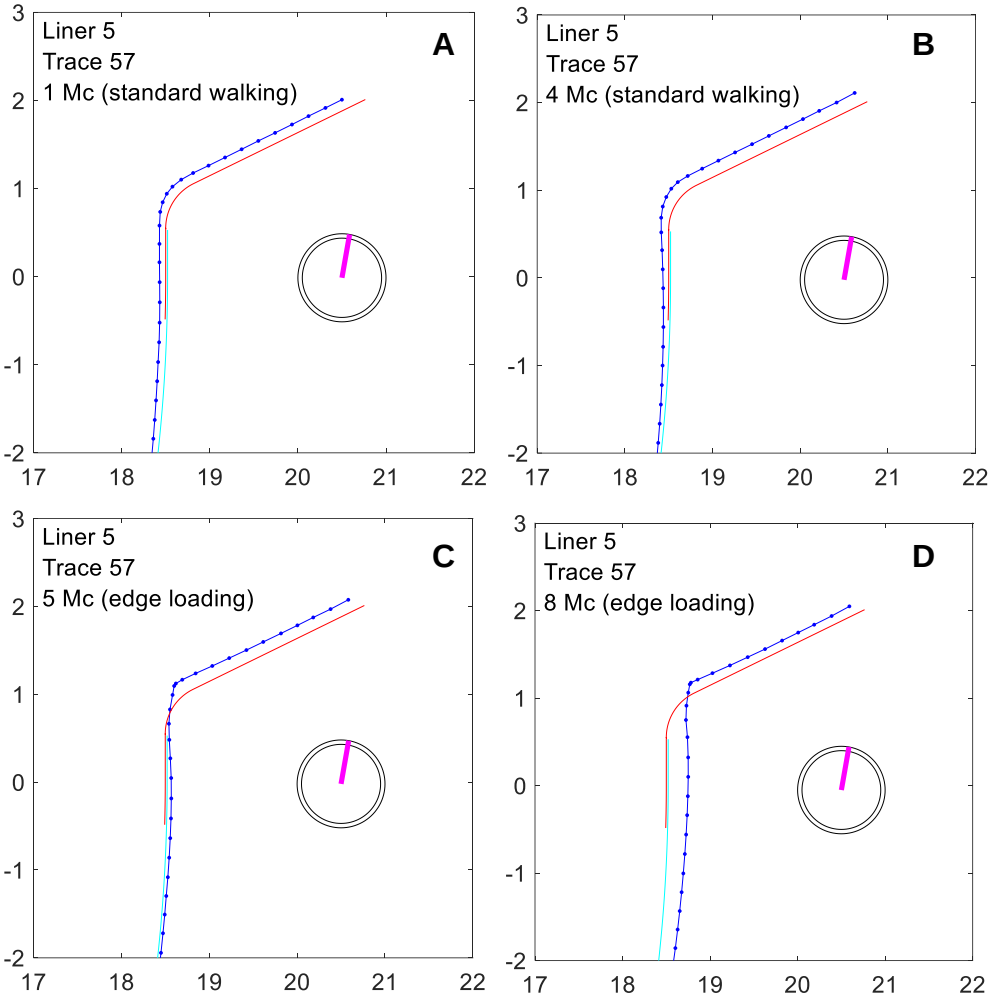

Figure 5.8. Two-dimensional profile plots of the most superior trace from liner 5 at four measurement points: (A) 1 Mc, (B) 4 Mc, (C) 5 Mc and (D) 8 Mc. The cyan line plots the pretest bearing surface profile. The red line indicates the pretest edge surface profile. The dark blue line and points display the measured CMM data. The clockface schematic with the pink hand indicates where on the liner the trace is located relative to the XY plane of the heatmap plots.

Figure 5.10 displays signs of plastic deformation on the liner backside which were synonymous with the signs observed in Chapter 3 (Figure 3.1). As before there were not any indications of surface fatigue damage (e.g. cracking or delamination). The marks were most prominent in the superior segment of the liner.

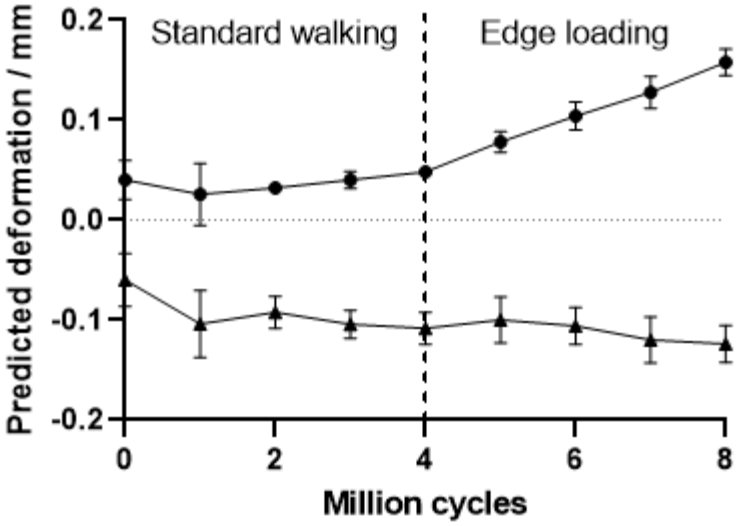

Figure 5.9. The deformation of the bearing surface was estimated by performing the analysis while excluding traces on which wear was apparent. Mean values (N=5) of positive and negative geometric deviation were plotted with 95% confidence intervals.

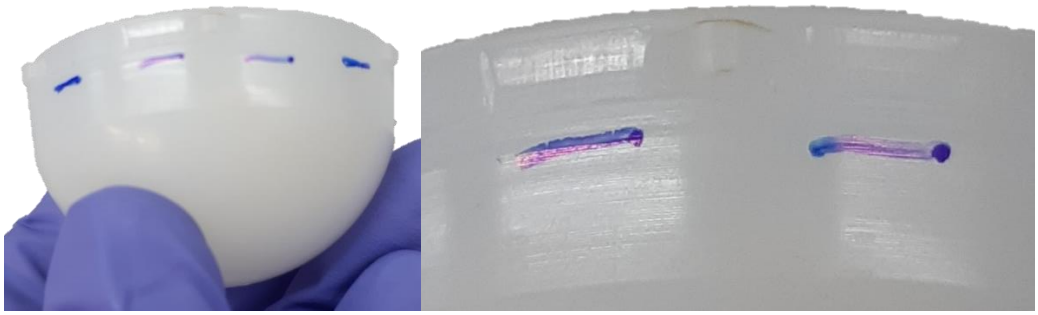

Figure 5.10. Signs of plastic deformation (not characterised by CMM) were visible on the backside of the liners (underlined in blue).

5.4.3 Non-destructive microstructural measurements by Raman spectroscopy

Raman spectroscopy was used to assess the changes to the surface microstructure as a result of the hip simulator loading cycles and compare the differences between values obtained at the bearing surface and liner rim. The grand mean obtained for crystalline, amorphous and third phase percentages was 45%, 32% and 22% respectively (Figure 5.11). The values obtained at the bearing surface had a higher crystallinity (by 3%) and lower amorphous value (by 3%) than at the rim. The differences between measurements at worn and unworn locations were 2% or below for all three phases.

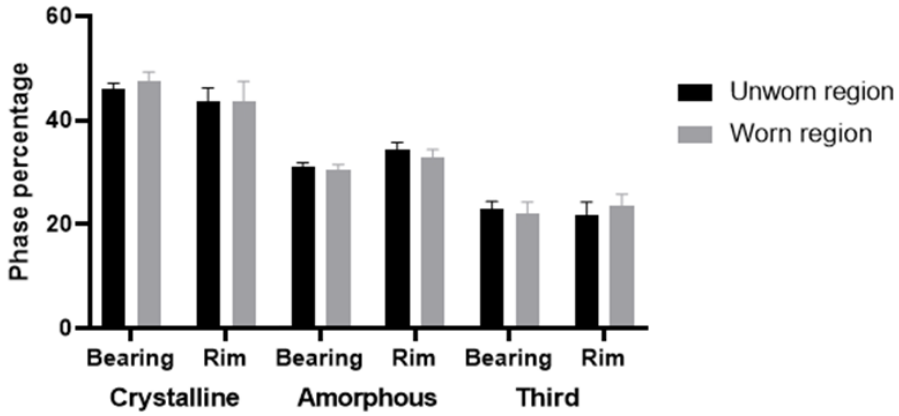

Figure 5.11. Crystalline, amorphous and third phase percentages were measured by Raman spectroscopy the bearing surface and liner rim. Comparisons were made between unworn and worn locations in these regions.

5.4.4 Microstructural measurements by Raman spectroscopy and DSC on sectioned components

The microstructural measurements on samples produced from liner sections aimed to evaluate whether any differences could be detected between surface and sub-surface measurements. Figure 5.12 displays the mean values obtained by DSC and Raman spectroscopy at two different measurement depths for crystalline, amorphous and third phase percentages. Comparisons were made between sample groups means without statistical analysis because the number of liners measured was only two.

The crystalline measurements by DSC indicated there was only 1% of variation between all depth and loading combinations. Raman spectroscopy analysis found only one instance of loading resulting in greater than 1.5% of difference; edge loading of the liner rim resulted in a 3.9% increase to the surface amorphous percentage compared to the non-loaded rim. In all other groups – whether surface and sub-surface crystallinity as well as sub-surface amorphous – edge loading did not make a noteworthy difference (< 1.5%).

The depth of measurement had slightly more of an effect on phase percentages. When considering unloaded and loaded samples together the crystallinity and amorphous contents of sub-surface measurements were 2.1% and 4.6% lower than surface measurements respectively.

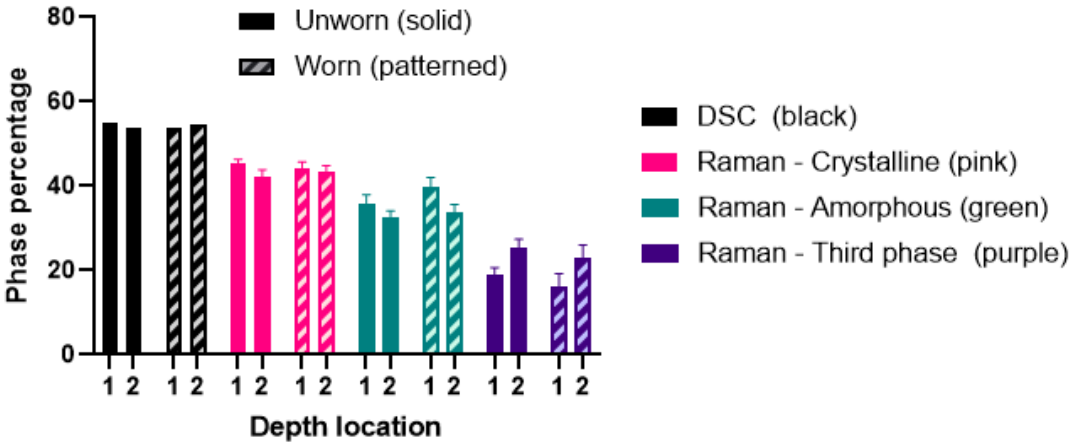

Figure 5.12. Crystalline, amorphous and third phase percentages were measured by Raman spectroscopy at liner rim. Comparisons were made between unworn and worn locations in these regions and between sample taken from two different depths.

5.5 Discussion

The overall aim of this study was to provide insights into the types of damage that occur when polyethylene liners were subjected to edge loading by component separation and whether they could lead to liner failure. The experimental simulation of edge loading was generated using ISO 14242-4. This involved a dynamic separation of the articulating surfaces during the swing phase of a gait cycle causing the liner rim to be loaded at heel strike. The evidence for dynamic separations occurring *in vivo* was provided by fluoroscopy studies where possible separations of up to 3.1 mm were reported despite only considering well-functioning patients (Lombardi *et al.*, 2000; Komistek *et al.*, 2002; Glaser *et al.*, 2008). The mean lateral translation (N=5) of 2.9 mm (range 2.4 mm to 3.2 mm) that was produced in this study was comparable in magnitude to the maximum separations reported *in vivo*.

However, the evidence provided for dynamic separation *in vivo* was challenged by replication as several other researchers reported separations distances of less than 1 mm during gait (Tsai *et al.*, 2014; Tsai, Dimitriou, *et al.*, 2015; Tsai, Li, *et al.*, 2015; Arauz *et al.*, 2018; Kiyohara *et al.*, 2019). In addition, Glaser *et al.* noted that separations occurred in both the stance and swing phase and were attributed to “jerky” motion during the articulation (Glaser *et al.*, 2008). This was in contrast to the mechanism of ISO 14242-4 where separation occurs only in the swing phase. Therefore, while

ISO14242-4 provides a repeatable experimental model of edge loading it does not necessarily reflect how edge loading may manifest *in vivo*. The precise manner of which was not particularly well understood at the time of writing.

The gravimetric wear rates for standard walking (12.5 mm^3/Mc versus 12.9 mm^3/Mc) and edge loading (22.7 mm^3/Mc versus 23.0 mm^3/Mc) displayed very good agreement with previous research using the same materials and loading conditions (Ali *et al.*, 2023). The measurements of maximum geometric deviation on the bearing surface were equally comparable (0.26 mm vs 0.28 mm) after 3Mc of edge loading. These comparisons provided good confidence about the reliability of this study. The geometric characterisation of the liner edge and microstructural measurements performed here extended beyond the research published by Ali *et al.*

Measurements were made by Raman spectroscopy to assess whether hip simulator loading resulted in any changes to the composition of the surface microstructure. The analysis indicated that the location of the measurement (i.e. at the bearing surface versus the liner rim or surface versus sub-surface) had more influence on microstructural phases than any loading or wear. The differences in the microstructure between the bearing surface and the liner rim were most likely a result of the machining these locations received during manufacture. Hip simulator loading (standard walking and edge loading) generally resulted in changes of less than 2% in all three microstructural phases. Changes of this magnitude would not amount to anything of mechanical or clinical significance.

The analysis of CMM measurements aimed to increase the understanding of the geometric changes that occur at the liner edge. The analysis demonstrated that edge loading increased the rate of geometric changes and shifted the principle location of the loading to the superiorly located rim of the liner. The two-dimensional profile plots of the rim morphology suggested that the rim morphology after 1 Mc of edge loading was very similar to the morphology after 4 Mc of edge loading. The implication being that the rim had the capacity to deform in a localised manner early on in the edge loading test period (most likely long before 1 Mc had elapsed) but subsequently remained relatively static. The subsequent geometric shift outwards was interpreted to be as a result of wear as well as deformation on a more global scale within the liner.

After 4 Mc of edge loading in a hip simulator the liners provided no evidence to suggest that the localised wear and deformation at the liner rim would pose a risk to liner failure. The study tentatively suggested that the disruption to liner fixation was a potential damage mechanism from edge loading but further research was required to provide more substantial evidence for this link. While being subjected to edge loading the liners shifted position within their shells to a slightly higher inclination angle and became increasingly pressed into the superior part of the shell as the test progressed. By the end of the test the protrusion of the inferior portion of the liner from the shell was sufficient for impingement to occur between the liner and the spigot of the femoral fixture. The occurrence of impingement was first identified after (at least) 3 Mc of edge loading had elapsed and at 4 Mc the test was stopped. Under more varied motion patterns the impingement resulting from the change in liner position could have been considerably more severe. It should be noted that the ranges of impingement free motion would be substantially altered if the spigot was replaced by a femoral stem component.

A significant limitation of the study, particularly with regards to assessing liner fixation, was the removal of the locking barb that runs around the outer circumference of the liners. The role of the locking barb would be to anchor the liner within the shell. Its removal severely hampered the ability to make any conclusions around the disruption of fixation as a result of edge loading or any subsequent effects. However, the study did provide evidence that edge loading would result in more stress being placed on the locking mechanisms than standard walking.

5.6 Conclusions

This experimental hip simulator study aimed to characterise the changes that occurred to polyethylene liners subjected to edge loading by component separation to provide insights into potential damage mechanisms that could lead to liner failure. Edge loading led to a substantial increase in both the gravimetric wear rate and the rate of geometric changes compared to a standard walking gait. However, after 4 Mc of edge loading there was no evidence that the localised wear and deformation at the liner rim would progress to liner failure. In addition, edge loading in a hip simulator did not result in any microstructural changes that would be of mechanical or clinical significance. The study tentatively suggested that the disruption to liner fixation as a result of edge loading was a damage mechanism worth further

research. The development of FE models of edge loading (in Chapter 6) to examine the internal stress strain environment within liners during edge loading were well equipped to provide further insights into the findings of this experimental hip simulator study. However, methods of experimentally accelerating damage generation would be required to provide better insights into potential damage mechanisms.

Chapter 6 – Development, verification and validation of a finite element model of edge loading in total hip replacements

6.1 Introduction

The experimental hip simulator study (Chapter 5) was combined with the development of new FE models of edge loading. The use of FE modelling augments the experimental hip simulator study by enabling the internal stress-strain environment within liners to be evaluated. The aim being to relate the field outputs of the FE model to the damage characterisation observed experimentally. The generation of a verified and experimentally validated FE model of edge loading has the potential to examine a wide range of design parameters or loading inputs. These parametric studies would be experimentally unfeasible because of the excessive time and cost required. In this chapter, an FE model of edge loading was developed which aimed to replicate the ISO 14242-4 edge loading conditions used in the experimental hip simulator study.

The research consisted of making several developments to a previously published FE model of edge loading (Jahani *et al.*, 2018, 2021; Etchels *et al.*, 2019, 2023). Firstly, a new material model was designed for Marathon UHMWPE to better represent the material properties used in the experimental hip simulator study. Secondly, a method of producing variable liner thicknesses was developed to provide insights into the links between thin regions of UHMWPE and liner failure (Tower *et al.*, 2007; Blumenfeld *et al.*, 2011; Waewsawangwong and Goodman, 2012). Finally, a method to introduce femoral head rotations (FHRs) into the FE model was devised to evaluate their effect on field outputs. Previously, the FE model incorporated the axial loading and dynamic separation of ISO 14242-4 edge loading but FHRs were not included (Etchels *et al.*, 2023).

Once these developments were made the final part of the Chapter details the comparisons made between the experimental hip simulator study and an equivalent solution from the FE model of edge loading. The dynamic separation behaviour and changes to rim geometry in the two studies was compared. Finally, the stress distributions and plastic strain accumulation was evaluated in order to provide insights into the possible damage mechanisms that might lead to liner failure as a result of edge loading.

6.2 The Baseline model of edge loading by component separation

6.2.1 An overview of the Baseline model and previous research

The Baseline model described in this Chapter was referred to as the "Recommended Mesh Model" by Etchels et al. and was the starting point of this research (Etchels *et al.*, 2023). The overarching aim of this model was to efficiently resolve the plastic strain accumulated at the bearing surface rim of a polyethylene liner when subjected to multiple cycles (< 10 c) of edge loading by component separation.

FE modelling of edge loading by component separation is computationally demanding because there are changing contact locations alongside a need for refined meshes and dynamic modelling. A combined mesh and mass-scaling sensitivity study was performed by Etchels et al. to optimise the "Recommended Mesh Model" which produced a solution time of approximately one hour per loading cycle with a refined mesh at the contact area on the bearing surface rim.

The "Recommended Mesh Model" was reported to underestimate the total plastic strain by 9% compared to the "Best Estimate Model" in the same paper which had a run time of 190 hours per loading cycle. The study also determined that the majority of the plastic strain was accumulated within the first load cycle (87%) which increased to 99% by the end of the third loading cycle (Etchels *et al.*, 2023).

6.2.2 Baseline model description

The Baseline model was a dynamic, deformable explicit finite element model of a total hip replacement under ISO 14242-4 edge loading (Figure 6.1) and was developed within the commercially available software package Abaqus (Abaqus Research v2022, Dassault Systémes, France).

<u>Geometry</u>

The geometries used were a 36 mm Pinnacle metal-on-polyethylene bearing design (DePuy Synthes, Leeds, UK). The geometry for the deformable UHMWPE liner was imported from a SolidWorks CAD file. The backside locking features and anti-rotation tabs were excluded from the model to reduce the number of elements required and improve the mesh quality for the edge contact. The femoral head was modelled as an analytical rigid sphere with a diameter of 36 mm. The resultant clearance between the femoral head and the UHMWPE liner was 0.5 mm.

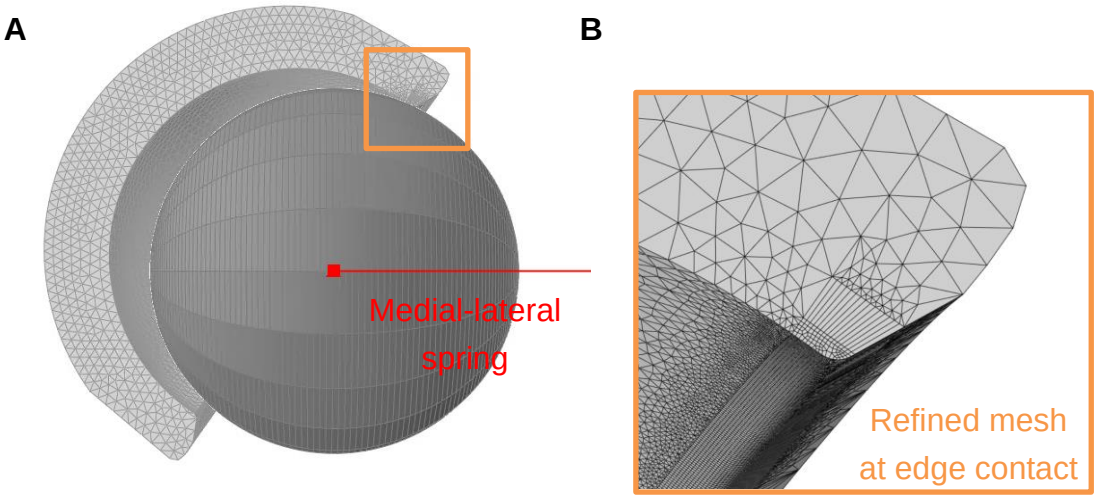

Figure 6.1. (A) The Baseline model of edge loading by component separation. A symmetry boundary condition was applied to the polyethylene liner which remained fixed throughout the model solution. All loads were applied to the femoral head. The components are depicted during the swing phase where a spring in the medial-lateral axis (red) applied the force to separate components and produce edge loading. (B) The Baseline model mesh contained refined hexahedral elements at the edge loaded rim – indicated on (A) in orange – behind which there were high aspect ratio elements. The remainder of the mesh was modelled using tetrahedral elements.

Material model

The liner was assigned an elastic-plastic material model of UHMWPE. The material model defined the stress-strain response up to a maximum stress of 29.9 MPa (12% strain) at which point the model becomes perfectly plastic. This limit reflected an endpoint in material model's definition but does not reflect the failure point of the material. The material model used a Young's modulus of 1000 MPa and a Poisson's ratio of 0.4.

Boundary conditions, loads and kinematics

Only half of the liner geometry was modelled with symmetry boundary condition applied in the coronal plane. The outer surface of the liner was fixed while the ISO 14242-4 axial load profile was applied to the femoral head (Figure 6.2). Femoral head rotations were not included. Unless otherwise stated it can be assumed that all results were obtained from a single loading cycle.

A spring in the medial-lateral axis was attached to the head to generate dynamic separation. A spring constant of 100 N/mm and a damping co-efficient of 1 N/mm was used which resulted in a critically damped system.

Extremely long beam connector elements (50 000 mm) were used to negate any error associated with head translations. A 2.5 kg mass was assigned to the femoral head to represent mass of the experimental hip simulator fixtures.

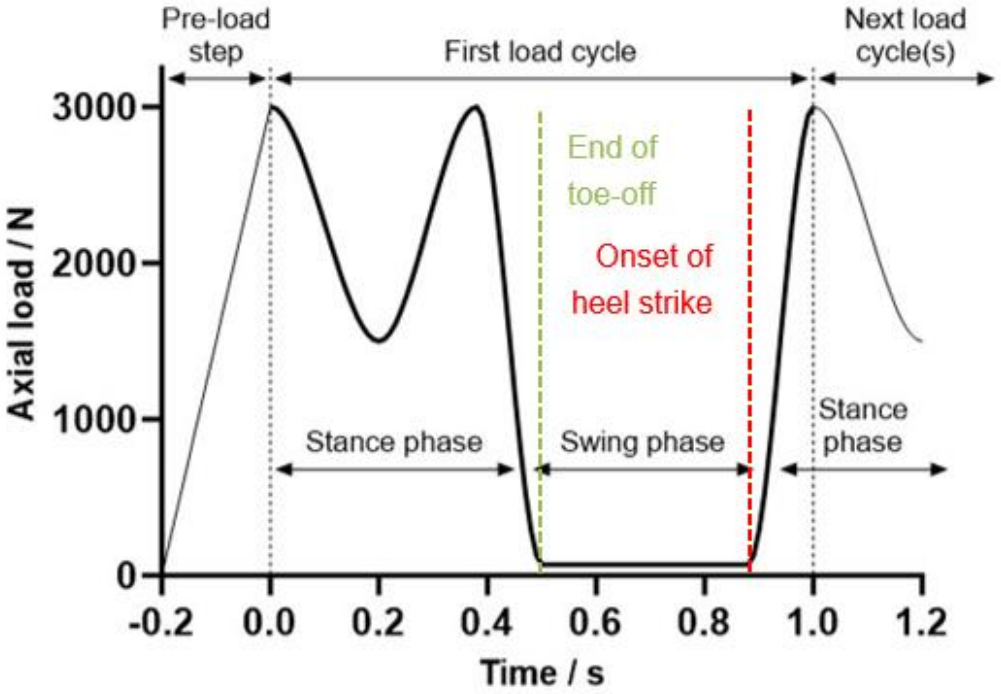

Figure 6.2. FE solutions began with a pre-load step to initialise the contacted between components. The first loading cycle begins with components centralised and the peak axial load being applied (3000 N). Toe-off (green) and heel strike (red) occurred around 0.5 s and 0.9 s into this loading cycle respectively as the gait transitions between the stance and swing phases.

Meshing and mass scaling

Explicit FE modelling uses many small but inexpensive time increments to solve analyses. Solution time is related to the maximum time increment at which the model can remain accurate – hence termed the stable time increment (Δt_{stable}). Equation 6.1 displays how the stable time increment is dependent on the element length (l_e), material stiffness (E) and material density (ρ).

Equation 6.1 $$\Delta t_{stable} = l_e \sqrt{\frac{\rho}{E}}$$

A combined mesh refinement and mass scaling optimisation was performed to achieve the optimal compromise between solution time and numerical accuracy while retaining a solution time of one hour per loading cycle (Etchels *et al.*, 2023). Mesh refinements increase numerical accuracy but decrease the stable time increment. Mass scaling is a method of increasing the stable time increment by artificially increasing material density. Similar to a mesh convergence, mass scaling creates a trade-off between reducing the stable time increment and increasing the numerical inaccuracy of the model due to artificial inertial effects.

Mass scaling was applied to the deformable elements of the liner which remains static throughout the solution. The amount of mass scaling required to achieve a target time increment was dependant on element size (Equation 6.1) indicating why a combined investigation of mesh refinement and mass scaling was necessary. The target time increment used in the Baseline model was 1E-05 s – the optimal stable time increment identified by the optimisation study (Etchels *et al.*, 2023).

Figure 6.1 displays the mesh used in the Baseline model. The total number of elements was 160 121. Refined linear hexahedral C3D8R elements (0.075 mm, 19 620) were used at contact locations on the bearing surface rim. There were also some high aspect ratio elements behind these refined elements that were to prevent the model from becoming too computationally expensive in more refined mesh cases. Linear tetrahedral C3D4 elements (1 mm, 140 501) were used for the rest of the liner geometry. A swept mesh was required to produce a uniformly smooth rim geometry. Linear elements were used because they were found to converge more efficiently for this problem due to the localisation of the plastic deformation (Etchels *et al.*, 2023).

Contact mechanics and loading steps

The head and the liner were initially positioned concentrically (while avoiding overclosure of the contact surfaces) and a pre-load cycle step was used to initialise the contact between components (Figure 6.2).

The contact algorithm used a hard penalty normal contact and penalty tangential contact with a coefficient of friction of 0.05 that was derived experimentally from components under concentric loading conditions in a hip friction simulator (Brockett *et al.*, 2007).

6.3 New developments to the FE model of edge loading by component separation

Several developments were made to the Baseline model to address some of the limitations identified. This aimed to better equip the model to investigate the effects of edge loading by component separation on UHMWPE liners and provide insights into the possible damage mechanisms. Figure 6.3 illustrates the developments made during this research – the details of which are presented in this Section. The effects of the material model used and the introduction of femoral head rotations on the field outputs of the FE model are assessed in Section 6.4. Cases with different rim thicknesses were assessed in Chapter 7.

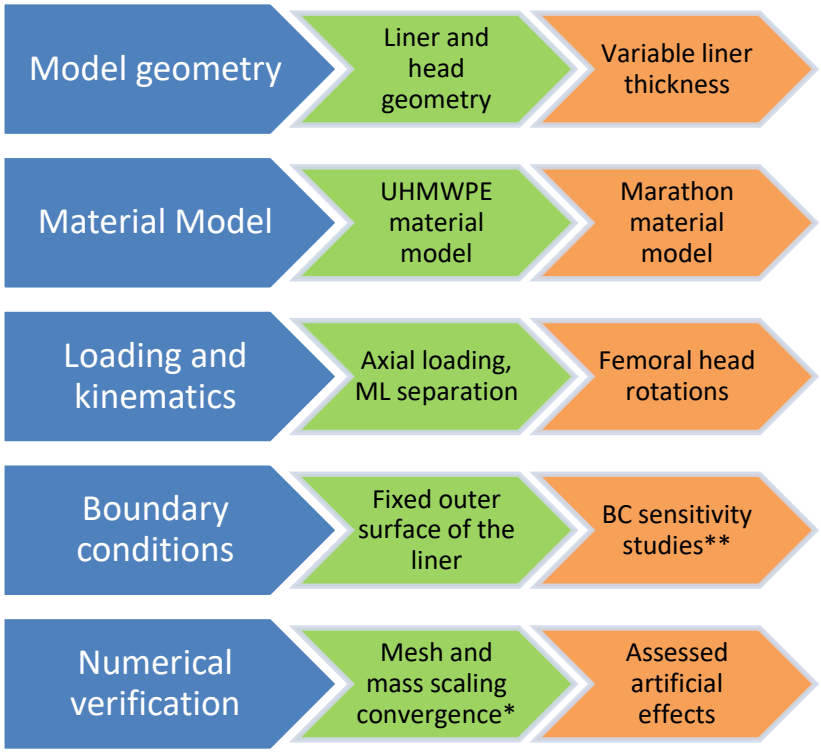

Figure 6.3. An overview of the developments made to the Baseline model. Green and orange chevrons represent the Baseline model and the new developments respectively. (*) The mesh and mass scaling optimisation was re-examined after adding the new developments. (**) Boundary condition sensitivity studies are presented in Chapter 7.

6.3.1 Variable liner thickness and the model script

Clinical case studies of liner failure after edge loading identified the presence of thin UHMWPE as a key contributing factor (Tower *et al.*, 2007; Blumenfeld *et al.*, 2011; Waewsawangwong and Goodman, 2012). A method of

producing cases of variable liner thickness was developed to provide insights into how liner thickness interacted with the stress-strain environment associated with edge loading by component separation. This was achieved used a custom Abaqus script written in Python to generate liner geometries – hence referred to as the model script.

The cross section of a Pinnacle liner (32 mm inner diameter, rim thickness 6 mm) was obtained from a CAD file. Thirteen points were used to define the geometry of the bearing surface, rim, chamfer, top and backside on the liner cross section. The model script scaled the relative positions of these points were based on a bearing diameter input. The points located on the backside of the liner were then translated based on a input for rim thickness while retaining the chamfer angle and backside shape. The rim thickness input defined the minimum thickness on the liner which was located between the bearing surface rim and the backside of the liner. Figure 6.4 illustrates two examples of how the liner cross section was altered by the bearing diameter and rim thickness inputs. The resultant cross section was revolved into a 3D part.

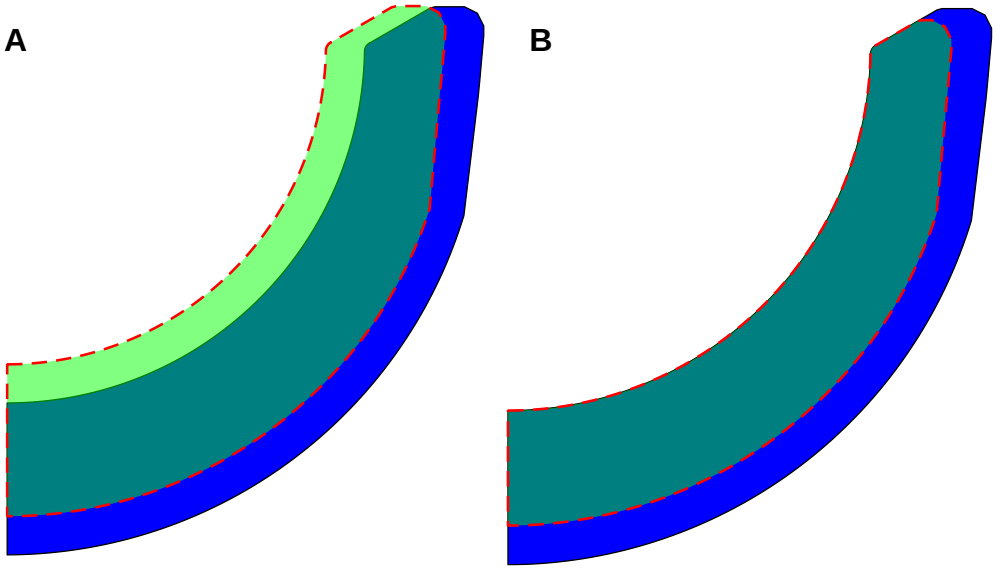

Figure 6.4. Liner geometry was altered by inputs of bearing diameter and rim thickness. (A) Compares two bearing diameters (blue 36 mm, green 32 mm) with the same thickness (5 mm). (B) Compares two thicknesses (blue 5 mm, green 3 mm) with the same bearing diameter (36 mm).

The Abaqus scripting used for part creation was just the first section of the model script within which the entire FE model of edge loading by component separation was contained. The model script was developed this way to avoid

the need to recreate the FE model for each new liner geometry. The partitioning, set creation and meshing of the liner was automated using points from the liner's cross-section. Many other variables within the FE model could also be controlled – including component positioning, mesh seed sizes and kinematic variables – making the model script well suited to performing parametric studies. Finally, there were added benefits related to model sharing, version control and storage by using a single Python script.

6.3.2 An elastic-plastic material model for Marathon UHMWPE

The elastic-plastic material model used in the Baseline model represented a non-specified UHMWPE material (hence referred to as EP-UHMWPE). A limitation of using the EP-UHMWPE material model was the lack of clarity around the sources of the data used. The source of the Young's modulus used could not be identified. The plastic stress-strain data used was attributed (via the references of multiple other published FE models) to an experimental uniaxial compression test of a UHMWPE (Barbour, Barton and Fisher, 1995). This test was not performed on a modern polyethylene material and the results of this compression test did not match the stress-strain data used in the elastic-plastic UHMWPE model. Therefore, the source of the plastic stress-strain data was also unidentifiable.

Substantial differences are known to occur between the mechanical properties of different clinical formulations of UHMWPE (Table 2.3). The chemical crosslinking and re-melting heat treatments used in RM HXLPEs are known to depleted various mechanical properties. Therefore, to improve the validity of comparisons between the FE model and the experimental hip simulator study (Chapter 5) a new material model (hence referred to as EP-Marathon) was created to represent Marathon UHMWPE.

The material properties for the Marathon UHMWPE were provided by DePuy Synthes and are held on file (*Private communication with Dr S. Tarsuslugil*, no date). Compared with the previous non-specified UHMWPE material model, the Marathon material model possessed a lower stiffness and the elastic-plastic response was defined up to a maximum stress of 21.8 MPa (equating to a 15% strain) before the model became perfectly plastic. As before, this limit reflected an endpoint in material model's definition but did not reflect the failure point of the material.

To better reflect the material response of Marathon UHMWPE at higher strains an extended version of EP-Marathon was developed by linear extrapolation of the final two data points up to a strain of 100% (hence referred to as Ext. EP-Marathon). Figure 6.5 displays all three of the material models. When compared to experimentally measured tensile test data (true stress-strain) (Spiegelberg, Kozak and Braithwaite, 2016) the Ext. EP-Marathon material model demonstrated the best agreement. The linear extrapolation here was shown to be a valid approximation and none of the FE models were close to exceeded strains of 100%.

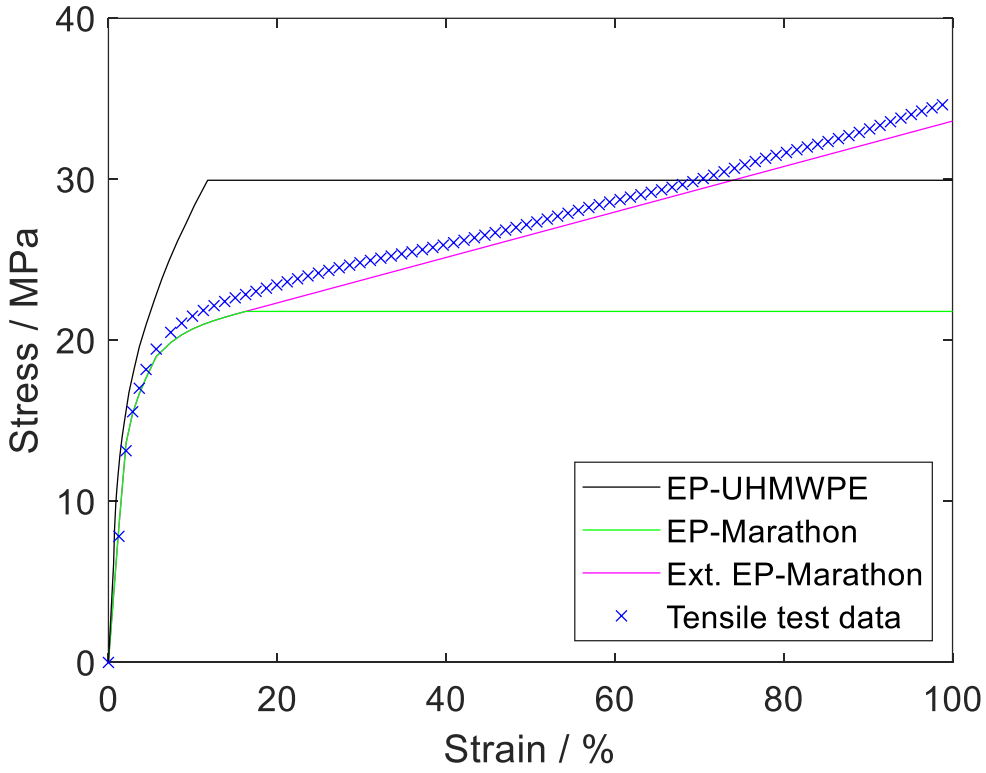

Figure 6.5. The EP-UHMWPE model (Baseline model) compared to the developed EP-Marathon models and representative tensile test data (Spiegelberg, Kozak and Braithwaite, 2016).

6.3.3 Femoral head rotations (FHRs)

The Baseline model incorporated the axial loading and dynamic separation of ISO 14242-4 edge loading but the femoral head rotations (FHRs) were not included. Therefore, the effect of FHRs on field outputs was not known. The aim of this development was to established whether the previously used assumption that FHRs can be omitted from the model was valid. Table 6.1 outlines the methods attempted to introduce FHRs to the FE model of edge loading.

Table 6.1. Methods to introduce femoral head rotations (FHRs) to the FE model of edge loading.

Attempted method	Notes on success / failure
Directly apply rotational BCs	Successful for one or two axes but when three axes were combined rotational drift was observed.
Incrementally corrected profiles	Adjusting kinematic profiles to achieve the desired FHRs would lack robustness over multiple cycles and transferability for new kinematic conditions.
Simulator ‘motors’	Replication the motors of a hip simulator would require the incremental iteration of the axes which applied the FHRs.
‘Joystick’ controlled rotation	FHRs were successfully controlled by the movement of three references points connected to the femoral head by beam connector elements.

Using ISO 14242-4 the femoral head begins and ends each kinematic cycle at the same orientation. In the FE model this relates to a centralised position at the first load peak of the cycle (occurring at 12%) as illustrated in Figure 6.2. However, applying rotational boundary conditions directly to the head failed to generate stable rotation once three axis of rotation were attempted because of the way the Abaqus solver combines three axes of rotation. Theoretically, the kinematic profiles could be incrementally corrected to produce a result with sufficient accuracy. However, the potential lack of robustness over multiple kinematic cycles and issues with transferability for new kinematic conditions were limitations considered too significant to attempt this strategy.

The FE model was essentially designed to replicate the motion of an electromechanical hip simulator. This inspired an alternative approach of producing stable head rotation where – like the simulator – the head was controlled by external ‘motors’ (which themselves are moving). Despite it being possible to generate moving axes, the rotations they applied were still being defined by a fixed axis. Consequently, the same limitations as the previous methods were encountered.

The successful method evolved the idea for simulator ‘motors’ into ‘joysticks.’ The rotation of the head was controlled by the movement of three reference points, placed in the principal axis directions, that were connected

to the head centre by beam connector elements. Figure 6.6 illustrates the Script model at two instances during the gait cycle to show the movement of reference points. Extremely long beam connector elements (50 000 mm) were used to negate the error associated with head translation as used previously for the medial-lateral spring connector elements. The maximum rotational error possible for a 4 mm component separation with the 50 000 mm beam element used was a nominal 8 E-05 radians.

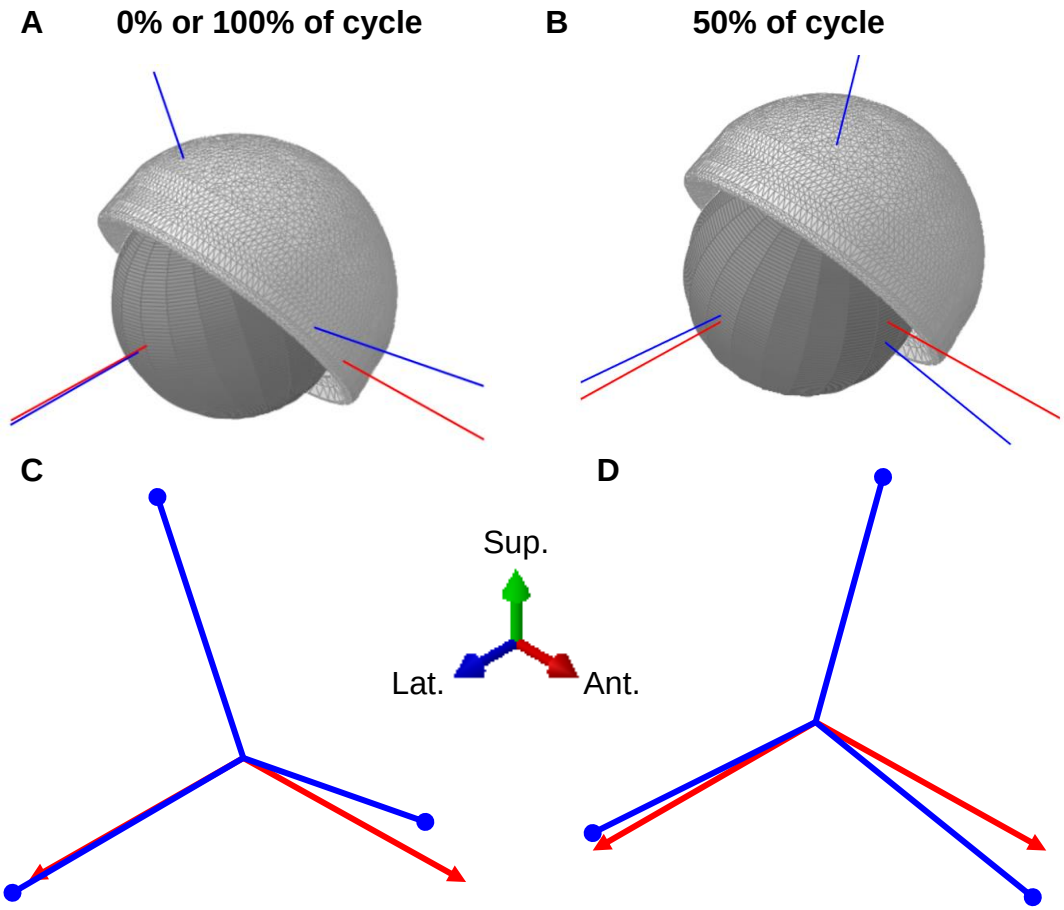

Figure 6.6. The Script model of edge loading by component separation was a further development of the Baseline model (Figure 6.1). Rotation of the femoral head was controlled by the movement of three reference points connected to the femoral head by beam elements (blue lines). The red lines indicate the medial-lateral and the (inactive) anterior-posterior springs which remain fixed throughout the cycle. The rotation of the femoral head required the polyethylene liner to be modelled without a symmetry boundary condition. (A) and (B) illustrate one instance of the model during the stance phase and swing phase respectively. (C) and (D) show the full relative length of the connector elements for the same cycle instances. Superior, anterior and lateral axis directions are also indicated. See also Figure 6.8.

A custom MATLAB script was developed to receive loading and motion input data, generate kinematic profiles and subsequently to calculate the path of the reference points. To illustrate this process Table 6.2 displays the input loading and kinematic data for ISO 14242-4 and Figure 6.7 depicts the profiles which were generated from this data points using interpolation with a piecewise polynomial structure ('pchip' function). The method allowed any desired loading and kinematics inputs to be used making it highly suited to applications using patient specific data.

Table 6.2. ISO 14242-4 loading and kinematics inputs.

Cycle / %	*Load / N*	*FE / deg.*	*AA / deg.*	*IE / deg.*
0	70	25	3	-10
12	3000			
21			7	
32	1500			
50	3000	-18		2
62	70		-4	
100	70	25	3	-10

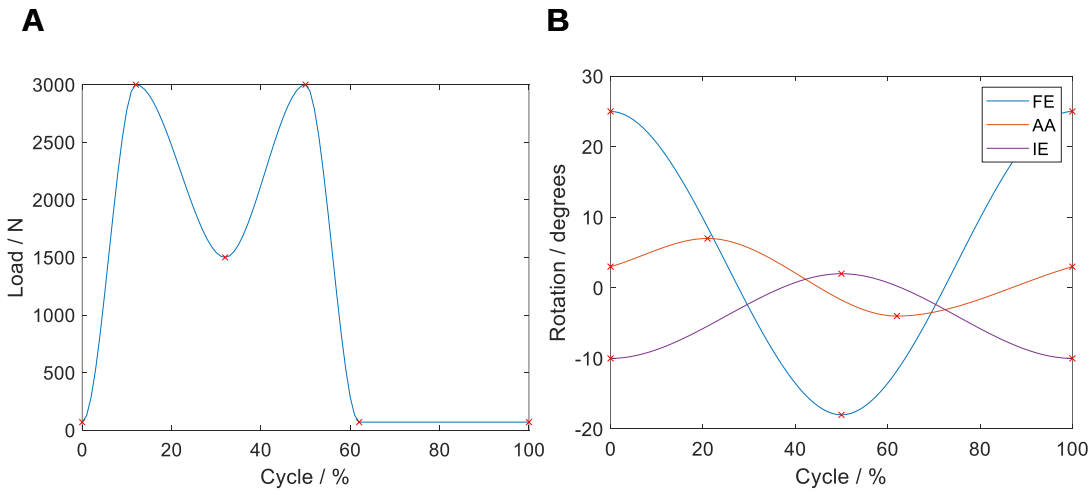

Figure 6.7. ISO 14242-4 loading (A) and kinematics (B) profiles created using a custom MATLAB script for ISO 14242-4 kinematics. The input points used were plotted as red crosses.

Figure 6.8 presents a visualisation of the motion paths that the reference points take during ISO 14242-4 kinematic cycles – in the FE model they begin at 12% of the ISO gait cycle. For each instance of the profile the MATLAB script performed the necessary matrix calculations to determine the position of each reference point. The order of the matrix calculations replicated the order in which rotations were applied in the hip simulator – abduction-adduction then flexion-extension then internal-external rotation. Any attempts which used less than three reference points or any other connector elements failed because they did not fully constrain the femoral head's rotation.

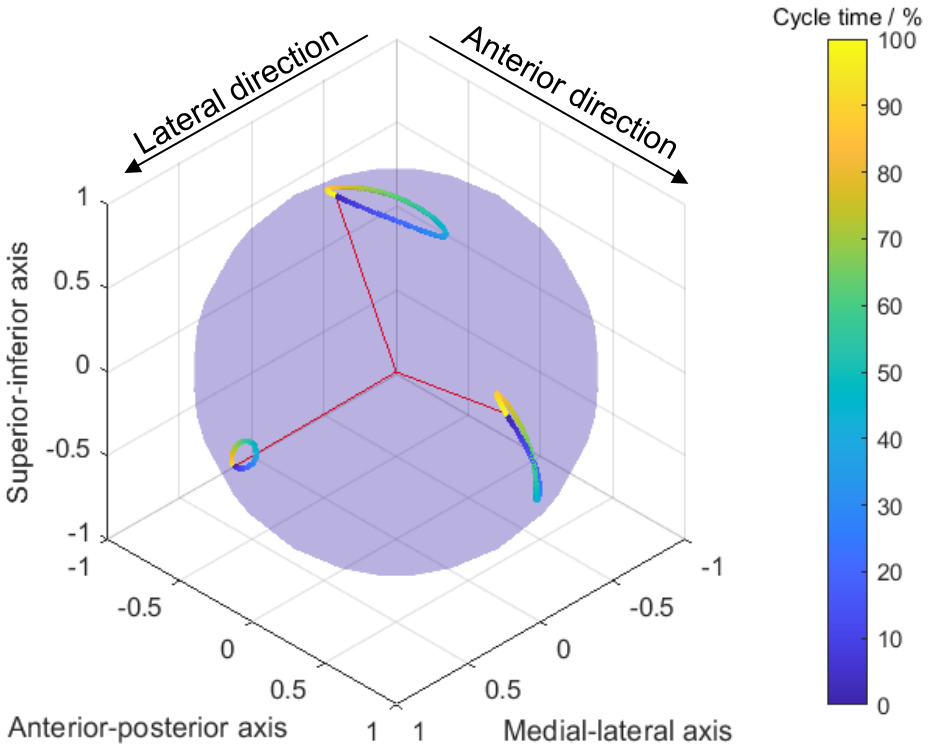

Figure 6.8. Schematic of the relative motion paths of the three reference points used to control femoral head rotation for ISO 14242-4. The references points are connected to the head centre by beam connector elements. The red axes indicate the orientation of the beam elements at the beginning of the cycle.

6.4 Assessments and verification of the FE model

6.4.1 FE model outputs used for assessments

Table 6.3 displays the outputs which were monitored to assess the effects of the developments to the model.

Table 6.3. The model outputs monitored and the instance in the cycle they were recorded. The instance relates to the loading cycle of the FE model which begins at 12% of the gait cycle as per Figure 6.2.

Output	Instance in cycle recorded
Rim deformation (max. nodal displacement)	End of cycle
Accumulated plastic strain energy (PSE)	End of cycle
Peak von Mises stress	Heel strike

The maximum nodal displacement at the bearing surface rim provided a measure of the permanent deformation of the bearing surface rim as a result of edge loading. This output was recorded at the end of the cycle when the femoral head had recentralised so the liner edge was unloaded. The accumulated plastic strain energy (PSE) was used as a numerical measure of the amount of material yielding that had occurred in the liner. This was the output of most interest because of its potential to provide insights into potential mechanisms of damage generation.

More than 80% of the PSE accumulated during heel strike when peak von Mises stresses were at their highest. The peak von Mises stress output aimed to assess whether developments to the model affected the stress conditions the liner was subjected to. The distributions of stress (von Mises and principle components) and strain (PEEQ and principle components) throughout the cycle were also assessed to understand the transmission of loads and material yielding through the liner provide insights into potential damage mechanisms.

6.4.2 Material model effects

The results presented in Section 6.4.2 were generated by the Baseline model as described in Section 6.2 where only the material model was changed. Rim deformation, von Mises and PSE outputs were recorded to assess the effect the material model had on the liner’s response to edge loading. Rim deformation increased from 0.13 mm 0.15 mm when the EP-

UHMWPE was change to either EP-Marathon and Ext. EP-Marathon (Figure 6.9). The Marathon properties were less stiff than the UHMWPE properties in both the elastic and plastic regions of strain (Figure 6.5) which generated an increase in deformation.

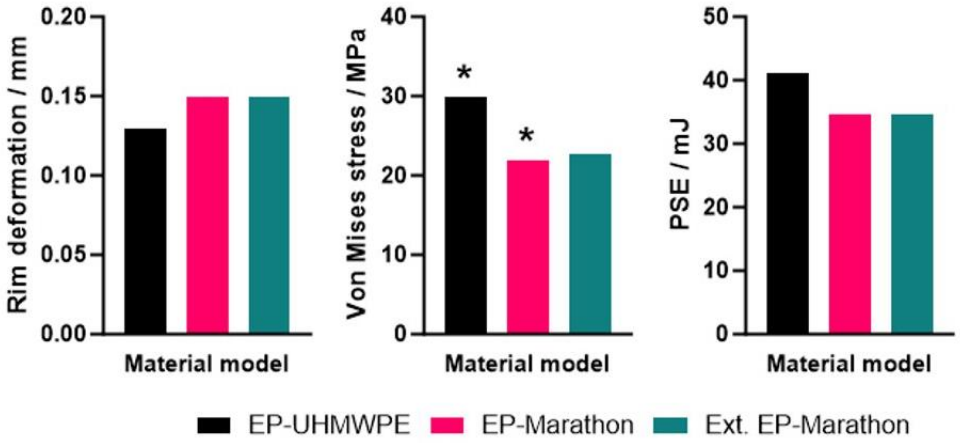

Figure 6.9. The effect of material model on rim deformation, von Mises stress and PSE. (*) Von Mises stress reached material model limit.

The von Mises stress for EP-UHMWPE (29.9 MPa) and EP-Marathon (21.8 MPa) both reached the maximum stress defined in the material model indicating that some perfectly plastic deformation had occurred. During perfectly plastic deformation the stress was redistributed to the adjacent nodes and strain can increase without any increase in stress. The peak von Mises for the Ext. EP-Marathon material model (22.7 MPa) was only 0.9 MPa above the non-extended EP-Marathon material model. In all three outputs there was very little difference between the EP-Marathon and Ext. EP-Marathon indicating that extending the material model had a very small effect.

PSE decreased from when the EP-UHMWPE (41.2 mJ) was change to either EP-Marathon (34.6 mJ) or Ext. EP-Marathon (34.7 mJ) (Figure 6.9). For the magnitudes of strain observed (< 30%) the area under the EP-UHMWPE curve was clearly greater than the EP-Marathon models (Figure 6.5) indicating more work was needed per unit volume for a given strain and resulting in a higher PSE.

Overall, the results highlighted how the material models for different UHMWPE materials can have a substantial effect on the field outputs of FE testing. The development of Marathon-specific material models was considered an important step to maximise the maximise the validity of all

experimental comparisons made and the Ext. EP-Marathon model was considered the more suited option. A limitation of all of three material models was that they only related to only one loading case. They neglect the fact that true UHMWPE stress-strain behaviour is both strain rate and temperature dependant. The mechanical response also includes viscoelastic and viscoplastic components which were not included. However, it is possible further improvements to the material model may see diminishing returns given the unsubstantial effect of using Ext. EP-Marathon under these loading conditions. Different modelling scenarios, that generated higher strains, might see more of a difference between Ext. EP-Marathon (or other more complex models) and the non-extended EP-Marathon.

6.4.3 The Baseline model versus the Script model

The main purpose behind the creation of the model script was to provide an efficient method of generating variable component geometries within the FE model of edge loading. Equivalent cases of the Baseline model and the Script model (36 mm bearing diameter, 5 mm rim thickness, Ext. EP-Marathon material model) were compared to evaluate the differences between the two FE models. A key difference was the presence or lack of high aspect ratio elements behind the refined rim that were removed for the Script model. Otherwise, the Script model was designed to replicate Baseline model.

Figure 6.10 displays how there was a substantial increase in PSE when using the Script model (51.1 mJ) compared to the Baseline model (34.7 mJ). A more moderate decrease in rim deformation was also observed (Baseline 0.15 mm; Script 0.13 mm). Both of these results were attributed to the improvement in mesh resolution at the rim in the Script model as a result of removing the high aspect ratio elements.

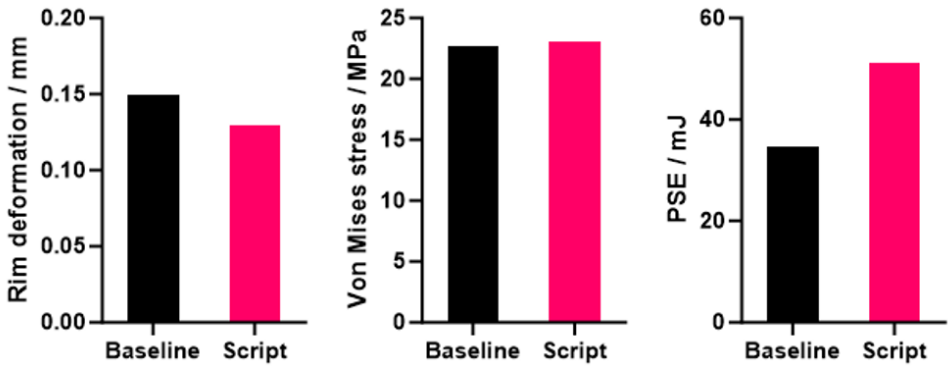

Figure 6.10. Rim deformation, von Mises stress and PSE outputs generated by the Baseline and Script models.

The transmission of stress and strain was also observed to be more even for the Script model when evaluating stress-strain distributions (Figure 6.11). This contributed to the justification to remove the high aspect ratio elements in the Script model because of the potential effect they had on field outputs and the transmission of stresses and strains. However, a consequence of this decision was an increase to the number of elements and run time (examined in Section 6.4.4).

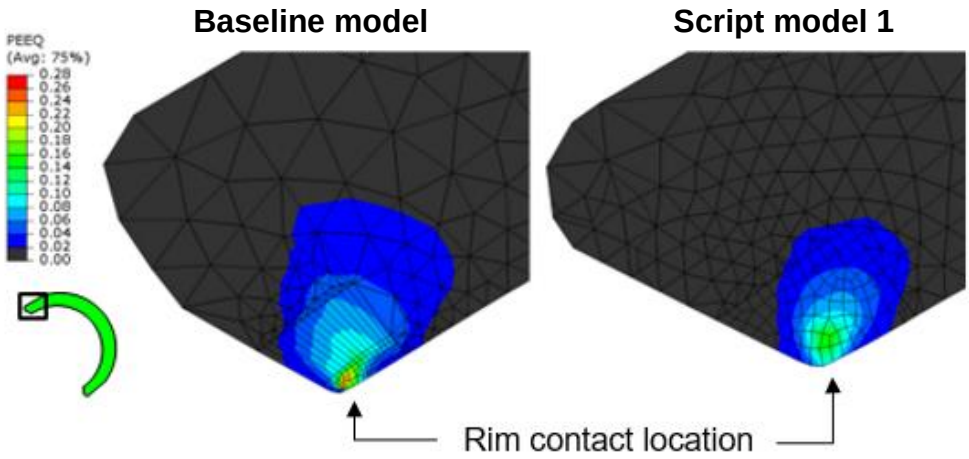

Figure 6.11. Plastic strain distributions at the superior liner edge for the Baseline model and Script model 1 (as per Table 6.4).

6.4.4 Mesh verification re-examination

Etchels *et al*. previously performed a comprehensive investigation into the optimal combination of mesh refinement and mass scaling as discussed in Section 6.2 (Etchels *et al.*, 2023). In explicit modelling the run time is proportional to the number of elements in the model (Dassault Systèmes, 2016). Using the same mesh parameters, the Script model resulted in around five times as many elements as the Baseline model. This was because of the removal of the liner symmetry condition (necessary for including FHRs) and the removal of the high aspect ratio elements from the refined rim region. A run time of over four hours per loading cycle was considered unsuitable for the completion of both parametric testing or multi-cycle solutions. Therefore, the optimal balance of accuracy and run time of the model was re-examined.

The investigation aimed to establish whether the model could achieve sufficient accuracy while retaining a one hour run time per loading cycle. The

target time increment used in all cases was 1E-05 s. This was the optimal stable time increment identified by the previous optimisation study (Etchels *et al.*, 2023). The tests were all performed on a 36 mm diameter liner with a thickness of 5 mm and used Ext. EP-Marathon.

The run time and outputs of the Baseline model was compared to four mesh cases using the Script model which incorporated two methods of mesh coarsening. Table 6.4 reports the relative mesh seed sizes used in the refined rim, the contact (superior hemisphere) and non-contact (inferior hemisphere) regions of the mesh. Rim coarsening (Script 3 and 4) affected the hexahedral elements at the rim. Global coarsening (Script 2 and 4) affected the tetrahedral mesh but only in the inferior portion of the liner where no contact occurred. Figure 6.12 illustrates both methods of mesh coarsening by comparing the mesh generated for Script 1 and Script 4.

Table 6.4. Mesh seed sizes of the refined rim, contact (superior hemisphere) and non-contact (inferior hemisphere). Coarsened seed sizes are marked in bold.

Mesh region	**Baseline**	**Script 1**	**Script 2**	**Script 3**	**Script 4**
Rim	0.075	0.075	0.075	**0.2**	**0.2**
Contact	1	1	1	1	1
Non-contact	1	1	**3**	1	**3**

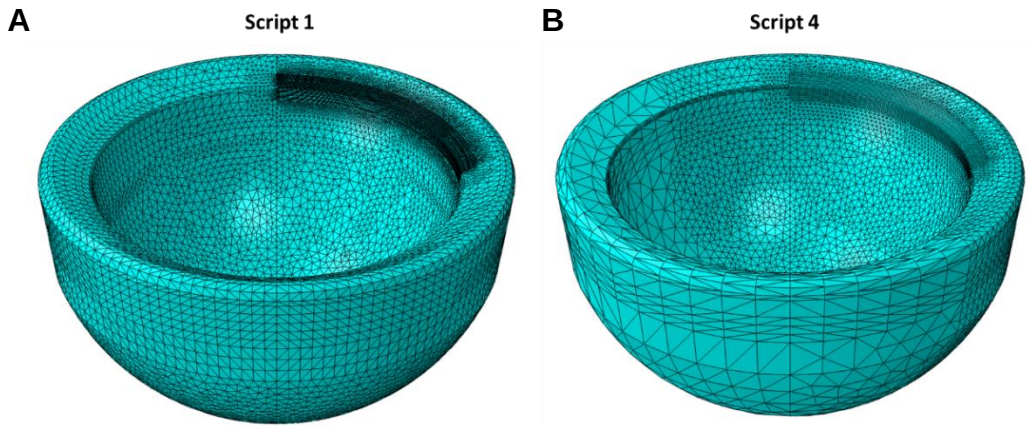

Figure 6.12. Visualisations of the mesh cases for (A) Script 1 and (B) Script 4. In Script 4 the mesh at the rim region and inferior half of the liner (non-contact) have been coarsened.

Figure 6.13 shows that rim coarsening had a much greater effect on the run time than global coarsening because it produced a larger reduction in elements. Script case 4, with coarsening of both rim and global seed sizes, solved in 54 minutes which achieved the aim set of under one hour.

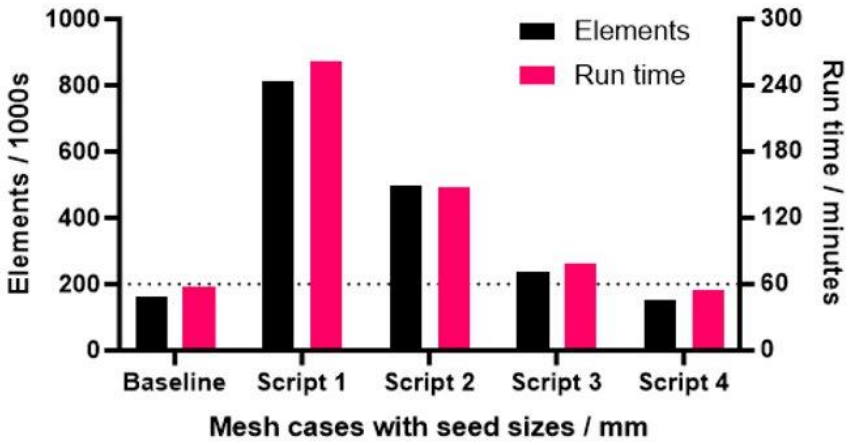

Figure 6.13. The number of elements and run time for the five mesh cases compared. The dotted line on the graph indicates the run time aim of one hour.

The suitability of this mesh case depended on whether the effects mesh coarsening had on model outputs were justifiable. Figure 6.14 illustrates the effects of mesh coarsening on the field outputs of the Script model cases. Percentage changes of -1.6%, -4.8% and -7.4% were determined for the rim deformation, von Mises stress and PSE respectively for Script 4 compared to Script 1. The rim deformation decreased by 0.002 mm. A geometric change of this magnitude was completely inconsequential when compared to the precision of the experimental measurements which were made to the nearest 0.01 mm. Therefore, comparisons between experimental geometric changes and rim deformations in the FE model would not be affected by the mesh coarsening in Script 4.

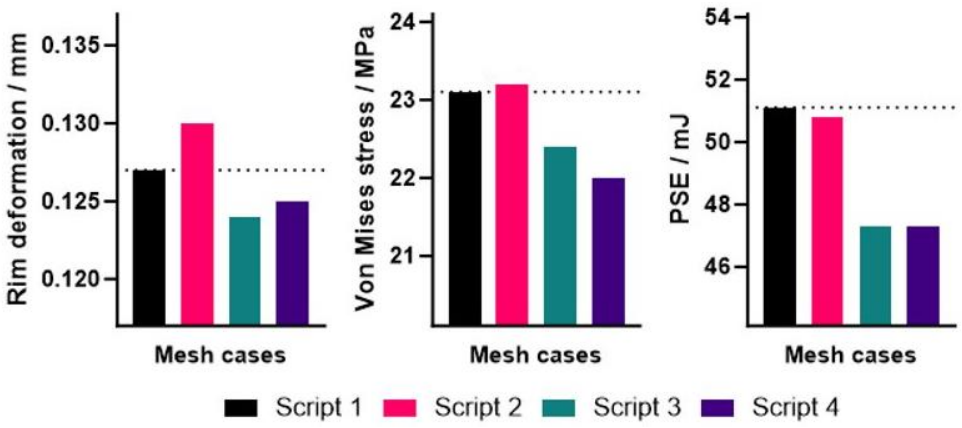

Figure 6.14. Rim deformation, von Mises stress and PSE outputs generated by the four mesh cases of the Script model. The dotted line represents the Script 1 output value.

The outputs of von Mises stress and PSE did not have experimental measures to be compared to. The key aim behind the FE model was to make comparisons between different liner geometries. Analysing the differences between cases would provide insights into the effect of design variables on potential edge loading damage mechanisms. It mattered less whether these outputs were an under- or over-estimate so long as outputs remained reasonable. For example, knowing a hypothetical case A resulted in a 10% increase in PSE compared to case B was more important than whether case A was 50 mJ or 55 mJ. Within this context, a difference of less than 10% was considered to be appropriate. The differences between the von Mises stress and PSE for Script 1 and Script 4 both achieved this criteria.

A second sensitivity test evaluated the effect of node location on model outputs. Altering the liner geometry would induce shifts to the precise nodal positions. To make valid comparison between liner geometry cases the model outputs must be insensitive to this. In two additional cases a small change was made to the rim seed size for Script 4. This adjusted the nodal positions without greatly influencing the mesh density. Figure 6.15 indicates that the variation observed for both von Mises stress and PSE was less than 0.5%. Rim deformation differences also remained inconsequential. These results indicated that von Mises stress and PSE outputs did not fluctuate with small changes to nodal positions. This provided confidence that comparisons between different liner geometries would be valid when equal mesh densities were used.

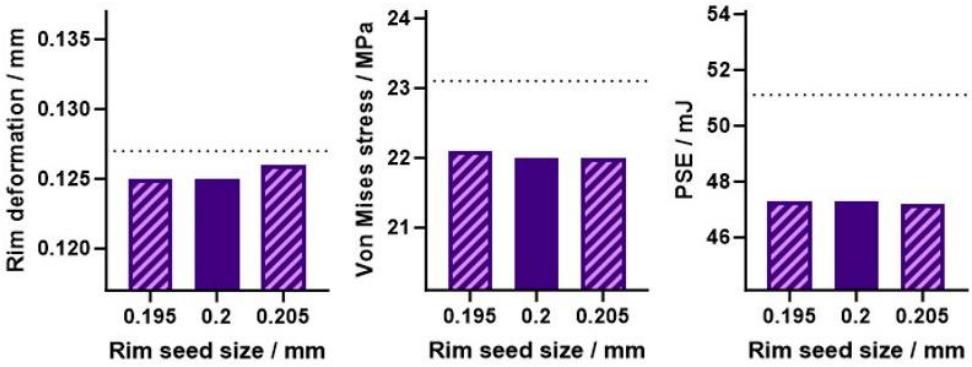

Figure 6.15. Rim deformation, von Mises stress and PSE for Script 4 compared to cases with small changes in rim seed size to assess the sensitivity of outputs to the nodal positions. The dotted line displays the output from Script 1.

The effect of mesh parameters on PSE accumulation was further examined by analysing the accumulation patterns across the cycle and the distributions of strain produced by each mesh case. Rim coarsening decreased PSE accumulation by 7.4%. Figure 6.16A illustrates how the differences predominantly resulted during heel strike at around 0.9s. However, over the cycle as a whole the pattern of strain accumulation was not altered.

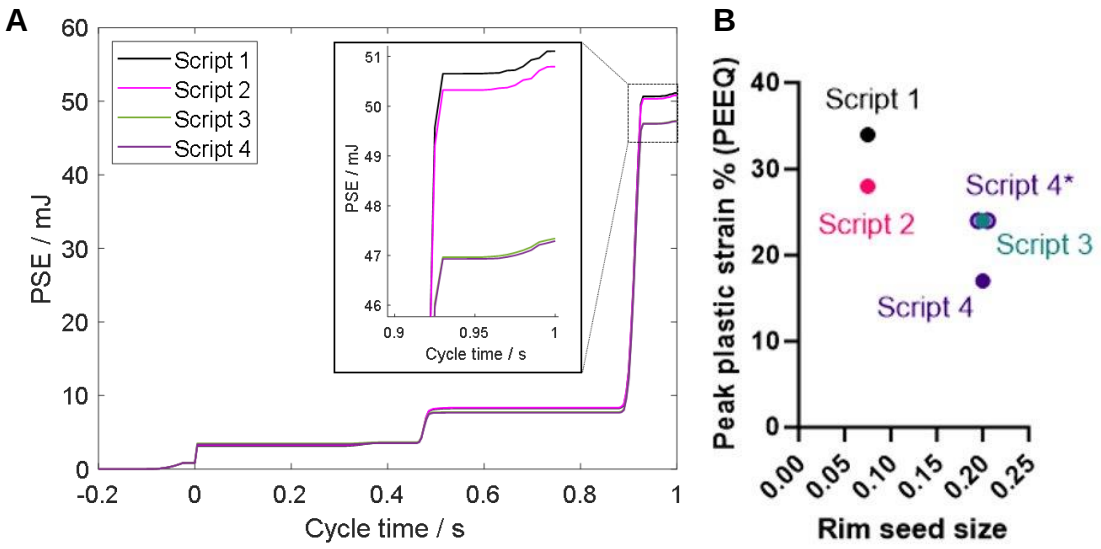

Figure 6.16. (A) PSE accumulation over the pre-load (< 0 s) and load cycle steps for the four mesh cases. The PSE at the end of the load cycle is magnified. (B) Peak plastic strain (PEEQ) plotted as a function of rim seed size. (*) values for the two additional Script 4 mesh cases.

Previously, Etchels *et al*. has also used peak plastic strain values as a comparative measure for plastic strain as well as PSE (Etchels *et al.*, 2023). However, Figure 6.16B illustrates how the peak nodal plastic strains (either principle or PEEQ) were not a robust output and were still sensitive to mesh parameters across the mesh densities tested. It appears probable that these outputs had not yet fully converged at the most refined case (where solve time exceeded four hours). Hence the level of mesh refinement needed to reach a convergence of the peak nodal plastic strains would be extremely computationally expensive. It may even reach the point where the numerical accuracy of the model would suffer because the amount of mass scaling required would begin to introduce artificial inertial effects. On this basis, comparisons of peak nodal plastic strains between FE cases were not made because they were not considered valid.

In contrast to the peak nodal strain values, Figure 6.17 illustrates how the strain distributions were considerably less sensitive to mesh parameters. At points away from the strain concentration, the PEEQ values displayed good agreement. Therefore, it was still considered a valid approach to compare strain distributions between model cases even while the peak strain values could be substantially different.

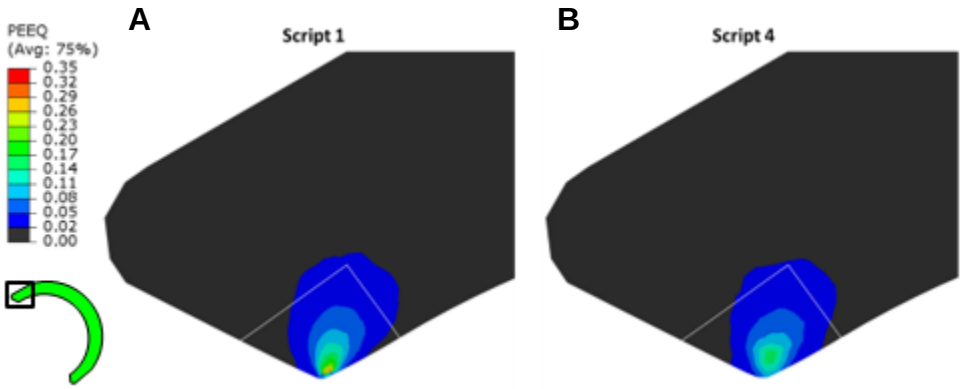

Figure 6.17. Plastic strain (PEEQ) distributions for (A) Script 1 and (B) Script 4 mesh cases. The white lines indicate the hexahedral refined mesh region. The mesh was not included to improve the clarity of the strain distribution.

In summary, the investigation in this section was relatively superficial because it built on more substantial research already published (Etchels *et al.*, 2023). Previously, an optimal target time increment of 1E-05 s was

established for the Baseline model which was also utilised in the Script model. The mesh parameters used were re-evaluated because the new developments to the model increased the number of elements by around five times.

Mesh case Script 4 was considered the optimal balance of computational cost and numerical accuracy for meeting the aims of this research. It achieved the aim of a run time under one hour. Mesh-based differences in rim deformation were considered inconsequential compared to the precision of the experimental measurements. The sensitivity of von Mises stress and PSE outputs to different mesh densities was deemed appropriate and these outputs were not sensitive to nodal positions. This provided good confidence that comparisons between different model cases with equal mesh densities would be valid. The distributions of von Mises stresses and peak plastic strain values could also be compared. However, comparisons between peak plastic strain values (PEEQ and principle) were not considered valid because of the sensitivity of these outputs to mesh parameters.

6.4.5 Verification of artificial model effects

The energy balance of the Script 4 model – the chosen mesh case – was examined to ensure that numerical accuracy of the model was not adversely affected by artificial effects. To ensure that inertial forces caused by mass scaling were not adversely affecting the model's accuracy the ratio of the kinetic energy (ALLKE) and the internal energy (ALLIE) of the liner was assessed. Abaqus documentation suggested that this ratio should not exceed 5-10% (Dassault Systèmes, 2016). After a brief settling period in the pre-load step (where both kinetic energy and internal energy were extremely small) the ratio did not exceed 3% for the duration of the model solution. This provided good confidence that artificial densities were not causing adverse effects.

The presence of excessive (and artificial) element distortion, known as hourglassing, was also assessed. Abaqus documentation suggested that the ratio of artificial strain energy (ALLAE) and the total internal energy (ALLIE) in the liner should not exceed 1-2% (Dassault Systèmes, 2016). This ratio peaked during the swing phase at 1.8%. This suggested that hourglassing remained at an acceptable level but that it was also reasonably close to the limit where it could become significant. An alternative method was to ensure that the ratio of artificial strain energy (ALLAE) to strain energy (ALLSE) remains below 5%. However, due to presence of plastic strains in the model

this approach was considered to be less meaningful because of the energy dissipated during plastic deformation (Dassault Systèmes, 2016).

In addition to Script 4, all of the mesh cases from Section 6.4.4 (including the Baseline model) also passed the assessments described in this section.

6.4.6 Femoral head rotations (FHRs)

A method of including femoral head rotations (FHRs) into the edge loading model was developed to assess their effect on model outputs and establish whether the previously used assumption that FHRs can be omitted from the model was valid. Figure 6.18 compares the dynamic separation behaviour of the FE model with and without FHRs (comparisons between the FE model and the experimental hip simulator study were discussed in Section 6.5). The inclusion of FHRs increased lateral translation by 0.1 mm to 3.6 mm and did not change vertical translation (-1.9 mm). The anterior posterior translation also increased from 0 mm to 0.1 mm when FHRs were included. Therefore, it was established that FHRs had minimal effect on the separation behaviour of the FE model. This was emphasized when the differences of 0.1 mm were compared the scale of the range observed experimentally (up to +/- 0.5 mm).

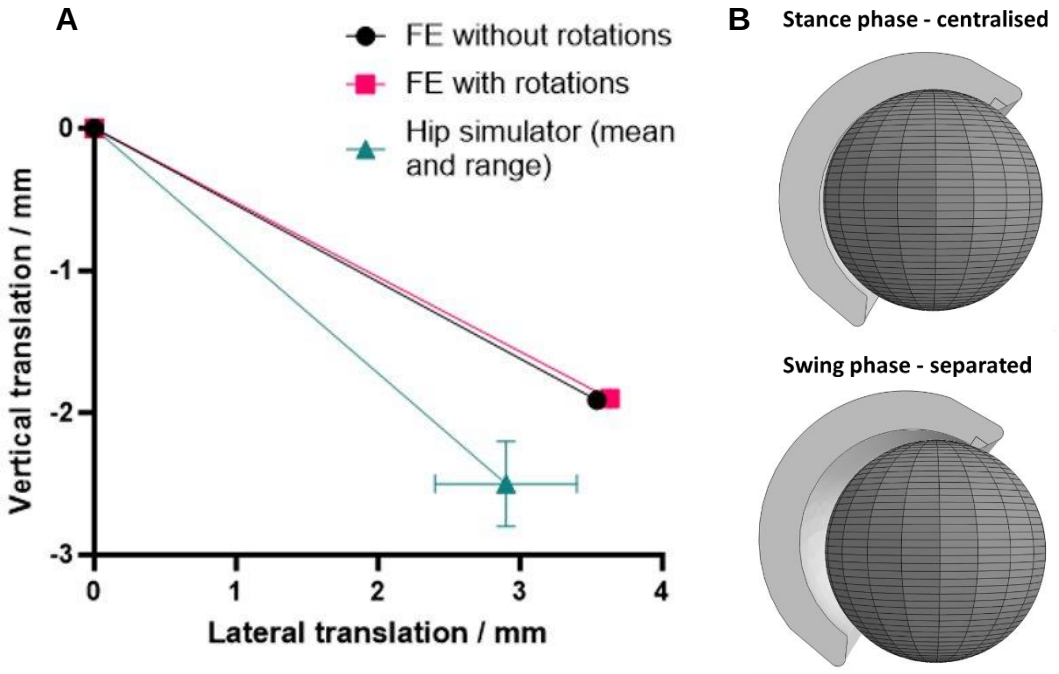

Figure 6.18. (A) Femoral head translations during edge loading observed in the Script model with and without femoral hip rotations. Measurements from the experimental hip simulator study (Chapter 5) are also included for comparison. (B) A visualisation of the femoral head translation from the FE model (without rotations).

Figure 6.19 illustrates the changes in rim deformation, von Mises stress and PSE after including femoral hip rotations into the model. For these two cases there was less than 0.5% difference between the outputs of rim deformation and von Mises stress. PSE increased by 1.5% to 48 mJ. The increase was generated by the small amount of anterior-posterior translation which increased the overall contact area across the cycle. Overall, the results indicated that for stress-strain analyses in a low friction scenario the inclusion of FHRs was not necessary because there were no substantial changes to the separation behaviour or field outputs. This meant that the symmetry condition used on the liner in the Baseline model could also be reinstated to reduce computational costs.

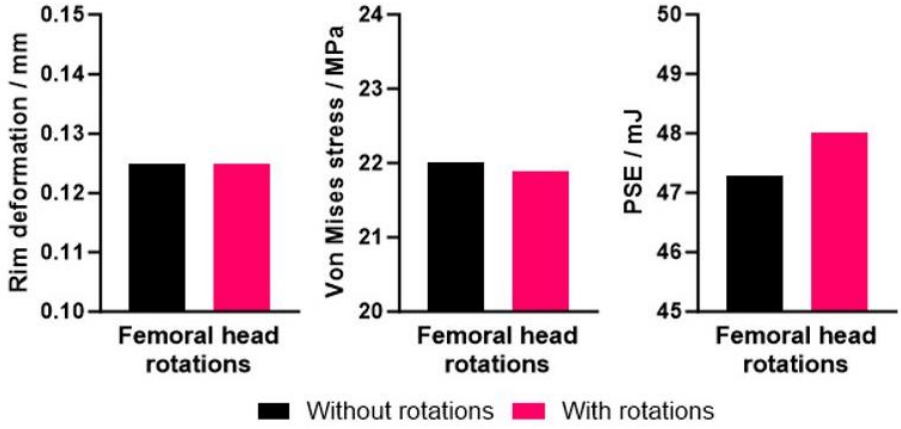

Figure 6.19. Rim deformation, von Mises stress and PSE outputs generated by the Script model with and without the inclusion of femoral head rotations (FHRs).

6.5 Experimental comparisons and sensitivity studies

6.5.1 Component separation sensitivity

Figure 6.20 illustrates the separation behaviour from both the FE model and the experimental hip simulator study presented in Chapter 5. When the equivalent cases were compared, lateral translations were 0.6 mm greater and the vertical translation were 0.6 mm smaller in the FE model compared to mean values (N=5) measured experimentally. To understand the source(s) behind this difference an investigation was performed which examined the effect of component positioning and medial-lateral spring stiffness on component translations. These tests were performed with an

extremely coarse mesh (seed size 5 mm) because only the separation behaviour of components was being examined. The separation behaviour of the coarse mesh model was less than 0.2% different from the fully meshed model verifying that this was a numerically accurate strategy.

During the hip simulator study a small increase in the inclination angle of liners was observed. Using the FE model a ten degree span of inclination angles (55 degrees +/- 5 degrees) was tested to examine whether differences in component positioning could be contributing to the differences in experimentally and FE derived separation behaviour. Figure 6.20 illustrates how component positioning affected the vertical translations (up to 18%) more strongly than the lateral translations (< 2%). This corresponded to the difference in height between the bearing surface and the liner rim based on the liner's inclination.

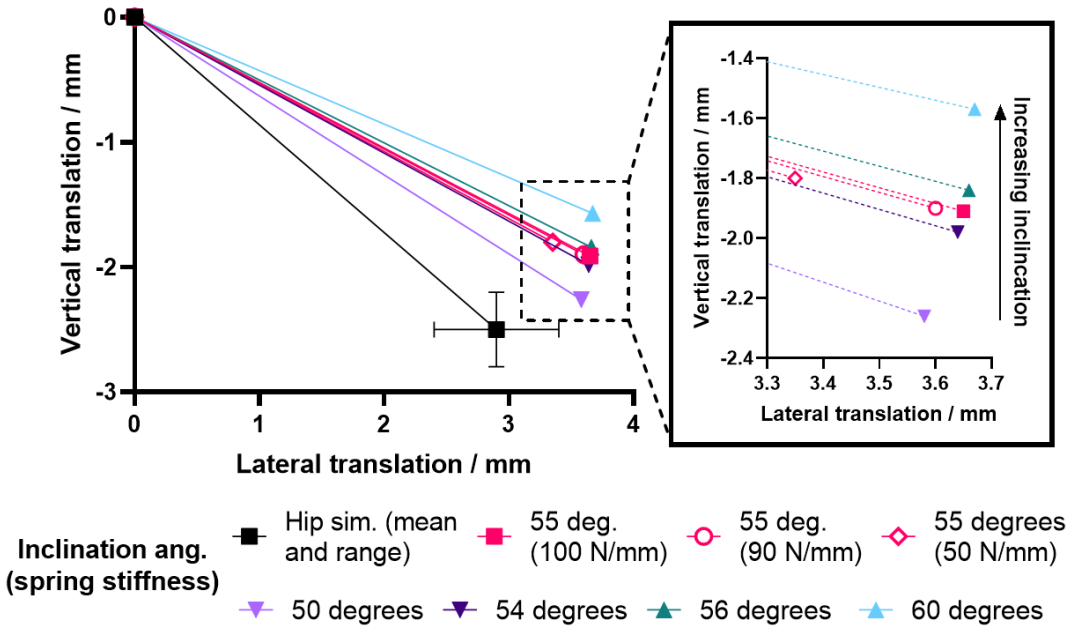

Figure 6.20. A comparison of experimentally and FE model derived femoral head translations during edge loading. The experimental hip simulator study (mean and range, N=5) from Chapter 5 was compared to FE solutions with different inclination angles (55 degrees +/- 5 degrees). Cases with a 10% and 50% reduction in spring stiffness is also presented.

A 60 degree inclination resulted in a smaller vertical translation (-1.57 mm) compared to a 55 degree inclination (-1.91 mm) and even further from the experimental measurement (-2.5 mm). Therefore, any changes in inclination observed experimentally were not able explain differences between hip

simulator and FE model separation behaviour. It was also unlikely that error in the initial positioning of the components could have been significant enough to be a major contributing factor as well. This study predicted that more than 5 degrees of error in component position would be necessary.

To evaluate the effect of spring stiffness on separation behaviour the 100 N/mm spring constant was reduced first by 10% and then 50%. This resulted in a decrease of 1.4% and 8.2% to the lateral translation respectively (Figure 6.20). In comparison, the lateral translation of the experimental hip simulator was 20.5% below the equivalent FE model. A previous investigation suggested that the effective stiffness of the medial-lateral spring in experimental hip simulators can be far below expected values (*Private communication with Dr L. Etchels*, no date). The use of a 100 N/mm was estimated to produce an effective spring stiffness of only 58 N/mm. This was calculated using the component separation and the associated measured medial-lateral force across several hip simulator studies.

On this basis, approximately half of the lateral translation overestimation in the FE model was considered likely to be due to compliance within the simulator reducing the effective spring stiffness. Resistive forces and friction within medial-lateral bearings were another potential contributing factor neglected by the FE model. Finally, the ability to experimentally measure and precisely apply the low swing phase loads during edge loading gait cycles was thought to be a challenge in the experimental hip simulator that could also affect component separation behaviour.

In the case of the vertical translations, simulator compliance was considered an ever more substantial contributor to the differences observed because of the 3000N of axial loading was applied in this axis. Simulator displacements were measured using gauges attached to the bearing. Therefore, compliance in the system would lead to an overestimation of the translation between the components themselves.

In conclusion, mechanical imperfections within the experimental simulator were thought to be the cause of differences in component separation behaviour. FE element models aiming to replicate experimental simulators should bear in mind that the experimental set up doesn’t necessarily correspond perfectly to the resultant mechanical environment.

6.5.2 Friction co-efficient sensitivity

Section 6.4.6 established that for a low friction scenario (a friction co-efficient of 0.05) the inclusion of hip rotations had minimal effect on the model

outputs. This finding was supported by Mattei and Di Puccio who found that wear predictions from FE wear modelling were insensitive to friction coefficients of below 0.1 where a frictionless contact condition could be assumed (Mattei and Di Puccio, 2023). The same study determined that friction coefficients above 0.1 did influence the contact and wear parameters.

The literature was examined to explore whether friction coefficients of above 0.1 were expected or possible in MoP THR bearings. Experimental research suggested that the friction coefficient decreased as contact stress increased. For contact stresses above 10 MPa, friction co-efficients reached a plateau of between 0.05 and 0.1 (Wang, Essner and Klein, 2001; Saikko, 2006). However, for a fixed contact pressure the friction coefficient was also dependent on the contact area (Saikko, 2017). A friction co-efficient of around 0.3 was reported for the lowest contact areas albeit with a contact stress of only 1.1 MPa. In the FE model, the contact stresses exceeded 14 MPa at all points of the cycle and exceeded 30 MPa the during the swing phase when contact area was lowest. So, while experimental results demonstrate the possibility of friction coefficients between 0.1 and 0.3 for MoP bearings, they all appear to have occurred for contact stresses well below 10 MPa. On the basis of this literature, it was believed that the contact stresses in an MoP THR bearing would be sufficient that the friction coefficient would not exceed 0.1 at any point of the gait cycle.

Several friction coefficients between 0.01 and 0.2 were examined to explore its effect on the model outputs both with and without FHRs. This included the effects of friction coefficients of above 0.1 that could be considered as either unlikely or particularly adverse.

Figure 6.21 illustrates the overarching finding that friction affected the speed of component separation but not its overall magnitude. At the instant prior to recentralisation (0.89s) the range of lateral separations was only 0.1 mm. However, three milliseconds later this range was 1.5 mm. FHRs had very little effect on lateral separation behaviour. The largest differences were observed at 1s where increasing friction impeded the recentralisation of the femoral head in the cases without FHRs.

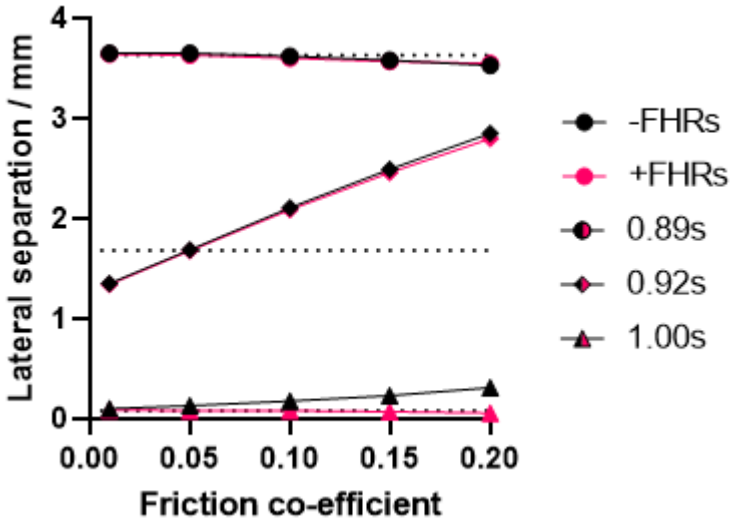

Figure 6.21. The lateral separation of the femoral head from the idealised centre of rotation of the liner. The colour of data points indicates whether femoral head rotations (FHRs) were included while their shape relates to cycle time. Dotted lines mark the values obtained using a friction co-efficient of 0.05 and with femoral head rotation.

Figure 6.22 displays the effect of increasing friction co-efficient has on model outputs. While maximum von Mises stresses were very similar, it was notable that higher von Mises stresses were sustained for longer (results presented for 0.93s) when the head recentralisation was slowed by the higher friction values. Etchels *et al.* observed similar effects when investigating the effect of swing phase load, fixture mass and spring dampening (Etchels *et al.*, 2023). The increases in rim deformation and PSE observed when friction was increased were primarily attributed to the speed of the component separation events. The differences in component separation at the end of the cycle (results for 1s, Figure 6.21) was considered a contributing factor to the divergence of the rim deformations when FHRs were included (Figure 6.22B).

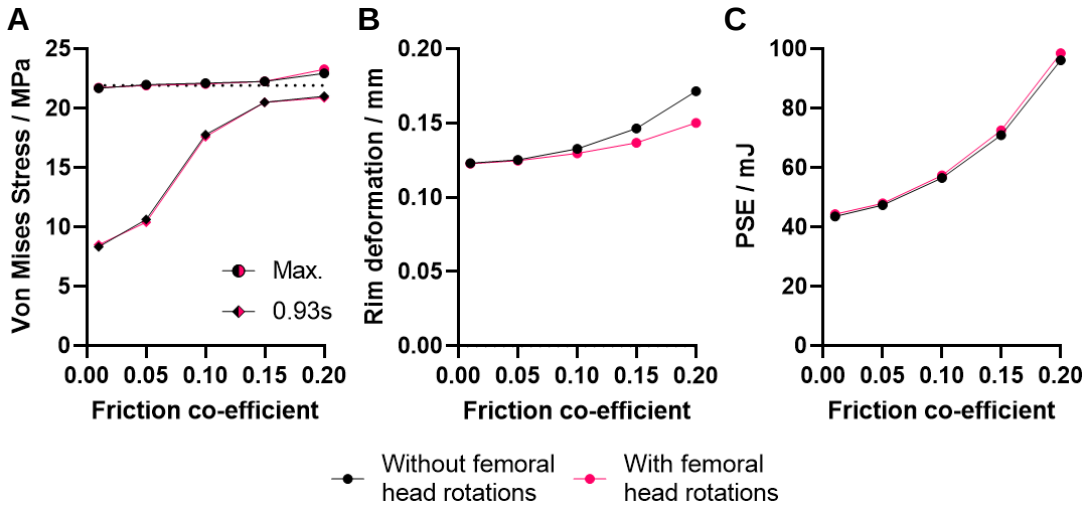

Figure 6.22. (A) Von Mises stress, (B) rim deformation and (C) PSE outputs generated using different co-efficients of friction. The colour of data points indicates whether femoral head rotations (FHRs) were included while their shape (von Mises stress only) relates to cycle time. Maximum von Mises stresses occurred at 0.91 s ± 0.01 s.

Overall PSE accumulation increased exponentially as friction co-efficient was increased and in all cases was very insensitive to the inclusion of FHRs (Figure 6.22C). Figure 6.23 illustrates how differences were observed in the accumulation of PSE throughout the cycle depending on whether FHRs were included. These results were not fully understood but it suggested that the inclusion of FHRs might become more significant in cases of with elevated friction despite the insensitvity of the overall PSE accumulation. Friction co-efficients sufficient enough for this to be significant were not expected to occur experimentally.

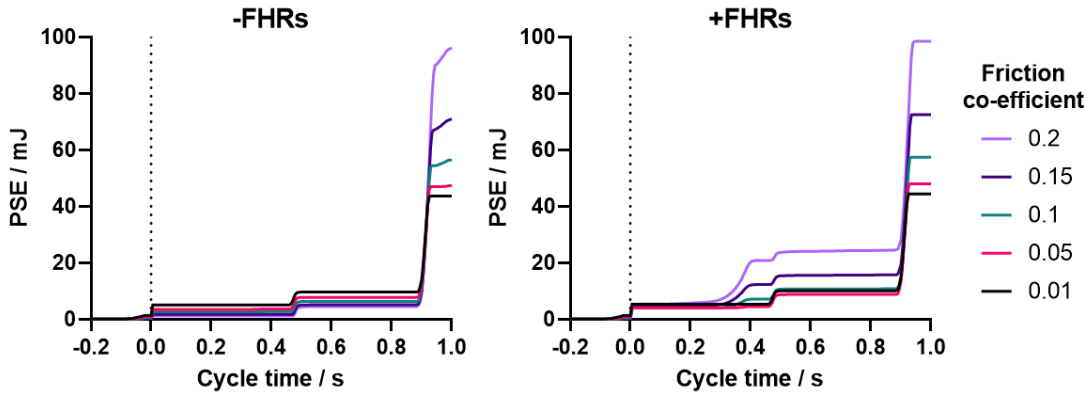

Figure 6.23. The accumulation of PSE with and without femoral head rotations (+/- FHRs) using different co-efficients of friction.

In summary, a review of literature suggested that for MoP THR bearings friction co-efficients were not expected to exceed 0.1 at any point of the gait cycle. Increasing the friction co-efficient from 0.01 to 0.1 sufficiently slowed down the dynamics of femoral head recentralisation causing elevated stresses to be sustained for milliseconds longer and slight increases to rim deformation and PSE accumulation. Critically, at these friction co-efficients the differences between model outputs with and without FHRs remained insubstantial. Therefore, previous suggestions in Section 6.4.6 to exclude FHRs from the model and reinstate liner symmetry to reduce computational costs remain valid.

6.5.3 Changes to rim morphology after edge loading

The FE model provided a prediction for the scale of deformation expected at the liner rim after one cycle. This was compared to the CMM measurement after 1 Mc of edge loading to provide insights into how the geometry of the liner rim may have been altered at the very beginning of the edge loading test. Visualisations of the changes in rim morphology showed that similar traits were observed (Figure 6.24). In both cases the curved rim became flattened resulting in a sharper transition between the bearing surface and the chamfer. The FE results supported the argument that geometric changes to the liner through deformation can occur over a relatively small number of cycles.

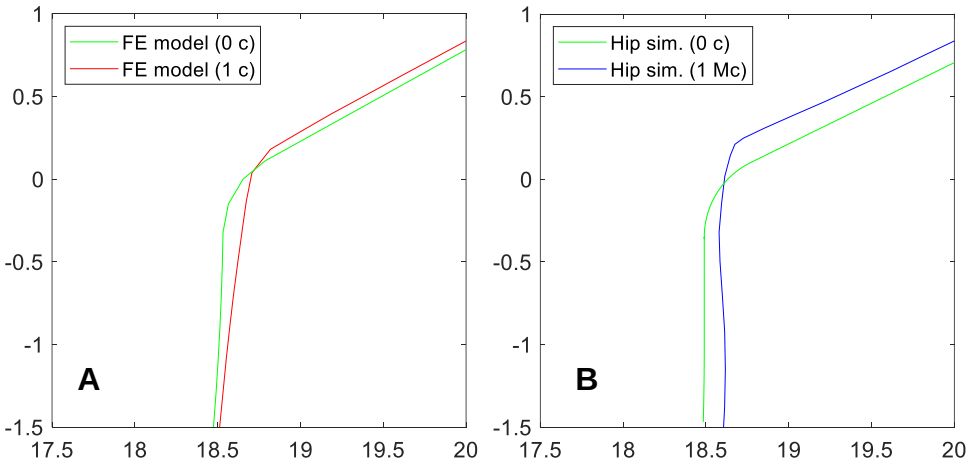

Figure 6.24. Changes to the rim morphology after edge loading in (A) the FE model (red) and (B) the experimental hip simulator study (Chapter 5, blue). Both are plotted against their respective pre-test geometries (green).

6.5.4 Damage mechanisms and the stress-strain environment

Inspection of the PSE accumulation in Figure 6.16A indicates that the majority of plastic strain was generated at heel strike with a much smaller amount of plastic strain generated toe-off. Heel strike was when the highest von Mises stresses were generated. They were located at the subsurface rim region which corresponds to the location of plastic strain accumulation as well (Figure 6.25).

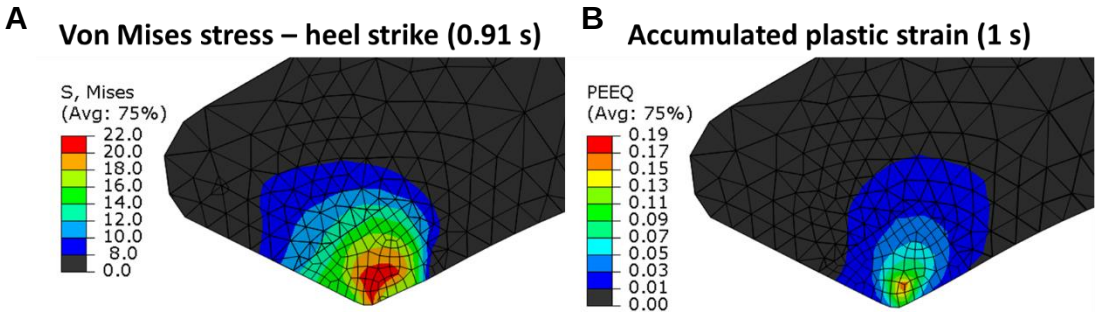

Figure 6.25. (A) A visualisation of the von Mises stresses at the superior rim during heel strike which exceeded the yield strength of Marathon UHMWPE. (B) Plastic strain accumulation (PEEQ) during one cycle of edge loading (> 1%).

The accumulation of plastic strain at the subsurface rim can be associated with the change in rim morphology. In the experimental hip simulator study once formed the changes to the liner rim were thought to remain stable over the remainder of the test. After 1 Mc of edge loading, 0.13 mm of wear and deformation was measured. This was equalled by the deformation predicted after one cycle in the FE model (0.13 mm). While suggesting these values are directly comparable is oversimplistic the FE model still supported the argument that localised rim deformation – similar to that seen experimentally – could occur in a very small number of cycles.

FE analysis also provided evidence that suggests the plastic strain could become stabilised here. During multi-cycle solutions where almost all of the plastic strain (99%) was accumulated within three load cycles (Etchels *et al.*, 2023) – a finding replicated exactly by the Script model during this research. However, it is important to recognise that the material models used in the FE models neglect visco-elastic-plastic behaviours that may contribute to a time-dependant material response.

The stabilisation of the rim morphology experimentally (at least up to 4 Mc) and plastic strains in the FE model provided reasonable confidence that

changes to the liner rim were not a damage mechanism that could be related to potential failure models of the polyethylene liner when subjected to edge loading. This analysis might have been different if earlier generations of UHMWPE were still being used. The presence of subsurface plastic strains could have placed the liner at risk of subsurface oxidation damage – resulting in whitening, loss of mechanical properties and subsequent vulnerability to fatiguing damage. However, in current generation polyethylenes, such as Marathon, that are more resistant to oxidation this damage mechanism was considered to be a minimal risk.

When considering the potential of other damage mechanisms, Figure 6.25 illustrated how plastic strains remained isolated in the subsurface rim region and von Mises stresses (which exceeded the material yield strength) were also not being transmitted through the liner thickness. Hence, for the conditions tested, the FE model does not predict that damage would occur at any other locations on the liner. Consequently, there were no further insights to be gained about potential damage mechanisms caused by edge loading.

6.6 Conclusions

In this Chapter, several new developments were made to an FE model of edge loading in THRs. A new material model designed to represent Marathon polyethylene generated a substantial difference to the predicted stress-strain outputs compared to the previous UHMWPE material model. Incorporating FHRs in the FE model had a very small effect on the FE outputs in cases over the range of friction values that were expected to occur experimentally. However, this development provides a necessary bridge to incorporating wear predictions into future dynamic models of THRs.

Collectively, the experimental hip simulator study (Chapter 5) and the FE modelling in this Chapter were unable to produce sufficient damage that might provide insights into the damage mechanisms that result from edge loading. The characterisation of the changes at the liner rim suggested that the localised deformation here would occur early and become stabilised. Future testing needs to incorporate methods of accelerating damage accumulation to provide insights into possible damage mechanisms and failure models. This research can utilise the development of the model script which enables cases of variable liner thickness to be generated for assessment.

Chapter 7 – Combined experimental and computational investigation into the effects of edge loading on thin polyethylene liners

7.1 Introduction

The evidence from the experimental hip simulator study and FE modelling in Chapter 5 and Chapter 6 suggested that a sufficiently thick liner that remained well supported liner under edge loading was at a relatively low risk of progressive damage accumulation that may lead to the failure of the liner. The localised plastic deformation characterised at the liner rim appeared to occur over a relatively small number of cycles and then became stabilised. In addition, there appeared to be no substantial transmission of stresses or strain through the liner.

To provide insights into the damage mechanisms and failure modes of polyethylene liners when subjected to edge loading it was necessary to use research methods which could accelerate damage accumulation. Clinical case studies identified the presence of thin and unsupported regions of polyethylene at the liner edge or locking mechanisms as being vulnerable to damage initiation when exposed to edge loading (Tower *et al.*, 2007; Blumenfeld *et al.*, 2011; Waewsawangwong and Goodman, 2012). Unsupported polyethylene may be introduced using liner designs which protrude above the acetabular shell (Figure 2.5) or through gaps in load support generated by locking mechanisms. By introducing these design features into the research methods it was hypothesised that different liner behaviours would be observed and the progression of damage mechanisms could be characterised.

As such, this Chapter aimed to investigate the effects of liner thickness and unsupported polyethylene on liner responses to edge loading using a combination of an experimental hip simulator study and FE modelling.

This aim was split into the following objectives:

- To perform an experimental hip simulator study with thin UHMWPE liners.
- To evaluate the differences between FE modelling of thin liners compared to the clinically relevant liner thickness.
- To examine the effect of introducing unsupported regions of UHMWPE in FE modelling by varying the boundary conditions of the liner fixation.

7.2 Experimental hip simulator study with thinner UHMWPE liners

7.2.1 Materials

Custom designed thin polyethylene liners were used in this study alongside clinically available femoral head and acetabular shell components. The liners were based on Pinnacle liner with a 28 mm/48 mm inner/outer bearing diameter that was redesigned to be thinned radially from the internal surface by 2 mm to generate a 32mm/48 mm liner (minimum thickness of 3 mm). The liners were made from Marathon UHMWPE – a HXLPE (50 kGy) with a re-melted heat treatment – using standard manufacturing processes. A taper lock mechanism anchors the liner within the shell and six anti-rotation tabs mated with scallops on the shell to provide rotational resistance. A locking barb which normally runs around the outer circumference of the liner was not included in the design. Figure 7.1 illustrates the difference in liner cross section of the liners used in this study compared to the previous hip simulator study in Chapter 5. The liners were press fit into a titanium alloy (Ti-6Al-4V) modular shell with a 48 mm outer diameter (Pinnacle, DePuy Synthes Joint Reconstruction, Leeds UK). The liners were articulated against 32 mm cobalt chromium heads (Articul/eze femoral heads, DePuy Synthes Joint Reconstruction, Leeds, UK).

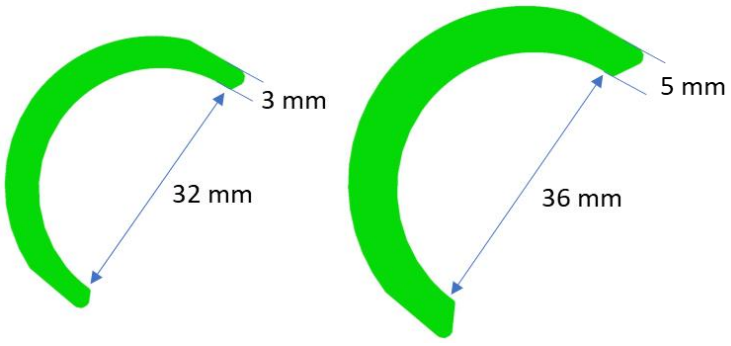

Figure 7.1. The relative cross section of the custom design thin liner used (A) compared to the clinically available liner used in Chapter 5 (B).

7.2.2 Methods

7.2.2.1 Simulator testing

A six station electromechanical Prosim hip simulator (Simulator Solutions, Stockport, UK) was used to assess the wear and damage of the thin THR

liners described in Section 7.2.1. Three liners were subjected to 3 Mc of edge loading conditions in the hip simulator. The stimulator testing methods used replicated the edge loading conditions described in Chapter 5 with the following exceptions:

The adduction/abduction rotation profile was translated by -10 degrees (-3° to -14°) to reduce risk of impingement between the spigot and UHMWPE liner that was observed in the previous hip simulator study.

Due to liner disassociation in the first 0.33 million cycles of the test, the liners were superglued into the shells and remained fixed in the shells for the remainder of the test.

7.2.2.2 Measurements

Geometric measurements of liners were made every 0.33 Mc using a Legex 322 CMM (Mitutoyo, Halifax, UK) to assess the geometric changes to the bearing surface and liner edge while the liners remained within their shells and simulator fixtures.

Microstructural measurements at the liner rim (Figure 7.2) were made using a Renishaw inVia Raman Microscope and Renishaw WiRE 5.2 software (Renishaw, Wotton-under-Edge, UK) to assess the changes to the surface microstructure after edge loading. Measurements were made at the end of the test once the liners were removed from shells (simulator fixtures did not fit into the Raman Microscope chamber). Group means (unworn versus worn) were compared without statistical analysis because the number of samples (N=3) was not sufficient to produce meaningful statistical analysis.

Figure 7.2. Microstructural measurements by Raman spectroscopy were taken at two locations: the unworn rim (WR) and worn rim (WR).

Full descriptions of these characterisation methods used were presented in Chapter 5. No gravimetric measurements were made because the liners were fixed to the shells for the majority of the test.

All three liners were also scanned using MicroCT to assess whether any cracking or subsurface damage was visible on the liners. The methods used were the same as described in Section 4.7. However, the optimisation of the procedure had been improved to generate clearer images. MicroCT scans were performed by Nagitha Wijayathunga, senior Research Fellow in the School of Mechanical Engineering at the University of Leeds.

7.2.3 Results

7.2.3.1 Test progression

Table 7.1 provides a summary of the timing of notable adverse events which occurred during the test. At the beginning of the test the liners were press fit into the shells in the same manner as the previous experimental hip simulator study (Chapter 5). At the first measurement point (0.33 Mc) all three liners had disassociated from their shells. Before resuming the liners were superglued into the shells to provide fixation. None of the liners were removed from their shell from this point until the conclusion of the test at 3 Mc. The first row of images in Figure 7.3 displays how the liners began this testing period (0.33 Mc to 3 Mc). Each liner was correctly seated and almost flush with top of the shell.

Table 7.1. The timepoints of adverse liner events in the study (see also Figure 7.3).

Measurement point	Details and observations
0.33 Mc	Liner dissociation had occurred in all three liners. They were subsequently superglued into the shells for the remained of the test.
1 Mc	Adverse liner deformation event had occurred in liner 1.
1.66 Mc	Adverse liner deformation events had occurred in liner 2 and liner 3.
3 Mc	There was no clear evidence of further substantial changes in liner position or seating up until the end of the test.

Figure 7.3. Photographs displaying the relative positioning of the liners within shells at measurement points from 0.6 Mc to the end of the test. Red rectangles highlight the incidences of adverse deformation events in each liners (see also Table 7.1). Either side of these events, no substantial changes in liner positioning or seating were visually identified. The edge loaded superior side of the liner is located on the left of the photos.

A second adverse deformation event was observed in all three liners later in the test (red rectangles, Figure 7.3). Despite differences in the timing of the adverse deformation events the liners exhibited very similar responses. Figure 7.3 clearly illustrates the shift in position that occurred. The liners

became pressed into the superior portion of the shell while on the inferior side the protrusion left a clear gap between the backside of the liner and the shell. Less apparent from the photographs was the large amount of deformation that accompanied the shift in position which was characterised by the CMM measurements. The superior portion of the liner remained largely in plane with the top of the shells. The inferior portion was evidently out of plane with the top of the shells as a result of the bending deformation.

7.2.3.2 Measurements of the geometric change by CMM

The scale of geometric deviation at the bearing surface and the liner edge was calculated as a mean of the three liners at 0.33 Mc intervals throughout the test by analysing the measured data compared to its pretest geometry. The effects of the two adverse events were focused on for this study because they resulted in substantial changes to the liner geometry compared to other timepoints.

Liner dissociation

The pretest geometric deviation measurements were all below the machining tolerance of +/- 0.05 mm. After 0.33 Mc, the first measurement point, all three liners had disassociated from the shells. The positive deviation of the bearing surface (surface displacement outwards) had increased to 0.10 mm (Figure 7.4A) which was isolated to the very upper regions of the bearing surface on the superior side where edge loading occurs (Figure 7.4B).

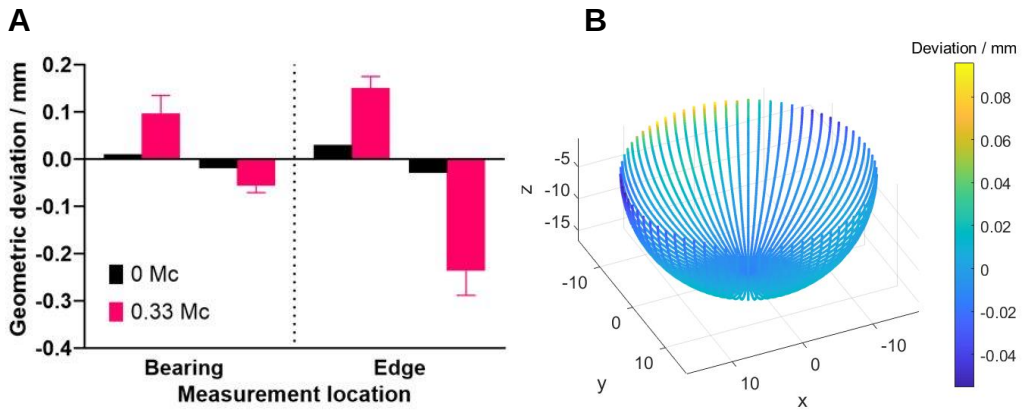

Figure 7.4. (A) Compares pretest geometric deviation measurements with those taken at 0.33 Mc after liner dissociation (mean and 95% confidence interval, N=3). (B) Surface deviation heatmap of the bearing surface at 0.33 Mc.

A more substantial negative deviation (surface displacement inwards) of -0.24 mm was measured at the liner edge (Figure 7.4A). Figure 7.5A and B display how the liner edge was bending upwards as a result of edge loading and its contact with the shell. Some local variation in the amount the edge was deformed was observed and related to the positioning of the anti-rotation scallops (Figure 7.5A). Measurement traces which corresponded to the scallops were deformed slightly less because the gaps left between the shell and the liner allowed some material relaxation here relative to the adject regions with contact between the shell and liner (Figure 7.5C and D). This effect occurred whether the scallops were mated with anti-rotation tabs or not. The red brackets used throughout Figure 7.5 illustrate the locations of the most deformed measurement traces and where they correspond to on the shell design.

Second adverse deformation events

A second adverse deformation event occurred in all three liners between the measurements of 0.66 Mc and 1.66 Mc (Table 7.1, Figure 7.3). After these events, the negative deviation (surface displacements inwards) measurements of the bearing surface and edge had substantially increased to -0.31 mm and -1.12 mm respectively (Figure 7.6A). In contrast, the positive deviations (surface displacements outwards) at the bearing surface and edge had decreased to 0.04 mm and 0.07 mm respectively. The yellow regions in Figure 7.6B illustrates how little of the bearing surface has remained near to its pretest position. For much of the bearing surface the negative deviations indicate how the bearing surface was being deformed inwards to a tighter curvature.

Figure 7.6C and D display how the effect was even more pronounced at the liner edge which had undergone severe deformation. A combination of liner repositioning and liner deformation was described in Section 7.2.3.1. Figure 7.6C illustrates of the contribution of deformation to the visuals in Figure 7.3. There was a clear contrast between deviations observed in the superior quadrant of the liner edge compared to the rest caused by the bending of the liner. In addition, the effect of the anti-rotations scallops on the deformation that was observed previously in Figure 7.5C was still apparent.

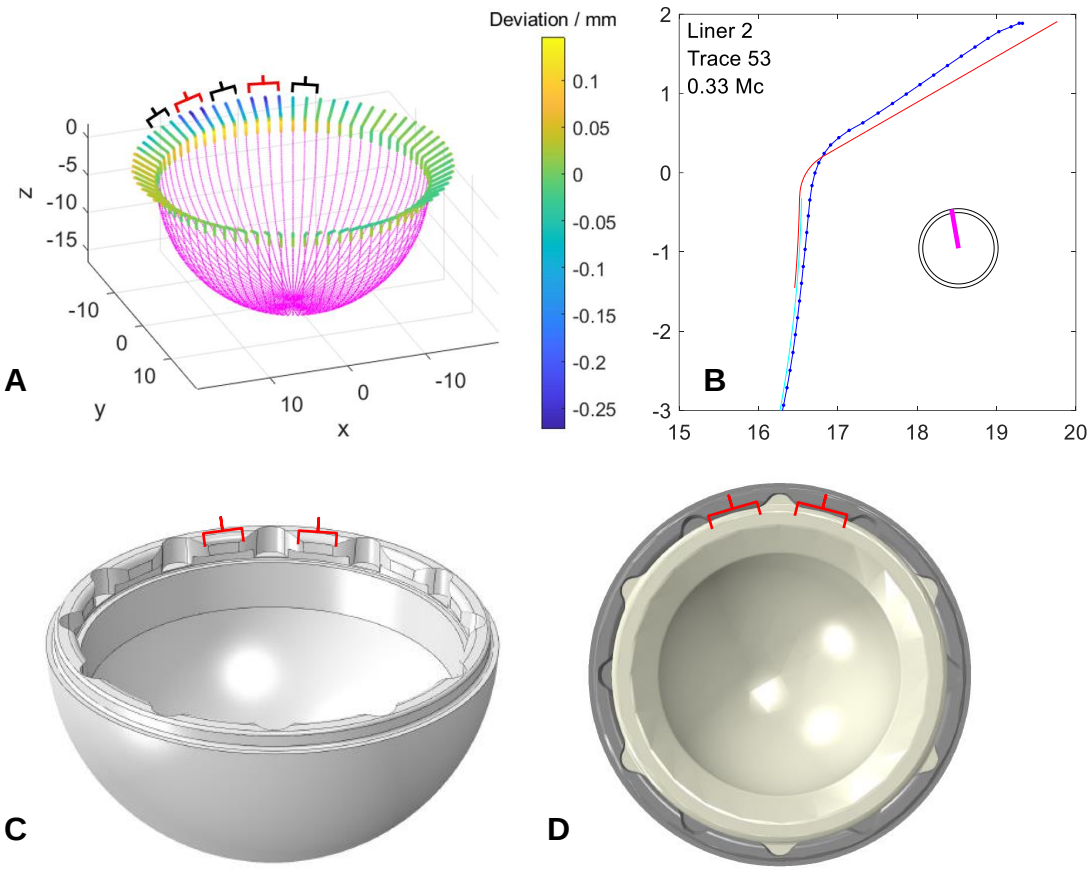

Figure 7.5. (A) Surface deviation heatmap of the liner edge at 0.33 Mc where the red brackets indicate the most deformed traces (see C-D). The pink data in is to provide a nominal liner shape to increase the clarity of the edge figures. (B) A two-dimensional profile plot of the maximum edge deformation. (C-D) The shell design has 12 anti-rotation scallops but only six are mated with anti-rotation tabs on the liners. The red brackets indicate the location of the most deformed traces as well as the location of plastic deformation on the liner backside (see also Figure 7.7 and Figure 7.9).

By the end of the test – a further 1.33Mc or 2 Mc depending on the liner – none of the mean geometric measurements had changed by more than +/- 0.05 mm from their post-adverse event timepoint (Figure 7.6A). During post-test visual inspections of liners the influence of the anti-rotations scallops on the plastic deformation was clear (Figure 7.6C). Plastic deformation was also evident on the backside of the liners (Figure 7.7) near to the top surface where the shell had pressed into the liner between anti-rotation scallops (as indicated in Figure 7.5).

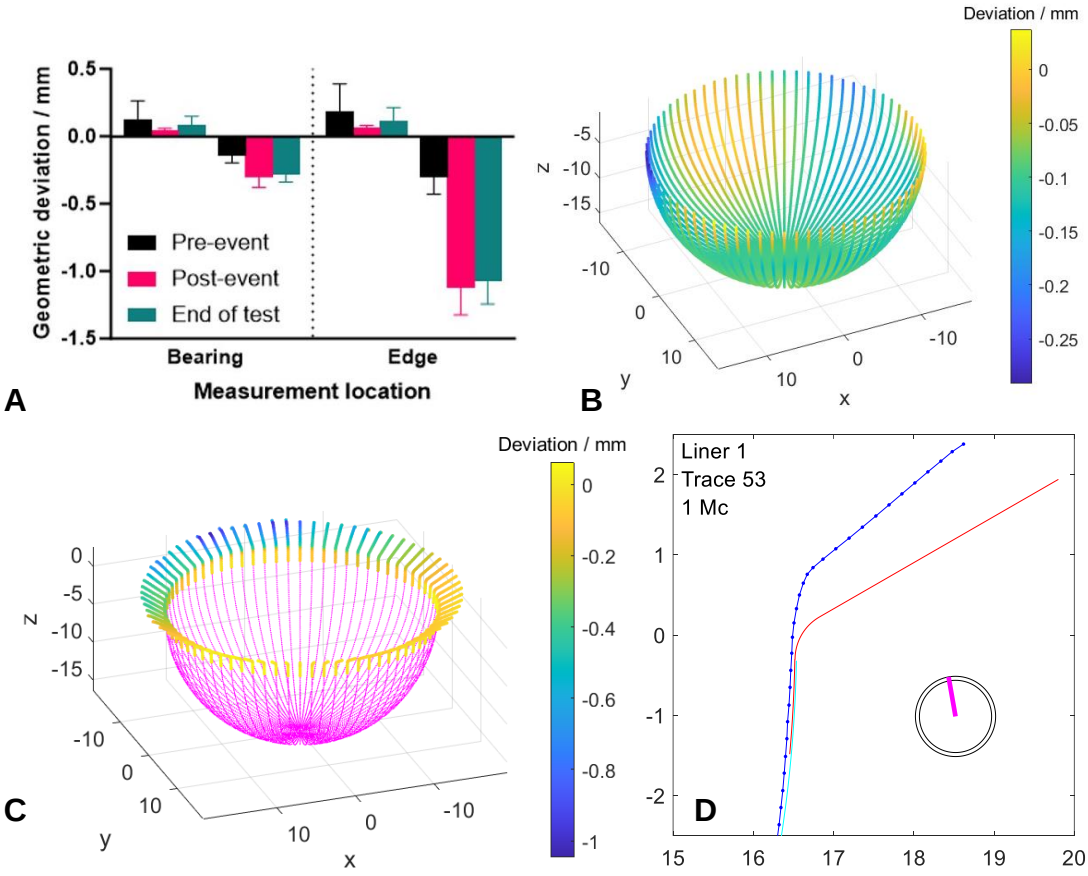

Figure 7.6. An adverse deformation event occurred in Liner 1 by 1 Mc. Similar events occurred in Liner 2 and 3 by 1.66 Mc. (A) Compares the pre-event geometric deviation measurements (mean and 95% confidence interval, N=3) with those taken post event (0.33 Mc later) and at the end of the test. (B-C) Surface deviation heatmap of the bearing surface and liner edge after the adverse deformation event. The pink data (C) is to provide a nominal liner shape to increase the clarity of the edge figure. (D) A two-dimensional profile plot of the edge deformation.

Figure 7.7. Signs of plastic deformation (not characterised by CMM) were visible on the backside of the liners (underlined in blue). The vertical blue line was positioned superiorly on the liner.

7.2.3.3 Microstructural measurements by Raman spectroscopy

Raman spectroscopy was used to assess the changes to the surface microstructure as a result of edge loading at the liner rim. Crystalline phase percentages were 6% lower at the edge loaded rim (46%) compared to the unloaded rim (52%). This was offset by increases to the amorphous and third phase percentages of 2% and 4% at the edge loaded rim (32% and 22%) compared to the unloaded rim (30% and 18%) respectively.

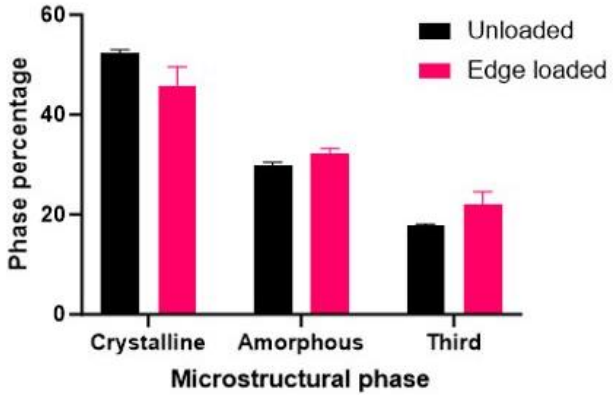

Figure 7.8. A comparison between the microstructural phase percentages at the unloaded rim (UR) and edge loaded rim (WR) determined by Raman spectroscopy.

7.2.4 MicroCT imaging

MicroCT was used to assess whether thin UHMWPE liners subjected to edge loading showed any signs of cracking or subsurface damage. Two of the three liners shows signs of potential crack formation (Figure 7.9). In both cases the damage was located on the backside surface of the liner, related to the positioning of anti-rotation scallops and being directed parallel to the liner's backside surface. In Liner 1 the damage had progressed more than Liner 2 and was visible at two locations. There was no damage visible on Liner 3 or at any other locations on Liners 1 and 2.

7.2.5 Experimental discussion

The custom design thin liners in this study were subjected to the same edge loading conditions as the previous hip simulator study which used a clinically available liner design and thickness (Chapter 5). Therefore, the effect of liner thickness on the liners' response to edge loading could be directly assessed. Reducing liner thickness in the present study increased the rate and scale of geometric changes as well as producing microstructural changes that

previously were not observed. For example, the magnitude of geometric change to the standard thickness liners after 4 Mc (edge deviation +0.36 mm) was exceeded by the thin liners after just 0.66 Mc (edge deviation -0.39 mm) and by 1.66 Mc the deviations in the thin liners were three times higher (edge deviation -1.16 mm). Thin liners had a considerably greater capacity to deform and also deformed at a faster rate.

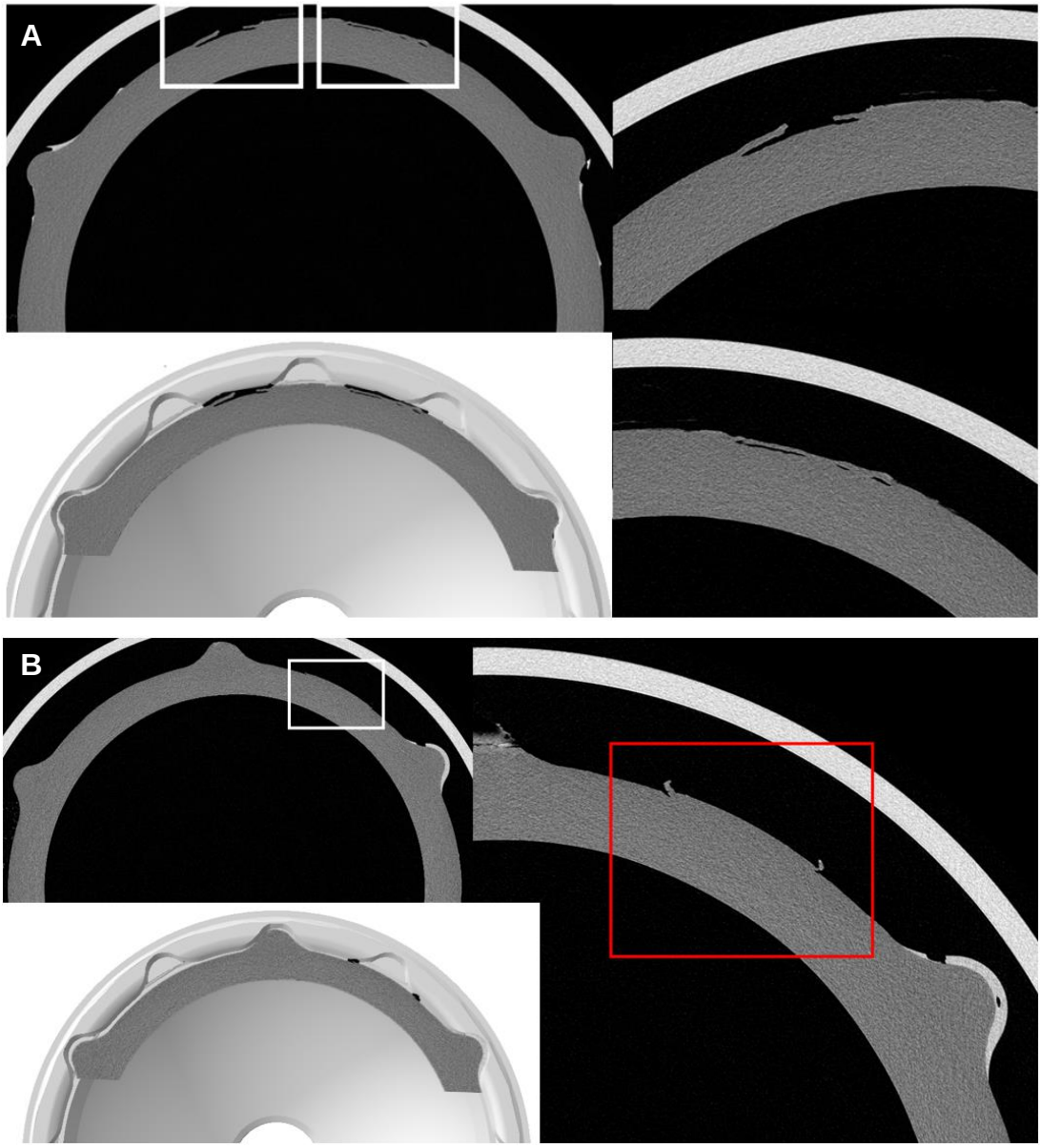

Figure 7.9. A MicroCT slice of the backside surface damage in (A) Liner 1 and (B) Liner 2. The slices were overlayed on a CAD model of the shell to correspond the locations of the damage with shell design features.

The geometric changes of standard thickness liners progressed in a distinctly linear manner. However, the changes to thin liners were dominated

by the test's two adverse events – both of which were related to disruption of the liner fixation. The first event led to complete dissociation of the liner within the shell with only isolated deformation to the liner edge. The second adverse event, after the liners had been superglued into the shell, repositioned the liner and was accompanied by a substantial amount of deformation. Given the timepoints of both events the contributions of wear to the geometric changes can be considered insignificant compared to the magnitudes of geometric change observed.

Measurements were made by Raman spectroscopy to assess whether edge loading cycles in a hip simulator resulted in any changes to the composition of the surface microstructure at the liner rim. In contrast to the standard thickness liners, in thin liners the crystalline phase percentages measured at the edge loaded rim were 6% lower than the unloaded rim. A crystalline to third phase transition was the predominant transition with some increase in amorphous phase contents as well. It suggested that the localised plastic deformation at the liner's surface was sufficient to disrupt some of the local crystalline ordering. Most of the chains retained some order by transitioning to the third phase.

The previous hip simulator study had tentatively suggested that the disruption of liner fixation was a possible damage mechanism of edge loading. The present study provided evidence that decreasing liner thickness increased the risk of liner fixation being disrupted when subjected to edge loading in a hip simulator. This was attributed to the increased capacity of the liner to undergo large scale deformation. As before, a significant limitation of the study was the removal of the locking barb that runs around the outer circumference of the liners. Therefore, two aspects of the liner design (thickness and locking mechanism) in this study were not directly applicable to currently used clinical practices.

Further than just disruption of the liner fixation, the MicroCT provided evidence of damage initiation on the backside of liners and generated by the design of the liner-shell interface. This finding suggested that reducing liner thickness increased the stress concentration generated by the interaction between the liner and the shell. The combination of increased deformability (into the scallop) and increased stress transmission created a situation where an edge in the shell's design was able to initiate cracking. There was no evidence of liner behaviour of this sort during the first hip simulator study presented in Chapter 5.

7.3 FE modelling investigations of edge loading with thin UHMWPE liners

7.3.1 Methods

A dynamic, deformable explicit finite element model of a total hip replacement under ISO 14242-4 edge loading was developed within the commercially available software package Abaqus (Abaqus Research v2022, Dassault Systémes, France). A full description of the model was provided in Chapter 6. The Script model used was an extension of the Baseline model which differed in the following ways:

The material model used was the extended elastic-plastic Marathon material model. ISO14242-4 femoral head rotations were included. The number of elements varied with the liner geometry (82 780 to 149 574) but the rim, contact and global seed sizes remained fixed at 0.2 mm, 1 mm and 3 mm respectively. There were no high aspect ratio elements behind the refined rim.

Study 1 – The effect of bearing diameter and liner thickness

The model script was used to create four cases with varied liner geometries to assess the effect of bearing diameter and rim thickness on the field outputs of the FE model (Table 7.2). The bearing diameters and rim thicknesses selected represented the two liner geometries tested in the experimental hip simulator (Case 1 and Case 4) as well as two intermediate cases which bridged the differences. Changes to peak von Mises, rim deformation and PSE were recorded and the stress and strain distributions within the liner were evaluated to provide insights into the effect of edge loading on a UHMWPE liner.

Table 7.2. The combinations of bearing diameter and rim thickness tested in the FE model. *Case 1 and Case 4 replicated the liners from the experimental hip simulator studies (Chapter 5 and Chapter 7).

Case number	Head diameter	Liner clearance	Rim thickness
1*	**36 mm**	**0.5 mm**	**5 mm**
2	36 mm	0.5 mm	3 mm
3	32 mm	0.5 mm	5 mm
4*	**32 mm**	**0.5 mm**	**3 mm**

Study 2 - Liner boundary condition sensitivity

The FE solutions presented so far fixed the whole of the backside surface of the liner to represent a well-seated neutral liner. This left approximately 1 mm of unsupported UHMWPE at the liner edge where the liner tapers away from the shell and hence would not be in contact. In the experimental hip simulator studies (Chapter 5 and Chapter 7) the repositioning of the liners observed would alter the contact conditions between the liner and shell. In addition, lateralised liner designs can purposefully leave up to around 4 mm of unsupported UHMWPE at the liner edge (DePuy Synthes, 2018).

Therefore, in this study, several cases with altered liner boundary conditions were explored to examine the effect unsupported polyethylene had on the liner's mechanical environment. This involved increasing the amount of unsupported UHMWPE at the liner edge from 1 mm up to a maximum of 4 mm as displayed in Figure 7.10. Each condition was tested on liners with a 36 mm bearing diameter and both thicknesses of 3 mm and 5 mm were tested to examine how the boundary conditions interacted with liner thickness. Changes to rim deformation and PSE were recorded and the stress-strain distributions within the liner were evaluated to provide insights into the effects of edge loading on a polyethylene liner.

Default boundary condition	*Unsupported liner edge cases*
Left 1 mm unsupported at the liner edge	Unsupported distance was increased to 1.5 mm, 2 mm, 3 mm and 4 mm respectively

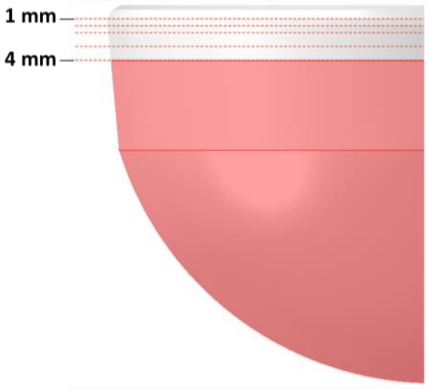

Figure 7.10. Diagram of the boundary conditions sensitivity cases. The 4 mm case (the least supported) is highlighted in red. The other cases are indicated by the dashed red lines.

7.3.2 Study 1 – The effect of bearing diameter and liner thickness

Four liner geometries were tested to evaluate the effect of bearing diameter and rim thickness on the field outputs of the FE model. The geometries were chosen to include the two liner geometries which have been tested in experimental hip simulator studies (Chapter 5 and Chapter 7). Table 7.3 reports the values for Case 1 (a replication of the liner studied in Chapter 6). To understand the effect bearing size and rim thickness the outputs from Case 2, 3 and 4 were displayed as a percentage change from Case 1 in Figure 7.11.

Table 7.3. Von Mises stress, rim deformation and PSE outputs for Case 1 (36 mm bearing diameter and 5 mm thickness). The percentage changes reported in Figure 7.11 are relative to these values.

FE output:	Von Mises stress	Rim deformation	PSE
Control liner: 36 mm bearing 5 mm thickness	21.9 MPa	0.125 mm	48 mJ

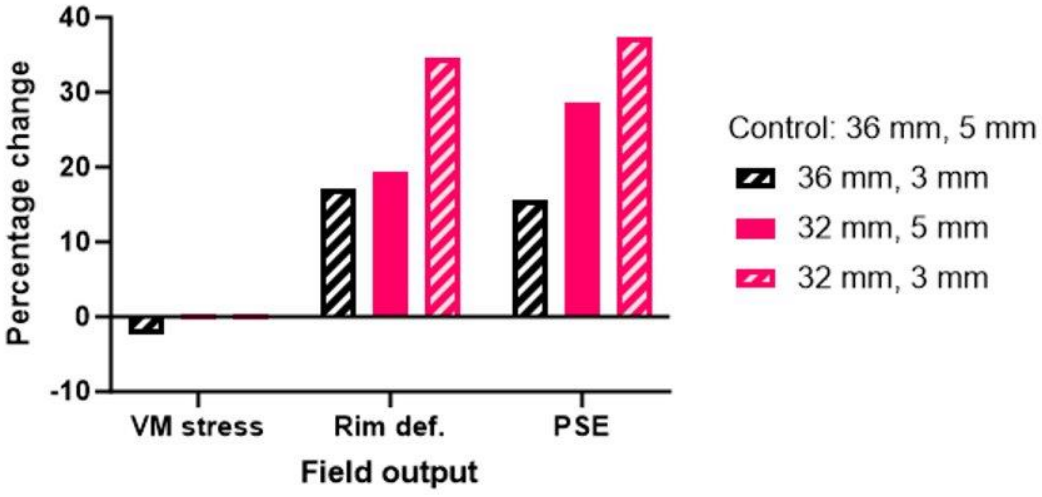

Figure 7.11. Percentage change of von Mises stress, rim deformation and PSE for Cases 2, 3 and 4 compared to the values obtained for Case 1 (which can be viewed in Table 7.3).

Changing the bearing diameter and rim thickness had very little effect on the peak stresses determined in the model. However, there were substantial changes to both rim deformation and PSE. This suggested that examination of peak von Mises stress was not an appropriate method of assessing the mechanical environment of the liners in response to edge loading. A more nuanced exploration of the distributions and durations of stresses was required.

A decrease in bearing diameter from 36 mm to 32 mm resulted in substantial increases in both rim deformation and PSE (Figure 7.11). Smaller bearing diameters have lower jumping distances. Therefore, comparatively the 4 mm component offset that was applied positioned the femoral head further out of the 32 mm liner than the 36 mm liner. As a consequence the recentralisation of the head at heel strike was slower which resulted in high loads at the rim and stresses which exceeded the material's yield strength were sustained for longer (peak stresses remained the same). Figure 7.12 illustrates the von Mises stresses 0.93 s into the load cycle (0.04 s after heel strike begins) and clearly demonstrates how higher stresses were sustained for longer the 32 mm bearing diameter liners. This finding highlights the importance of dynamic modelling for edge loading to incorporate inertial forces.

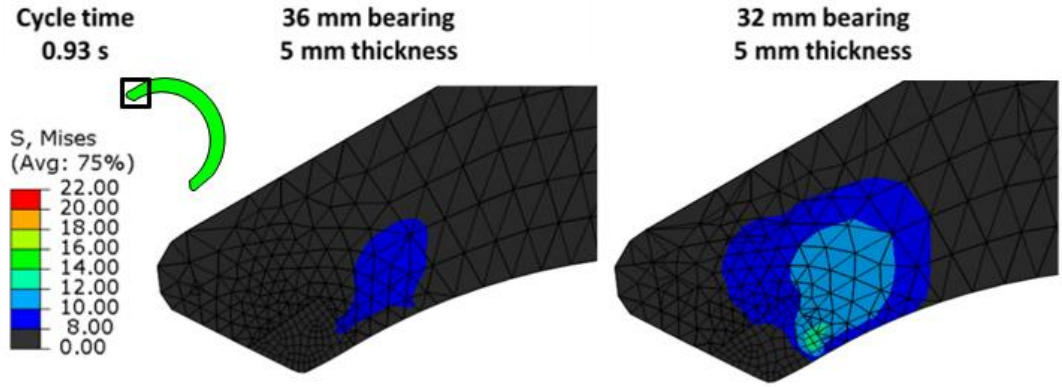

Figure 7.12. Von Mises stress distributions in 5 mm thickness liners with bearing diameters of 36 mm and 32 mm at 0.93 s (0.04 s after heel strike begins) showing how higher stresses were sustained for longer in the 32 mm bearing liner.

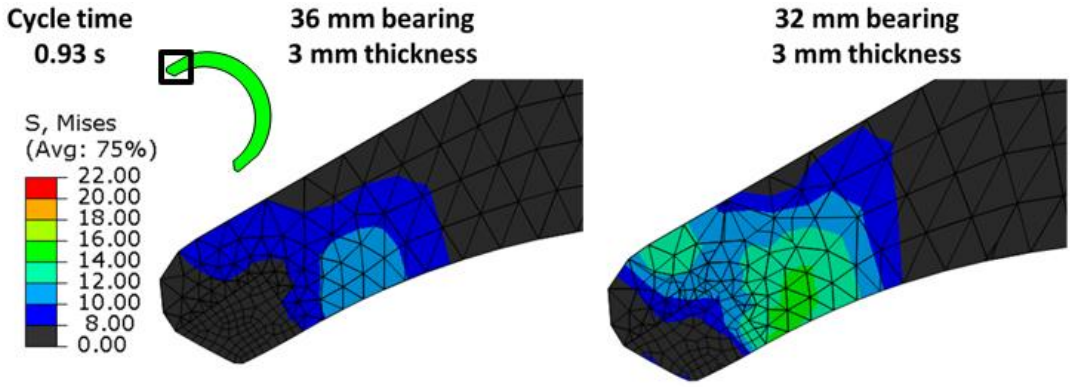

Figure 7.13. Von Mises stress distributions in 3 mm thickness liners with bearing diameters of 36 mm and 32 mm at 0.93 s (0.04 s after heel strike begins) showing how higher stresses were able to reach the backside of liners in 3 mm thickness liners.

Reducing liner thickness also increased both the liner deformation and PSE accumulation (Figure 7.11). The analysis identified that a key difference between liners with 5 mm and 3 mm thicknesses were the stresses and strains observed on the backside of the liner. To illustrate this Figure 7.13 displays directly comparable von Mises stress to the visualisations in Figure 7.12 but for the 3 mm thickness liners. In both cases stresses which exceed the yield stress of Marathon polyethylene were able to reach the backside of the liner where in 5 mm thickness liners they were not.

Similar findings were observed in the plastic strain distribution where in both of the 3 mm thickness liners the plastic strains extend to the backside of the liners (Figure 7.14). While the strains remain small a limitation of the model was its simplified the backside geometry. Design features which could potentially act as stress risers were omitted to reduce computational demands. In addition, the boundary conditions make the assumption that the liner is perfectly supported by the shell across the whole backside surface. However, shell design features can generate gaps in the load support – the effects of which have already been seen in the experimental hip simulator study in this Chapter.

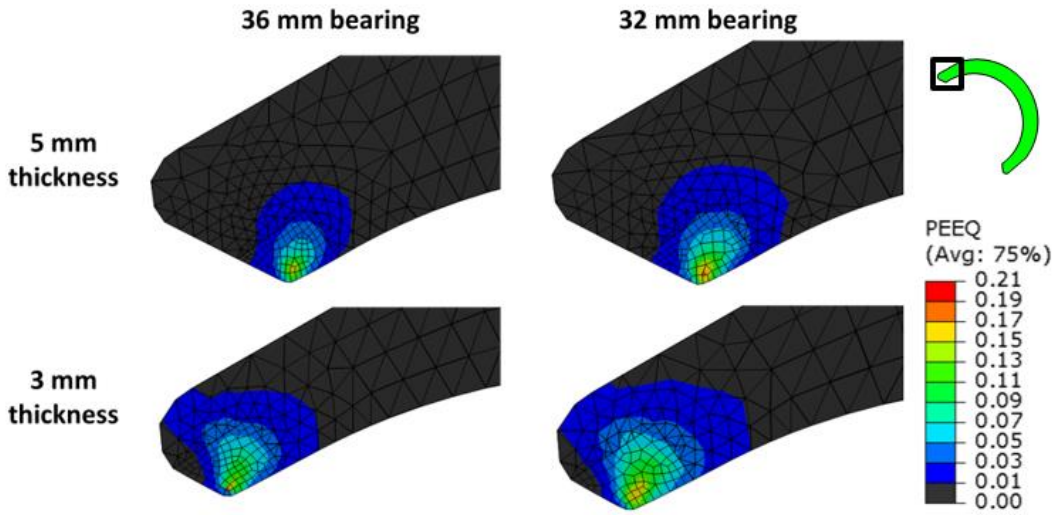

Figure 7.14. The plastic strain distributions (PEEQ > 1% strain) for the four liner geometry cases. 3 mm thickness liners displayed plastic strains at the backside of the liner while the 5 mm thickness liners do not.

7.3.3 Study 2 – Liner boundary condition sensitivity

Cases with varying amounts of unsupported UHMWPE at the liner edge were tested to assess how changes in load support in the liner affected its mechanical environment. In addition, the cases involved thicknesses of 3 mm and 5 mm to examine how the boundary conditions interacted with liner thickness. Figure 7.15 illustrates how there were positive linear relationships between the amount of unsupported polyethylene at the liner edge and both the rim deformation and PSE. However, there was a substantial difference in the gradient for liners with different thicknesses. The 3 mm liner was considerably more sensitive to the effects of being unsupported than 5 mm liners.

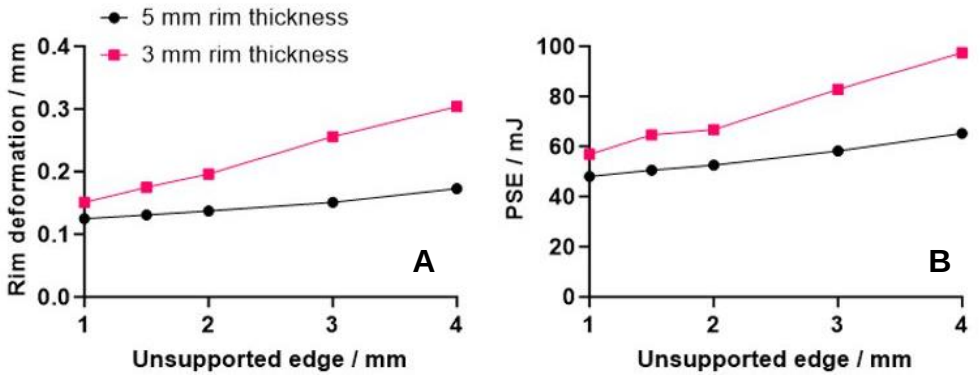

Figure 7.15. (A) Rim deformation and (B) PSE plotted as a function of the amount of unsupported UHMWPE at the liner edge for 5 mm and 3 mm liner thicknesses respectively.

The stress and strain distributions provide further insight into the damage mechanisms that may occur when polyethylene is left unsupported. Figure 7.16 displays the von Mises stress distributions for the most supported and least supported cases at liner thicknesses of 5 mm and 3 mm. When the 5 mm thickness liner was fully supported the stress was concentrated at the subsurface rim region. In contrast, when the load support was reduced the stresses were able to transmit vertically through the liner thickness to the backside surface. A similar effect was observed in the thinner liner but even greater stresses were able to reach the backside of the liner (in both cases).

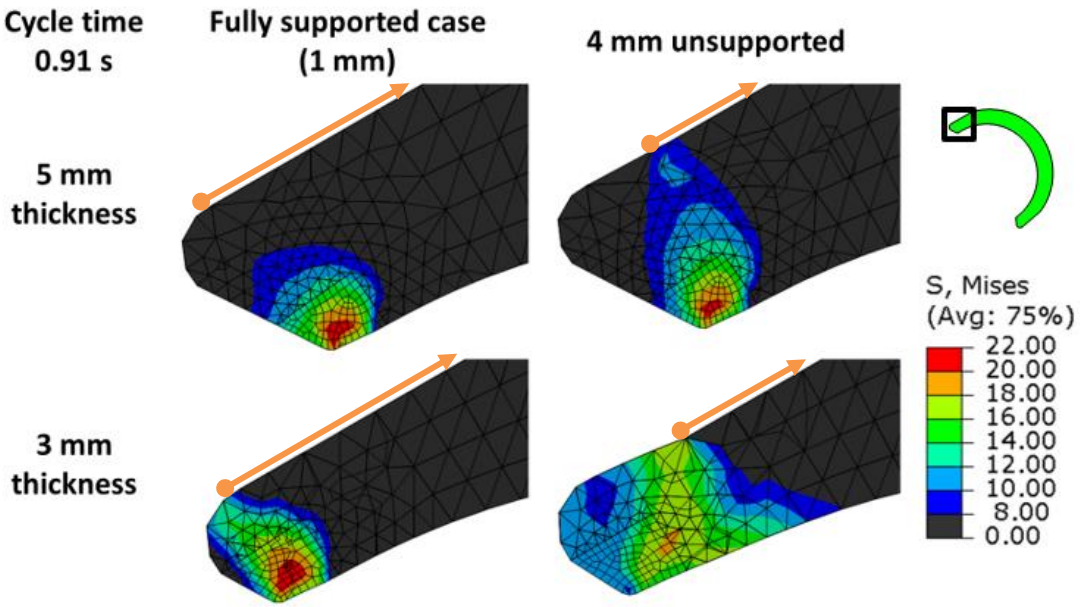

Figure 7.16. Von Mises stress distributions for the fully supported case and with 4 mm of polyethylene unsupported at 0.91 s (0.02 s after heel strike begins) comparing liner thicknesses of 5 mm and 3 mm. The orange arrows indicate where the liner was fixed (i.e. supported) by boundary conditions on the cross section.

These findings were also reflected in the distributions of plastic strain which had accumulated at the end of the load cycle displayed in Figure 7.17. When the 5 mm thickness liner was fully supported the plastic strain remains localised to the subsurface rim region. However, both reducing liner thickness and reducing the load support enabled plastic strains to reach the liner backside.

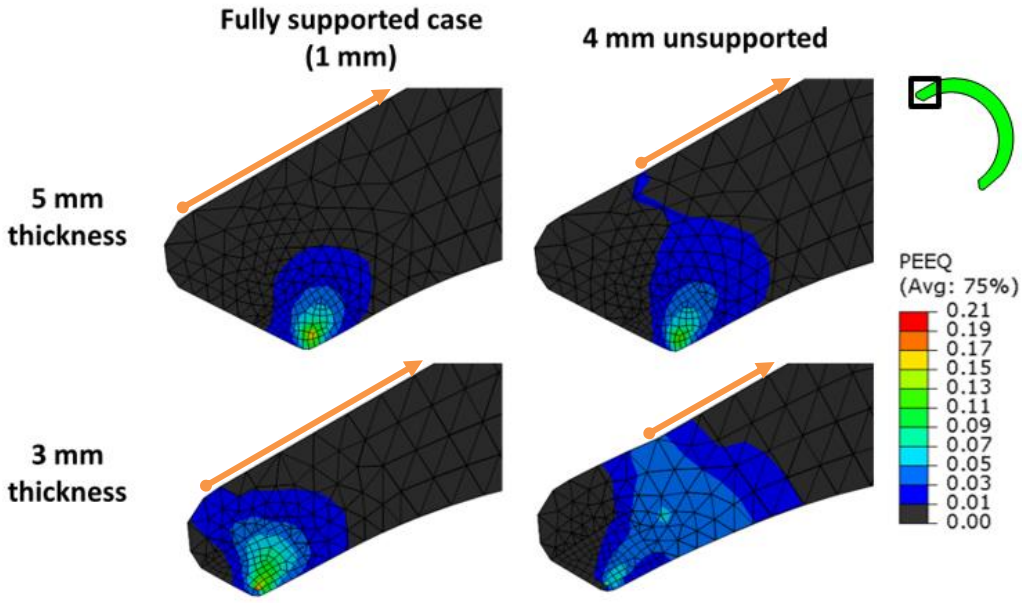

Figure 7.17. The plastic strain distributions (PEEQ > 1% strain) at the end of the cycle for the fully supported case and with 4 mm of polyethylene unsupported comparing liner thicknesses of 5 mm and 3 mm. The orange arrows indicate where the liner was fixed (i.e. supported) by boundary conditions on the cross section.

The results here demonstrated an unintuitive characteristic of the strain distributions – the presence of the strain concentration at the subsurface rim region actually indicated that the liner was well supported. Higher localised strains indicated that a small area of nodes was undergoing a relatively large amount of plastic flow. It was limited to a small area (while being higher in magnitude) because any material flow further into the material thickness was being prevented by sufficient load support. In the case of the 3 mm thickness liner with 4 mm of unsupported polyethylene (the case with the least load support) there were much lower peak strain values but the strain was spread across a much wider area and were being transmitted through the material thickness.

The simplified backside geometry and boundary conditions used in the FE model is a limitation which prevents deeper insights to be gained around the possible damage mechanisms at the backside of liners. The model identified that the transmission of stress and strain can transmit to the liner backside where they might interact with stress concentrating design features such as the liner locking mechanisms. However, the model stops short of being able to provide insights into what the consequences of this might be. This was reflected in the fact that the model was primarily designed to evaluate the

plastic strain accumulation at the subsurface rim region. It had not been designed to evaluate backside stress or strain. Therefore, further development of the model is necessary to meet this adjustment in aim.

7.4 Conclusions

This Chapter used a combination of an experimental hip simulator study and FE modelling to investigate the effects of liner thickness and unsupported polyethylene on the liner responses to edge loading. As a result of these design features several new liner behaviours were observed. In the hip simulator study the rate and scale of geometric changes drastically increased and microstructural changes were measured that were not observed when using thicker liners. The study suggested a link between reduced liner thickness and an increased risk of liner fixation disruption. However, it should be recognised that the liners tested did not possess a clinically relevant liner thickness or their complete locking mechanisms. In addition to disrupting liner fixation, MicroCT imaging provided evidence of damage at the liner backside caused by its interaction with the shell's design. FE modelling provided evidence that both reducing liner thickness or reducing load support increased the magnitude of stresses and strains transmitted to the backside of liners. This would potentially influence how the stress-strain field would interact with stress concentrating features of the liner or shell design.

Chapter 8 – Discussion and future work

8.1 Introduction

Over 1 million total hip replacements (THRs) are performed around the world every year (Ferguson *et al.*, 2018). It is a very successful intervention for late stage osteoarthritis (OA) and one of the most successful surgical interventions in healthcare (Colic and Sedmak, 2016). Clinical case studies demonstrate the possibility of liner fracture occurring in THRs. In all these cases, the liner failure was attributed to at least one aspect of the liner's design – such as thin or unsupported polyethylene – which initiated the damage when the liner experienced edge loading or impingement (Rowell *et al.*, 2007; Tower *et al.*, 2007; Moore *et al.*, 2008; Duffy *et al.*, 2009; Furmanski *et al.*, 2009; Waewsawangwong and Goodman, 2012; Ansari *et al.*, 2013). However, the fatigue and fracture mechanisms in polyethylene liners are still not well understood. At the time of writing, reliable prediction of these behaviours was still a developing area of research area even in simplified geometries and loading scenarios.

The aim of this research was to better understand the types of damage in polyethylene liners when subjected to physiologically relevant edge loading conditions and whether they may progress to liner failure. New methods of geometric and microstructural characterisation were developed to examine the changes to liners tested in an experimental hip simulator. This was augmented by the development of FE models of the liners to visualise the mechanical environment within the liners when subjected to edge loading. Investigations of a clinically available liner (5 mm thickness) did not produce signs of liner damage or potential failure after 4 million cycles (Mc) of edge loading in the hip simulator. However, when damage was accelerated by testing specially thinned liners (3 mm thickness) new behaviours were observed and more substantial insights about possible damage mechanisms were generated.

8.2 Advancements to experimental characterisation methods and finite element modelling of edge loading

8.2.1 Geometric analysis by CMM

The analysis methods developed in this research represents the most comprehensive evaluation of geometric changes at the liner edge at the time

of writing. Previous methods using CMM in the literature were limited by the area of the liner edge that was examined by only analysing either the chamfer region or using a small number of traces (Partridge, Buckley, *et al.*, 2018; Pryce, 2019). The development process performed here recognised that a combination of quantitative and qualitative analysis was required to gain the most insight into the geometric changes at the liner edge.

The overall progression of the geometric changes and the variability observed between liner specimens was provided by the quantitative measurements. The results indicated the importance of considering the variation within and between liners prior to testing given that the scale of the geometric changes for modern polyethylene materials can be similar to the variation from machining the liner (tens of microns). Hence a method was developed that produced a pretest profile of each liner individually to which the test data was compared to determine geometric deviation.

These quantitative measurements provided the context which underpinned the qualitative evaluations. The iterative two-dimensional in-profile visualisations of the liners provided an effective method of qualitatively assessing the localised changes to rim morphology. In Chapter 5, using these analysis tools it was found that during hip simulator testing polyethylene wear, global liner deformation and local liner deformations all contributed to the overall geometric change during edge loading. However, the localised deformation at the bearing surface rim occurred early in the test then remained largely stable. Hence the localised rim deformation was not thought to be a particular concern with regards to the potential of liner failure despite being the location of the peak plastic strains in the FE modelling. On the other hand, the use of thin polyethylene liners in Chapter 7 resulted in considerably larger deformations that placed the liner at more risk of liner fixation disruption and damage to the liner backside (discussed further in Section 8.3).

8.2.2 Microstructural analysis by Raman spectroscopy

The aim of the microstructural measurements by Raman spectroscopy was to evaluate whether microstructural transitions in the liner could be linked to the inception of microscopic damage. Previously, increased surface crystallinity after wear was found by some research groups using hip simulators (Bertoluzza *et al.*, 2000; Trommer *et al.*, 2015). However, other hip simulator studies found no significant changes to microstructural phases or chain alignment at the surface after wear (Affatato *et al.*, 2002; Taddei *et al.*, 2002; Taddei, Di Foggia and Affatato, 2011).

Through the development of the Raman spectroscopy method in Chapter 4, some significant weaknesses were identified in the existing literature which failed to acknowledge the importance of the decisions during curve fitting procedures when reporting methods. Increasing the transparency of the methods used and raw data sharing would both aid the ability to scrutinise future research and increase the robustness and generalisability of analysis tools.

In Chapter 7, a crystalline phase transition of 6% in the thinned liners was identified after being subjected to edge loading while in the clinical thickness liners (Chapter 5) no such transition was observed. This suggested that there was more potential for microstructural transitions to occur in thinner polyethylene specimens. These microstructural changes were only observed in liners for which large deformation were already apparent. Therefore, in its current form Raman spectroscopy was not considered to be generating insights that particularly extended the knowledge gained by other measurements and observations. The results also suggested that the processes of liner manufacture and machining (i.e. measurement location) were a more influential factor than loading or wear from the hip simulator.

With respect to the aims of the research, the method developed provides a strong foundation for microstructural evaluation of polyethylene. A key limitation was that measurements were taken on a very localised level – both spatially and in depth. The use of Confocal Raman spectroscopy was suggested to overcome this; it would enable measurements to be recorded at specific depths from the liner's surface (e.g. < 100 μm) that would be able to generate insights on microstructural changes with more clarity and certainty.

In addition to evaluating microstructural phases, Raman spectroscopy has also been used to examine changes in chain orientations. This (used alongside confocal Raman spectroscopy) would offer a promising route to generate relationships between Raman spectroscopy measurements to FE plastic strain outputs. This could possibly be through an experimental test with a simpler mechanical environment such as a Rockwell hardness test.

Despite these suggestions for the potential further development and use of the Raman spectroscopy technique, caution must be taken with presumptions that the formation of microscopic damage will progress to macroscopic cracking or failure. Evidence from literature suggests that the formation of microscopic damage at stress concentration will occur at sub-yield stresses (Furmanski *et al.*, 2009). These stresses were sufficiently low

to allow the presence of microscopic damage to be effectively assumed at the point of liner implantation. However, decades of clinical evidence of the rarity of liner fracture also suggests that the presence of microscopic damage is a poor predicter for macroscopic damage. Therefore, building a greater understanding of the stress-strain conditions which causes microscopic damage to progress to macroscale cracking should be considered a much greater priority for the future direction of this research. This particular research direction would be unlikely to utilise Raman spectroscopy.

8.2.3 Finite element modelling of edge loading

Finite element modelling was combined with the experimental hip simulator studies to visualise the mechanical environment of the liners under edge loading. The importance of using dynamic modelling for edge loading to incorporate inertial effects had previously been established using the baseline model for this research (Jahani *et al.*, 2021; Etchels *et al.*, 2023). This model incorporated the axial loading and medial-lateral separation of the femoral head during a gait cycle but there were no femoral rotations. To the author's knowledge femoral rotations had only previously been used in static models of THRs. A method of including femoral rotations was developed by controlling the head using the movement of three reference points.

In the low friction scenarios expected during THR articulation, the incorporation femoral rotations were shown to only have small effects on the kinematic and stress-strain outputs of the model. In addition, the model became more computationally expensive because the inclusion of femoral rotations was incompatible with the use of symmetry boundary conditions for the liner. Therefore, for purely stress-strain evaluations of UHMWPE liners subjected to edge loading it is recommended not to include femoral rotations and to utilise the symmetry boundary conditions on the liner. However, femoral rotations will be a vital component in developing future wear prediction models which require dynamic modelling such as the case of edge loading. At the time of writing, there were no published FE models which have predicted the increased wear rates observed experimentally using edge loading conditions.

8.3 Damage mechanisms and possible failure modes from edge loading

On the basis of this research there were two possible failure modes associated with edge loading. The first pertained to the failure of the liner locking mechanism. The clinical cases studies identified the liner locking mechanism as a prominent initiation site for damage and subsequent failure. Often it was where the thinnest regions of polyethylene were located. High inclination angles and subluxation events placed abnormal loads on the liner edge, including the locking mechanisms, leading to failure.

Both experimental hip simulator studies (Chapter 5 and Chapter 7) observed liner repositioning within the shell. It led to the inferior liner edge protruding from the shell. With the single motion pattern used in these tests this did not expose the liners to any further adverse effects. However, under more varied motion patterns (as would occur during activities of daily living) it would undoubtedly have increased the chances of impingement and subsequently the risk for liner damage or liner dissociation.

The repositioning in these studies was primarily attributed to the removal of the equatorial locking barb from the liner backside. The incomplete locking mechanisms during this testing was a limitation necessary to allow the removal of liners for gravimetric measurement. It was also thought the deformations of the liner on a global scale may have impaired the effectiveness of the taper locking system – particularly in the sub-clinical thickness liners leading to the early dissociation.

The second potential failure mode related to the cracking observed on the backside of the thin liners (Chapter 7). In all of the edge loaded liners, plastic deformation on the backside of the liners was visible. It was generated because of gaps the in the shell design which accommodate the anti-rotation tabs. The extra deformability of the thin polyethylene liners allowed them to be pressed further into these recess sufficiently for the metal edge of the recesses to initiate cracking on the liner backside.

If the test was to continue it was believed the cracking could progress in a manner similar to that observed in the clinical case studies. Firstly, by continuing to propagate equatorially (possibly until the next anti-rotation scallop) before propagating through the thickness of the liner and fracturing off a segment of the liner edge. The higher rigidity of the clinically available liners (due to material thickness) prevented these liners from pressing into the recess as much and less stress would be transmitted to the liner

backside. Therefore, the interaction with the metal edge feature of the shell was not severe enough to initiate damage.

8.4 Considerations for minimising the risk of polyethylene liner damage and failure

In 2022, HXLPE and AO-HXLPE liners were the primary material of choice for the acetabulum bearing surface of THRs (AJRR, 2022; Australian Orthopaedic Association, 2023). Irradiation crosslinking of UHMWPE was instrumental in increasing THR longevity by reducing polyethylene wear and wear-based failures compared to conventional UHMWPE liners. Previous research presented in Section 2.5 highlighted that chemical crosslinking (as well as re-melting) reduced the fatigue and fracture resistance of these materials compared with conventional UHMWPEs. Despite this, with modern THR constructs only around 1% of revisions were attributed specifically to the breakage of acetabular components (Australian Orthopaedic Association, 2023). This suggests the reductions in some material properties has not affected clinical performance and HXLPEs and AO-HXLPEs remain an excellent material choice for THR acetabular liners. The case studies of liner failure presented in Section 2.4.7 suggested that a confluence of factors contributed to these instances of liner failure. Typically, improper component positioning or seating exposed thin and unsupported regions of polyethylene to edge loading conditions leading to liner failure within five years of implantation.

The research presented in this Thesis compared the response of a clinically available liner (5 mm thick) to a custom made thin liner (3 mm thick) designed specifically to accelerate the progression of damage. After three million cycles of edge loading crack initiation at the liner backside was identified using MicroCT in two out of three thin liners, as reported in Chapter 7. The confluence of factors contributing to damage initiation was a thin polyethylene liner, an incomplete locking mechanism leading to the unintentional malpositioning of components during testing and the adverse edge loading scenario of the test. No signs of damage were observed in the 5 mm thick liners during equivalent testing presented in Chapter 5.

The results of these studies suggested that retaining sufficient polyethylene thickness could be considered as an overarching factor helping liners to be resilient against the effects of edge loading. This argument was supported

by previous case studies of liner failure reviewed in Section 2.4.7 which almost exclusively reported liner thicknesses of between 2 mm and 4 mm. In liners with thicknesses below 4 mm the effects of edge loading appear to become more severe and, therefore, should be fully considered during at the design phase and during surgical planning.

The hip simulator testing in this research subjected polyethylene liners with extremely high inclination angles to repeated component separation events during gait cycles. This experimental simulation represented an exceedingly non-optimal clinical scenario and placed elevated stresses on the edge of liners and the liner locking mechanism. The result was a malpositioning of the liners within their shell and the increased potential for damage initiation on the liner backside. Clinically, edge loading can also result from prosthetic impingement which has been associated with particularly low inclination angles and high anteversion angles (combined femoral and acetabular anteversion). Optimal positioning and seating of components with correctly balanced provides the best chance that the occurrence and severity of edge loading can be reduced.

The final factor in the confluence of conditions that generated damage to liners in Chapter 7 was the presence of stress rising design features. Cracking was initiated at the liner backside by the interface between the shell and liner. Gaps in the load support of the liner due to the locking mechanism design generated the stress concentration capable of initiating damage. The case studies of liner failure in Section 2.4.7 identified other mechanisms of stress concentration. Firstly, regions of unsupported polyethylene which protruded above the shell generated bending stresses in the liner when subjected to edge loading. Secondly, geometric features on the liner with small radii were able act initiation sites for cracking. Locking mechanisms and anti-rotational features will inevitably introduce stress risers into liner designs. When being combined with thin regions of polyethylene or in cases where the risk of edge loading is increased additional consideration should be given to the possible effects of stress risers during the design of THR components.

In summary, this research suggested that, within a simulated environment, a combination of multiple adverse factors were able to increase the risk of damage to polyethylene liners. By thoroughly understanding each contributing factor individually the risks associated with them can be mitigated against more effectively. This will help ensure that the benefits accrued from using component designs or surgical practices outweigh

potential risks compared with other options in order to meet each patient's specific needs.

8.5 Research limitations

The research established that under edge loading conditions the liner backside and the liner-shell interface were the critical areas of interest with regards to liner failure and fracture. However, the research which has supported this finding generally neglected the liner backside in its methodology or characterisation. This was ultimately the core limitation of the research.

In both hip simulator studies the liner locking mechanism used was incomplete through the removal of the equatorial locking barb from the liners. Therefore, the behaviour of the liners did not fully replicate the *in vivo* scenario within an *in vitro* environment. It can only be speculated that the inclusion of the locking barb would have helped the liner to retain its seating within the shell which may have made the liners more resilient to edge loading.

In the FE model the shell was omitted from the model entirely to reduce the computational demands. Therefore, the model was limited to the analysis of the stresses and strains being transmitted through the thickness of the liner. The model could not provide insights into stress-strain environment generated at the liner-shell interface. In addition, the optimisation of the model focused on the evaluation of plastic strains at the subsurface rim region. The changes at this region were subsequently determined not to be likely to progress to liner failure. In future work, the FE model of edge loading should be adapted to rectify both of these aspects to provide better insights into the stress strain environment at the liner backside.

8.6 Future work

If the research were to continue the first experimental hip simulator study would be to subject thin polyethylene liners (3 mm) which include the full locking mechanism design to 3 Mc of edge loading. This would provide stronger evidence on the links between edge loading and the disruption of liner fixation and or the occurrence of backside damage. MicroCT scanning

is well equipped to evaluate the generation of surface and subsurface cracking in the liners. However, the inability of being able to remove liners from fixtures would have to be navigated. CMM measurements of the liners every 0.33 million cycles would accompany characterisation by microCT at the end of the test.

This test would be complemented by developments to the FE model of edge loading to focus on the backside of the liner and the liner-shell interface. The first priority would involve including the complete backside liner geometry and a rigid shell part into the FE model. The mesh refinement at the liner rim would be de-prioritised and a more equal mesh distribution through the liner thickness would be used to improve the evaluation of stress and strain transmission.

Using this new FE model, analysis of the stress-strain environment can build on the current research. This thesis provided evidence that the locations of peak stresses and strains (at the sub-surface rim contact region) do not necessarily predict the generation of macroscopic damage or cracking in the liner. The inclusion of the liner-shell interface in the model will improve the validity of the stress-strain environment that may highlight vulnerable locations at the liner-shell interface.

The stress-strain analysis should be deepened by evaluating the locations and directions of nodal principle stress and strain components. The aim being to establish more precisely the conditions which not only generate macroscopic cracking but facilitate (or prevent) its propagation. In order to achieve these goals it might be necessary to examine the stress-strain environment of simple mechanical environments where crack opening is known to occur such as that of a compact tension specimen. This could seek to replicate experimental tests already present in the literature to understand how notch geometry alters the severity of the stress-strain environment.

An additional and separate direction for the FE model would be to incorporate a polyethylene wear algorithm into the geometry prediction of the articulating surfaces. At the time of writing, wear modelling of edge loading fails to predict the increased polyethylene wear observed experimentally. The inclusion of femoral head rotations in a dynamic model of edge loading provides an excellent foundation for this research direction. HXLPE and AO-HXLPE have dramatically reduced the prevalence of polyethylene wear and wear particle based failure modes; orthopaedic practices must ensure that

increased wear rates are not predicted for new construct designs. Therefore, wear modelling predictions under adverse loading conditions would be a vital component of preclinical testing. These models would improve *in vitro* testing planning and streamline testing towards the cases expected to be worst case scenarios.

Overall, the research methodologies developed and used in this thesis as well as the further developments suggested equip researchers with the tools needed to evaluate the risk of crack initiation and propagation in different THR constructs. This will enable problematic scenarios to be identified and help inform device design and surgical guidance to minimise the risk of fatigue failures and fractures of polyethylene liners in the future.

8.7 Conclusions

This research provides evidence that the backside of the liner and the shell-liner interface are the most critical areas for attention when evaluating liner failure associated with edge loading conditions. Edge loading can place abnormal loading onto the liner edge and liner locking mechanisms leading to failure or fracture. Appropriate component positioning and joint forces can minimise the occurrence of edge loading. Then ensuring that liners remain sufficiently thick and well supported will help them to remain more resilient to the effects of edge loading. Further research is required to better understand the precise stress-strain environments which increase the likelihood of crack initiation and propagation.

Appendices

Appendix 1 – Conference presentations and publication strategy

Conference presentations

Nicholas Cooper, Lee Etchels, Oscar O'dwyer Lancaster-Jones, Sophie Williams, Ruth Wilcox. Experimental and Computational Modelling Assessment of Edge Loaded Marathon Total Hip Replacement Liners. UHMWPE/PEEQ, Torino 2022. Poster presentation.

Nicholas Cooper, Lee Etchels, Oscar O'dwyer Lancaster-Jones, Sophie Williams, Ruth Wilcox. Experimental and Computational Modelling Assessment of Edge Loaded Total Hip Polyethylene Liners. ICORS, Edinburgh 2022. Podium presentation.

Nicholas Cooper, Lee Etchels, Oscar O'dwyer Lancaster-Jones, Sophie Williams, Ruth Wilcox. Experimental Characterization and Finite Element Modelling of Total Hip Replacement Liners under Edge Loading. ORS, Dallas 2023. Poster presentation.

Lee Etchels, **Nicholas Cooper**, Ruth Wilcox, Alison Jones. Pre-Clinical Edge Loading Testing of Hip Replacements: Do We Need to Incorporate Cup Version? ISTA, New York, 2023. Podium presentation (presenting author Lee Etchels).

Nicholas Cooper, Lee Etchels, Nagitha Wijayathunga Oscar O'dwyer Lancaster-Jones, Sophie Williams, Ruth Wilcox. Deformation and Damage Patterns of Thin Total Hip Replacement Liners Under Adverse Loading Conditions. ESB, Edinburgh 2024. Podium presentation.

Planned publications

Planned manuscript: ‘CMM analysis methodology for evaluating changes to the rim of polyethylene liners. To be submitted to the Proceedings of the Institution of Mechanical Engineers, Part H. The manuscript details the methods used to evaluate geometric changes to the liner edge as developed in Chapter 3.

Planned manuscript ‘Geometric analyses of the wear and deformation during edge loading of THRs using an experimental hip simulation and finite element modelling.’ Submitted to an appropriate journal. The results from the experimental hip simulator study (Chapter 5) will be compared to wear and deformation predictions from the FE model of edge loading. However, additional developments (as part of a research assistant role) will be made to the FE model of edge loading to incorporate a wear prediction into the geometric changes.

List of References

Abu-Amer, Y., Darwech, I. and Clohisy, J.C. (2007) ‘Aseptic loosening of total joint replacements: Mechanisms underlying osteolysis and potential therapies’, *Arthritis Research and Therapy*. BioMed Central, p. S6. Available at: https://doi.org/10.1186/ar2170.

Affatato, S. *et al.* (2002) ‘Effects of the sterilisation method on the wear of UHMWPE acetabular cups tested in a hip joint simulator’, *Biomaterials*, 23(6), pp. 1439–1446. Available at: https://doi.org/10.1016/S0142-9612(01)00265-4.

Affatato, S. *et al.* (2012) ‘In vitro wear performance of standard, crosslinked, and vitamin-E-blended UHMWPE’, *Journal of Biomedical Materials Research - Part A*, 100 A(3), pp. 554–560. Available at: https://doi.org/10.1002/jbm.a.33297.

AJRR (2022) ‘The Ninth Annual Report of the AJRR on Hip and Knee Arthroplasty’. Available at: https://connect.registryapps.net/hubfs/PDFs%20and%20PPTs/2022%20AJRR%20Annual%20Report.pdf (Accessed: 5 February 2024).

Al-Hajjar, M. *et al.* (2010) ‘Effect of cup inclination angle during microseparation and rim loading on the wear of BIOLOX® delta ceramic-on-ceramic total hip replacement’, *Journal of Biomedical Materials Research Part B: Applied Biomaterials*, 95B(2), pp. 263–268. Available at: https://doi.org/10.1002/JBM.B.31708.

Al-Hajjar, M., Fisher, J., Williams, S., *et al.* (2013) ‘Effect of femoral head size on the wear of metal on metal bearings in total hip replacements under adverse edge-loading conditions’, *Journal of Biomedical Materials Research Part B: Applied Biomaterials*, 101B(2), pp. 213–222. Available at: https://doi.org/10.1002/JBM.B.32824.

Al-Hajjar, M., Fisher, J., Tipper, J., *et al.* (2013) ‘Wear of 36-mm BIOLOX delta ceramic-on-ceramic bearing in total hip replacements under edge loading conditions’, *Proceedings of the Institution of Mechanical Engineers, Part H: Journal of Engineering in Medicine*, 227(5), pp. 535–542. Available at: https://doi.org/10.1177/0954411912474613/ASSET/IMAGES/LARGE/10.1177_0954411912474613-FIG6.JPEG.

Ali, M. *et al.* (2016) ‘Influence of hip joint simulator design and mechanics on the wear and creep of metal-on-polyethylene bearings’, *Proceedings of the*

Institution of Mechanical Engineers, Part H: Journal of Engineering in Medicine, 230(5), pp. 389–397. Available at: https://doi.org/10.1177/0954411915620454/ASSET/IMAGES/LARGE/10.1177_0954411915620454-FIG8.JPEG.

Ali, M. *et al.* (2023) 'Wear and deformation of metal-on-polyethylene hip bearings under edge loading conditions due to variations in component positioning', *Biotribology*, 33–34, p. 100238. Available at: https://doi.org/10.1016/j.biotri.2023.100238.

Alotta, G. *et al.* (2018) 'The finite element implementation of 3D fractional viscoelastic constitutive models', *Finite Elements in Analysis and Design*, 146, pp. 28–41. Available at: https://doi.org/10.1016/J.FINEL.2018.04.003.

Anil, U., Singh, V. and Schwarzkopf, R. (2022) 'Diagnosis and Detection of Subtle Aseptic Loosening in Total Hip Arthroplasty', *Journal of Arthroplasty*, 37(8), pp. 1494–1500. Available at: https://doi.org/10.1016/J.ARTH.2022.02.060.

Ansari, F. *et al.* (2013) 'Designing for Crosslinked UHMWPE Implants: Clinical Consequences of Stress Concentrations', in *Proceedings of the ASME 2013 Summer Bioengineering Conference*. Available at: https://asmedigitalcollection.asme.org/SBC/proceedings-pdf/SBC2013/55614/V01BT38A002/4206044/v01bt38a002-sbc2013-14301.pdf.

Ansari, F. *et al.* (2016) 'Notch fatigue of ultrahigh molecular weight polyethylene (UHMWPE) used in total joint replacements', *Journal of the Mechanical Behavior of Biomedical Materials*, 60, pp. 267–279. Available at: https://doi.org/10.1016/j.jmbbm.2016.02.014.

Arauz, P. *et al.* (2018) 'In-vivo 3-Dimensional gait symmetry analysis in patients with bilateral total hip arthroplasty', *Journal of Biomechanics*, 77, pp. 131–137. Available at: https://doi.org/10.1016/J.JBIOMECH.2018.07.013.

Ardestani, M.M., Amenábar Edwards, P.P. and Wimmer, M.A. (2017) 'Prediction of Polyethylene Wear Rates from Gait Biomechanics and Implant Positioning in Total Hip Replacement', *Clinical Orthopaedics and Related Research*, 475(8). Available at: https://doi.org/10.1007/s11999-017-5293-x.

Ast, M.P. *et al.* (2014) 'Fractures of a single design of highly cross-linked polyethylene acetabular liners: An analysis of voluntary reports to the united states food and drug administration', *Journal of Arthroplasty*, 29(6), pp. 1231–1235. Available at: https://doi.org/10.1016/j.arth.2013.12.022.

ASTM (2022) *D638-22 Standard Test Method for Tensile Properties of Plastics*. Available at: https://www.astm.org/d0638-22.html (Accessed: 22 February 2024).

Australian Orthopaedic Association (2023) *AOA National Joint Replacement Registry 2023*. Available at: https://doi.org/10.25310/YWQZ9375.

Baker, D.A., Bellare, A. and Pruitt, L. (2003) 'The effects of degree of crosslinking on the fatigue crack initiation and propagation resistance of orthopedic-grade polyethylene', *Journal of Biomedical Materials Research Part A*, 66A(1), pp. 146–154. Available at: https://doi.org/10.1002/jbm.a.10606.

Baker, P. *et al.* (2013) 'Center and surgeon volume influence the revision rate following unicondylar knee replacement an analysis of 23,400 medial cemented unicondylar knee replacements', *Journal of Bone and Joint Surgery - Series A*, 95(8), pp. 702–709. Available at: https://doi.org/10.2106/JBJS.L.00520.

Barbour, P.S.M., Barton, D.C. and Fisher, J. (1995) 'The influence of contact stress on the wear of UHMWPE for total replacement hip prostheses', *Wear*, 181–183, pp. 250–257. Available at: https://doi.org/10.1016/0043-1648(95)90031-4.

Barrett, M.O., Van Citters, D.W. and Hamilton, W.G. (2011) 'Mechanical Failure of Marathon Cross-Linked Polyethylene Acetabular Liner After Total Hip Arthroplasty', *American Journal of Orthopedics (Belle Mead NJ)* [Preprint]. Available at: www.amjorthopedics.com (Accessed: 18 July 2023).

Barron, D. *et al.* (2008) 'Crystal ageing in irradiated ultra high molecular weight polyethylene', *Journal of Materials Science: Materials in Medicine*, 19(6), pp. 2293–2299. Available at: https://doi.org/10.1007/s10856-007-3333-x.

Barron, D. and Birkinshaw, C. (2008) 'Ultra-high molecular weight polyethylene – Evidence for a three-phase morphology', *Polymer*, 49(13–14), pp. 3111–3115. Available at: https://doi.org/10.1016/j.polymer.2008.05.004.

Bates, M.D. and Mauerhan, D.R. (2015) 'Early Fracture of a Vitamin-E-Infused, Highly Cross-Linked Polyethylene Liner After Total Hip Arthroplasty', *JBJS Case Connector*, 5(3), p. e65. Available at: https://doi.org/10.2106/JBJS.CC.N.00157.

Bayliss, L.E. *et al.* (2017) ‘The effect of patient age at intervention on risk of implant revision after total replacement of the hip or knee: a population-based cohort study’, *The Lancet* [Preprint]. Available at: https://doi.org/10.1016/S0140-6736(17)30059-4.

Beecher, B. *et al.* (2014) ‘Material Properties of a Highly Anteverted Vitamin E-Stabilized Polyethylene Liner After Sixteen Months In Vivo’, *JBJS Case Connector*, 4(3), p. e57. Available at: https://doi.org/10.2106/JBJS.CC.M.00134.

Berend, K.R. *et al.* (2016) ‘Risk of Periprosthetic Fractures With Direct Anterior Primary Total Hip Arthroplasty’, *Journal of Arthroplasty*, 31(10), pp. 2295–2298. Available at: https://doi.org/10.1016/j.arth.2016.03.007.

Bergmann, K. and Nawotki, K. (1967) ‘Eine neue Interpretation der Breitlinien-Kernresonanzspektren von linearem Polyäthylen’, *Kolloid-Zeitschrift & Zeitschrift für Polymere*, 219(2), pp. 132–144. Available at: https://doi.org/10.1007/BF02086201/METRICS.

Berry, D.J. *et al.* (1994) ‘Catastrophic failure of the polyethylene liner of uncemented acetabular components’, *Journal of Bone and Joint Surgery - Series B*, 76(4), pp. 575–578. Available at: https://doi.org/10.1302/0301-620X.76B4.8027143/LETTERTOEDITOR.

Bertoluzza, A. *et al.* (2000) ‘Micro-Raman spectroscopy for the crystallinity characterization of UHMWPE hip cups run on joint simulators’, *Journal of Molecular Structure*, 521(1–3), pp. 89–95. Available at: https://doi.org/10.1016/S0022-2860(99)00427-5.

Bevill, S.L. *et al.* (2005) ‘Finite element simulation of early creep and wear in total hip arthroplasty’, *Journal of Biomechanics*, 38(12), pp. 2365–2374. Available at: https://doi.org/10.1016/j.jbiomech.2004.10.022.

Blumenfeld, T.J. *et al.* (2011) ‘Fracture of a Cross-Linked Polyethylene Liner’, *The Journal of Arthroplasty*, 26(4), pp. 666.e5-666.e8. Available at: https://doi.org/10.1016/j.arth.2010.07.009.

Board, T. (2020) ‘Philosophy of uncemented stems’, in *The Leeds Orthopaedic Biomechanics course*.

Bowden, A.E. and Bergström, J. (2016) *Computer Modeling and Simulation of UHMWPE*. Third Edit, *UHMWPE Biomaterials Handbook*. Third Edit. Elsevier Inc. Available at: https://doi.org/10.1016/B978-0-323-35401-1/00039-9.

Bowsher, J.G. *et al.* (2008) '"Severe" wear challenge to 36 mm mechanically enhanced highly crosslinked polyethylene hip liners', *Journal of Biomedical Materials Research - Part B Applied Biomaterials*, 86(1), pp. 253–263. Available at: https://doi.org/10.1002/JBM.B.31013.

Bowsher, J.G. and Shelton, J.C. (2001) 'A hip simulator study of the influence of patient activity level on the wear of crosslinked polyethylene under smooth and roughened femoral conditions', *Wear*, 250(1–12), pp. 167–179. Available at: https://doi.org/10.1016/S0043-1648(01)00619-6.

Bozic, K.J. *et al.* (2015) 'Comparative Epidemiology of Revision Arthroplasty: Failed THA Poses Greater Clinical and Economic Burdens Than Failed TKA', *Clinical Orthopaedics and Related Research*® [Preprint]. Available at: https://doi.org/10.1007/s11999-014-4078-8.

Bracco, P. *et al.* (2007) 'Stabilisation of ultra-high molecular weight polyethylene with Vitamin E', *Polymer Degradation and Stability*, 92(12), pp. 2155–2162. Available at: https://doi.org/10.1016/j.polymdegradstab.2007.02.023.

Bracco, P. *et al.* (2017) 'Ultra-High Molecular Weight Polyethylene: Influence of the Chemical, Physical and Mechanical Properties on the Wear Behavior. A Review', *Materials*, 10(7), p. 791. Available at: https://doi.org/10.3390/ma10070791.

Brockett, C. *et al.* (2007) 'Friction of total hip replacements with different bearings and loading conditions', *Journal of Biomedical Materials Research - Part B Applied Biomaterials*, 81(2), pp. 508–515. Available at: https://doi.org/10.1002/JBM.B.30691.

Brown, T.D. and Callaghan, J.J. (2008) '(ii) Impingement in total hip replacement: mechanisms and consequences', *Current Orthopaedics*, 22(6), pp. 376–391. Available at: https://doi.org/10.1016/j.cuor.2008.10.009.

Callaghan, J.J. *et al.* (2003) 'Clinical biomechanics of wear in total hip arthroplasty.', *The Iowa orthopaedic journal*, 23, pp. 1–12. Available at: http://www.ncbi.nlm.nih.gov/pubmed/14575243 (Accessed: 3 August 2023).

Charnley, J. (1961) 'Arthroplasty Of The Hip A New Operation', *The Lancet*, 277(7187), pp. 1129–1132. Available at: https://doi.org/10.1016/S0140-6736(61)92063-3.

Choudhury, D. *et al.* (2018) 'Mechanical wear and oxidative degradation analysis of retrieved ultra high molecular weight polyethylene acetabular

cups', *Journal of the Mechanical Behavior of Biomedical Materials*, 79, pp. 314–323. Available at: https://doi.org/10.1016/j.jmbbm.2018.01.003.

Colic, K. and Sedmak, A. (2016) 'The current approach to research and design of the artificial hip prosthesis: a review', *Rheumatology and Orthopedic Medicine*, 1(1), pp. 1–7. Available at: https://doi.org/10.15761/rom.1000106.

Collier, J.P. *et al.* (2003) 'Comparison of Cross-Linked Polyethylene Materials for Orthopaedic Applications', *CLINICAL ORTHOPAEDICS AND RELATED RESEARCH Number*, 414, pp. 289–304. Available at: https://doi.org/10.1097/01.blo.0000073343.50837.03.

Conaghan, P.G. *et al.* (2015) 'Impact and therapy of osteoarthritis: the Arthritis Care OA Nation 2012 survey', *Clinical Rheumatology*, 34(9), pp. 1581–1588. Available at: https://doi.org/10.1007/s10067-014-2692-1.

Crowninshield, R.D. *et al.* (2004) 'Biomechanics of large femoral heads: What they do and don't do', *Clinical Orthopaedics and Related Research*, 429, pp. 102–107. Available at: https://doi.org/10.1097/01.BLO.0000150117.42360.F9.

Dargel, J. *et al.* (2014) 'Dislocation Following Total Hip Replacement', *Deutsches Ärzteblatt international*, 111, pp. 884–890. Available at: https://doi.org/10.3238/arztebl.2014.0884.

Dassault Systèmes (2016) 'Abaqus 2016 Online Documentation'.

DePuy Synthes (2018) 'PINNACLE ® Hip Solutions - Surgical Technique'.

D'lima, D.D., Chen, P.C. and Colwell, C.W. (2001) 'Optimizing Acetabular Component Position to Minimize Impingement and Reduce Contact Stress'.

Dobner, J. and Kaser, S. (2018) 'Body mass index and the risk of infection - from underweight to obesity', *Clinical Microbiology and Infection*. Elsevier B.V., pp. 24–28. Available at: https://doi.org/10.1016/j.cmi.2017.02.013.

Duffy, G.P. *et al.* (2009) 'Fracture of a Cross-Linked Polyethylene Liner Due to Impingement', *The Journal of Arthroplasty*, 24(1), pp. 158.e15-158.e19. Available at: https://doi.org/10.1016/j.arth.2007.12.020.

Dumbleton, J.H., Manley, M.T. and Edidin, A.A. (2002) 'A literature review of the association between wear rate and osteolysis in total hip arthroplasty', *Journal of Arthroplasty*, 17(5), pp. 649–661. Available at: https://doi.org/10.1054/arth.2002.33664.

Essner, A. *et al.* (2005) ‘Acetabular liner functional fatigue performance of crosslinked UHMWPE’, in *Transactions of the 51st Annual Meeting of the Orthopaedic Research Society*.

Etchels, L. *et al.* (2019) ‘Computationally efficient modelling of hip replacement separation due to small mismatches in component centres of rotation’, *Journal of Biomechanics*, 95, p. 109296. Available at: https://doi.org/10.1016/j.jbiomech.2019.07.040.

Etchels, L. *et al.* (2023) ‘Dynamic finite element analysis of hip replacement edge loading: Balancing precision and run time in a challenging model’, *Journal of the Mechanical Behavior of Biomedical Materials*, 143, p. 105865. Available at: https://doi.org/10.1016/j.jmbbm.2023.105865.

Evans, J.T. *et al.* (2019) ‘How long does a hip replacement last? A systematic review and meta-analysis of case series and national registry reports with more than 15 years of follow-up’, *Lancet (London, England)*, 393(10172), pp. 647–654. Available at: https://doi.org/10.1016/S0140-6736(18)31665-9.

Ezquerra, L. *et al.* (2017) ‘Range of Movement for Impingement and Dislocation Avoidance in Total Hip Replacement Predicted by Finite Element Model’, *Journal of Medical and Biological Engineering*, 37(1), pp. 26–34. Available at: https://doi.org/10.1007/S40846-016-0210-4/FIGURES/7.

Fagnano, C. *et al.* (2001) ‘A study on solid-state drawn fibers of polyethylene by confocal Raman microspectrometry: evaluation of the orientation profiles of amorphous and crystalline phases across the fiber section’, *Polymer*, 42(13), pp. 5871–5883. Available at: https://doi.org/10.1016/S0032-3861(00)00913-7.

FDA (2019) *Characterization of Ultrahigh Molecular Weight Polyethylene (UHMWPE) Used in Orthopedic Devices*, *Guidance for Industry and Food and Drug Administration Staff*.

Ferguson, R.J. *et al.* (2018) ‘Hip replacement’, *The Lancet*. Lancet Publishing Group, pp. 1662–1671. Available at: https://doi.org/10.1016/S0140-6736(18)31777-X.

Fialho, J.C. *et al.* (2007) ‘Computational hip joint simulator for wear and heat generation’, *Journal of Biomechanics*, 40(11), pp. 2358–2366. Available at: https://doi.org/10.1016/j.jbiomech.2006.12.005.

Fox, A.J.S., Bedi, A. and Rodeo, S.A. (2009) ‘The Basic Science of Articular Cartilage: Structure, Composition, and Function’. Available at: https://doi.org/10.1177/1941738109350438.

Furmanski, J. *et al.* (2009) ‘Clinical fracture of cross-linked UHMWPE acetabular liners’, *Biomaterials*, 30(29), pp. 5572–5582. Available at: https://doi.org/10.1016/j.biomaterials.2009.07.013.

Furmanski, J. and Pruitt, L.A. (2007) ‘Peak stress intensity dictates fatigue crack propagation in UHMWPE’, *Polymer*, 48(12), pp. 3512–3519. Available at: https://doi.org/10.1016/J.POLYMER.2007.04.006.

Furmanski, J. and Pruitt, L.A. (2018) ‘Static mode fatigue crack propagation and generalized stress intensity correlation for fatigue–brittle polymers’, *International Journal of Fracture*, 210(1–2), pp. 213–221. Available at: https://doi.org/10.1007/s10704-018-0267-x.

Galetz, M.C. and Glatzel, U. (2010) ‘Molecular Deformation Mechanisms in UHMWPE During Tribological Loading in Artificial Joints’, *Tribology Letters*, 38(1), pp. 1–13. Available at: https://doi.org/10.1007/s11249-009-9563-y.

Gao, Y., Zhang, J. and Jin, Z. (2015) ‘Explicit finite element modeling of kinematics and contact mechanics of artificial hip and knee joints’, in *The 14th IFToMM World Congress*. Available at: https://doi.org/10.6567/IFToMM.14TH.WC.OS2.002.

Garcia-Gonzalez, D., Garzon-Hernandez, S. and Arias, A. (2018) ‘A new constitutive model for polymeric matrices: Application to biomedical materials’, *Composites Part B: Engineering*, 139, pp. 117–129. Available at: https://doi.org/10.1016/J.COMPOSITESB.2017.11.045.

Girard, J. (2015) ‘Femoral head diameter considerations for primary total hip arthroplasty’, *Orthopaedics and Traumatology: Surgery and Research*. Elsevier Masson SAS, pp. S25–S29. Available at: https://doi.org/10.1016/j.otsr.2014.07.026.

Glaser, D. *et al.* (2008) ‘Clicking and squeaking: In vivo correlation of sound and separation for different bearing surfaces’, *Journal of Bone and Joint Surgery*, 90(SUPPL. 4), pp. 112–120. Available at: https://doi.org/10.2106/JBJS.H.00627.

Goebel, P. *et al.* (2013) ‘The influence of head diameter and wall thickness on deformations of metallic acetabular press-fit cups and UHMWPE liners: a finite element analysis’, *Journal of Orthopaedic Science*, 18(2), pp. 264–270. Available at: https://doi.org/10.1007/s00776-012-0340-7.

Goyal, P. (2015) *Effects of Acetabular Positioning in Total Hip Arthroplasty*. The University of Western Ontario. Available at: https://ir.lib.uwo.ca/etd.

Gray, H. (1918) *Gray's Anatomy: Open access 'Illustration of a male pelvis' and 'Illustration of right hip joint'*, *Gray's Anatomy (20th edition)*.

Grupp, T.M. *et al.* (2014) 'Biotribology of a vitamin E-stabilized polyethylene for hip arthroplasty – Influence of artificial ageing and third-body particles on wear', *Acta Biomaterialia*, 10(7), pp. 3068–3078. Available at: https://doi.org/10.1016/J.ACTBIO.2014.02.052.

Hadley, M. *et al.* (2018) 'Wear of different materials for total hip replacement under adverse stop-dwell-start in vitro wear simulation conditions', *Proceedings of the Institution of Mechanical Engineers, Part H: Journal of Engineering in Medicine*, 232(12). Available at: https://doi.org/10.1177/0954411918813385.

Haider, H. *et al.* (2012) 'Does Vitamin E–Stabilized Ultrahigh-Molecular-Weight Polyethylene Address Concerns of Cross-Linked Polyethylene in Total Knee Arthroplasty?', *The Journal of Arthroplasty*, 27(3), pp. 461–469. Available at: https://doi.org/10.1016/J.ARTH.2011.03.024.

Halley, D., Glassman, A. and Crowninshield, R.D. (2004) 'Recurrent dislocation after revision total hip replacement with a large prosthetic femoral head. A case report.', *The Journal of bone and joint surgery. American volume*, 86(4), pp. 827–830. Available at: https://doi.org/10.2106/00004623-200404000-00025.

Halma, J.J. *et al.* (2014) 'Edge loading does not increase wear rates of ceramic-on-ceramic and metal-on-polyethylene articulations', *Journal of Biomedical Materials Research Part B: Applied Biomaterials*, 102(8), pp. 1627–1638. Available at: https://doi.org/10.1002/JBM.B.33147.

Hansen, E. and Hassani, A. (2022) 'Quantitative Evaluation of Phase Distribution in UHMWPE as Derived from a Combined Use of NMR FID Analysis and Monte Carlo Simulation', *Applied Magnetic Resonance*, 53(2), pp. 417–439. Available at: https://doi.org/10.1007/S00723-021-01456-6/TABLES/6.

Hara, D. *et al.* (2013) 'Late failure of annealed highly cross-linked polyethylene acetabular liner', *Journal of the Mechanical Behavior of Biomedical Materials*, 28, pp. 206–212. Available at: https://doi.org/10.1016/j.jmbbm.2013.08.003.

Harris, W.H. (2001) ‘Wear and periprosthetic osteolysis the problem’, *Clinical Orthopaedics and Related Research*, (393), pp. 66–70. Available at: https://doi.org/10.1097/00003086-200112000-00007.

Hart, A.J. *et al.* (2013) ‘Which factors determine the wear rate of large-diameter metal-on-metal hip replacements? Multivariate analysis of two hundred and seventy-six components’, *Journal of Bone and Joint Surgery*, 95(8), pp. 678–685. Available at: https://doi.org/10.2106/JBJS.J.01447.

Herrera, L. *et al.* (2007) ‘Hip simulator evaluation of the effect of femoral head size on sequentially cross-linked acetabular liners’, *Wear*, 263(7–12), pp. 1034–1037. Available at: https://doi.org/10.1016/j.wear.2007.02.010.

Higa, M. *et al.* (2014) ‘Effects of adduction, internal rotation, and flexion angles on dislocation for total hip arthroplasty’, *IFMBE Proceedings*, 43, pp. 311–314. Available at: https://doi.org/10.1007/978-3-319-02913-9_79/COVER.

Higgins, B.T. *et al.* (2015) ‘Anterior vs. Posterior Approach for Total Hip Arthroplasty, a Systematic Review and Meta-analysis’, *Journal of Arthroplasty*, 30(3), pp. 419–434. Available at: https://doi.org/10.1016/j.arth.2014.10.020.

Holley, K.G. *et al.* (2005) ‘Impingement of Acetabular Cups in a Hip Simulator’, *The Journal of Arthroplasty*, 20(7), pp. 77–86. Available at: https://doi.org/10.1016/j.arth.2005.04.026.

Hua, X., Li, J., *et al.* (2014) ‘Contact mechanics of modular metal-on-polyethylene total hip replacement under adverse edge loading conditions’, *Journal of Biomechanics*, 47(13), pp. 3303–3309. Available at: https://doi.org/10.1016/j.jbiomech.2014.08.015.

Hua, X., Wang, L., *et al.* (2014) ‘Experimental validation of finite element modelling of a modular metal-on-polyethylene total hip replacement.’, *Proceedings of the Institution of Mechanical Engineers. Part H, Journal of engineering in medicine*, 228(7), pp. 682–692. Available at: https://doi.org/10.1177/0954411914541830.

Hua, X. *et al.* (2016) ‘The contact mechanics and occurrence of edge loading in modular metal-on-polyethylene total hip replacement during daily activities’, *Medical Engineering & Physics*, 38(6), pp. 518–525. Available at: https://doi.org/10.1016/j.medengphy.2016.03.004.

Huff, D.N., Myers, C.A. and Rullkoetter, P.J. (2020) ‘Impact of alignment and kinematic variation on resistive moment and dislocation propensity for THA

with lipped and neutral liners', *Biomechanics and Modeling in Mechanobiology*, 19(4), pp. 1297–1307. Available at: https://doi.org/10.1007/S10237-020-01359-8/FIGURES/9.

Insull, P.J. *et al.* (2014) 'The use of a lipped acetabular liner decreases the rate of revision for instability after total hip replacement', *The Bone & Joint Journal*, 96-B(7), pp. 884–888. Available at: https://doi.org/10.1302/0301-620x.96b7.33658.

Ismail, R. *et al.* (2014) 'Numerical Study of Salat Movements for Total Hip Replacement Patient', *Applied Mechanics and Materials*, 493, pp. 426–431. Available at: https://doi.org/10.4028/WWW.SCIENTIFIC.NET/AMM.493.426.

Jaeger, S. *et al.* (2020) 'Comparison of Different Locking Mechanisms in Total Hip Arthroplasty: Relative Motion between Cup and Inlay', *Materials*, 13(6), p. 1392. Available at: https://doi.org/10.3390/ma13061392.

Jahani, F. *et al.* (2018) 'Development of an explicit finite element model to predict the occurence and severity of edge loading for ceramic-on-polyethylene total hip replacements', in *Orthopaedic Proceedings*. Boston. Available at: https://online.boneandjoint.org.uk/doi/abs/10.1302/1358-992X.99BSUPP_4.ISTA2016-031.

Jahani, F. *et al.* (2021) 'Importance of dynamics in the finite element prediction of plastic damage of polyethylene acetabular liners under edge loading conditions', *Medical Engineering & Physics*, 95, pp. 97–103. Available at: https://doi.org/10.1016/j.medengphy.2021.07.010.

Jamari, J. *et al.* (2014) 'The Effect of Repeated Impingement on UHMWPE Material in Artificial Hip Joint during Salat Activities', *Advanced Materials Research*, 896, pp. 272–275. Available at: https://doi.org/10.4028/WWW.SCIENTIFIC.NET/AMR.896.272.

Jordan, J.M. *et al.* (2009) 'Prevalence of hip symptoms and radiographic and symptomatic hip osteoarthritis in African Americans and Caucasians: The Johnston County osteoarthritis project', *Journal of Rheumatology*, 36(4), pp. 809–815. Available at: https://doi.org/10.3899/jrheum.080677.

Kamada, K. *et al.* (2019) 'Influence of liner offset and locking mechanism on fatigue durability in highly cross-linked polyethylene total hip prostheses', *Journal of Biomedical Materials Research Part B: Applied Biomaterials*, p. jbm.b.34540. Available at: https://doi.org/10.1002/jbm.b.34540.

Kandahari, A.M. *et al.* (2016) 'A review of UHMWPE wear-induced osteolysis: The role for early detection of the immune response', *Bone*

Research. Sichuan University, p. 16014. Available at: https://doi.org/10.1038/boneres.2016.14.

Kang, L. *et al.* (2006) 'A simple fully integrated contact-coupled wear prediction for ultra-high molecular weight polyethylene hip implants', *Proceedings of the Institution of Mechanical Engineers, Part H: Journal of Engineering in Medicine*, 220(1), pp. 33–46. Available at: https://doi.org/10.1243/095441105X69033.

Kelly, N.H. *et al.* (2010) 'High Stress Conditions Do Not Increase Wear of Thin Highly Crosslinked UHMWPE', *Clinical Orthopaedics & Related Research*, 468(2), pp. 418–423. Available at: https://doi.org/10.1007/s11999-009-1154-6.

Keresztury, G. and Földes, E. (1990) 'On the Raman spectroscopic determination of phase distribution in polyethylene', *Polymer Testing*, 9(5), pp. 329–339. Available at: https://doi.org/10.1016/0142-9418(90)90004-W.

Kessler, O. *et al.* (2008) 'Bony impingement affects range of motion after total hip arthroplasty: A subject-specific approach', *Journal of Orthopaedic Research*, 26(4), pp. 443–452. Available at: https://doi.org/10.1002/JOR.20541.

Kim, J.T. and Yoo, J.J. (2016) 'Implant Design in Cementless Hip Arthroplasty', *Hip & Pelvis*, 28(2), p. 65. Available at: https://doi.org/10.5371/hp.2016.28.2.65.

Kiyohara, M. *et al.* (2019) 'Do component position and muscle strength affect the cup-head translation during gait after total hip arthroplasty?', *European Journal of Orthopaedic Surgery and Traumatology*, 29(6), pp. 1263–1269. Available at: https://doi.org/10.1007/S00590-019-02443-1/TABLES/3.

Kluess, D. *et al.* (2007) 'Influence of femoral head size on impingement, dislocation and stress distribution in total hip replacement', *Medical Engineering & Physics*, 29(4), pp. 465–471. Available at: https://doi.org/10.1016/j.medengphy.2006.07.001.

Komistek, R.D. *et al.* (2002) 'IN VIVO COMPARISON OF HIP SEPARATION AFTER METAL-ON-METAL OR METAL-ON-POLYETHYLENE TOTAL HIP ARTHROPLASTY', *The Journal of Bone and Joint Surgery-American Volume*, 84(10), pp. 1836–1841. Available at: https://doi.org/10.2106/00004623-200210000-00015.

Korduba, L.A. *et al.* (2014) *Effect of Acetabular Cup Abduction Angle on Wear of Ultrahigh-Molecular-Weight Polyethylene in Hip Simulator Testing*

AJO DO NOT COPY, *The American Journal of Orthopedics*. Available at: www.amjorthopedics.com.

Korhonen, R.K. *et al.* (2005) 'The effect of geometry and abduction angle on the stresses in cemented UHMWPE acetabular cups-finite element simulations and experimental tests'. Available at: https://doi.org/10.1186/1475-925X-4-32.

Kotwal, R.S. *et al.* (2009) 'Outcome of treatment for dislocation after primary total hip replacement', *J Bone Joint Surg [Br]*, 91, pp. 321–327. Available at: https://doi.org/10.1302/0301-620X.91B3.

Kumakura, T. *et al.* (2009) 'In-Depth Oxidation and Strain Profiles in UHMWPE Acetabular Cups Non-Destructively Studied by Confocal Raman Microprobe Spectroscopy', *Journal of Biomaterials Science, Polymer Edition*, 20(12), pp. 1809–1822. Available at: https://doi.org/10.1163/156856208X386417.

Kumar, A., Bloch, B. V and Esler, C. (2017) 'Trends in total hip arthroplasty in young patients - results from a regional register.', *Hip international : the journal of clinical and experimental research on hip pathology and therapy*, 27(5), pp. 443–448. Available at: https://doi.org/10.5301/hipint.5000485.

Kurtz, S.M. *et al.* (1999) 'Evolution of morphology in UHMWPE following accelerated aging: The effect of heating rates', *Journal of Biomedical Materials Research*, 46(1), pp. 112–120. Available at: https://doi.org/10.1002/(SICI)1097-4636(199907)46:1<112::AID-JBM13>3.0.CO;2-U.

Kurtz, S.M. (2016) *A Primer on UHMWPE*. Third Edit, *UHMWPE Biomaterials Handbook: Ultra High Molecular Weight Polyethylene in Total Joint Replacement and Medical Devices: Third Edition*. Third Edit. Elsevier Inc. Available at: https://doi.org/10.1016/B978-0-323-35401-1.00001-6.

Kurtz, S.M., Edidin, A.A. and Bartel, D.L. (1997) 'The role of backside polishing, cup angle, and polyethylene thickness on the contact stresses in metal-backed acetabular components', *Journal of Biomechanics*, 30(6), pp. 639–642. Available at: https://doi.org/10.1016/S0021-9290(96)00181-9.

Kurtz, S.M. and Ong, K. (2016) *Contemporary Total Hip Arthroplasty: Alternative Bearings*. Third Edit, *UHMWPE Biomaterials Handbook: Ultra High Molecular Weight Polyethylene in Total Joint Replacement and Medical Devices: Third Edition*. Third Edit. Elsevier Inc. Available at: https://doi.org/10.1016/B978-0-323-35401-1.00010-7.

Kurtz, S.M. and Patel, J.D. (2016) *The Clinical Performance of Highly Cross-linked UHMWPE in Hip Replacements*. Third Edit, *UHMWPE Biomaterials Handbook: Ultra High Molecular Weight Polyethylene in Total Joint Replacement and Medical Devices: Third Edition*. Third Edit. Elsevier Inc. Available at: https://doi.org/10.1016/B978-0-323-35401-1.00006-5.

Laerd Statistics (2015) *Statistical tutorials and software guides.*, *https://statistics.laerd.com/*.

Lagaron, J.M. (2002) 'On the use of a Raman spectroscopy band to asses the crystalline lateral packing in polyethylene', *Journal of Materials Science*, 37(19), pp. 4101–4107. Available at: https://doi.org/10.1023/A:1020027601042.

Leslie, I.J. *et al.* (2009) 'High Cup Angle and Microseparation Increase the Wear of Hip Surface Replacements', *Clinical Orthopaedics & Related Research*, 467(9), pp. 2259–2265. Available at: https://doi.org/10.1007/s11999-009-0830-x.

Lespasio, M.J. *et al.* (2018) 'Hip Osteoarthritis: A Primer', *The Permanente Journal*, 22. Available at: https://doi.org/10.7812/TPP/17-084.

Lewinnek, G.E. *et al.* (1978) *Dislocations after total hip-replacement arthroplasties*, *This is an enhanced PDF from The Journal of Bone and Joint Surgery*. Available at: www.jbjs.org.

Lewis, G. and Nyman, J.S. (1999) 'A new method of determining the J-integral fracture toughness of very tough polymers: application to ultra high molecular weight polyethylene.', *Journal of Long-term Effects of Medical Implants*, 9(4), pp. 289–301. Available at: https://europepmc.org/article/med/10847969 (Accessed: 22 February 2024).

Lin, W. *et al.* (2007) 'The application of Raman spectroscopy to three-phase characterization of polyethylene crystallinity', *Polymer Testing*, 26(6), pp. 814–821. Available at: https://doi.org/10.1016/j.polymertesting.2007.05.004.

Lin, Y.-T., Wu, J.S.-S. and Chen, J.-H. (2016) 'The study of wear behaviors on abducted hip joint prostheses by an alternate finite element approach', *Computer Methods and Programs in Biomedicine*, 131, pp. 143–155. Available at: https://doi.org/10.1016/j.cmpb.2016.04.015.

Lindahl, H. (2007) 'Epidemiology of periprosthetic femur fracture around a total hip arthroplasty', *Injury*, 38(6), pp. 651–654. Available at: https://doi.org/10.1016/j.injury.2007.02.048.

Lindalen, E. *et al.* (2019) ‘Low wear rate at 6-year follow-up of vitamin E-infused cross-linked polyethylene: a randomised trial using 32- and 36-mm heads’, *HIP International*, 29(4), pp. 355–362. Available at: https://doi.org/10.1177/1120700018798790.

Lindgren, V. *et al.* (2014) ‘Deep Infection after Total Hip Replacement: A Method for National Incidence Surveillance’, *Infection Control & Hospital Epidemiology*, 35(12), pp. 1491–1496. Available at: https://doi.org/10.1086/678600.

Liu, F. *et al.* (2011) ‘A New Formulation for the Prediction of Polyethylene Wear in Artificial Hip Joints’, *Proceedings of the Institution of Mechanical Engineers, Part H: Journal of Engineering in Medicine*, 225(1), pp. 16–24. Available at: https://doi.org/10.1243/09544119JEIM819.

Liu, F., Fisher, J. and Jin, Z. (2013) ‘Effect of motion inputs on the wear prediction of artificial hip joints’, *Tribology International*, 63, pp. 105–114. Available at: https://doi.org/10.1016/j.triboint.2012.05.029.

Lombardi, A. V *et al.* (2000) ‘An in vivo determination of total hip arthroplasty pistoning during activity’, *The Journal of Arthroplasty*, 15(6), pp. 702–709. Available at: https://doi.org/10.1054/arth.2000.6637.

Lombardo, G. *et al.* (2016) ‘Crystallization pathways to alter the nanostructure and tensile properties of non-irradiated and irradiated, vitamin E stabilized UHMWPE’, *European Polymer Journal*, 75, pp. 354–362. Available at: https://doi.org/10.1016/j.eurpolymj.2015.12.028.

Loving, L. *et al.* (2015) ‘Dual mobility bearings withstand loading from steeper cup-inclinations without substantial wear’, *Journal of Orthopaedic Research*, 33(3), pp. 398–404. Available at: https://doi.org/10.1002/JOR.22774.

Lu, Y.C. *et al.* (2018) ‘Elastoplastic behavior of highly cross-linked and vitamin E-stabilized polyethylene – A biomechanical study’, *Clinical Biomechanics*, 59, pp. 152–158. Available at: https://doi.org/10.1016/J.CLINBIOMECH.2018.09.021.

Lundberg, H.J. *et al.* (2007) ‘Nonidentical and outlier duty cycles as factors accelerating UHMWPE wear in THA: A finite element exploration’, *Journal of Orthopaedic Research*, 25(1), pp. 30–43. Available at: https://doi.org/10.1002/jor.20265.

Macdonald, D., Bowden, A.E. and Kurtz, S.M. (2016) *MicroCT Analysis of Wear and Damage in UHMWPE*. Third Edit, *UHMWPE Biomaterials*

Handbook. Third Edit. Elsevier Inc. Available at: https://doi.org/10.1016/B978-0-323-35401-1/00041-7.

Malito, L.G. *et al.* (2018) 'Material properties of ultra-high molecular weight polyethylene: Comparison of tension, compression, nanomechanics and microstructure across clinical formulations', *Journal of the Mechanical Behavior of Biomedical Materials*, 83, pp. 9–19. Available at: https://doi.org/10.1016/j.jmbbm.2018.03.029.

Malito, L.G. *et al.* (2019) 'Fracture toughness of ultra-high molecular weight polyethylene: A basis for defining the crack-initiation toughness in polymers', *Journal of the Mechanics and Physics of Solids*, 122, pp. 435–449. Available at: https://doi.org/10.1016/j.jmps.2018.09.022.

Marchetti, E. *et al.* (2011) 'Component impingement in total hip arthroplasty: Frequency and risk factors. A continuous retrieval analysis series of 416 cup', *Orthopaedics and Traumatology: Surgery and Research*, 97(2), pp. 127–133. Available at: https://doi.org/10.1016/J.OTSR.2010.12.004.

Matsoukas, G. and Kim, I.Y. (2009) 'Design optimization of a total hip prosthesis for wear reduction', *Journal of Biomechanical Engineering*, 131(5). Available at: https://doi.org/10.1115/1.3049862.

Mattei, L. and Di Puccio, F. (2023) 'Effect of Friction on Finite Element Contact and Wear Predictions of Metal-on-Plastic Hip Replacements', *Biotribology*, 35–36, p. 100230. Available at: https://doi.org/10.1016/j.biotri.2022.100230.

Matthies, A. *et al.* (2011) 'Retrieval analysis of 240 metal-on-metal hip components, comparing modular total hip replacement with hip resurfacing', *Journal of Bone and Joint Surgery - Series B*, 93 B(3), pp. 307–314. Available at: https://doi.org/10.1302/0301-620X.93B3.25551/LETTERTOEDITOR.

Maxian, T.A. *et al.* (1996a) '3-Dimensional sliding/contact computational simulation of total hip wear.', *Clinical Orthopaedics and Related Research*, 333, pp. 41–50.

Maxian, T.A. *et al.* (1996b) 'A sliding-distance-coupled finite element formulation for polyethylene wear in total hip arthroplasty', *Journal of Biomechanics*, 29(5), pp. 687–692. Available at: https://doi.org/10.1016/0021-9290(95)00125-5.

Maxian, T.A. *et al.* (1996c) 'Adaptive finite element modeling of long-term polyethylene wear in total hip arthroplasty', *Journal of Orthopaedic*

Research, 14(4), pp. 668–675. Available at: https://doi.org/10.1002/JOR.1100140424.

Medel, F.J. *et al.* (2007) ‘Comparative fatigue behavior and toughness of remelted and annealed highly crosslinked polyethylenes’, *Journal of Biomedical Materials Research Part B: Applied Biomaterials*, 83B(2), pp. 380–390. Available at: https://doi.org/10.1002/jbm.b.30807.

Medel, F.J. *et al.* (2013) ‘Microstructure, thermooxidation and mechanical behavior of a novel highly linear, vitamin e stabilized, UHMWPE’, *Materials Science and Engineering C*, 33(1), pp. 182–188. Available at: https://doi.org/10.1016/j.msec.2012.08.028.

Medel, F.J. and Furmanski, J. (2016) *Fatigue and Fracture of UHMWPE*. Third Edit, *UHMWPE Biomaterials Handbook*. Third Edit. Elsevier Inc. Available at: https://doi.org/10.1016/B978-0-323-35401-1/00036-3.

Meek, R.M.D. *et al.* (2011) ‘The risk of peri-prosthetic fracture after primary and revision total hip and knee replacement’, *Journal of Bone and Joint Surgery - Series B*, 93 B(1), pp. 96–101. Available at: https://doi.org/10.1302/0301-620X.93B1.25087.

Mitutoyo (2015) *LEGEX Coordinate Measuring Machines*. Available at: https://www2.mitutoyo.co.jp/eng/support/service/catalog/01/E4172_356.pdf (Accessed: 30 October 2023).

Monaghan, B. *et al.* (2017) ‘Randomised controlled trial to evaluate a physiotherapy-led functional exercise programme after total hip replacement’, *Physiotherapy (United Kingdom)*, 103(3), pp. 283–288. Available at: https://doi.org/10.1016/j.physio.2016.01.003.

Moon, N.H. *et al.* (2020) ‘Wear and osteolysis outcomes for highly cross-linked polyethylene in primary total hip arthroplasty compared with conventional polyethylene: a 15- to 18-year single-centre follow-up study’, *HIP International*, p. 112070001989697. Available at: https://doi.org/10.1177/1120700019896970.

Moore, K.D. *et al.* (2008) ‘Early Failure of a Cross-Linked Polyethylene Acetabular Liner’, *The Journal of Bone and Joint Surgery-American Volume*, 90(11), pp. 2499–2504. Available at: https://doi.org/10.2106/JBJS.G.01304.

Muratoglu, O.K. *et al.* (2001) ‘Larger diameter femoral heads used in conjunction with a highly cross-linked ultra-high molecular weight polyethylene: A new concept’, *Journal of Arthroplasty*, 16(8 SUPPL. 1), pp. 24–30. Available at: https://doi.org/10.1054/arth.2001.28376.

Muratoglu, O.K. and Bragdon, C.R. (2016) *Highly Crosslinked and Melted UHMWPE*. Third Edit, *UHMWPE Biomaterials Handbook*. Third Edit. Elsevier Inc. Available at: https://doi.org/10.1016/B978-0-323-35401-1/00015-6.

Mutter, R., Stille, W. and Strobl, G. (1993) 'Transition regions and surface melting in partially crystalline polyethylene: A raman spectroscopic study', *Journal of Polymer Science Part B: Polymer Physics*, 31(1), pp. 99–105. Available at: https://doi.org/10.1002/polb.1993.090310113.

Naylor, C.C. *et al.* (1995) *Raman Spectroscopy Employed for the Determination of the Intermediate Phase in Polyethylene*, *Macromolecules*.

NJR (2023) *National Joint Registry 2023 - 20th Annual Report*. Available at: www.njrcentre.org.uk.

O'Dwyer Lancaster-Jones, O. *et al.* (2018) 'An *in vitro* simulation model to assess the severity of edge loading and wear, due to variations in component positioning in hip joint replacements', *Journal of Biomedical Materials Research Part B: Applied Biomaterials*, 106(5), pp. 1897–1906. Available at: https://doi.org/10.1002/jbm.b.33991.

O'Haver, T. (2022) 'peakfit.m (https://www.mathworks.com/matlabcentral/fileexchange/23611-peakfit-m), MATLAB Central File Exchange. Retrieved August 15, 2022.'

Ong, K.L. *et al.* (2010) 'Risk of Subsequent Revision after Primary and Revision Total Joint Arthroplasty', *Clinical Orthopaedics and Related Research* [Preprint]. Available at: https://doi.org/10.1007/s11999-010-1399-0.

Onişoru, J., Capitanu, L. and Iarovici, A. (2006) 'PREDICTION OF WEAR OF ACETABULUM INSERTS DUE TO MULTIPLE HUMAN ROUTINE ACTIVITIES', *Tribology* , 8, pp. 28–33.

Oral, E. *et al.* (2006) 'Wear Resistance and Mechanical Properties of Highly Cross-linked, Ultrahigh–Molecular Weight Polyethylene Doped With Vitamin E', *The Journal of Arthroplasty*, 21(4), pp. 580–591. Available at: https://doi.org/10.1016/j.arth.2005.07.009.

Oral, E. *et al.* (2009) 'Improved resistance to wear and fatigue fracture in high pressure crystallized vitamin E-containing ultra-high molecular weight polyethylene', *Biomaterials*, 30(10), pp. 1870–1880. Available at: https://doi.org/10.1016/j.biomaterials.2008.12.029.

Oral, E., Malhi, A. and Muratoglu, O. (2006) ‘Mechanisms of decrease in fatigue crack propagation resistance in irradiated and melted UHMWPE’, *Biomaterials*, 27(6), pp. 917–925. Available at: https://doi.org/10.1016/j.biomaterials.2005.06.025.

Partridge, S. (2016) *Wear and rim damage of UHMWPE acetabular cups in total hip replacement*. University of Leeds.

Partridge, S., Buckley, P., *et al.* (2018) ‘A novel method to measure rim deformation in UHMWPE acetabular liners’, *Medical Engineering & Physics*, 59, pp. 56–62. Available at: https://doi.org/10.1016/j.medengphy.2018.04.023.

Partridge, S., Tipper, J.L., *et al.* (2018) ‘Evaluation of a new methodology to simulate damage and wear of polyethylene hip replacements subjected to edge loading in hip simulator testing’, *Journal of Biomedical Materials Research Part B: Applied Biomaterials*, 106(4), pp. 1456–1462. Available at: https://doi.org/10.1002/jbm.b.33951.

Pascaud, R.S. *et al.* (1997) ‘Influence of gamma-irradiation sterilization and temperature on the fracture toughness of ultra-high-molecular-weight polyethylene’, *Biomaterials*, 18(10), pp. 727–735. Available at: https://doi.org/10.1016/S0142-9612(96)00207-4.

Patil, S. *et al.* (2003) ‘Polyethylene wear and acetabular component orientation.’, *The Journal of bone and joint surgery. American volume*, 85-A Suppl 4(SUPPL. 4), pp. 56–63. Available at: https://doi.org/10.2106/00004623-200300004-00007.

Paxton, E.W. *et al.* (2019) ‘An international comparison of THA patients, implants, techniques, and survivorship in Sweden, Australia, and the United States’, *Acta Orthopaedica*, 90(2), pp. 148–152. Available at: https://doi.org/10.1080/17453674.2019.1574395.

Pedersen, D.R., Callaghan, J.J. and Brown, T.D. (2005) ‘Activity-dependence of the “safe zone” for impingement versus dislocation avoidance’, *Medical Engineering & Physics*, 27(4), pp. 323–328. Available at: https://doi.org/10.1016/j.medengphy.2004.09.004.

Penmetsa, J.R. *et al.* (2006) ‘Influence of polyethylene creep behavior on wear in total hip arthroplasty’, *Journal of Orthopaedic Research*, 24(3), pp. 422–427. Available at: https://doi.org/10.1002/jor.20042.

Perticarini, L., Rossi, S.M.P. and Benazzo, F. (2020) ‘Unstable total hip replacement: why? Clinical and radiological aspects’, *HIP International*,

30(2_suppl), pp. 37–41. Available at: https://doi.org/10.1177/1120700020971725.

Peters, R.M. *et al.* (2020) ‘Patient Characteristics Influence Revision Rate of Total Hip Arthroplasty: American Society of Anesthesiologists Score and Body Mass Index Were the Strongest Predictors for Short-Term Revision After Primary Total Hip Arthroplasty’, *Journal of Arthroplasty*, 35(1), pp. 188–192.e2. Available at: https://doi.org/10.1016/j.arth.2019.08.024.

Pezzotti, G. *et al.* (2007) ‘Confocal Raman spectroscopic analysis of cross-linked ultra-high molecular weight polyethylene for application in artificial hip joints’, *Journal of Biomedical Optics*, 12(1), p. 014011. Available at: https://doi.org/10.1117/1.2710247.

Pezzotti, G. (2017) ‘Raman spectroscopy of biomedical polyethylenes’, *Acta Biomaterialia*, 55, pp. 28–99. Available at: https://doi.org/10.1016/j.actbio.2017.03.015.

Pigeon, M., Prud’homme, R.E. and Pézolet, M. (1991) ‘Characterization of Molecular Orientation in Polyethylene by’, *Macromolecules*, 24, pp. 5687–5694.

Pivec, R. *et al.* (2012) ‘Hip arthroplasty’, in *The Lancet*. Elsevier, pp. 1768–1777. Available at: https://doi.org/10.1016/S0140-6736(12)60607-2.

Plank, G.R. *et al.* (2007) ‘Contact stress assessment of conventional and highly crosslinked ultra high molecular weight polyethylene acetabular liners with finite element analysis and pressure sensitive film’, *Journal of Biomedical Materials Research Part B: Applied Biomaterials*, 80B(1), pp. 1–10. Available at: https://doi.org/10.1002/jbm.b.30560.

Private communication with Dr L. Etchels (no date).

Private communication with Dr S. Tarsuslugil (no date).

Pruitt, L.A. (2005) ‘Deformation, yielding, fracture and fatigue behavior of conventional and highly cross-linked ultra high molecular weight polyethylene’, *Biomaterials*, 26(8), pp. 905–915. Available at: https://doi.org/10.1016/j.biomaterials.2004.03.022.

Pryce, G.M. (2019) *Polyethylene acetabular liner rim damage in total hip replacements*. The University of Leeds.

Puértolas, J.A. *et al.* (2006) ‘Influence of the remelting process on the fatigue behavior of electron beam irradiated UHMWPE’, *Journal of Biomedical*

Materials Research - Part B Applied Biomaterials, 76(2), pp. 346–353. Available at: https://doi.org/10.1002/jbm.b.30378.

Puppulin, L. *et al.* (2016) 'Surface modifications induced by in-vitro wear and oxidation on γ-irradiated UHMWPE hip liners belonging to different commercial generations', *Journal of the Mechanical Behavior of Biomedical Materials*, 53, pp. 414–426. Available at: https://doi.org/10.1016/j.jmbbm.2015.08.035.

Renishaw (2023) *Automatic intelligent background removal*. Available at: https://www.renishaw.com/en/automatic-intelligent-background-removal--25934 (Accessed: 12 July 2023).

Ries, M.D. and Pruitt, L. (2005) 'Effect of Cross-linking on the Microstructure and Mechanical Properties of Ultra-High Molecular Weight Polyethylene', *Clinical Orthopaedics and Related Research*, 440(NA;), pp. 149–156. Available at: https://doi.org/10.1097/01.blo.0000185310.59202.e5.

Rimnac, C. and Pruitt, L. (2008) 'How do material properties influence wear and fracture mechanisms?', *Journal of the American Academy of Orthopaedic Surgeons*, 16, pp. S94–S100. Available at: https://doi.org/10.5435/00124635-200800001-00019.

Rowell, S.L. *et al.* (2007) 'Failure of a Marathon™ UHMWPE acetabular liner: a case study', in.

Rowell, S.L. *et al.* (2011) 'In Vivo Performance of Highly Cross-linked UHMWPE', in *The 5th UHMWPE International Meeting*. Philidelphia.

Rull, F. *et al.* (1993) 'Estimation of crystallinity in polyethylene by Raman spectroscopy', *Journal of Raman Spectroscopy*, 24(8), pp. 545–550. Available at: https://doi.org/10.1002/jrs.1250240813.

Saikko, V. (2006) 'Effect of contact pressure on wear and friction of ultra-high molecular weight polyethylene in multidirectional sliding', *Proceedings of the Institution of Mechanical Engineers, Part H: Journal of Engineering in Medicine*, 220(7), pp. 723–731. Available at: https://doi.org/10.1243/09544119JEIM146.

Saikko, V. (2017) 'Effect of Contact Area on the Wear and Friction of UHMWPE in Circular Translation Pin-on-Disk Tests', *Journal of Tribology*, 139(6). Available at: https://doi.org/10.1115/1.4036448.

Saikko, V. (2019) 'Wear and friction of thin, large-diameter acetabular liners made from highly cross-linked, vitamin-E-stabilized UHMWPE against CoCr

femoral heads', *Wear*, 432–433, p. 202948. Available at: https://doi.org/10.1016/j.wear.2019.202948.

Santaguida, P.L. *et al.* (2008) 'Patient characteristics affecting the prognosis of total hip and knee joint arthroplasty: A systematic review', *Canadian Journal of Surgery*, 51(6), pp. 428–436. Available at: https://doi.org/10.1016/S0008-428X(08)50119-6.

Saputra, E. *et al.* (2013) 'Finite Element Analysis of Artificial Hip Joint Movement During Human Activities', *Procedia Engineering*, 68, pp. 102–108. Available at: https://doi.org/10.1016/j.proeng.2013.12.154.

Saputra, E. *et al.* (2014) 'Numerical Simulation of Artificical Hip Joint Movement for Western and Japanese-Style Activities', *Jurnal Teknologi*, 66(3), pp. 2180–3722. Available at: www.jurnalteknologi.utm.my (Accessed: 3 August 2023).

Scheerlinck, T. and Casteleyn, P.-P. (2006) 'The design features of cemented femoral hip implants', *The Journal of Bone and Joint Surgery. British volume*, 88-B(11), pp. 1409–1418. Available at: https://doi.org/10.1302/0301-620X.88B11.17836.

Scifert, C.F. *et al.* (1997) 'Effects of acetabular component lip design on dislocation resistance in THA', *Advances in Bioengineering*, 36. Available at: http://asmedigitalcollection.asme.org/IMECE/proceedings-pdf/IMECE97/18237/295/6856841/295_1_imece1997-0345.pdf (Accessed: 4 August 2023).

Scifert, C.F. *et al.* (1998) 'A Finite Element Analysis of Factors Influencing Total Hip Dislocation', *Clinical Orthopaedics and Related Research*, 355(355), pp. 152–162. Available at: https://doi.org/10.1097/00003086-199810000-00016.

Scifert, C.F., Brown, T.D. and Lipman, J.D. (1998) 'Computational Analysis of the Dislocation Resistance of a New Total Hip Component Design', in *Advances in Bioengineering*. American Society of Mechanical Engineers, pp. 229–230. Available at: https://doi.org/10.1115/IMECE1998-0114.

Seagrave, K.G. *et al.* (2017) 'Acetabular cup position and risk of dislocation in primary total hip arthroplasty A systematic review of the literature Acetabular cup position and risk of dislocation in primary total hip arthroplasty A systematic review of the literature', *Acta Orthopaedica*, 88(1), pp. 10–17. Available at: https://doi.org/10.1080/17453674.2016.1251255.

Shen, F.-W., Lu, Z. and McKellop, H.A. (2011) ‘Wear versus Thickness and Other Features of 5-Mrad Crosslinked UHMWPE Acetabular Liners’, *Clinical Orthopaedics & Related Research*, 469(2), pp. 395–404. Available at: https://doi.org/10.1007/s11999-010-1555-6.

Sheth, D. *et al.* (2015) ‘Anterior and Anterolateral Approaches for THA Are Associated With Lower Dislocation Risk Without Higher Revision Risk’, *Clinical Orthopaedics and Related Research*, 473(11), pp. 3401–3408. Available at: https://doi.org/10.1007/s11999-015-4230-0.

Sheth, Neil P *et al.* (2016) ‘Evaluation and management of chronic total hip instability’, *Article in Bone and Joint Journal*, 98(1). Available at: https://doi.org/10.1302/0301-620X.98B1.36516.

Shia, D.S. *et al.* (2009) ‘THA with highly cross-linked polyethylene in patients 50 years or younger’, *Clinical Orthopaedics and Related Research*, 467(8), pp. 2059–2065. Available at: https://doi.org/10.1007/s11999-008-0697-2.

Silverman, E.J., Ashley, B. and Sheth, N.P. (2016) ‘Metal-on-metal total hip arthroplasty: is there still a role in 2016?’, *Current Reviews in Musculoskeletal Medicine*. Humana Press Inc., pp. 93–96. Available at: https://doi.org/10.1007/s12178-016-9323-1.

Simis, K.S. *et al.* (2006) ‘The combined effects of crosslinking and high crystallinity on the microstructural and mechanical properties of ultra high molecular weight polyethylene’, *Biomaterials*, 27(9), pp. 1688–1694. Available at: https://doi.org/10.1016/j.biomaterials.2005.09.033.

Sirimamilla, A., Furmanski, J. and Rimnac, C. (2013) ‘Peak stress intensity factor governs crack propagation velocity in crosslinked ultrahigh-molecular-weight polyethylene’, *Journal of Biomedical Materials Research Part B: Applied Biomaterials*, 101B(3), pp. 430–435. Available at: https://doi.org/10.1002/jbm.b.32850.

Sirimamilla, A. and Rimnac, C.M. (2019) ‘Crack initiation from a clinically relevant notch in a highly-crosslinked UHMWPE subjected to static and cyclic loading’, *Journal of the Mechanical Behavior of Biomedical Materials*, 91, pp. 366–372. Available at: https://doi.org/10.1016/j.jmbbm.2018.12.032.

Sirimamilla, P.A., Rimnac, C.M. and Furmanski, J. (2018) ‘Viscoplastic crack initiation and propagation in crosslinked UHMWPE from clinically relevant notches up to 0.5 mm radius’, *Journal of the Mechanical Behavior of Biomedical Materials*, 77, pp. 73–77. Available at: https://doi.org/10.1016/j.jmbbm.2017.08.030.

Sobieraj, M.C. *et al.* (2008) ‘Notched stress–strain behavior of a conventional and a sequentially annealed highly crosslinked UHMWPE’, *Biomaterials*, 29(35), pp. 4575–4583. Available at: https://doi.org/10.1016/j.biomaterials.2008.08.010.

Sobieraj, M.C. *et al.* (2013) ‘Monotonic and fatigue behavior of five clinically relevant conventional and highly crosslinked UHMWPEs in the presence of stress concentrations’, *Journal of the Mechanical Behavior of Biomedical Materials*, 28, pp. 244–253. Available at: https://doi.org/10.1016/J.JMBBM.2013.07.024.

Sobieraj, M.C., Kurtz, S.M. and Rimnac, C.M. (2005) ‘Notch strengthening and hardening behavior of conventional and highly crosslinked UHMWPE under applied tensile loading’, *Biomaterials*, 26(17), pp. 3411–3426. Available at: https://doi.org/10.1016/j.biomaterials.2004.09.031.

Sobieraj, M.C. and Rimnac, C.M. (2009) ‘Ultra high molecular weight polyethylene: Mechanics, morphology, and clinical behavior’, *Journal of the Mechanical Behavior of Biomedical Materials*, 2(5), pp. 433–443. Available at: https://doi.org/10.1016/j.jmbbm.2008.12.006.

Søren Solgaard and Anne Grete Kjersgaard (2014) ‘Increased risk for early periprosthetic fractures after uncemented total hip replacement’, *Danish Medical Journal*, 61(2). Available at: www.danmedj.dk.

Spiegelberg, S., Kozak, A. and Braithwaite, G. (2016) *Characterization of Physical, Chemical, and Mechanical Properties of UHMWPE*. Third Edit, *UHMWPE Biomaterials Handbook: Ultra High Molecular Weight Polyethylene in Total Joint Replacement and Medical Devices: Third Edition*. Third Edit. Elsevier Inc. Available at: https://doi.org/10.1016/B978-0-323-35401-1.00029-6.

de Steiger, R.N., Lorimer, M. and Solomon, M. (2015) ‘What Is the Learning Curve for the Anterior Approach for Total Hip Arthroplasty?’, *Clinical Orthopaedics and Related Research*, 473(12), pp. 3860–3866. Available at: https://doi.org/10.1007/s11999-015-4565-6.

Stephens, C.P. *et al.* (2005) ‘The effect of dose rate on the crystalline lamellar thickness distribution in gamma-radiation of UHMWPE’, *Nuclear Instruments and Methods in Physics Research Section B: Beam Interactions with Materials and Atoms*, 236(1–4), pp. 540–545. Available at: https://doi.org/10.1016/j.nimb.2005.04.037.

Strobl, G.R. and Hagedorn, W. (1978) ‘Raman spectroscopic method for determining the crystallinity of polyethylene’, *Journal of Polymer Science: Polymer Physics Edition*, 16(7), pp. 1181–1193. Available at: https://doi.org/10.1002/pol.1978.180160704.

Sultan, P.G. *et al.* (2002) ‘Independent contribution of elevated-rim acetabular liner and femoral head size to the stability of total hip implants’, *Journal of Arthroplasty*, 17(3), pp. 289–292. Available at: https://doi.org/10.1054/arth.2002.30415.

Taddei, P. *et al.* (2002) ‘Vibrational spectroscopy of ultra-high molecular weight polyethylene hip prostheses: influence of the sterilisation method on crystallinity and surface oxidation’, *Journal of Molecular Structure*, 613(1–3), pp. 121–129. Available at: https://doi.org/10.1016/S0022-2860(02)00141-2.

Taddei, P., Di Foggia, M. and Affatato, S. (2011) ‘Raman characterisation of conventional and cross-linked polyethylene in acetabular cups run on a hip joint simulator’, *Journal of Raman Spectroscopy*, 42(6), pp. 1344–1352. Available at: https://doi.org/10.1002/jrs.2867.

Takahashi, Y. *et al.* (2010) ‘Raman tensor analysis of ultra-high molecular weight polyethylene and its application to study retrieved hip joint components’, *Acta Biomaterialia*, 6(9), pp. 3583–3594. Available at: https://doi.org/10.1016/j.actbio.2010.02.051.

Takahashi, Y., Masaoka, T., Pezzotti, G., *et al.* (2014) ‘Highly Cross-Linked Polyethylene in Total Hip and Knee Replacement: Spatial Distribution of Molecular Orientation and Shape Recovery Behavior’, *BioMed Research International*, 2014, pp. 1–13. Available at: https://doi.org/10.1155/2014/808369.

Takahashi, Y., Sugano, N., *et al.* (2014) ‘Raman spectroscopic study of remelting and annealing-induced effects on microstructure and compressive deformation behavior of highly crosslinked UHMWPE for total hip arthroplasty’, *Journal of Biomedical Materials Research - Part B Applied Biomaterials*, 102(8), pp. 1762–1770. Available at: https://doi.org/10.1002/jbm.b.33164.

Takahashi, Y., Yamamoto, K., *et al.* (2014) ‘Strain-induced microstructural rearrangement in ultra-high molecular weight polyethylene for hip joints: A comparison between conventional and vitamin E-infused highly-crosslinked liners’, *Journal of the Mechanical Behavior of Biomedical Materials*, 31, pp. 31–44. Available at: https://doi.org/10.1016/j.jmbbm.2012.12.009.

Takahashi, Y., Masaoka, T., Yamamoto, K., *et al.* (2014) ‘Vitamin-E blended and infused highly cross-linked polyethylene for total hip arthroplasty: A comparison of three-dimensional crystalline morphology and strain recovery behavior’, *Journal of the Mechanical Behavior of Biomedical Materials*, 36, pp. 59–70. Available at: https://doi.org/10.1016/j.jmbbm.2014.04.004.

Takahashi, Y. *et al.* (2015) ‘Mechanisms of plastic deformation in highly cross-linked UHMWPE for total hip components—The molecular physics viewpoint’, *Journal of the Mechanical Behavior of Biomedical Materials*, 42, pp. 43–53. Available at: https://doi.org/10.1016/j.jmbbm.2014.11.002.

Takahashi, Y., Tateiwa, T., Pezzotti, G., *et al.* (2016) ‘Improved Resistance to Neck-Liner Impingement in Second-Generation Highly Crosslinked Polyethylene—The Role of Vitamin E and Crosslinks’, *The Journal of Arthroplasty*, 31(12), pp. 2926–2932. Available at: https://doi.org/10.1016/j.arth.2016.05.049.

Takahashi, Y., Tateiwa, T., Shishido, T., *et al.* (2016a) ‘Post-deformation shape-recovery behavior of vitamin E-diffused, radiation crosslinked polyethylene acetabular components’, *Journal of the Mechanical Behavior of Biomedical Materials*, 63, pp. 399–406. Available at: https://doi.org/10.1016/j.jmbbm.2016.07.015.

Takahashi, Y., Tateiwa, T., Shishido, T., *et al.* (2016b) ‘Size and thickness effect on creep behavior in conventional and vitamin E-diffused highly crosslinked polyethylene for total hip arthroplasty’, *Journal of the Mechanical Behavior of Biomedical Materials*, 62, pp. 399–406. Available at: https://doi.org/10.1016/j.jmbbm.2016.05.020.

Takahashi, Y., Pezzotti, G. and Yamamoto, K. (2016) ‘On the physical and structural effects of vitamin-E blending in highly cross-linked polyethylene for total hip arthroplasty’, in *Orthopaedic Proceedings*. Available at: https://online.boneandjoint.org.uk/doi/abs/10.1302/1358-992X.98BSUPP_4.ISTA2014-044.

Takahashi, Y., Yamamoto, K. and Pezzotti, G. (2015) ‘Effects of vitamin E blending on plastic deformation mechanisms of highly crosslinked ultrahigh molecular weight polyethylene (HXL-UHMWPE) in total hip arthroplasty’, *Acta Biomaterialia*, 15, pp. 227–236. Available at: https://doi.org/10.1016/j.actbio.2014.12.022.

Tapash, A., Deslauriers, P.J. and White, J.L. (2015) ‘Simple NMR Experiments Reveal the Influence of Chain Length and Chain Architecture on the Crystalline/Amorphous Interface in Polyethylenes’, *Macromolecules*,

48, pp. 3040–3048. Available at: https://doi.org/10.1021/acs.macromol.5b00475.

Taylor, M. and Prendergast, P.J. (2015) ‘Four decades of finite element analysis of orthopaedic devices: Where are we now and what are the opportunities?’, *Journal of Biomechanics*, 48(5), pp. 767–778. Available at: https://doi.org/10.1016/j.jbiomech.2014.12.019.

The Turing Way Community (2022) *‘Guide for Reproducible Research - Definitions’*, *The Turing Way: A handbook for reproducible, ethical and collaborative research.*

Tower, S.S. *et al.* (2007) ‘Rim Cracking of the Cross-Linked Longevity Polyethylene Acetabular Liner After Total Hip Arthroplasty’, *The Journal of Bone & Joint Surgery*, 89(10), pp. 2212–2217. Available at: https://doi.org/10.2106/JBJS.F.00758.

Traina, F. *et al.* (2012) ‘Risk factors for ceramic liner fracture after total hip arthroplasty’. Available at: https://doi.org/10.5301/HIP.2012.10339.

Troelsen, A. *et al.* (2013) ‘A Review of Current Fixation Use and Registry Outcomes in Total Hip Arthroplasty: The Uncemented Paradox’, *Clinical Orthopaedics and Related Research*, 471, pp. 2052–2059. Available at: https://doi.org/10.1007/s11999-013-2941-7.

Trommer, R.M. *et al.* (2015) ‘Multi-Scale Evaluation of Wear in UHMWPE-Metal Hip Implants Tested in a hip Joint Simulator’, *Biotribology*, 4, pp. 1–11. Available at: https://doi.org/10.1016/j.biotri.2015.08.001.

Tsai, T.Y. *et al.* (2014) ‘In-vivo 6 degrees-of-freedom kinematics of metal-on-polyethylene total hip arthroplasty during gait’, *Journal of Biomechanics*, 47(7), pp. 1572–1576. Available at: https://doi.org/10.1016/J.JBIOMECH.2014.03.012.

Tsai, T.-Y., Dimitriou, D., *et al.* (2015) ‘Asymmetric hip kinematics during gait in patients with unilateral total hip arthroplasty: In vivo 3-dimensional motion analysis’, *Journal of Biomechanics*, 48(4), pp. 555–559. Available at: https://doi.org/10.1016/j.jbiomech.2015.01.021.

Tsai, T.-Y., Li, J.-S., *et al.* (2015) ‘Does component alignment affect gait symmetry in unilateral total hip arthroplasty patients?’, *Clinical Biomechanics*, 30(8), pp. 802–807. Available at: https://doi.org/10.1016/j.clinbiomech.2015.06.010.

Tsikandylakis, G. *et al.* (2018) ‘Head size in primary total hip arthroplasty’, *EFORT Open Reviews*, 3(5), pp. 225–231. Available at: https://doi.org/10.1302/2058-5241.3.170061.

Turell, M.B. and Bellare, A. (2004) ‘A study of the nanostructure and tensile properties of ultra-high molecular weight polyethylene’, *Biomaterials*, 25(17), pp. 3389–3398. Available at: https://doi.org/10.1016/j.biomaterials.2003.10.027.

Unpublished report received by private communication with Dr M. Al-Hajjar (no date).

Urriés, I. *et al.* (2004) ‘Comparative cyclic stress-strain and fatigue resistance behavior of electron-beam- and gamma-irradiated ultrahigh molecular weight polyethylene’, *Journal of Biomedical Materials Research - Part B Applied Biomaterials*, 70(1), pp. 152–160. Available at: https://doi.org/10.1002/jbm.b.30033.

Varadarajan, R. and Rimnac, C.M. (2008) ‘Evaluation of J-initiation fracture toughness of ultra-high-molecular-weight polyethylene used in total joint replacements’, *Polymer Testing*, 27(5), pp. 616–620. Available at: https://doi.org/10.1016/j.polymertesting.2008.03.007.

Vasiljeva, K. *et al.* (2020) ‘Dynamic Acetabular Cup Version in Total Hip Arthroplasty Patients’, in *Orthopaedic Proceedings*.

Waewsawangwong, W. and Goodman, S.B. (2012) ‘Unexpected Failure of Highly Cross-Linked Polyethylene Acetabular Liner’, *The Journal of Arthroplasty*, 27(2), pp. 323.e1-323.e4. Available at: https://doi.org/10.1016/j.arth.2011.04.010.

Wang, A., Essner, A. and Klein, R. (2001) ‘Effect of contact stress on friction and wear of ultra-high molecular weight polyethylene in total hip replacement’, in *Proceedings of the Institution of Mechanical Engineers, Part H: Journal of Engineering in Medicine*, pp. 133–139. Available at: https://doi.org/10.1243/0954411011533698.

Wang, L. *et al.* (2019) ‘Finite element analysis of polyethylene wear in total hip replacement: A literature review’, *Proceedings of the Institution of Mechanical Engineers, Part H: Journal of Engineering in Medicine*, 233(11), pp. 1067–1088. Available at: https://doi.org/10.1177/0954411919872630.

Wannomae, K.K. *et al.* (2006) ‘The effect of real-time aging on the oxidation and wear of highly cross-linked UHMWPE acetabular liners’, *Biomaterials*,

27(9), pp. 1980–1987. Available at: https://doi.org/10.1016/J.BIOMATERIALS.2005.10.002.

Weber, M. *et al.* (2022) 'Which Safe Zone Is Safe in Total Hip Arthroplasty? The Effect of Bony Impingement', *Journal of Personalized Medicine 2022, Vol. 12, Page 812*, 12(5), p. 812. Available at: https://doi.org/10.3390/JPM12050812.

Wiersma, J. and Sain, T. (2023) 'A coupled viscoplastic-damage constitutive model for semicrystalline polymers', *Mechanics of Materials*, 176, p. 104527. Available at: https://doi.org/10.1016/J.MECHMAT.2022.104527.

Wilkinson, J.M. *et al.* (2005) 'Polyethylene wear rate and osteolysis: Critical threshold versus continuous dose-response relationship', *Journal of Orthopaedic Research*, 23(3), pp. 520–525. Available at: https://doi.org/10.1016/j.orthres.2004.11.005.

Williams, M. and DeVries, K. (1970) 'Strain Rate and Cyclic Effects on Bond Rupture During Flow in Polymers.', in *Proceedings of the Fifth International Congress on Rheology*.

Williams, S. *et al.* (2003) 'Wear and deformation of ceramic-on-polyethylene total hip replacements with joint laxity and swing phase microseparation', *Proceedings of the Institution of Mechanical Engineers, Part H: Journal of Engineering in Medicine*, 217(2), pp. 147–153. Available at: https://doi.org/10.1243/09544110360579367.

Williams, S. *et al.* (2004) 'Metal-on-metal bearing wear with different swing phase loads', *Journal of Biomedical Materials Research - Part B Applied Biomaterials*, 70(2), pp. 233–239. Available at: https://doi.org/10.1002/JBM.B.30052.

Willie, B.M. *et al.* (2006) 'Oxidative degradation in highly cross-linked and conventional polyethylene after 2 years of real-time shelf aging', *Biomaterials*, 27(10), pp. 2275–2284. Available at: https://doi.org/10.1016/J.BIOMATERIALS.2005.11.010.

Won, Y.S. *et al.* (2005) 'Impingement in total hip arthroplasty: A study of retrieved acetabular components', *Journal of Arthroplasty*, 20(4), pp. 427–435. Available at: https://doi.org/10.1016/j.arth.2004.09.058.

Wu, G.L. *et al.* (2016) 'Hip squeaking after ceramic-on-ceramic total hip arthroplasty', *Chinese Medical Journal*, 129(15), pp. 1861–1866. Available at: https://doi.org/10.4103/0366-6999.186654/ASSET/9217FA49-35D0-

4DF5-976B-CCC0E9A29907/ASSETS/GRAPHIC/0366-6999-129-15-017-F001.PNG.

Wyatt, M. *et al.* (2014) ‘Survival outcomes of cemented compared to uncemented stems in primary total hip replacement’. Available at: https://doi.org/10.5312/wjo.v5.i5.591.

Yao, Y., Jiang, S. and Rastogi, S. (2014) ‘13C solid state NMR characterization of structure and orientation development in the narrow and broad molar mass disentangled UHMWPE’, *Macromolecules*, 47(4), pp. 1371–1382. Available at: https://doi.org/10.1021/MA402232C/SUPPL_FILE/MA402232C_SI_001.PDF.

Zerbi, G. *et al.* (1989) ‘Structural depth profiling in polyethylene films by multiple internal reflection infra-red spectroscopy’, *Polymer*, 30(12), pp. 2324–2327. Available at: https://doi.org/10.1016/0032-3861(89)90269-3.

Zijlstra, W.P. *et al.* (2017) ‘Effect of femoral head size and surgical approach on risk of revision for dislocation after total hip arthroplasty: An analysis of 166,231 procedures in the Dutch Arthroplasty Register (LROI)’, *Acta Orthopaedica*, 88(4), pp. 395–401. Available at: https://doi.org/10.1080/17453674.2017.1317515.